Numerical modelling of landslide behaviour

Author:
Caitlin Chalk

Supervisors:
Prof. Raul Fuentes
Dr. Duncan Borman
Dr. William Murphy
Prof. Manuel Pastor
Prof. Jeff Peakall
Dr. Andrew Sleigh

A thesis submitted in accordance with the requirements for the degree of Doctor of Philosophy

University of Leeds

CDT in Fluid Dynamics

School of Computing

July, 2019

Declaration of Authorship

The candidate confirms that the work submitted is her own and that appropriate credit has been given where reference has been made to the work of others.

UNIVERSITY OF LEEDS

Abstract

Faculty of Engineering
School of Computing

Doctor of Philosophy

Numerical modelling of landslide behaviour

by Caitlin Chalk

Landslides exhibit complicated and destructive behaviour with disastrous consequences. A landslide event is preceded by slope failure, which is governed by laws of soil mechanics. Once initiated, landslides often propagate downslope at rapid rates, exhibiting fluid-like behaviour. Landslide propagation is therefore frequently characterised by laws of fluid dynamics. Numerical models are vital for an improved understanding of these catastrophic events. Existing models are incapable of adequately simulating the dynamics of both initiation and propagation. Smoothed Particle Hydrodynamics (SPH) is a meshless method that is able to capture large displacements and rapid velocities, and it has been frequently applied to simulate landslide propagation. However, SPH is susceptible to numerical instabilities, that are particularly detrimental with regards to simulations of soil. These must be eliminated for SPH to be an ideal tool for general landslide modelling. The majority of approaches at removing the numerical instabilities from SPH are not universal – some are applicable for small displacements problems only, while others require the tuning of artificial model parameters. In this research, a novel numerical model is developed capable of accurately simulating landslide behaviour – including initiation and propagation. The numerical model – Stress-Particle SPH – removes instabilities in a way that does not require artificial parameter tuning. The method is an extension of SPH, and involves calculating velocities and stresses on two separate sets of particles – nodes and stress-points. Previous literature suggests that the addition of stress-points have the potential to effectively stabilise SPH. Despite this, their implementation within SPH is relatively unexplored, and stress-points have only been applied to a limited range of problems. In this research, Stress-Particle SPH is extended for applicability to landslide behaviour, allowing the numerically stable simulation of high displacement problems with Stress-Particle SPH for the first time. The developments presented in this research offer the potential for SPH to tackle a broad range of problems beyond its current capabilities.

Acknowledgements

First of all, I would like to thank my primary supervisor, Prof. Raul Fuentes, for his guidance over the past four years. He has provided me with consistent support and encouragement with my work, and never doubted my abilities. It has been a pleasure to be one of his PhD students. I would also like to thank my other supervisors at the University of Leeds - Jeff Peakall, Duncan Borman, Andy Sleigh and Bill Murphy. Their input has been extremely helpful. I'd particularly like to thank Jeff for the extensive comments on my thesis drafts, and Duncan for the lengthy discussions on the numerical modelling.

The completion and analysis of the experiments that I conducted as part of my research would not have been possible if it weren't for the help and guidance of Gareth Keevil, Rob Thomas and Helena Brown. They put in a tremendous amount of effort, and ensured the smooth (and often fun) execution of the experiments. I am extremely grateful for this.

During my research, I made several trips to the Technical University of Madrid to visit my external supervisor Prof. Manuel Pastor. The time spent here, with Manuel's advice and insight into landslide modelling, was invaluable to my progression. I'd like to thank everyone at the department – Manuel, Ângel, Saeid, Miguel, Diego, Chuan – for welcoming me to Madrid, and making my time there really enjoyable.

As part of the CDT in Fluid Dynamics, my fellow cohort members have created a fun and positive working environment for the duration of this course. This has been via work-related discussions, lunch time crosswords, games of ping pong and pints in the pub. I'd especially like to thank Hannah, for being an amazing housemate and an even better friend for the past four years. Also, a special thanks goes to Claire, the CDT centre manager, for her efforts and support for all CDT students.

The support that I've received from my family and friends has made everything easier. Thank you to my Mum, Dad and sister Aimee for your understanding and encouragement. Also to my best friends, for your patience over the past year in particular. Last but certainly not least, thank you Freddie for everything that you do to take care of me. This would have definitely been much harder without you.

Contents

Declaration of Authorship iii

Abstract v

Acknowledgements vii

1 Introduction 1

2 Background and literature review 7
2.1 Introduction . . . 7
2.2 Soil behaviour: an application to landslides . . . 8
2.2.1 Landslide initiation . . . 10
2.2.2 Landslide propagation . . . 11
2.2.3 Physical models . . . 12
2.3 Mathematical modelling of soil: an application to landslides . . . 12
2.3.1 Soil mechanics models . . . 13
2.3.2 Fluid dynamics models . . . 15
2.3.3 Depth-integrated models . . . 16
2.3.4 Two-phase models . . . 17
2.4 Numerical models for the simulation of soil behaviour and landslides 18
2.5 Shortcomings of SPH and available solutions . . . 23
2.5.1 Zero-energy modes . . . 25
2.5.2 Tensile instability . . . 28
2.6 Conclusion . . . 33

3 Mathematical description of soil 35
3.1 The stress tensor . . . 35
3.1.1 Invariants of the stress tensor . . . 36
3.1.2 Plane strain condition . . . 37
3.2 Equations of motion . . . 38
3.3 Constitutive model . . . 38
3.3.1 Yield criteria . . . 39
Strain hardening and softening . . . 40
3.3.2 Elastoplastic model . . . 41
3.3.3 Perzyna model . . . 42
3.3.4 A generalised system of equations . . . 44

3.4 Summary of the governing equations 45

4 Stress-Particle SPH **47**

4.1 Introduction 47
4.2 Standard SPH 51
4.2.1 Particle and mass distribution 55
4.3 Discrete mathematical model 56
4.3.1 Stress modification in computational plasticity 60
4.4 Boundary treatment 62
4.4.1 Free surface detection 65
4.5 SPH improvement techniques 65
4.5.1 Artificial viscosity 65
Alternative damping terms 66
4.5.2 Corrective Smoothed Particle Method 66
4.5.3 Artificial stress 68
4.5.4 Particle shifting method 69
4.6 Time discretisation 71
4.7 Nearest neighbouring particle searching 73
4.8 Stress-Particle SPH 73
4.8.1 Average method 75
4.8.2 SPH-CSPM method 75
4.8.3 MLS method 76
4.8.4 Node-stress-point arrangement 78
Mass distribution 79
4.8.5 Stress-point position update procedure 80
4.8.6 Boundary treatment 80
4.9 A summary of Stress-Particle SPH 82
4.10 Computational implementation 85
4.11 Conclusion 87

5 Stress-Particle inside approach results **89**

5.1 Introduction 89
5.2 Shock wave in a one-dimensional bar 90
5.3 Vertical slope 91
5.3.1 Elastic slope 93
5.3.2 Viscoplastic slope 96
5.4 Strain localisation in a soil sample with strain softening 97
5.5 Soil failure 108
5.5.1 Cohesive soil 109
Particle position update 117
5.5.2 Non-cohesive soil 119
5.6 Conclusion 121

6 Stress-Particle SPH for large displacement problems 125
6.1 Introduction . . . 125
6.2 Non-cohesive soil failure . . . 127
6.2.1 Adaptation at the boundaries . . . 129
6.2.2 Adaptation at isolated nodes . . . 131
6.2.3 Updating the stress-point positions . . . 132
6.3 Cohesive soil failure . . . 132
6.4 The outside approach: improvements . . . 136
6.4.1 Concentration criteria approach . . . 137
6.4.2 Velocity vector approach . . . 138
6.5 Collapse of a Von Mises material . . . 141
6.6 Conclusion . . . 147

7 Spatial and temporal evolution of an experimental debris flow, exhibiting coupled fluid and particulate phases 151
7.1 Introduction . . . 151
7.2 Experimental methodology . . . 154
7.2.1 Particle Image Velocimetry (PIV) . . . 158
7.3 Results . . . 160
7.4 Discussion . . . 175
7.5 Conclusion . . . 181

8 Two-phase Stress-Particle SPH 183
8.1 Introduction . . . 183
8.2 Mathematical framework . . . 185
8.3 Equations of motion . . . 186
8.4 Two-phase Stress-Particle SPH . . . 190
8.4.1 SPH approximation of the volume fraction . . . 191
8.4.2 SPH approximation of mass conservation for water . . . 191
8.4.3 SPH approximation of momentum conservation for soil . . . 192
8.4.4 SPH approximation of the soil constitutive equation . . . 193
8.4.5 SPH approximation of momentum conservation for water . . . 193
8.4.6 Pore water pressure . . . 194
Speed of sound . . . 195
8.4.7 SPH approximation of the interaction force . . . 195
8.4.8 Boundary treatment . . . 196
8.4.9 Computational implementation . . . 196
8.4.10 Model validation . . . 197
Collapse of a water column . . . 197
Submerged soil sample . . . 200
8.5 Experimental debris flow . . . 201
8.6 Conclusion . . . 211

9 Conclusions **215**

9.0.1 Suggestions for future work 218

9.1 Concluding remarks 220

References **221**

List of Figures

2.1 The slip surface of a rotational slide, Columbia River Valley. 10
2.2 A depiction of the Tresca yield surface in the principal stress space. The axes σ_1, σ_2 and σ_3 denote the principal stresses. 14
2.3 The slip surface simulated by Bui et al. (2011), with an elastoplastic constitutive model implemented within SPH. The profile coincides with that of the limit equilibrium method of Bishop (1955). 15
2.4 A depiction of the SPH particle approximation within the support domain of the smoothing kernel W, for a particle i. The image is adapted from Wang et al. (2016a). The support domain of W is defined by the smoothing length, multiplied by a constant κ. 20
2.5 The results of a landslide simulation conducted by Bui et al. (2011), comparing the SPH solution with that of FEM. Notice that for FEM, the displaced material cannot detach from the failure surface. 20
2.6 Photographs of the aftermath of the Tsing Shan debris flow, compared against the numerical SPH model results of Pastor et al. (2015a). . . 22
2.7 Values of stress and stress gradients with their corresponding kernel approximations, for the one-dimensional simulation of two impacting solid bodies (Swegle et al., 1994). 26
2.8 A depiction of a row of SPH particles. 28
2.9 The collision of two rubber rings showing non-physical fractures. . . 29
2.10 The appearance of fractures as a result of the tensile instability, from SPH simulation results provided in the literature. 30
2.11 An illustration of the Node-Element method and its application, taken from Blanc and Pastor, 2013. 33

3.1 A depiction of the three-dimensional stress tensor in the Cartesian plane. 36
3.2 Yield criteria in the $(-I_1, \sqrt{J_2})$ plane 40

4.1 Stress-Particle SPH configurations in one and two dimensions. 48
4.2 The node-stress-point arrangements considered in the stability analysis performed by Belytschko et al. (2000). 49
4.3 The cubic smoothing kernel and its first derivative. 54
4.4 An illustration of the initial particle and mass distribution for SPH in two dimensions. 55

4.5 An illustration of the stress states in tension cracking, and imperfectly plastic behaviour. 61
4.6 A schematic depiction of dummy nodes. 63
4.7 Examples of different node-stress-point arrangements. 78
4.8 A depiction of the Stress-Particle outside approach. 79
4.9 A sketch depicting the stress-points following their associated node in the Stress-Particle outside approach. 81
4.10 A depiction of the nodes and stress-points in the outside approach, in the proximity of the wall boundary. 82

5.1 The velocity u_x evolution at $x = 0$ m in a one-dimensional bar subjected to a tensile stress. The Standard SPH and Stress-Particle SPH results are compared with those of Dyka, Randles, and Ingel (1995). 91
5.2 The stress σ_{xx} evolution at $x = 0.035$ m in a one-dimensional bar subjected to a tensile stress. The Standard SPH and Stress-Particle SPH results are compared with those of Dyka, Randles, and Ingel (1997). 91
5.3 A schematic diagram of the vertical slope. 92
5.4 Contours of stress and velocity in the elastic slope at $t = 2$ s, comparing the Standard SPH and Stress-Particle SPH results with those of Blanc (2011). 94
5.5 A comparison of the stress and displacement profiles at $t = 2$ s for the elastic slope problem for Standard SPH, with and without artificial viscosity. 95
5.6 Profiles of vertical stress σ_{yy} (Pa) for the elastic slope problem at $t = 2$ s for Stress-Particle SP3, comparing the results from different node-stress-point interpolation methods. 95
5.7 A comparison of the evolution of deviatoric plastic strain $\bar{\epsilon}^p$ (dimensionless) and total displacement $|s|$ (m) between the current Stress-Particle SPH model, a Standard SPH model, and the results presented by Blanc and Pastor (2013), for the viscoplastic vertical slope failure 98
5.8 The deviatoric plastic strain $\bar{\epsilon}^p$ (dimensionless) and total displacement $|s|$ (m) evolution in the viscoplastic slope, calculated with SP1 with and without extra boundary stress-points (as highlighted in the figure legend), compared against the results of Blanc and Pastor (2013). . . 99
5.9 A schematic diagram of the strain localisation problem. 99
5.10 The strain localisation in the soil sample presented by Mabssout and Herreros (2013). 100
5.11 The evolution of deviatoric plastic strain $\bar{\epsilon}^p$ (dimensionless) in the soil sample, computed with the Stress-Particle SPH inside approach and Standard SPH. 101

5.12 A comparison of deviatoric plastic strain, stress and velocity profiles for the strain localisation problem at $t = 0.02$ s, for Standard SPH, SP1, SP2 and SP3. The node and stress-point positions were not updated. 102
5.13 The dependency of the shear band profile on the node-stress-point configuration, in the strain localisation problem. 103
5.14 A comparison of deviatoric plastic strain, stress and velocity profiles for the strain localisation problem at t = 0.02 s, for Standard SPH (with artificial viscosity), SP1, SP2 and SP3 (with no artificial viscosity). The node and stress-point positions were updated. 104
5.15 Deviatoric plastic strain, stress and velocity profiles at $t = 0.02$ s in the strain localisation problem. Results were calculated with Stress-Particle SPH with configuration SP1, comparing three different node-stress-point interpolation methods. The node and stress-point positions were updated. 106
5.16 Profiles of deviatoric plastic strain $\bar{\epsilon}^p$ (dimensionless) at $t = 0.035$ s in the triaxial test simulation, comparing the results from different node-stress-point configurations. The imposed dashed line represents an inclination angle of 45°. 107
5.17 The evolution of the cohesive and the non-cohesive soil failure, provided by Bui et al. (2008). The contours show deviatoric plastic strain (no scale is provided in the literature). 109
5.18 Snapshots of the progressive failure of the cohesive soil, for Standard SPH with no treatment for the tensile instability, Standard SPH with the artificial stress (Monaghan, 2000), and Standard SPH with the particle shifting method (Xu and Yu, 2018). The material is coloured by values of deviatoric plastic strain $\bar{\epsilon}^p$ (dimensionless). 110
5.19 Free surface profiles for the cohesive soil problem. The markers denote the results from the current Standard SPH model, while the dashed line represents the results provided by Bui et al. (2008). 111
5.20 Particle positions at different times for the cohesive soil failure, calculated with SP2. The results compare the node behaviour with and without the treatment of isolated SPH nodes – note the behaviour of the isolated nodes when no treatment is included. 112
5.21 Snapshots of the progressive failure of the cohesive slope, for SP1, SP2 and SP3. The material is coloured by values of deviatoric plastic strain $\bar{\epsilon}^p$ (dimensionless). 113
5.22 The node positions at the front of the material at $t = 2.5$ s for the cohesive soil problem, calculated with configurations SP1, SP2 and SP3 of the inside approach. Note the small fractures that are present at the free surface for the SP1 configuration, which are not present in the SP2 and SP3 configurations. 114

5.23 Free surface profiles for the cohesive soil failure problem. The different markers correspond to the results calculated with Standard SPH with the artificial stress, Standard SPH with particle shifting, SP1, SP2 and SP3. 115
5.24 Free surface profiles of the cohesive soil at $t = 1.28$ s, calculated with Standard SPH with the artificial stress. The different markers correspond to different values of the tuning parameter ϵ. 116
5.25 Node positions at the end of the cohesive soil failure problem, for Standard SPH with the artificial stress, Standard SPH with particle shifting and Stress-Particle SPH with the SP3 configuration. The nodes are coloured by values of vertical stress σ_{yy} (Pa). 117
5.26 The node positions at the front of the material at $t = 2.5$ s, for the cohesive soil failure problem. The results show the effect of updating the node and stress-point positions via the XSPH method, for SP1, SP2 and SP3. 118
5.27 Profiles of the cohesive soil when the material had stopped deforming. Compared are the results of Standard SPH with and without the XSPH particle update method. 119
5.28 Free surface profiles for the non-cohesive soil problem. The markers denote the results of the current Standard SPH model, while the dashed line represents the results provided by Bui et al. (2008). . . . 120
5.29 Particle positions at $t = 2.5$ s for the non-cohesive soil failure problem, calculated with the SP1, SP2 and SP3 configurations. The nodes are represented by the black points, while the stress-points are denoted by the smaller, red points. 121

6.1 A depiction of the Stress-Particle outside approach. 126
6.2 A sketch depicting the stress-points positions following their associated node in the Stress-Particle outside approach. 126
6.3 A depiction of the nodes and stress-points in the outside approach, in the proximity of the wall boundary. 127
6.4 Node positions at $t = 2.5$ s for the non-cohesive soil failure problem. The different outside approach configurations are shown in Figure 6.1. 129
6.5 Free surface profiles for the non-cohesive soil problem. The black circle markers denote the results from the current Standard SPH model with the artificial stress, while the other markers represent the outside approach results. 130
6.6 Node positions at $t = 2.5$ seconds for the non-cohesive soil failure problem, coloured by vertical stress σ_{yy} (Pa). Note the noisy areas of the stress profile for the Standard SPH results. 130

6.7 The node evolution for the non-cohesive soil failure with configuration IIB. Compared are the results where all of the stress-points were moved via their interpolated velocities, against when certain stress-points were adapted as described in Sections 6.2.1 and 6.2.2. 133
6.8 The deformed material at $t = 2.5$ s in the cohesive soil failure problem, coloured by values of deviatoric plastic strain $\bar{\epsilon}^p$ (dimensionless). Displayed are the results computed with Standard SPH and different configurations of the outside approach. 135
6.9 Node (blue) and stress-point (red) positions at $t = 2.5$ s for the cohesive soil problem with the Stress-Particle outside approach, configuration IIB. Compared are the results where the positions of the stress-points were updated according to their interpolated velocity, against those where the stress-points were assigned to follow their associated node. 136
6.10 A contour plot of initial stress-point concentration (dimensionless), for the cohesive soil problem with configuration IIB of the outside approach. 138
6.11 Node positions at $t = 2.5$ s for the cohesive and non-cohesive soil failure problems, calculated with configuration IIB of the outside approach. The material is coloured by values of vertical stress σ_{yy} (Pa). The interior stress-points were adapted for the nodes that had a the stress-point concentration less than C_{tol}. 139
6.12 A depiction of updating the stress-point positions according to the velocity vector at each node. 140
6.13 Node positions at $t = 2.5$ s with contour plots of vertical stress σ_{yy} (Pa), where all stress-point positions were updated to align with the velocity vector at each node. 141
6.14 Node positions at $t = 2.5$ s with contour plots of vertical stress σ_{yy} (Pa), where the stress-point positions were updated to align with the velocity vector at each node. The method was only applied to the nodes that had displaced more than $s_{tol} = 0.125\Delta x$ every $n_t = 1000$ time steps. 142
6.15 A schematic diagram of the Von Mises material collapse problem. . . 142
6.16 Snapshots of node positions for the collapse of the Von Mises material: displayed are the results calculated with Standard SPH, along with the inclusion of the artificial stress and the particle shifting technique. . 143
6.17 Snapshots of the material evolution for the Von Mises material collapse, comparing the Stress-Particle SPH and Standard SPH results. The nodes are coloured by contours of vertical stress σ_{yy} (Pa). 144
6.18 Node positions at $t = 1.2$ s and $t = 2.5$ s of the Von Mises material collapse, for the different node-stress-point configurations shown in Figure 6.1. 145

6.19 Node positions at $t = 2.5$ s for the Von Mises material collapse, with configuration IIA of the outside approach. The nodes are coloured by values of vertical stress σ_{yy} (Pa). 146
6.20 Snapshots of the material evolution for the Von Mises material collapse, comparing Stress-Particle SPH and Standard SPH. The nodes are coloured by contours of vertical stress σ_{yy} (Pa). 147
6.21 Free surface profiles for the Von Mises material collapse. The black markers represent the results from Standard SPH with the artificial stress, while the red markers represent the results from the outside approach, where the stress-points were defined to align with the node velocity field 148

7.1 The different velocity profile shapes expected in an idealised water-granular free surface steady flow, from Kaitna, Dietrich, and Hsu (2014). The horizontal axis is horizontal velocity and the vertical is flow height. The profiles were derived under the assumption of a wide flow with uniform cross-stream conditions, constant flow height and a non-erodible bed. The types of profile are linear (dashed line), granular-type (dashed-dotted line), half-parabolic viscous-type (solid line) and a viscoplastic plug-type (dotted line). 153
7.2 A schematic depiction of the experimental flume. 155
7.3 Particle size distribution for the glass grit. 155
7.4 Shear box test data. 156
7.5 The initial placement of the water-granular mixture behind the lock gate. 157
7.6 A photograph of the experimental set-up just prior to flow initiation. The set-up consists of a perspex channel with a roughened bed, that runs out onto a broader surface (at the bottom of the picture). A high speed camera and multiple LED lamps are used to visualise the flow. 158
7.7 An snapshot of the water-granular mixture for Run 1, at $t = 0.035$ s after reaching the field of view of the camera. 161
7.8 Snapshots of the propagating soil-water mixture for the experimental flow, Run 1. The area of the camera field of view is 0.05×0.03 m^2. 162
7.9 Contour plots of standard deviation as a percentage of the average velocity $100 \times \frac{\bar{e}}{\bar{u}_x}$ at different times of flow for Run 1 of the experiment. The upper limit on the scale bar is defined as 20% of the velocity average. 164
7.10 Contour plots of standard deviation $\bar{e}$ at different times of flow for the experimental water-granular mixture, Run 1. The lower limit on the scale bar is defined as $\bar{e} = 0.15$ m s^{-1}, which is the suggested cut-off between fluctuating and non-fluctuating behaviour used in the experiments of Paleo Cageao (2014). 165

7.11 Snapshots of the propagating soil-water mixture for Run 1 of the experimental flow, with the overlaid time-averaged PIV velocity vectors. The area of the camera field of view is 0.05×0.03 m^2. 167
7.12 Contour plots of horizontal velocity u_x at different times for Run 1 of the experimental flow. Note the difference in scale for each image. . . 168
7.13 Velocity profiles obtained from the PIV data at various times for the three experimental runs. The horizontal position of the profiles is in the centre of the camera viewing frame (1.102 m downstream from the lock gate). 170
7.14 Plots of horizontal velocity against height at $x = 1.102$ m downstream from the lock gate. On each graph the plotted profiles are from eight different flow times, ranging between $t = 0.6$ s and $t = 2.8$ s, for the three different experimental runs. 172
7.15 Plots of shear stress against height at $x = 1.102$ m downstream from the lock gate, for Run 1 of the experiment. 174
7.16 A comparison of the internal velocity profiles in the steady, solid bed flow experiments of Armanini et al. (2005), and those in the body of the current experiment. For the former, plotted on the x-axis is horizontal velocity $\bar{u}$ normalised by the mean velocity U. The y-axis shows $(y_w - y)/H$, where y_w is the saturation line (obtained by visual inspection), and H is the flow free surface. The points correspond to the experimental velocity values, where the different symbols refer to results from different runs with the bed slope varying from $19° - 23°$. The solid line is the line of best fit. 177
7.17 Normalised velocity profiles in the sheared region for Run 1 of the experimental debris flow, with a best fit granular and viscous scaling. 180

8.1 A depiction of the two-phase Stress-Particle SPH method. 190
8.2 A depiction of the boundary treatment in the two-phase Stress-Particle SPH method. 196
8.3 A flow chart depicting the calculation steps of two-phase Stress-Particle SPH. The blue and orange entries represent the water and soil phase calculations respectively, while the green entries correspond to actions that are relevant to both the water and soil phase. 198
8.4 The collapse of a water column, comparing the results of the current SPH model with those of Crespo, Gómez-Gesteira, and Dalrymple (2007) at $t = 0.4$ s, $t = 0.8$ s, $t = 1.1$ s and $t = 1.8$ s. The nodes are coloured by contours of horizontal velocity. 199
8.5 Contours of vertical effective stress σ'_{yy} (Pa) in a submerged elastic soil sample, calculated with Stress-Particle SPH (for the SP3 configuration). 201

8.6 Plots of vertical effective stress σ'_{yy} (Pa) and pore water pressure p_w (Pa) against soil elevation (m), for Standard SPH, SP1, SP2 and SP3. The data correspond to a horizontal location of $x = 5$ m. The SPH solution is depicted by the markers, while the continuous line represents the analytical solution. Note the change in sign convention for the stress – the compressive stress is positive, for plotting purposes only. 202

8.7 The initial material placement in the simulation of the experimental debris flow. 203

8.8 A comparison of the soil and water phases for the Standard SPH simulation of the experimental debris flow, for three different particle resolutions. The labels 'Fine', ' Medium' and 'Coarse' correspond to 15555, 9949 and 6873 soil particles respectively, with 23843, 15344 and 10402 water particles. The fine, medium and coarse results are represented by the blue, red and green vectors respectively. The volume fraction was not updated, and no interaction force was included. . . 205

8.9 Soil (orange) and water (blue) node evolution for three different particle resolutions, within the area corresponding to the camera field of view in the experiments (0.05×0.03 m^2). In each subfigure, the particle resolution increases from left to right, where $n_s = 6873, 9949, 15555$ and $n_w = 10402, 15344, 23843$. For visualisation purposes, the water nodes are approximately 1.2 times larger than the soil nodes. 206

8.10 SPH velocity vectors for the simulation of the experimental debris flow, with the chosen node-stress-point configuration for the Stress-Particle method. 207

8.11 The evolution of the soil and water phases in the numerical simulation of the experimental debris flow, with no interaction force. The soil and water phases are represented by the orange and blue nodes respectively. The red, horizontal line represents the height of the experimental flow at the corresponding times. 208

8.12 The evolution of the soil and water phases in the numerical simulation of the experimental debris flow, with the volume fraction update. The soil and water phases are represented by the orange and blue nodes respectively. The vertical lines encompass the area captured by the camera field of view. 209

8.13 Snapshots of the experimental debris flow, with the SPH results. The orange nodes depict the soil phase while the blue nodes depict the water. The solid red line corresponds to the free surface of the experiment. The area of the camera field of view is 0.05×0.03 m^2. From top to bottom, the results are shown at $t = 0.3$ s, $t = 0.6$ s, $t = 0.8$ s and $t = 1.2$ s. For visualisation purposes, the water nodes are approximately 1.2 times larger than the soil nodes. 210

8.14 The positions of the soil nodes at the point of the material reaching the end of the flume ($t = 0.35$ s). The nodes are coloured by horizontal velocity u_x (m s^{-1}). 211
8.15 The effect of stress-point placement on the Stress-Particle SPH simulation of the two-phase experimental debris flow. The results on the left correspond to the horizontal stress-point placement as shown, where $r = \frac{\Delta x}{3}$. The results on the right were simulated with a diagonal stress-point placement, also for $r = \frac{\Delta x}{3}$. 214

List of Tables

4.1 A summary of the various numerical routines and features (written in Fortran 90) of Stress-Particle SPH and Standard SPH. The column headers detail the authors of the routines. 86

5.1 Perzyna model parameters for the elastic and viscoplastic vertical slope problems. 92
5.2 Perzyna model parameters for the strain localisation problem. 100
5.3 Drucker-Prager material parameters for the cohesive and non-cohesive soil failure. 108
5.4 The computational time taken (hours, to one decimal place) to simulate 2.5 seconds of the cohesive soil problem, comparing Standard SPH, SP1, SP2 and SP3 123

6.1 Perzyna model parameters for the Von Mises material collapse. . . . 142

7.1 Properties of the material used in the debris flow experiments. 157
7.2 A summary of the relevant experimental parameters in the current work, and selected investigations in the literature. The notation x_f refers to the flume run-out length (from the lock gate position), c_w is the channel width, d_d is the diameter of the rotating drum, θ is the flume inclination, ϕ_s is solid volume fraction, d_{50} is the mean particle size and C_U is the coefficient of uniformity. The ✗symbol denotes information that was not provided in the literature. 178

8.1 Material parameters for the submerged, elastic soil. 200
8.2 Elastoplastic material parameters for the soil and water phases in the experimental debris flow. 202

List of Abbreviations

CFL	**C**ourant-**F**riedrichs-**L**ewy
CSPM	**C**orrective **S**moothed **P**article **M**ethod
EFGM	**E**lement **F**ree **G**alerkin **M**ethod
FDM	**F**inite **D**ifference **M**ethod
FEM	**F**inite **E**lement **M**ethod
LEM	**L**imit **E**quilibrium **M**ethod
MLS	**M**oving **L**east **S**quares
MPM	**M**aterial **P**oint **M**ethod
PIV	**P**article **I**mage **V**elocimetry
RK4	Fourth order **R**unge **K**utta Method
SPH	**S**moothed **P**article **H**ydrodynamics

Dedicated to my parents, for their kindness and support throughout my life so far.

Chapter 1

Introduction

Landslides are a complex phenomena that are the source of immense destruction around the globe. The term *landslide* is defined as the movement of a mass of rock, debris or soil down a slope (Cruden and Varnes, 1996), and encompasses a vast array of geophysical events, including rock falls, mud flows and debris flows. The velocity of the displaced material can be of the order of millimetres per year, in the case of creeping slopes (Mansour, Morgenstern, and Martin, 2011), to metres per second for rapid debris flows (Costa, 1984). In extreme cases, the run-out distance achieved by the propagating material can exceed 100 km (Plafker and Ericksen, 1978). Thus, landslides pose a serious threat to infrastructure, roads, water supplies and human life (Schuster, 1996). Examples of highly destructive landslide events are well-documented throughout history – in 1963 a rock fall occurred suddenly on the slope of the Vajont dam, Italy, and propagated into the underlying reservoir. The subsequent wave had disastrous effects: over 2000 people lost their lives and approximately 200 million dollars of damage was caused (Barla and Paronuzzi, 2013). The triggering mechanism is thought to be associated with weak bands of clay that were present within the slope (Genevois and Ghirotti, 2005). Another example of a catastrophic landslide is that of Aberfan, Wales. Triggered by intense rainfall, a colliery spoil tip collapsed on a slope in 1966. The resulting landslide engulfed numerous buildings, including a primary school, that were located near the bottom of the slope. This resulted in the deaths of 166 people (Schuster and Fleming, 1986). A particularly mobile landslide occurred in Oso, Washington in 2014, which travelled the entire length of a one-half-mile wide valley. The aftermath of the landslide included a buried river, blocked highway, the destruction of over 40 buildings and 43 casualties. The triggering mechanism remains unclear, although this event was preceded by a period of heavy precipitation (Henn et al., 2015). These cases provide only a few examples of the numerous catastrophic landslides that have occurred throughout time. Worldwide, landslides are responsible for thousands of deaths each year (Petley, 2012).

By nature, landslides are extremely unpredictable. This is partly due to the fact that there are a number of different triggers that are responsible for the occurrence of landslides (such as earthquakes, rainfall and human activity (Wieczorek, 1996)). Moreover, it is difficult to predict exactly where an event will occur. There are many

areas that have a high susceptibility to landslides, such as the mountainous regions of Southern Italy (Carrara and Merenda, 1976; Cascini, 2004) and the islands of Hong Kong (Dai et al., 2001; Chau and Chan, 2005). These areas can be monitored using advanced techniques and instrumentation (Tarchi et al., 2003; Bitelli, Dubbini, and Zanutta, 2004; Merritt et al., 2018) in order to assess the likelihood of a future event occurring, and to inform the development of *hazard maps*. Hazard maps display information regarding the probability of a landslide occurring in a given area, as well as potential run-out paths (Hungr, 2018). This information is essential for the implementation of slope stabilisation methods and protective measures (Holtz and Schuster, 1996; Wyllie and Norrish, 1996). However, the post-failure behaviour of a landslide is uncertain and run-out lengths typically vary greatly. Factors such as the type of material, slope inclination and water content play a vital role in the potential run-out lengths achieved by landslides (Legros, 2002). For the purpose of hazard map development, predictions of landslide run-out may be determined in an empirical manner: utilising information from past events to predict information regarding potential future events (Fannin and Wise, 2001; Chung and Fabbri, 2008). Alternatively, numerical models can be used to simulate landslide run-out behaviour, with user-specified conditions. Numerical simulations are crucial for an improved understanding of landslide behaviour, and extensive research has been devoted to the development of a sophisticated landslide model (Savage and Hutter, 1989; Iverson, 1997; McDougall and Hungr, 2004; Pastor et al., 2008; Pastor, Blanc, and Pastor, 2009). Simulations of landslides can be performed for a variety of different conditions, allowing a thorough investigation into the physical parameters of interest and how they affect landslide run-out (and behaviour in general) (Pirulli and Sorbino, 2008; Cascini et al., 2014).

While numerical models of landslides are invaluable tools, their development and implementation is far from straightforward. Landslides are extremely complex from initiation to deposition, and typically exhibit both solid and fluid behaviour (Cruden and Varnes, 1996). Landslide initiation is associated with the failure of a slope, which is governed by solid dynamics (Palmer and Rice, 1973; Martel, 2004). Conversely, post-failure behaviour is often characterised by fluid-like features (Iverson, Reid, and LaHusen, 1997; Crosta et al., 2005). Therefore, landslide motion is governed by laws of both solid dynamics and fluid dynamics. The mathematical description of landslide material is consequently a non-trivial matter, particularly when interested in modelling both failure and post-failure behaviour. There is currently no mathematical model in existence that can accurately describe all features of a landslide. Nonetheless, significant progress has been achieved in this area, and current mathematical approaches are capable of capturing complex features of landslide behaviour, such as the transition from a solid to a fluid state (Bui et al., 2008; Pastor et al., 2008; Pastor et al., 2015a), and the coupled feedback between a soil skeleton and interstitial fluid (Pitman and Le, 2005; Pudasaini, 2012; Iverson and George, 2014).

A pressing challenge regarding landslide simulation lies in the numerical implementation of the governing mathematical equations. A numerical model must also be capable of capturing solid and fluid dynamics, for it to be applicable to general landslide behaviour. To numerically approximate a continuous mathematical system, it is necessary to divide the governing equations into discrete sub-domains. This process is referred to as *numerical discretisation*. In classic methods, the continuous system is discretised via the use of a connected mesh, where material information is carried on each node or element of the mesh. Mesh-based methods are well established in the field of computational modelling, and have been applied to simulate problems that are relevant to landslide behaviour (Chen and Mizuno, 1990; George and Iverson, 2014; Crosta, Imposimato, and Roddeman, 2015). However, the presence of a mesh imposes restrictions that are related to the dynamics of the simulated material. These restrictions pose severe limitations for problems involving large deformations, and computationally expensive remedies are required (Li and Liu, 2002). As an alternative to mesh-based methods, recent decades have seen a rise in the development of numerical schemes that do not utilise a mesh (Idelsohn et al., 2003; Liu and Liu, 2010; Li and Liu, 2002). Meshless methods are well-adapted for modelling large deformation problems (such as landslides), mainly due to the fact that there is less restriction on material deformation and displacement. Therefore, meshless numerical models are frequently applied to the simulation of landslide behaviour (McDougall and Hungr, 2004; Pastor et al., 2009a; Bandara and Soga, 2015; Calvo et al., 2015; Soga et al., 2015; Nguyen et al., 2017). The original meshless method – Smoothed Particle Hydrodynamics (SPH) (Gingold and Monaghan, 1977; Lucy, 1977) – arguably remains the most popular choice due to the relative simplicity of its implementation (Liu and Liu, 2010).

SPH is a particle-based method, where the governing system of equations are discretised over a set of particles, as opposed to a mesh. Information such as stress and velocity is calculated at each particle via a summation over the neighbouring particles, combined with a smoothing function. There is no restriction on the movement of each particle. SPH has been employed to simulate a wide variety of problems regarding landslide initiation and propagation, producing promising results (Bui et al., 2008; Pastor et al., 2009a; Haddad et al., 2010; Bui et al., 2011; Pirulli and Pastor, 2012; Dai et al., 2014). Unfortunately, despite the successful applications of SPH, it suffers from serious numerical instabilities that are often detrimental to the model performance. Namely, these are: the instability due to *zero-energy modes*, and the *tensile instability*. Zero-energy modes were originally identified in mesh-based methods (Maenchen and Sack, 1963), and occur when a zero stress gradient is incorrectly calculated at individual particles. Their presence is related to the fact that stress and velocity are calculated at the same location (Swegle et al., 1994), and they result in noisy stress and velocity profiles, with spurious values at individual particles. The effects of zero-energy modes are typically most severe when considering solid problems (Swegle et al., 1994; Belytschko et al., 2000). The tensile instability is unique to

meshless methods, and arises in materials with a cohesive strength when subjected to a tensile state of stress. A consequence of the tensile instability is particle clumping, which leads to the development of non-physical material fractures (Swegle et al., 1994; Monaghan, 2000). Clearly, the effects of zero-energy modes and the tensile instability pose a serious threat to problems regarding different stages of landslide behaviour. Zero-energy modes have been documented in SPH simulations of material failure (Vidal, Bonet, and Huerta, 2007; Blanc, 2011), while the tensile instability has been shown to have detrimental effects in simulations involving cohesive soil (Bui et al., 2008). To obtain a universal numerical model, that can be applied to all types and stages of landslide behaviour, it is essential that the problems of zero-energy modes and the tensile instability are eliminated from SPH.

There have been numerous attempts to eliminate the tensile instability within SPH. The majority of the proposed solutions are complicated to implement, which counteracts the favourable simplicity of the SPH method (Dilts, 1999; Monaghan, 2000). What's more, some of these remedies place restrictions on the movement of the SPH particles – thereby diverging from the true, meshless nature of SPH (Belytschko et al., 2000). Arguably the most frequently applied remedy is the artificial stress method (Monaghan, 2000), which applies a small repulsive force to particles that are in close proximity to one another when under a state of tensile stress. Although the results are effective, the method requires the tuning of artificial, numerical parameters that do not have a physical interpretation. Conversely, the problem of zero-energy modes is relatively unexplored within SPH, and little work has been devoted to a solution. Regarding mesh-based methods, the zero-energy mode problem can be completely eliminated by utilising a staggered grid approach, where the stress and velocity are calculated on two separate meshes (Patankar, 1980). Motivated by this approach, Dyka, Randles, and Ingel, 1995 believed that the same concept could be used to eliminate the tensile instability in SPH, and consequently introduced two sets of particles to SPH, in one dimension. This method, known as *Stress-Particle SPH*, was able to accurately predict the wave propagation in an elastic bar under a state of tensile stress – a problem that standard SPH was unable to model due to the tensile instability. The Stress-Particle SPH method was later extended to higher dimensions (Randles and Libersky, 2000; Vignjevic, Campbell, and Libersky, 2000), and used to simulate a number of benchmark problems related to solid dynamics. A full stability analysis of Stress-Particle SPH was later performed by Belytschko et al. (2000), where it was shown that the method is capable of completely eliminating zero-energy modes in SPH, while also stabilising the scheme in tension.

Stress-Particle SPH is a stabilised version of SPH that is capable of eliminating both of the detrimental instabilities of the classic SPH method. What's more, Stress-Particle SPH removes the instabilities in a 'natural' way, and does not involve any artificial tuning parameters. Therefore, the method has the potential to provide a generalised numerical tool that is applicable for all stages of landslide behaviour.

However, since its introduction, very little attention has been dedicated to this numerical method, despite the initial promising results. The reason for this is partly due to the fact that it is unclear how the particle positions should be updated. In Stress-Particle SPH, one set of particles carry the material velocity, while the second set of particles carry stress information. The particle positions within SPH are updated according to their velocity. Therefore, updating the position of the second set of particles (that do not carry velocity), is a non-trivial task. In all existing applications of Stress-Particle SPH, the velocities from the first set of particles are interpolated onto the second set in order to update their positions. This method is expected to break down in the simulation of high displacement problems (Vignjevic, Campbell, and Libersky, 2000), and all applications of Stress-Particle SPH are consequently confined to problems within solid dynamics that exhibit relatively low displacements. The meshless nature of SPH is therefore not utilised, and the method is unlikely to be applicable for simulating post-failure landslide behaviour.

The primary aim of the current research is to develop a numerical model that is capable of simulating the range of behaviour exhibited by landslides regarding both failure and post-failure. Due to the high velocities and large run-out distances achieved by many landslides, the choice of framework for the model implementation is SPH. To enable SPH to accurately predict different stages of landslides, the zero-energy modes and tensile instability must be eliminated. Therefore, the Stress-Particle SPH method, which can remove both of these instabilities, is revisited and further developed. A mathematical description of soil is implemented into the Stress-Particle SPH framework for the first time, and applied to low displacement problems that are representative of landslide initiation procedures. For the Stress-Particle method to be capable of simulating the post-failure behaviour of landslides, it must be capable of handling large displacements and fluid-like behaviour. Therefore, to fulfil the primary aim of this research, the Stress-Particle SPH technique is extended, so that the particle positions can be updated in a way that allows the simulation of large displacement problems. To validate the newly developed model, results are compared with those presented in the literature. A secondary aim of this investigation is to obtain a deeper insight into the internal mechanisms of a particularly destructive type of landslide – a debris flow. Small scale flume experiments are performed with a granular-water mixture, and the propagating flow is recorded with a high speed camera. The results of the experiment are used to assess the extent of the capabilities of the new SPH model, by employing Stress-Particle SPH to simulate the experimental flow.

The remainder of this investigation is structured as follows. First, Chapter 2 provides relevant background information and a review of the current literature regarding landslide modelling techniques. This includes a description of the alternative mathematical and numerical approaches that are typically employed to simulate landslide behaviour. Furthermore, a detailed review of SPH, and the current methods of stabilisation, is also provided. Secondly, a complete mathematical description

of a single phase soil is given in Chapter 3, that is used to model landslide material in the current work. Stress-Particle SPH is presented in full in Chapter 4, containing a description of how the particle positions are updated (in both the classic and the new methods). The governing mathematical equations of a single phase soil are discretised within the framework of Stress-Particle SPH. In Chapter 5, the Stress-Particle SPH model is applied to the simulation of a number of benchmark problems that are relevant to soil failure, landslide initiation and landslide propagation. For this, the standard interpolation method of updating the two sets of particles is employed, and the extent of the method regarding the simulation of large displacement problems is highlighted. Subsequently, in Chapter 6, the extended Stress-Particle SPH method – with a novel technique of updating the particle positions – is applied to large displacement problems that are relevant to landslide propagation. Following the development and validation of Stress-Particle SPH, Chapter 7 presents the results of a small scale experimental debris flow. The experimental flow exhibits rapid velocities, and the internal dynamics are captured through the use of a high speed camera. To further examine the capabilities of the novel Stress-Particle SPH method, in Chapter 8 it is applied to simulate the results of the experimental debris flow. For this purpose, a two-phase soil-water model is incorporated within SPH. Finally, Chapter 9 presents the conclusions of the present investigation, and summarises how it contributes to the current literature regarding landslide modelling.

Chapter 2

Background and literature review

2.1 Introduction

The term landslide refers to the movement of material on a slope, and encompasses a wide range of geophysical events (Varnes, 1958). An event can be categorised based on the type of material involved and the type of movement. According to Cruden and Varnes (1996), landslide material is grouped into one of two categories – soil and rock. Furthermore, the type of movement is divided into three groups – falls, slides and flows. Falls are identified by the rapid movement of soil or rock through the air, with little interaction between the separate bodies. In slides, the material moves along a defined, continuous surface as a result of shear failure, where the surface of movement is often visible. Slides are subcategorised into two types – those where the deformation of the moving material is relatively small, and those where the deformation is large. Flows can exhibit viscous fluid-like behaviour, and consist of multiple, short-lived failure surfaces. The material in flows can be dry or wet, and they include rock avalanches, mud flows and debris flows. Slides often develop into flows, and in reality, a landslide event is likely to consist of multiple types of movements, as well as material. Moreover, the triggering of landslides adds further complexity to the event, as stationary mass becomes mobile. As a consequence, landslides exhibit a wide variety of behaviour, and are governed by processes concerning solid mechanics, soil mechanics and fluid dynamics. The current research aims to numerically model aspects of both landslide initiation and propagation, composed of soil. Regarding propagation, attention is focused on landslides that exhibit large deformations and displacements. This encompasses both slides and flows.

There are a vast number of different approaches in which to approximate landslide behaviour with a mathematical model. Furthermore, there are also contrasting approaches with regards to the numerical implementation of these models. This chapter aims to provide an extensive summary of the different mathematical and numerical models that have been used to simulate landslide initiation and propagation within the literature. In the first section of this chapter, key characteristics of soil behaviour are explained, with a description of landslide triggering mechanisms and features of propagation. Secondly, alternative mathematical models for soil are described, with their application to landslide behaviour. Following this, the

different numerical methods that can be used to simulate landslide behaviour are summarised. Emphasis is placed on Smoothed Particle Hydrodynamics (SPH) – a numerical technique with a number of desirable features regarding the simulation of landslides initiation and propagation. The current pitfalls of SPH are explored in detail. Finally, the current state of field regarding the numerical modelling of landslides is summarised. The areas that require further attention are highlighted, with a description of how the current work aims to contribute to this large area of research.

2.2 Soil behaviour: an application to landslides

The behaviour of landslides from initiation to deposition is strongly influenced by soil behaviour. Soil refers to granular material that ranges in size from the order of microns to millimetres, and includes clay, silt, gravel, sand and fragmented rock (Powrie, 2004). A fundamental aspect regarding both initiation and propagation is the strength of the slope material, and its susceptibility to failure. In soil mechanics, the strength of a soil is defined by its ability to endure a shear stress. The total amount of shear stress that can be withstood before failure occurs defines the *shear strength* of a soil. The shear strength varies between different types of soil, depending on their composition and initial state, and is mostly determined by the inter-particle friction within the material.

A soil is constituted of a granular skeleton separated by voids, or pores. The soil may be saturated (all voids are completely filled with water), dry, or partially saturated (some of the voids are filled with water). The degree of saturation influences the state of the soil significantly. Furthermore, unlike soil, water cannot withstand any shear stress, so that for a saturated soil, all shear stresses are carried by the soil skeleton. This leads to the decomposition of the total stress (for a saturated soil) into a component carried by the skeleton, and a component carried by the pore water:

$$\boldsymbol{\sigma} = \boldsymbol{\sigma}' - \mathbf{I}p_w, \tag{2.1}$$

where $\boldsymbol{\sigma}$ is the stress taken by the soil-water mixture, $\boldsymbol{\sigma}'$ is the stress taken by the soil skeleton – the *effective stress*, and $\mathbf{I}p_w$ is the stress carried by the water phase. In the latter term, p_w is the pore water pressure, and the identity matrix $\mathbf{I}$ is included as the pore water pressure is zero for the shearing (i.e. non-diagonal) components of the stress tensor. Equation (2.1) was proposed by Terzaghi (1936), and is considered the most fundamental law of soil mechanics. Note that in the current research, a negative value of stress corresponds to compression.

Depending on the inter-particle friction, there is a maximum amount of shear stress that can be carried by the soil skeleton. The maximum shear stress corresponds to the shear strength of the soil. The inter-particle friction is defined via the *angle of friction* ϕ, where a greater angle corresponds to a greater frictional resistance of the skeleton. The total amount of shear stress that can be carried by the soil skeleton is

then defined as

$$\tau = \sigma' \tan \phi, \tag{2.2}$$

where τ is the shear stress and σ' is the normal effective stress (i.e. the stress acting normal to the soil skeleton). Equation (2.2) defines the maximum shear stress that can be endured for a given angle of friction and normal effective stress. This relationship stems from the pioneering work of Coulomb (1773) regarding the stability of piles and embankments, and the subsequent stress analysis of Mohr (1900). It is therefore referred to as *Coulomb's criterion*. Equation (2.2) is valid for a material where the soil strength is determined solely by the inter-particle friction. Cohesive forces may also contribute to the strength of the soil, which can be included in Equation (2.2):

$$\tau = \sigma' \tan \phi + c_{oh}, \tag{2.3}$$

where c_{oh} is the soil cohesion. Equation (2.1) shows that for a given total stress, an increase in pore water pressure leads to a reduction in the soil effective stress. According to Equations (2.2) and (2.3), a lower effective normal stress results in less resistance to shear and a lower shear strength. Therefore, pore water pressures play a significant role in governing the strength of a soil.

The strength of a soil also depends on its ability to change volume when sheared. When an initially compact soil sample is sheared, the individual grains rearrange such that void ratio within the sample (and therefore the volume) increases. Subsequently, the shearing of the loose sample results in the movement of grains into the void spaces, and the sample volume is decreased. This change in volume is referred to as *dilation*, and affects the soil peak strength (Rowe, 1962). Dilation is defined as an angle, and can be included in Equation (2.3) by substituting the angle of friction ϕ with $\phi + \psi$, where ψ is the angle of dilation. The change in void ratio associated with soil dilation also governs the movement of pore water.

When a soil is subjected to an external force, a change in the stress state is induced, and the material deforms in response. These deformations are characterised as *strains* – the relative displacement of a material. The stress-strain relationship of a soil depends on its strength, which in turn depends on the material properties and its history. For a soil subjected to an increasing load, an increase in strain is accompanied by an increase in stress. Furthermore, if the load is removed (unloaded), the deformed soil can return to its original state. This type of behaviour is called *elastic*, where a one-to-one relationship exists between stress and strain. However, if the stress reaches the maximum value that can be endured, the soil is weakened. Beyond this, it can no longer return to its initial state, and the material deformations are irreversible. Such strains are referred to as being *plastic*. Once the stress-strain behaviour within a soil transforms from elastic to partly plastic, it is said to have yielded. The regions of plastic strain may spread and increase, which is associated with soil failure. The precise definition of failure depends on the problem under consideration, and is typically defined as when the regions of plastic strain

FIGURE 2.1: The slip surface of a rotational slide, Columbia River Valley (Varnes, 1978).

occupy a certain area. Note that after plastic strains have occurred, the stress-strain relationship varies depending on the type of soil and its strength. The response of a soil to an external load also depends on the rate at which the load is applied, and whether the soil has previously been subjected to loads which may have changed the soil state (Chen and Mizuno, 1990; Powrie, 2004).

2.2.1 Landslide initiation

At a fundamental level, landslide initiation is characterised by the transformation of a stationary mass on a slope to a dynamic state. This transformation is associated with the failure of the slope, and therefore the failure of the soil that comprises it. One possible type of failure mechanism is *localised failure*. A section of the slope undergoes plastic deformations, which localise and spread to form a well-defined failure surface, called a *slip surface*. The material within the failure surface has less strength than its surroundings, and defines the surface upon which the slide moves. The formation of slip surfaces precedes landslides of the slide type. For the assessment of slope stability, information regarding slip surface profiles is required for limit equilibrium methods (LEMs), such as Bishop's modified method (Bishop, 1955). LEMs consider the equilibrium of an idealised slope with a given slip surface, that is assumed to obey Coulomb's equation (Equation (2.3)), to determine the factor of safety of the slope (Duncan, Wright, and Brandon, 2014). Slip surfaces can be curved and concave, as shown in Figure 2.1, corresponding to *rotational slides*. Alternatively, *translational slides* displace along a planar slip surface (Varnes, 1978).

An alternative method responsible for triggering landslide events is *diffuse failure* (Laouafa and Darve, 2002). Diffuse failure occurs over a large area of the slope, and describes the rapid reduction of effective stress over this area. The shear strength is decreased significantly and liquefaction occurs – in which the soil exhibits liquid-like behaviour. The sudden reduction of strength over a large area can be a result of an earthquake or severe rain fall, and precedes landslides of the flow-type (Cascini et al., 2009; Take et al., 2004). Loosely compacted soils (such as sand) on relatively shallow slopes are more susceptible to this type of failure mechanism (Laouafa and Darve,

2002; Fernández-Merodo et al., 2004). In reality, landslide triggering mechanisms are complex and may in fact be a combination of both localised and diffuse failure methods, in addition to alternative factors. All cases of slope failure are concerned with a reduction of material strength, which can be caused by rainfall, earthquake motion, volcanic eruption, water-level change and slope erosion (Wieczorek, 1996).

2.2.2 Landslide propagation

Once initiated, the nature of landslide propagation depends on the type of failed material, the slope inclination and the surrounding topography. For a landslide of the slide type, the mass propagates as a continuous block along the failure surface. The movement is therefore generally controlled by the frictional resistance between the dynamic material, and the failure surface. However, landslides of the flow-type exhibit much more complex and diverse behaviour. Furthermore, slides may develop into a flow, depending on the material content and mobility. A slide to flow situation may arise due to the destruction of cohesive soil bonds, a change in slope inclination, or an increase in water content (Cruden and Varnes, 1996). In the absence of water, the motion of granular material is influenced by rapid granular collisions, as well as enduring frictional contacts (Drake, 1990). When water is encountered, the material water content is a major feature regarding flow mobility. High pore water pressures lubricate the material and reduce the soil effective stress, leading to flows with greater run-out distances (Costa, 1984). Moreover, high pressures can be sustained via a coupling between the rearrangement of individual grains and the resultant motion of the pore water (Iverson, 1997).

A particularly destructive type of flow is a debris flow, which is defined by Iverson (1997) as a landslide where both solid and fluid forces play a vital role in the dynamics. Under this definition, the term debris flow encompasses a wide range of events, including mud flows, earth flows and lahars. Debris flows typically contain a varied mixture of granular material, with grain diameters that may range in size from the order of microns to tens of metres (Iverson, 1997). As a result, grain size segregation is frequently observed in field and experimental debris flows, where the largest particles accumulate to the head of the flow (Johnson et al., 2012). Particle segregation also occurs in the vertical direction. Fine particles drop to the base of the flow, often producing a lubricating effect that can enhance flow run-out. Debris flows are subjected to collisional forces due to large grain interactions at the head, in addition to viscous effects created by the the presence of smaller particles and water in the flow body. Certain types of flow, such as mud flows, exhibit a more uniform grain size distribution (Johnson, 1970). Mud flows generally display the behaviour of a highly viscous fluid with a yield strength (Coussot, 2017). The physics of debris flows is complex, and their behaviour is controlled by a vast number of factors in addition to those discussed here, such as dilation, granular temperature, erosion and entrainment (Iverson, 1997). Although debris flows are diverse in nature, they all

feature large deformations and long run-out lengths. It is therefore essential that a numerical model for general landslide simulations can capture this type of behaviour.

2.2.3 Physical models

Data such as velocity, displacement and run-out length are essential for the validation and verification of numerical models. Due to the unpredictable nature of landslides and the environment in which they occur, it is often difficult to record measurements in the field, particularly in the case of rapid flows. As a result, landslide events can be recreated via controlled physical models, with specific instrumentation to record data of interest. A notable series of debris flow experiments have been conducted at a large scale with the U.S. Geological Survery (USGS) flume (Iverson et al., 2010; Iverson et al., 2011). The experiments involved a non-uniform and unsteady flow of unsorted water-saturated sediment consisting of sand, gravel and mud along a slope of length 95 m, inclined at 31°. The material was instantaneously released from behind a lock gate, as a *dam break*. The large scale set-up allowed the investigation of debris flows that are similar in size to those that occur in the field. The USGS experiments provided evidence that transient pore water pressures occur in debris flows. They also showed that flow run-out length is much greater when mud is present in the mixture than when it is not, as it promotes the presence of pore fluid pressures. Experiments on such a large scale are expensive and difficult to implement. Therefore, small scale experiments are often favoured. Small scale landslide experiments are relatively simple to perform, have a high repeatability and allow the implementation of a range of instrumentation (Kaitna, Rickenmann, and Schatzmann, 2007; Sanvitale and Bowman, 2012; Turnbull, Bowman, and McElwaine, 2015). Small scale experiments of debris flows are discussed in further detail in Chapter 7.

2.3 Mathematical modelling of soil: an application to landslides

Mathematical descriptions of soil are based on continuum mechanics, where the soil skeleton is assumed to consist of a continuous material. This considers the behaviour of the bulk material, as opposed to that of the individual soil grains. The fundamental governing equations of a continuum consist of the conservation of mass, and the conservation of linear momentum, written respectively as

$$\frac{D\rho}{Dt} = -\frac{1}{\rho}\nabla \cdot \mathbf{u}, \tag{2.4}$$

$$\frac{D\mathbf{u}}{Dt} = \frac{1}{\rho}\nabla \cdot \boldsymbol{\sigma} + \mathbf{b}, \tag{2.5}$$

where ρ is the material density, $\mathbf{u}$ is velocity, $\boldsymbol{\sigma}$ is the stress tensor and $\mathbf{b}$ is external body forces. Equations (2.4) and (2.5) describe the motion of soil, water, and a soil-water mixture as a whole. The behaviour of soil is governed by the description of the

stress, specifically the relationship between the stress and strains. The mathematical relationship between the stress and strain is termed the *constitutive model*.

Constitutive models for soil are typically derived under soil mechanics or fluid dynamics. In soil mechanics models, a relationship is required to describe the evolution of the effective stress $\boldsymbol{\sigma}'$. For a dry material, the total stress in Equation (2.5) is equal to the effective stress. However, for a saturated material, $\boldsymbol{\sigma} = \boldsymbol{\sigma}' - p_w$, and a description of the pore water pressure must also be included. For a full, two-phase model, separate equations of motion are defined to describe the soil and the water. Conversely, traditional models derived under fluid dynamics assume that the soil-water mixture can be approximated as one single phase fluid. A constitutive relationship is included to describe the evolution of the total stress of the mixture $\boldsymbol{\sigma}$. In reality, soils exhibit complex behaviour that cannot be captured with a single constitutive approach. This section provides a summary of the different constitutive models and mathematical approaches that are relevant for capturing the behaviour observed in landslides.

2.3.1 Soil mechanics models

Soils exhibit both reversible (elastic) and irreversible (plastic) deformations, depending on the applied stress and the state of the material (Chen and Mizuno, 1990). The notion of a material exhibiting both elastic and plastic strains is known as *plasticity* (Ancey, 2007). The concept was initially introduced to model metal deformation (Tresca, 1864), and constitutive models were developed to describe the transformation from elastic to plastic behaviour observed in metals. In the same way as for soil, the deformation of metal depends on the rate at which an external load is applied. Therefore constitutive models based upon plasticity are typically rate-dependent, where a relationship is defined between stress and strain rates (Chen and Mizuno, 1990). The fundamental feature of plasticity models is the definition of the limiting stress state, to distinguish between elastic and plastic deformations. The limiting state of stress is defined by the *yield function*, which is a function of components of the stress tensor. The yield function can be visualised as a three-dimensional surface in the stress space, and is also referred to as a *yield surface*. The Tresca yield surface was developed by Tresca (1864) for metals, and is depicted in Figure 2.2. The surface is defined according to the principal stresses, which denote the stress components of a body that is rotated such that the shear stresses are zero (Powrie, 2004) (see Chapter 3.1 for further details on the stress tensor). According to the Tresca yield criterion, the material strain is elastic if the corresponding stress state lies within the surface shown in Figure 2.2. The surface itself denotes the limit at which plastic deformations occur.

Motivated by the theory of plasticity in metals, Drucker and Prager, 1952 developed the work for applicability to soil behaviour, in what is called *classic plasticity*. The simple, one-dimensional, Mohr-Coulomb failure criterion defined in Equation (2.2) was extended to a full, three-dimensional yield surface, which can be interpreted

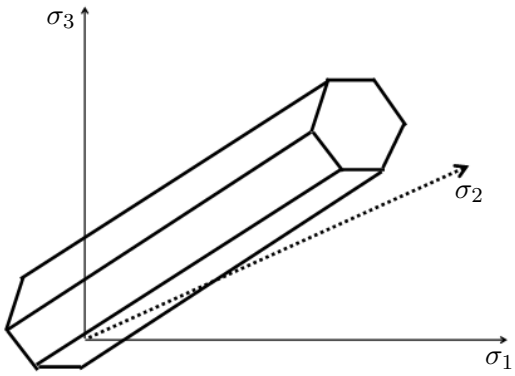

FIGURE 2.2: A depiction of the Tresca yield surface in the principal stress space. The axes σ_1, σ_2 and σ_3 denote the principal stresses.

as a modified Tresca yield surface. However, as detailed by Shield (1955), the Mohr-Coulomb failure surface is an irregular, hexagonal pyramid in the principal stress space. The surface contains singularities, which pose problems regarding mathematical and numerical models. Drucker and Prager (1952) therefore approximated the Mohr-Coulomb criterion with a smooth yield surface, known as the Drucker-Prager yield criterion. The key model parameters in the Drucker-Prager yield criterion are the soil cohesion and the angle of internal friction. Another yield surface that is applicable to soil behaviour is that of Von Mises (Von Mises, 1913), which was derived as an alternative to the Tresca condition to describe the yield surface in metals. Friction is not included in the Von Mises criterion, and it is only applicable for the failure of certain types of soils (such as clay, where cohesive forces dominate material behaviour (Chen and Mizuno, 1990)). In their extension of plasticity for soil, Drucker and Prager, 1952 also introduced the concept of a flow rule, which describes how plastic strains develop upon further loading via a plastic potential function. This function can take the same form as the yield function, producing a flow rule of an associated type. Otherwise, the flow rule is said to be non-associated. Constitutive models that are based on classic plasticity, where a yield surface defines elastic and plastic, are denoted *elastoplastic* (Chen and Mizuno, 1990).

Plastic deformations within soil are often confined to narrow regions, known as shear bands (Bardet and Proubet, 1991). Elastoplastic models have frequently been used to predict shear band formation in soils with a variety of different yield surfaces, producing results that agree well with experiments and theory (Hutchinson and Tvergaard, 1981; Chen and Mizuno, 1990; Bardet and Proubet, 1991; Anand, Aslan, and Chester, 2012). As described in Section 2.2.1, landslide movement is often preceded by the development of a slip surface (in localised failure). Slip surfaces correspond to regions of localised shear, and have been successfully predicted with elastoplastic models in the literature (see Figure 2.3) (Zheng, Liu, and Li, 2005; Griffiths and Marquez, 2007; Bui et al., 2008; Bui et al., 2011; An et al., 2016). Furthermore, the rapid collapse and propagation of a frictional soil has been described with an elastoplastic model with a Drucker-Prager yield surface, representing an

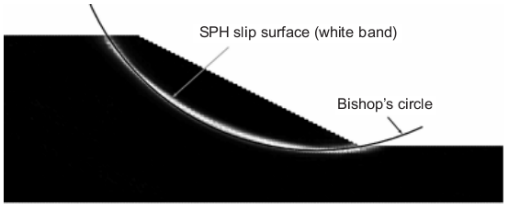

FIGURE 2.3: The slip surface simulated by Bui et al. (2011), with an elastoplastic constitutive model implemented within SPH. The profile coincides with that of the limit equilibrium method of Bishop (1955).

idealised landslide propagation problem, (Bui et al., 2008; Nguyen et al., 2017).

An alternative constitutive model was proposed by Perzyna (1966), motivated by the fact that many solid materials exhibit viscous effects. The Perzyna model bears numerous similarities to the classic plasticity model, including the concept of a yield surface. A key difference between the elastoplastic and Perzyna approach is that in addition to the components mentioned above, the latter model includes extra parameters that define the material 'viscosity'. Also, the stress state in the Perzyna model is allowed to exceed the yield surface, producing an effect called overstress. Perzyna's constitutive relationship has been implemented in numerical models to simulate the formation of shear bands in soil (Sluys, 1992; Blanc and Pastor, 2012; Blanc and Pastor, 2013; Mabssout and Herreros, 2013). Moreover, the Perzyna model is able to describe the transformation of a material from an elastic solid to a viscous-like fluid. It is therefore referred to as being elasto-viscoplastic (Troncone, 2005), or more often, viscoplastic (Sluys, 1992; Pastor et al., 2015a). Note that the term viscoplastic is also used to refer to the constitutive behaviour of certain fluids (Ancey, 2007), which is discussed in further detail in the following section. While the Perzyna model can describe fluid behaviour, its underlying framework is rooted within soil mechanics. The capabilities of the Perzyna model at capturing the transition from solid to fluid behaviour is particularly relevant to landslides, where material on a slope evolves from a stationary to a dynamic state, often exhibiting fluid-like features (Iverson, Reid, and LaHusen, 1997). As a consequence, the Perzyna model has been applied to the simulation of slip surfaces within a slope, that develop into slow-moving landslides (of the slide type) (Conte, Donato, and Troncone, 2014; Fernández-Merodo et al., 2014; Troncone, Conte, and Donato, 2014).

2.3.2 Fluid dynamics models

Constitutive models describe the relationship between stress and strain within a material in general. Bingham (1922) introduced the term *rheology* to describe the stress-strain relationship within fluids that exhibit both stationary (plug) and viscous-flow regions, and proposed an empirical law to define this behaviour. This model – the Bingham model – defines a simple one-dimensional relationship between the shear stress and shear strain rate, and is characterised by a constant yield stress value.

The one-dimensional Bingham model describes a fluid that is stationary when the shear stress is less than the yield value, and flows with a constant viscosity otherwise. The model was later generalised in the form of the Herschel-Bulkley model (Herschel and Bulkley, 1926), where the viscosity can be defined to vary with the shear rate, producing either shear-thinning or shear-thickening behaviour. Such models that describe both plug and viscous flow are typically referred to as viscoplastic models (Ancey, 2007). However, unlike the viscoplastic Perzyna and elastoplastic models, they are derived under the laws of fluid dynamics, as opposed to solid and soil dynamics. To avoid confusion when referring to the two types of model, here the term 'viscoplastic fluid' is used in reference to the fluid-derived model, and 'plasticity' is used to denote both the elastoplastic and Perzyna models. Despite their simplicity, viscoplastic fluid models are able to capture the behaviour of a wide range of fluids, including mud, industrial slurries, blood and certain food products (Bird, Dai, and Yarusso, 1983). Furthermore, it has been observed that some landslides, for example mud flows, behave as viscous fluids with plug regions (Johnson, 1970; Takahashi, 1981; Hunt, 1994; Iverson, 1997). As a result, Bingham and Herschel-Bulkley models have been frequently used within the literature to model the run-out of such flows (Laigle and Coussot, 1997; Fraccarollo and Papa, 2000; Haddad et al., 2010; Imran et al., 2001; Calvo et al., 2015). In a similar way to the extension of the simple Mohr-Coulomb equation to a three-dimensional surface, a complete tensorial formulation of the one-dimensional Bingham law was proposed by Oldroyd (1947) and Prager (2004). Little work has been undertaken since, and there is no representation of the yield stress as a three-dimensional yield surface for viscoplastic fluids (unlike for elastoplastic solids) (Ancey, 2007). However, it was shown by Pastor et al. (2015b) that the viscoplastic Perzyna model can reduce to the Bingham model once plastic flow has occurred, for a Von Mises yield criterion.

Viscoplastic fluid models approximate a soil-water mixture as one single viscous material, and describe a relationship between strains and the total stress. This assumption is only valid for certain types of soil where the overall composition is homogeneous, such as mud and clay. For this reason, it has been argued within the literature that viscoplastic fluid models are unsuitable for simulating landslide behaviour (Iverson, 2003; Pudasaini, 2012). Although it may be appropriate to approximate some types of landslide as a single phase fluid (such as mud flows), viscoplastic fluid models do not provide a general description of landslide behaviour.

2.3.3 Depth-integrated models

Landslides of the flow-type, such as debris flows, may exhibit large run-out distances. A complete mathematical description of this behaviour is computationally expensive when incorporated into numerical simulations. The governing equations can be reduced via depth-integration, which was originally performed for granular materials by Savage and Hutter (1989). Depth-integration consists of integrating the governing equations between the upper and lower flow boundaries (e.g. the flow bed and the

free surface). All flow variation in the normal direction to the bed is approximated as a depth-averaged value, which reduces the numerical expense when solving the equations. Depth-integration is considered a reasonable approximation for *thin flows*, that have a significantly greater length than height (Savage and Hutter, 1989). This is often the case for landslides of the flow-type, particularly debris flows. All current mathematical models of rapid landslides and debris flows are depth-integrated (Pitman and Le, 2005; Pastor, Blanc, and Pastor, 2009; Pudasaini, 2012; Iverson and George, 2014; Pastor et al., 2015a). Note that depth-integrated models cannot capture full three-dimensional flow behaviour, and are not appropriate for problems with significant vertical variations.

Depth-integrated models do not require a full three-dimensional relationship for the stress tensor, which allows the direct implementation of Coloumb's equation (Equation (2.2)) to relate the shear and normal stress components. The incorporation of Coulomb's law into the depth-integrated equations of motion provides a *frictional model*, where inter-particle friction is the main component governing material behaviour. Depth-integrated frictional models have been applied to simulate granular flows and landslide run-out (Savage and Hutter, 1989; Pastor et al., 2015a). Voellmy (1964) introduced an additional term into the frictional model to account for turbulence dissipation, which adds extra frictional resistance. The inclusion of the Voellmy term enabled the correct simulation of the run-out lengths of snow avalanches, which were overpredicted without it. Since its introduction, Voellmy's model has been used to simulate rapid landslides and debris flows, where it has provided more accurate results (in terms of material run-out) than the standard frictional model (Hungr, 2008; Pirulli and Pastor, 2012). The Voellmy term includes a model parameter that requires calibration for model input.

2.3.4 Two-phase models

Extensive work has been dedicated to the development of a generalised mathematical and constitutive model with an application to debris flows, where both solid and fluid phases control the flow dynamics. Such models are derived under a complete two-phase framework, where separate equations are used to describe the motion of the water and the soil skeleton. The two-phases are coupled via an interaction term in the equation of momentum, in addition to the assumption of Terzaghi's equation to describe the total soil stress. Iverson (1997) developed a depth-integrated two-phase debris flow model, where a frictional, Coulomb law was used to describe the constitutive behaviour of the soil skeleton. The evolution of pore water pressures was included in the model, although the vertical variation was lost due to depth-integration. An advection-diffusion equation was introduced to predict the vertical pressure distribution. The authors later extended the debris flow model to include additional effects, such as evolving dilatancy, volume fraction and erosion (Iverson and George, 2014; Iverson and Ouyang, 2015). Similar two-phase, depth-integrated debris flow models have been developed by Pastor and co-workers (Pastor et al.,

2009a; Pastor et al., 2014; Pastor et al., 2015a), Pitman and Le (2005) and Pudasaini et al. (2005). In the majority of two-phase debris flow models, the relative velocities between the soil and water phases are neglected. Recently, models have been developed that explicitly account for the distinct soil and water velocities (Pudasaini, 2012; Pastor et al., 2018). Two-phase models are described in further detail in Chapter 8.

2.4 Numerical models for the simulation of soil behaviour and landslides

The governing mathematical equations that determine landslide behaviour are complex, and must be approximated as a discrete system to obtain a numerical solution. The implementation of a numerical model consists of two components – a spatial discretisation of the material of interest, and a temporal discretisation. The gradient terms within the equations of motion are approximated according to the spatial discretisation scheme, while a time stepping scheme is applied to update the discrete variables from one time to the next. Classic numerical methods include the Finite Difference Method (FDM) and the Finite Element Method (FEM), which utilise a fixed mesh to discretise a system. Variable information (such as velocity and stress) is calculated at the nodes or elements of the mesh. Such methods employ an Eulerian specification, where the grid points are stationary and the material motion is described with respect to this fixed frame. Regarding landslide behaviour, the numerical method must be capable of tracking the history of the material in order to predict the formation of failure surfaces. Furthermore, it is required that the model can capture large deformations and complex free surfaces, that are associated with propagating landslides. Although Eulerian mesh-based methods have been used with some success to simulate landslide failure and propagation (Chen and Mizuno, 1990; George and Iverson, 2014; Crosta, Imposimato, and Roddeman, 2015), they require additional complex processes in order to fulfil these requirements, such as re-meshing and remapping of variables (Li and Liu, 2002).

As an alternative to mesh-based numerical methods, the past decades have seen the development of techniques that do not require a mesh, which are referred to as *meshless*. Meshless methods are Lagrangian in nature, where material information is stored at positions that are updated according to the material velocity. This allows the material history to be tracked in a natural way, and material failure can be simulated with ease. Furthermore, meshless methods are well adapted for modelling problems involving large deformations and free surfaces, and complex re-meshing processes are avoided. The oldest modern meshless method is Smoothed Particle Hydrodynamics (SPH), which was developed independently by Gingold and Monaghan (1977) and Lucy (1977) to model astrophysical problems. The governing, continuum equations of motion for a given problem are discretised over a set of particles, as opposed to a grid. The material of interest is therefore represented by the

particles (or nodes), where each one carries information about the material, such as the mass and density. Variables such as velocity and stress are approximated at each particle according to the discretised governing equations. This involves performing a summation over the surrounding particles within a specified domain of influence, defined by a smoothing length. The summation is multiplied by a smoothing function, called a *kernel*. The SPH approximation of a function $f(\mathbf{x}_i)$ is calculated at a specific particle i as

$$f(\mathbf{x}_i) = \sum_{j=1}^{N} \frac{m_j}{\rho_j} f(\mathbf{x}_j) W(\mathbf{x}_i - \mathbf{x}_j, h_s), \tag{2.6}$$

where the subscript j denotes the particles (with position vector $\mathbf{x}$) within the domain of influence of particle i, N is the number of neighbouring particles, W denotes the smoothing kernel and h_s is the smoothing length. The simplest form of the SPH approximation for the gradient of a function $(\nabla f(\mathbf{x}))_i$ is

$$(\nabla f(\mathbf{x}))_i = \sum_{j=1}^{N} \frac{m_j}{\rho_j} f(\mathbf{x}_j) \nabla W(\mathbf{x}_i - \mathbf{x}_j, h_s), \tag{2.7}$$

where ∇W is the gradient of the smoothing kernel.

A depiction of the SPH approximation is provided in Figure 2.4. The kernel must satisfy a number of requirements, and is weighted so that the closest neighbouring particles to a given node have a higher influence than those further away. The positions of the SPH particles are updated according to the material velocity, and the simulation of large, material deformations is straightforward. SPH has been applied to model a vast range of problems including geophysical flows (Gutfraind and Savage, 1997), free surface fluid flows (Crespo, Gómez-Gesteira, and Dalrymple, 2008), solid-fluid interaction problems (Gómez-Gesteira and Dalrymple, 2004), astrophysical flows (Schuessler and Schmitt, 1981) and multiphase problems (Monaghan and Kocharyan, 1995).

The first application of SPH to model soil behaviour was undertaken by Maeda and Sakai (2004), who attempted to simulate the seepage failure of a shallow slope. However, the soil was modelled as a purely elastic material and plastic deformations were not considered, which is a highly idealised assumption. Plastic deformation of soil was subsequently implemented within SPH (in two dimensions) for the first time by Bui et al. (2008), using an elastoplastic constitutive model with a Drucker-Prager yield surface. The model was applied to simulate the localisation of plastic strain in a cohesive soil, representing a simplified case of slope failure. Furthermore, the collapse of a non-cohesive, purely frictional soil, was also simulated. This problem exhibited large deformations and represented an idealised landslide of the flow-type. The model was validated by simulating the dam break collapse of a small scale experiment consisting of metal rods. The evolution of the material was accurately simulated with the SPH model. Following this pioneering development in the application of

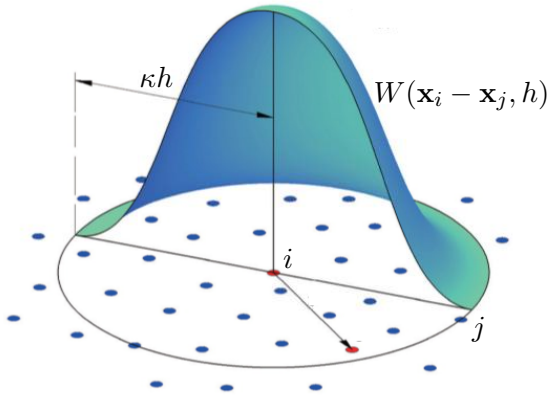

FIGURE 2.4: A depiction of the SPH particle approximation within the support domain of the smoothing kernel W, for a particle i. The image is adapted from Wang et al. (2016a). The support domain of W is defined by the smoothing length, multiplied by a constant κ.

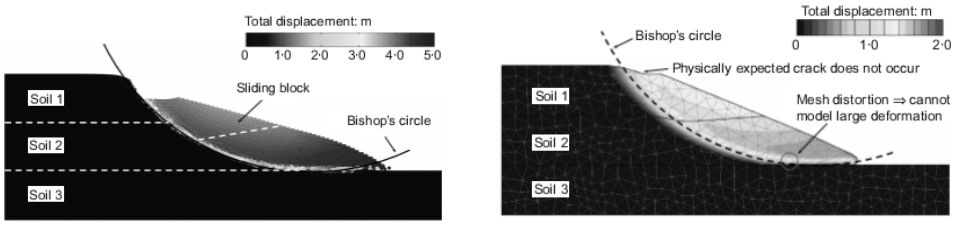

(A) SPH simulation (B) FEM simulation

FIGURE 2.5: The results of a landslide simulation conducted by Bui et al. (2011), comparing the SPH solution with that of FEM. Notice that for FEM, the displaced material cannot detach from the failure surface.

SPH to model soil behaviour, the authors applied the model to accurately predict the formation of slope slip surfaces and the subsequent post-failure landslide (Bui et al., 2011). The meshless nature of SPH allowed the separation of the propagating landslide from the slope, as shown in Figure 2.5a. The results were compared with those computed with an FEM method, which was unable to simulate the expected separation of the propagating material along the slip surface as a result of the mesh (see Figure 2.5b). These results highlight the potential of SPH at simulating both the failure and post-failure stages of landslides. The SPH model was later extended to simulate two-phase soil-water coupling, with an application to seepage flow (Bui and Nguyen, 2017). Following the work of Bui et al. (2008), a three-dimensional elastoplastic constitutive model was implemented within SPH by An et al. (2016), to simulate slope failure in three dimensions. The results showed that three-dimensional effects played a vital role in the simulations, and produced features which could not be captured with a two-dimensional model.

Significant progress has been achieved in the field of modelling rapid landslides

with an SPH model that was designed specifically for run-out analysis (Pastor et al., 2009a). The model utilises a depth-integrated system of equations derived under the two-phase theory of soil-water mixtures (the Biot-Zienkiewicz model). Using appropriate simplifications and assumptions, the governing equations describe a granular material with a single velocity, where pore water pressure terms may be included to approximate a soil-water mixture. Within the model it is possible to implement a variety of different constitutive laws to describe a wide range of material. The different constitutive models that have been applied to simulate landslide run-out include Bingham (Haddad et al., 2010; Pastor et al., 2014; Žic et al., 2015; Calvo et al., 2015), frictional (Pastor et al., 2015a; Pastor et al., 2014; Pastor, Blanc, and Pastor, 2009; Pastor et al., 2009b), Voellmy (Pastor et al., 2014; Pirulli and Pastor, 2012) and Perzyna (Pastor et al., 2015a). As SPH is not restricted by a mesh, simulations can be conducted over complex geometries. The depth-integrated SPH model has been combined with digital terrain models, which provide a topographic mesh of sites where landslides have previously occurred. These data allow the simulation of past events, where the SPH nodes represent the failed material and the digital terrain model defines the boundary conditions. Landslides that have been simulated in this way include: a series of flow-type landslides that occurred in the Campania region of Italy, 1998 (Pastor et al., 2009a); the 2001 lahar of Popocatèpetl, Mexcio (Haddad et al., 2010); the 1903 Frank rock avalanche, Canada (Pastor et al., 2015a); the 2000 Tsing Shan debris flow, Hong Kong (Pirulli and Pastor, 2012; Pastor et al., 2015a) and the 1966 Aberfan flow-type landslide, Wales (Dutto et al., 2017). These investigations aimed to recreate the run-out distances and velocities recorded at the actual event via back-analyses, and provided a close match between the numerical results and the available data. This was achieved by performing parametric studies regarding the relevant rheological parameters, which provides insight on the actual behaviour of the material within the landslide. The simulation of the Tsing Shan debris flow with the depth-integrated SPH model, performed by Pastor et al. (2015a), is shown in Figure 2.6. The material was described with a non-cohesive frictional constitutive law, with an additional model to include erosive effects in the governing equations. The qualitative behaviour of the debris flow was captured well with the depth-integrated SPH model. The SPH model has recently been extended to explicitly account for distinct soil and water phases, with two sets of SPH nodes for the two phases (Pastor et al., 2018). The two-phase model was applied to recreate the run-out path of the 1999 Tseng San Tsuen debris flow, Hong Kong, and was able to simulate the areas of debris deposition that occurred in the event.

In addition to the depth-integrated model of Pastor et al. (2009a), there are several other SPH models within the literature that have been utilised to simulate propagating landslides of the flow-type. Huang et al. (2015) combined the Bingham model with a Mohr-Coulomb definition of the yield stress to simulate the Bayi Gully debris flow, triggered by the Wenchuan earthquake in China, 2008. The final free surface of the SPH model compared well with the profile of the actual landslide, after

(A) The aftermath of the debris flow (King, 2001)

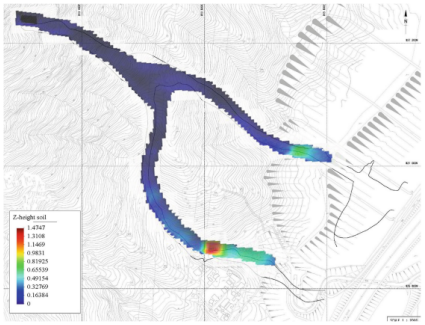

(B) The final material run-out simulated with SPH, coloured by material height (m)

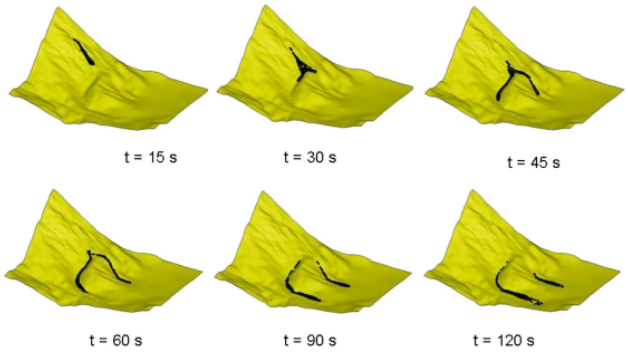

(C) The temporal evolution of the debris flow, modelled with SPH

FIGURE 2.6: Photographs of the aftermath of the Tsing Shan debris flow, compared against the numerical SPH model results of Pastor et al. (2015a).

600 seconds of simulation. Similar studies have been conducted, where past landslide events have been back-analysed using a Bingham rheological model (Dai et al., 2014; Hu et al., 2015; Wang et al., 2016b; Dai et al., 2017). In these investigations, the final flow paths have been predicted well with SPH, and good agreement with the field data was provided. However, unlike the depth-integrated SPH model of Pastor et al. (2009a), the aforementioned models are relevant to only a certain type of landslide, where the approximation of a viscoplastic fluid is justified.

There are alternative particle-based methods besides SPH that are also suitable for modelling large deformation problems which have been applied to landslide behaviour. The Material Point Method (MPM) is a Lagrangian numerical scheme that approximates a continuum material over a discrete set of particles. Unlike SPH, MPM utilises a background mesh to solve the governing equations of motion. At each time step, the discrete particles are projected onto the nodes of the background mesh, and the model equations are solved at the mesh nodes. The updated variables (i.e. velocity and stress) are then projected from each mesh node back to the material points, and the mesh is reinitialised. MPM has been applied to numerous problems related to landslide behaviour, including slip surface development, progressive dam failure and the large deformation of a soil-water mixture (Zabala and Alonso, 2011; Abe, Soga, and Bandara, 2013; Bandara and Soga, 2015; Soga et al., 2015). However, as a result of the multiple steps involved, the computational cost of MPM is particularly high. Furthermore, the method is not truly meshless due to the addition of the background grid. Although MPM is better suited to large deformation problems than Eulerian mesh-based methods, the presence of the grid poses restrictions on material displacement that are not present within SPH. Further examples of particle-based methods include the Particle-Finite Element Method (Moresi, Dufour, and Mühlhaus, 2003) and the Element-Free Galerkin Method (Lu, Belytschko, and Gu, 1994). There are drawbacks and benefits associated with every particle-based scheme, which are described in detail in Li and Liu (2002) and Soga et al. (2015). Nonetheless, SPH remains the single, completely meshless particle method, and is favoured due to its simplicity with respect to alternative methods.

2.5 Shortcomings of SPH and available solutions

With the benefits that SPH brings to modelling large deformation problems come several well documented shortcomings. Since its introduction, the method has been developed significantly and there are a number of available solutions to the majority of the identified problems. For example, compared to traditional mesh-based methods, SPH has a high computational expense that increases rapidly with increasing particle resolution. Recent advances in high performance computing methods have considerably improved the efficiency of SPH (Domínguez, Crespo, and Gómez-Gesteira, 2011). Furthermore, the implementation of boundary conditions within SPH is non-trivial, and the deficiency of particles in the boundary region can lead

to inaccurate calculations in this area (Liu, Shao, and Chang, 2012). There are several effective treatments for boundary conditions, including the addition of 'dummy nodes' to represent different types of boundaries (Morris, Fox, and Zhu, 1997). Moreover, SPH can suffer from low computational accuracy, which is associated with the consistency of the kernel function (Liu and Liu, 2006). The concept of consistency originates from FEM and is defined such that an approximation has nth order consistency if it can exactly reproduce a polynomial up to the order n. The standard SPH kernel approximations cannot always satisfy the consistency conditions and the method is therefore said to exhibit particle inconsistency (Liu, Liu, and Lam, 2003). The inconsistency occurs due to the kernel truncation at the boundary, but can also occur for interior particles that have an irregular distribution. Several methods have been proposed to restore the particle consistency via a corrected kernel function (Liu, Jun, and Zhang, 1995; Li and Liu, 1999; Chen, Beraun, and Carney, 1999; Liu, Liu, and Lam, 2003).

A serious shortcoming of SPH is its susceptibility to numerical instabilities, which can lead to the complete degradation of numerical simulations (Swegle et al., 1994; Monaghan, 2000). Numerical instabilities pose problems in all numerical methods, particularly regarding the simulation of shock waves – disturbances that propagate at a higher velocity than the local speed of sound within a material. These produce sharp discontinuities in variables such as velocity, density and pressure, that are difficult to resolve numerically (Anderson, 1982). Shock wave-induced instabilities produce particularly severe effects in SPH due to the absence of a mesh. Shocks within SPH induce irregular particle motions on the length scale of the initial particle separation, which results in large fluctuations of pressure (Monaghan and Gingold, 1983). Von Neumann and Richtmyer (1950) introduced the concept of *artificial viscosity* to calculate problems with shocks with classic mesh-based methods. The Von Neumann-Richtmyer artificial viscosity is defined to act only when material is under compression in order to smooth over (dampen) shocks, and solve the governing equations without the need for any complex shock boundary treatment. The artificial viscosity was later adapted and developed for implementation within SPH (Monaghan and Gingold, 1983; Monaghan, 1989; Monaghan, 1992). It is now viewed as an essential component in the majority of SPH simulations (even those without shocks), to dampen irregular particle motions (Liu and Liu, 2010). The inclusion of artificial viscosity requires the appropriate values of two input parameters that are not directly associated with any physical properties. Excessive viscosity may be produced for large parameter values, which can lead to unrealistic material behaviour (Swegle et al., 1994). Alternative methods have recently been proposed to dampen particle oscillations that involve physically relevant parameters (Bui and Fukagawa, 2013; Bui et al., 2014; Nguyen et al., 2017).

2.5.1 Zero-energy modes

A comprehensive stability analysis of SPH was performed by Swegle et al. (1994), where a problem was identified with the kernel smoothing function. The simulation of two impacting, solid bodies was performed in one dimension, where each body was represented by a horizontal line of 100 particles with an inter-particle spacing of 0.01 cm. The stress profile along the length of the two bodies after 1 microsecond of impact is shown in Figure 2.7a. It can be seen that the profile exhibits large stress fluctuations – referred to as *noise*, that are most severe at the interface between the two bodies. The noise was not eliminated by increasing the magnitude of artificial viscosity, nor by varying the time step and smoothing length. Furthermore, contrary to the expected behaviour, the stress oscillations did not dampen with time. To investigate the cause of the instability, Swegle et al. (1994) examined the discrete values of stress around the impact interface. This is provided in Figure 2.7b, where the particle stress values are depicted by the points. Also plotted is the SPH kernel approximation of the discrete points (according to Equation (2.6)), which is depicted by the continuous line. The figure shows that the kernel approximation (which is simply a polynomial fit to the data) follows the oscillating pattern of stress. However, the local minima and maxima of the kernel function naturally share the same location as the discrete particles. As a result, the gradients of the kernel, and therefore the gradients of stress, are zero at the discrete points. This is shown in Figure 2.7c, where the stress gradients are plotted for the discrete particles in the region of the impact. The continuous line represents the SPH kernel gradient approximation of the stress field. While the continuous kernel gradient approximation is oscillatory, the gradient values at the particles are approximately zero. Clearly, the stress field over the two bodies is not constant and the resulting stress gradient should therefore not be zero. Moreover, in the absence of external body forces, a zero stress gradient results in zero acceleration (because the acceleration is directly proportional to the stress gradients in the equation of momentum). Thus, the particles do not accelerate in response to the stress field and the fluctuations are not reduced.

The zero stress gradients that are calculated at nodes within a non-constant stress field are referred to as *zero-energy modes* (Belytschko et al., 2000). Their occurrence is due to the anti-symmetric form of the gradient of the smoothing kernel. To illustrate this, consider a simple one-dimensional problem of a row of equally spaced particles subjected to an oscillatory stress field, as depicted in Figure 2.8. The stresses are assumed to be of equal magnitude for each particle, and alternative in sign between adjacent particles. According to Equation (2.7), the calculation of the stress gradient at particle p_2 is:

$$\left(\frac{\partial \sigma}{\partial x}\right)_{p2} = \sum_{j=1}^{N} \frac{m_j}{\rho_j} \sigma_j \frac{\partial W_{ij}}{\partial x}. \tag{2.8}$$

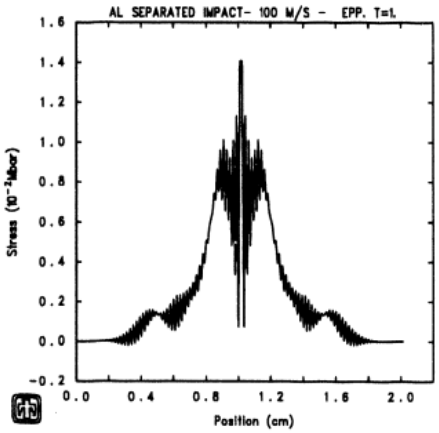

(A) Full stress profile

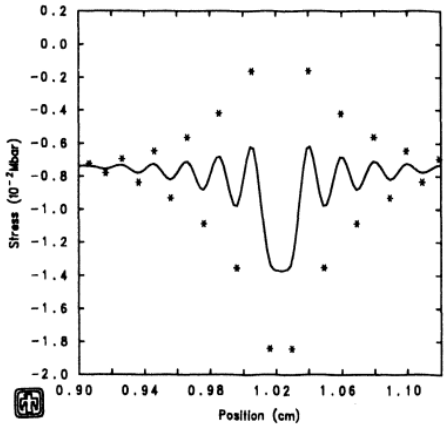

(B) Stress values around impact

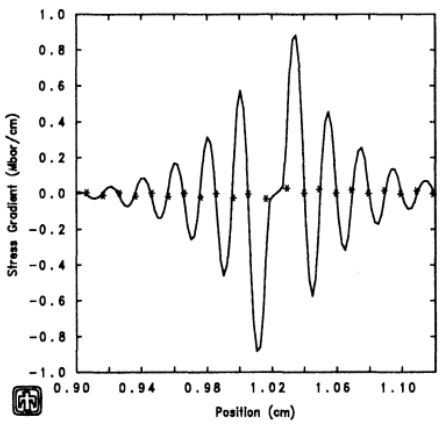

(C) Stress gradient values around impact

FIGURE 2.7: Values of stress and stress gradients with their corresponding kernel approximations, for the one-dimensional simulation of two impacting solid bodies (Swegle et al., 1994).

Assuming that the particles are equal in mass and density, Equation (2.8) becomes

$$\left(\frac{\partial \sigma}{\partial x}\right)_{p2} = \frac{m}{\rho}\left(\sigma_1 \frac{\partial W_{21}}{\partial x} + \sigma_3 \frac{\partial W_{23}}{\partial x}\right). \tag{2.9}$$

Due to the anti-symmetric form of the kernel gradient, $\frac{\partial W_{21}}{\partial x} = -\frac{\partial W_{23}}{\partial x}$, and Equation (2.9) reduces to

$$\left(\frac{\partial \sigma}{\partial x}\right)_{p2} = \frac{m}{\rho}\frac{\partial W_{21}}{\partial x}\left(\sigma_1 - \sigma_3\right). \tag{2.10}$$

For the assumed oscillatory stress field, the stresses at particles p_1 and p_3 are equal and the stress gradient (and therefore the acceleration) at particle p_2 is calculated as zero. According to Equation (2.10), the stress gradient at particle p_2 is equal to zero regardless of the stress value at the particle itself. Therefore, the incorporation of the particle itself in the gradient calculation would lead to a more realistic approximation of the overall stress gradient field (Patankar, 1980; Dyka, Randles, and Ingel, 1997). Note that the simple calculation described above is a simplified case used to illustrate the occurrence of zero-energy modes. The same problem occurs for more complex cases in higher dimensions. The calculation outlined in Equations (2.8) to (2.10) is very similar to the equivalent computation with FDM, in which the problem of zero-energy modes was originally identified (Maenchen and Sack, 1963). It has also been shown that the problem still occurs when the finite difference nodes are not equally spaced (Patankar, 1980). An effective solution to this problem was introduced in FDM in the form of a *staggered grid* (Harlow and Welch, 1965; Patankar and Spalding, 1983). In the staggered grid approach, a second set of nodes are introduced that are positioned in a staggered arrangement to the first set. The velocities are calculated on one set of nodes, and the remaining variables (including stress) are calculated on the second set. Therefore the stress gradient calculation depends on the difference between two adjacent nodes from the second set, rather than two alternative nodes on the first set. It was acknowledged by Swegle et al. (1994) that the problem of zero-energy modes in SPH was due to the fact that the velocity and the stress are evaluated at the same location. Zero-energy modes have been frequently documented within FEM, where they produce spurious velocity values at the element nodes (Hughes, 2012; Belytschko et al., 2013). This may result in the velocities at neighbouring nodes having an equal magnitude but opposite direction, producing a deformed 'hourglass' mesh (Belytschko et al., 1984).

While extensive research has focused on eliminating the zero-energy modes in FDM and FEM (e.g. Flanagan and Belytschko (1981), Belytschko et al. (1984), Belytschko and Bachrach (1986)), little work has been undertaken in this area regarding SPH. In a review of the SPH method, Liu and Liu (2010) claimed that the occurrence of zero-energy modes is not as serious within SPH as for FDM and FEM. The reason provided was that the zero-energy modes are normally found in a regular particle configuration, while SPH typically exhibits an irregular configuration due to the movement of the particles. However, for the simulation of solid problems in

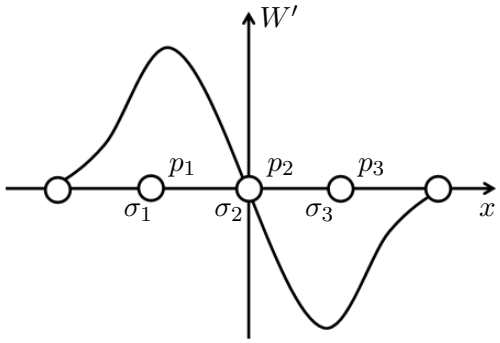

FIGURE 2.8: A depiction of a row of SPH particles denoted p_1, p_2 and p_3, with respective stresses σ_1, σ_2 and σ_3.

the literature, a regular particle configuration is often favoured (Bui et al., 2008; Blanc and Pastor, 2012; Bui and Fukagawa, 2013). Furthermore, Liu and Liu (2010) reported that the conditions for triggering zero-energy modes are specific, and not usually encountered. In fact, stress oscillations are a well-documented feature of SPH within both solids (Blanc and Pastor, 2012; Nguyen et al., 2017; Bui and Fukagawa, 2013), and fluids (Xu and Yu, 2018; Monaghan, 2012), which are often a result of short-length-scale noise. Therefore, such oscillations have the potential to trigger zero-energy modes. Bui and Fukagawa (2013) reported the presence of zero-energy modes in the application of a load to a soil sample, and used a viscous damping term to reduce the resultant fluctuations. Moreover, Nguyen et al. (2017) documented severe stress and strain oscillations in the collapse of a granular column. A regularisation technique was performed every specified number of time steps to control the noisy profiles, where the values of stress and strain were smoothed by interpolating over neighbouring nodes with a Moving Least Squares method.

2.5.2 Tensile instability

In their investigation of SPH, Swegle et al. (1994) also discovered that certain problems exhibit artificial fractures when under a tensile state of stress. This was illustrated in the simulation of two rubber rings impacting one another at 50 m s^{-1}. It was observed that fractures developed within the material as the rings deformed after impact, as shown in Figure 2.9. The fractures only occurred in regions under tension, and they were not a physical feature of the problem (the material strength was significantly higher than the stress state when fractures occurred). The formation of the fractures was triggered by unstable, non-uniform particle behaviour under tension. Uneven particle movement caused certain particles to clump together, resulting in a loss of communication between neighbours and subsequent fracturing. This numerical instability is known as the *tensile instability*. To pinpoint the root cause of the tensile instability, Swegle et al. (1994) performed a rigorous stability analysis for SPH in one dimension, for an elastic solid material. For the discrete, one-dimensional SPH equations, the governing equation of momentum reduced to a

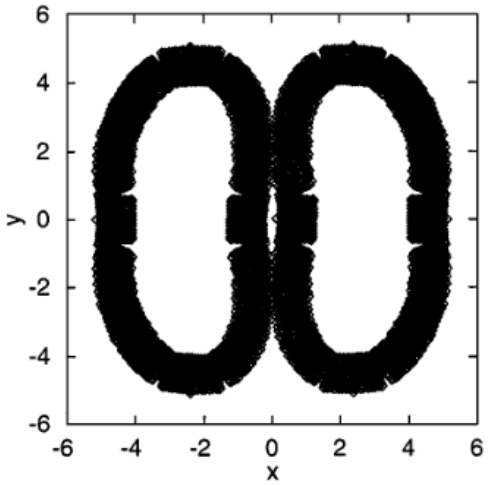

FIGURE 2.9: The collision of two rubber rings showing non-physical fractures. The problem was originally simulated by Swegle et al. (1994) and recreated by Monaghan (2000) (this image is taken from the latter).

relationship between displacements and the product of the stress and the derivative of the kernel. The resulting stress-strain relationship was examined for an elastic material. Rather then exhibit the linear stress-strain profile governed by the constitutive relationship for an elastic material, the strain displayed nonlinear behaviour for a stress-kernel product that exceeded a certain threshold. This region of nonlinear behaviour corresponded to the occurrence of the numerical instability. The results of the stability analysis quantified the onset of the instability as a relationship between the second derivative of the kernel function multiplied by the stress. A condition for unstable behaviour was defined as

$$W''\sigma > 0, \tag{2.11}$$

where W'' is the second derivative of the kernel and σ is the stress (in one dimension). Therefore, in a similar way to the zero-energy mode instability, the tensile instability is due to the form of the kernel function. However, the occurrence of the tensile instability depends on the sign of the product of the stress and the second derivative of the kernel. The second derivative is positive for most particle-particle interactions, and the tensile instability occurs in a tensile state. Note that instabilities could also occur in a compressive state if $W'' < 0$, which occurs for particles that are located close to one another (in one dimension, $W'' < 0$ for particles located within a distance of $2/3$ times the smoothing length). The effects of the instability have been only observed within the literature for material under a tensile stress (Monaghan, 2000).

The tensile instability initiates in the form of variable oscillations at individual particles, which can lead to particle clumping and material fractures. As a result, the effects of the tensile instability are dependent on the growth rate of the instability, and the amount of time the simulation remains in an unstable regime (Swegle et al.,

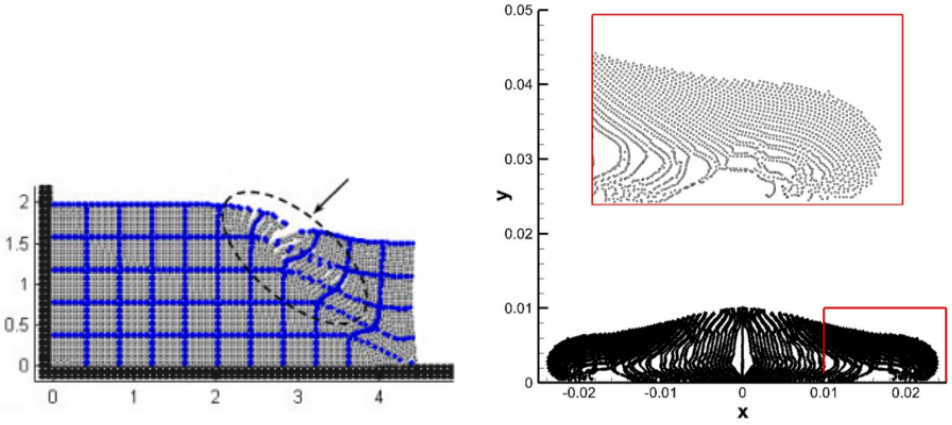

(A) Cohesive soil collapse (Bui et al., 2008)

(B) Viscoelastic droplet impact (Xu and Yu, 2018)

FIGURE 2.10: The appearance of fractures as a result of the tensile instability, from SPH simulation results provided in the literature.

1994). The instability has been observed in a range of applications (Schuessler and Schmitt, 1981; Steinmetz and Mueller, 1993), although the severity of the effects depends on the problem under consideration. For problems involving fluids and brittle solids, the material usually breaks up before the effects of the instability manifest (Monaghan, 2000). Simulations of material with a cohesive strength are particularly susceptible to the effects of the instability (see Figure 2.9). Bui et al. (2008) simulated the collapse of a cohesive soil, where severe fracturing occurred due to the tensile instability, as shown in Figure 2.10a. Serious fractures have also been exhibited in the simulations of viscous fluids (Fang et al., 2006; Xu and Yu, 2018), which are displayed in Figure 2.10b. Unless a technique is employed to prevent the manifestation of the tensile instability, the simulations of cohesive soils and viscous fluids are inaccurate, non-physical and unstable. Thus, regarding simulations of landslide behaviour with SPH, it is essential to include a remedy for the tensile instability.

It was shown by Swegle et al. (1994) that an increase in artificial viscosity can dampen the effects of the instability, but is not able to eliminate them. The instability was also found to be independent of smoothing length, initial particle distribution and the time stepping scheme. Therefore, a number of solutions have been proposed within the literature to suppress the effects of the tensile instability. The most well known remedy is the artificial repulsive force proposed by Monaghan (2000), and extended to elastic solids by Gray, Monaghan, and Swift (2001). This method involves the application of a short range repulsive force between particles that are under a tensile state of stress, to prevent them from clumping. The results are effective, and it has been implemented in a number of applications (Gómez-Gesteira and Dalrymple, 2004; Fang et al., 2006; Dolag and Stasyszyn, 2009), including the simulations of cohesive soil by Bui et al. (2008). However, the method requires the tuning of parameters that do not have a physical interpretation. Furthermore, recent analyses

have indicated that the method is less accurate than alternative techniques (Mao and Liu, 2018; Xu and Yu, 2018). A method based on particle shifting was proposed by Xu, Stansby, and Laurence (2009) and Lind et al. (2012), and recently applied to remove the effects of fractures in a viscoelastic fluid (Xu and Yu, 2018). In this technique, particles in areas of low concentration are shifted according to a diffusive flux to prevent fractures from forming. The performance of the method was shown to be more effective than the artificial repulsive force at removing fractures in a viscoelastic drop (Xu and Yu, 2018). An alternative approach for the tensile instability is to implement a different form of the kernel function. Dilts (1999) utilised a Moving Least Squares (MLS) interpolation function within a particle-based method. The MLS function has a higher degree of accuracy than the standard SPH kernel, which can prevent the onset of the instability. However, these functions are significantly more complex and time consuming to implement within SPH, counteracting the benefits of SPH in terms of simplicity and efficiency. Moreover, it has been shown that certain types of kernel function are able to completely eliminate the onset of the tensile instability (Belytschko et al., 2000). However, these types of kernel – a Lagrangian kernel – are defined so that the SPH particles have the same neighbours throughout the duration of the simulation. As a result, this method is not appropriate for modelling problems that exhibit large deformations and displacements.

Following the investigation of Swegle et al. (1994), a unique approach in which to alleviate the tensile instability within SPH was introduced by Dyka, Randles, and Ingel (1995). It was shown by Swegle et al. (1994) that the occurrence of zero-energy modes was directly related to the fact that the velocities and stresses are calculated at the same location. Furthermore, in FDM this problem is eliminated by using a staggered grid approach, where the velocity and stress are calculated on different sets of nodes. In addition to eliminating the zero-energy modes, the staggered grid approach essentially allows the stress information at a specific node to be included in the calculation of the stress gradients at that node. This improves the accuracy of the gradient calculation significantly (Patankar, 1980). Dyka, Randles, and Ingel (1995) believed that such an increase in accuracy could prevent the occurrence of the tensile instability in SPH, and therefore developed a one-dimensional 'staggered grid' equivalent within SPH. The velocities are calculated on the SPH nodes, while a separate set of nodes, denoted as *stress-points*, are used to calculate the stresses. The nodes and stress-points are positioned in a staggered arrangement. The method was applied to simulate a number of cases that suffer from both zero-energy modes and the tensile instability, including an elastic bar under tension, and a bar subjected to an alternating velocity field (Dyka, Randles, and Ingel, 1995; Dyka, Randles, and Ingel, 1997). The problems were modelled with success, without the development of numerical instabilities. This dual-particle method was later extended to higher dimensions to simulate a variety of small deformation, solid problems (Randles and

Libersky, 2000; Vignjevic, Campbell, and Libersky, 2000). Despite the method exhibiting promising results in terms of stability and accuracy, it has not been developed within SPH beyond these initial investigations. The main reason for this is that it is unclear how to update the positions of the stress-points, as velocity is not calculated on these particles. As a meshless method, the most attractive feature of SPH is that the positions of the particles are updated, allowing the simulation of large deformation problems. In the dual-particle SPH methods presented in the literature, the velocity was updated via an interpolation method from the nodes to the stress-points. While it is applicable to problems that do not exhibit a large particle displacement, the method is expected to break down for large deformation simulations (Vignjevic, Campbell, and Libersky, 2000). Therefore in their current form, dual-particle methods do not provide a universal remedy for the instabilities encountered in SPH.

Blanc (2011) developed a stable numerical scheme for the simulation of landslide behaviour that combined SPH with the high-accuracy Taylor-Galerkin Finite Elements method. The method uses SPH for the spatial discretisation of the governing equations, with the Corrective Smoothed Particle Method (Chen and Beraun, 2000) to improve the accuracy of the SPH kernel approximations. The time derivatives of the unknown variables are solved according to a forward-time Taylor series expansion, based on the two-step Taylor-Galerkin method. In the combined SPH-Taylor method, the calculation is split up over two sets of SPH nodes, referred to as *nodes* and *elements*. The method is therefore referred to in this research as the *Node-Element method*. As the Taylor time discretisation involves two steps, the first step is solved on the SPH elements, and the second step is solved on the SPH nodes. In a similar way to the splitting of the velocity and stress in the staggered grid approach, the Node-Element method allows information at a specific node to be included in the gradient calculations at that node. Therefore, the method is capable of producing stable and accurate results for various problems regarding soil dynamics and landslide behaviour. The Node-Element SPH method (with a viscoplastic Perzyna rheological model) has been applied to produce stable simulations of simple elastic slopes, the propagation of shear bands, a bearing capacity problem and the large deformation of a viscoplastic, cohesive slope (Blanc and Pastor, 2012; Blanc and Pastor, 2013; Mabssout and Herreros, 2013). The Node-Element method requires that an SPH element is positioned in the centre of every four neighbouring nodes at each time step. As a result, the positions of the particles are somewhat restricted and the method is not truly meshless. This is depicted in Figure 2.11a, where the intersections of the grid depict the positions of the SPH nodes, and the crosses depict the SPH elements. With this restriction, it is possible to simulate problems of a relatively large deformation, such as the deformation of the viscoplastic slope shown in Figure 2.11b. However, the method cannot be applied to problems with high velocities and very large displacements, such as landslide propagation of the flow-type.

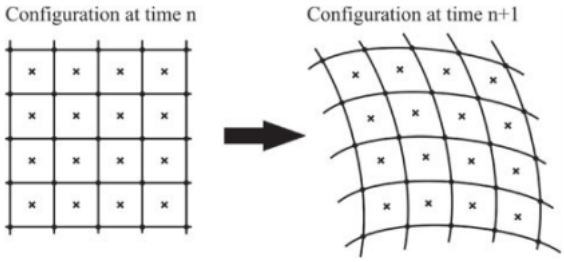

(A) A depiction of the position update of the nodes and elements.

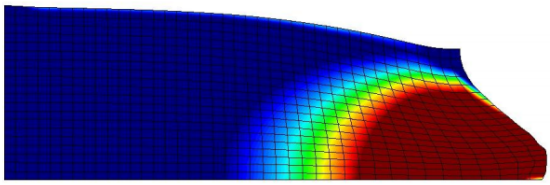

(B) The viscoplastic slope at $t = 35$ s. The contours represent regions of irreversible, plastic strain.

FIGURE 2.11: An illustration of the Node-Element method and its application, taken from Blanc and Pastor, 2013.

2.6 Conclusion

The processes that occur in landslides within initiation and propagation are complex and are governed by solid, fluid and soil mechanics. A numerical model for general landslide behaviour should be capable of simulating the gradual development of failure surfaces in landslide initiation, in addition to rapid, propagating flows. SPH is a meshless method that is able to handle these features with ease, and has been frequently applied to landslide behaviour (Bui et al., 2008; Bui et al., 2011; Pastor et al., 2009a; Pastor et al., 2015a; Dai et al., 2017). However, numerical instabilities seriously affect the performance of SPH, which is particularly detrimental regarding the simulation of solids, soil and viscous fluids (see Figures 2.7, 2.9 and 2.10). Although there are a number of proposed remedies for the instabilities, they are only suitable for specific types of problem (e.g. the Lagrangian kernel method (Belytschko et al., 2000)), or require the tuning of artificial parameters (e.g. the artificial repulsive force (Monaghan, 2000)). The two most serious instabilities within SPH (the zero-energy modes and the tensile instability) have been related to the fact that all variable information is calculated at the SPH nodes (Swegle et al., 1994; Dyka, Randles, and Ingel, 1997). Similar problems are found in mesh-based methods, and a common stabilisation technique is to split up the stress and velocity calculations over two sets of grids (Harlow and Welch, 1965; Caretto, Curr, and Spalding, 1972; Patankar, 1980; Patankar and Spalding, 1983). This technique has also been implemented within SPH, and has provided promising results in terms of numerical stability and model performance (Dyka, Randles, and Ingel, 1995; Dyka, Randles, and Ingel, 1997; Randles and Libersky, 2000; Vignjevic, Campbell, and

Libersky, 2000). However, very little attention has been devoted to this method since its introduction. This is partly because its implementation within SPH – a meshless method – is non-trivial. Furthermore, the existing set-up produces major restrictions on particle movement within SPH, which counteract its applicability for modelling problems with large displacements.

This research aims to revisit the method – the *Stress-Particle SPH method* – in order to develop an improved SPH model for simulating landslide behaviour. This involves implementing stress-points within SPH and applying the technique to problems regarding soil and landslides for the first time. What's more, the method is extended so that it is capable of capturing the large displacements that are relevant to landslide propagation, for the first time. Note that although in FDM the staggered grid approach can completely eliminate zero-energy modes, the SPH calculations are more complex. When approximating the gradient of a variable with FDM, only the information from two nodes is used. This is not the case for SPH in general. Furthermore, the particle positions are updated at each time step and the number of neighbours varies. Therefore, an initial 'staggered grid' arrangement of SPH nodes and stress-points does not necessarily stabilise SPH, and a higher ratio of stress-points to nodes may be required (Belytschko et al., 2000). This factor is also investigated in the subsequent chapters.

Regarding the mathematical description of landslide behaviour, plasticity-based models have been used with success to model slip surface formation, in addition to the solid-fluid transition in landslides (Bui et al., 2008; Bui et al., 2011; Blanc and Pastor, 2012; Blanc and Pastor, 2013). As a result, both the elastoplastic and viscoplastic Perzyna model are implemented within the Stress-Particle SPH model. To assess the applicability of the new SPH model for landslide initiation and propagation, simplified approximations of these two stages are considered. Regarding landslide initiation, attention is focused on the model capabilities at capturing the development of shear bands and slip surfaces. The capabilities of the model at simulating landslide propagation are assessed by considering the rapid flow of soil, that exhibits large displacements. In both cases, the model results are compared against results from the literature. Moreover, the model is applied to simulate an experimental debris flow, providing further validation and verification. In the following chapter, the elastoplastic and viscoplastic Perzyna models are described in detail.

Chapter 3

Mathematical description of soil

This chapter presents the governing equations of a soil continuum, that are implemented in the SPH framework in the following chapter. The constitutive behaviour of the soil is described using the theory of plasticity, with both elastoplastic and viscoplastic Perzyna models. This chapter is structured as follows. First, a description of the stress tensor is provided, along with relevant invariants of the stress. Second, the equations of motion for a single phase soil are presented. Then, the general constitutive framework under the theory of plasticity is detailed, followed by an explanation of the distinct elastoplastic and viscoplastic models. Due to the Lagrangian nature of SPH the following mathematical equations are written in a Lagrangian frame of reference.

3.1 The stress tensor

In three-dimensional space, the stress tensor $\sigma_{\alpha\beta}$ is

$$\sigma_{\alpha\beta} = \begin{pmatrix} \sigma_{xx} & \sigma_{xy} & \sigma_{xz} \\ \sigma_{xy} & \sigma_{yy} & \sigma_{yz} \\ \sigma_{xz} & \sigma_{yz} & \sigma_{zz} \end{pmatrix}, \tag{3.1}$$

where α and β represent the x, y and z components in Cartesian coordinates. The stress tensor is symmetric, in that $\sigma_{\alpha\beta} = \sigma_{\beta\alpha}$. Together, the components of the stress tensor completely describe the stress state at a point within a continuum material. This is visualised in Figure 3.1, which shows the stress components of an idealised, cubical element. Each face contains two stress components that act parallel to the face, at a right angle from one another – these are the *shear stresses* $\sigma_{xy}, \sigma_{xz}, \sigma_{yz}$. The third stress component acts perpendicular to the face, and is known as the *normal stress* $(\sigma_{xx}, \sigma_{yy}, \sigma_{zz})$. Recall that in the current work, a compressive stress is defined to be negative. The corresponding three-dimensional strain tensor $\epsilon_{\alpha\beta}$ is

$$\epsilon_{\alpha\beta} = \begin{pmatrix} \epsilon_{xx} & \epsilon_{xy} & \epsilon_{xz} \\ \epsilon_{xy} & \epsilon_{yy} & \epsilon_{yz} \\ \epsilon_{xz} & \epsilon_{yz} & \epsilon_{zz} \end{pmatrix}. \tag{3.2}$$

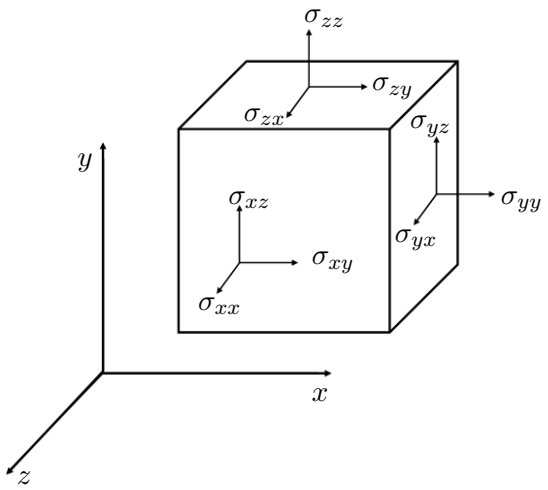

FIGURE 3.1: A depiction of the three-dimensional stress tensor in the Cartesian plane.

The stress tensor can be decomposed into two components: a hydrostatic pressure p and a deviatoric stress $s^{\alpha\beta}$:

$$\sigma_{\alpha\beta} = -p\delta_{\alpha\beta} + s_{\alpha\beta}, \tag{3.3}$$

where $\delta_{\alpha\beta}$ is the Kronecker delta ($\delta_{\alpha\beta} = 1$ if $\alpha = \beta$, $\delta_{\alpha\beta} = 0$ if $\alpha \neq \beta$). The hydrostatic pressure of a soil is defined as the negative average of the normal stress components, i.e.

$$p = -\frac{\sigma_{\gamma\gamma}}{3} = -\frac{1}{3}\left(\sigma_{xx} + \sigma_{yy} + \sigma_{zz}\right). \tag{3.4}$$

Naturally, the deviatoric stress represents the deviation of the stress from the hydrostatic state

$$s_{\alpha\beta} = \sigma_{\alpha\beta} + p\delta_{\alpha\beta}. \tag{3.5}$$

The hydrostatic pressure is the isotropic stress that is responsible for volumetric changes of a material element. The deviatoric stress is responsible for shape deformations of the element due to shear.

3.1.1 Invariants of the stress tensor

Invariants of the stress tensor are functions that are independent of the coordinate system. These are useful in terms of defining a generalised failure criteria. The stress invariants are obtained on rotation of the stress tensor into a frame of reference where all shear stresses are zero. Consequently, the non-zero elements of the stress tensor consist of the normal components only, which are known as the *principal stresses* – denoted σ_1, σ_2 and σ_3. This stress tensor transformation is defined according to:

$$(\sigma_{\alpha\beta} - \sigma\delta_{\alpha\beta})n_\beta = 0, \tag{3.6}$$

where σ denotes the principal stress and n_β denotes the unit normal in the transformed stress state (corresponding to zero shear stresses). The solution of the system (3.6) leads to the following characteristic equation:

$$\sigma^3 - I_1\sigma^2 + I_2\sigma - I_3 = 0, \tag{3.7}$$

where I_1, I_2 and I_3 are the three invariants of the stress tensor:

$$I_1 = \sigma_{\alpha\alpha} \tag{3.8}$$

$$I_2 = \frac{1}{2}\left(I_1^2 - \sigma_{\alpha\beta}\sigma_{\beta\alpha}\right), \tag{3.9}$$

$$I_3 = \frac{1}{6}\left(2\sigma_{\alpha\beta}\sigma_{\beta\gamma}\sigma_{\gamma\alpha} - 3I_1\sigma_{\alpha\beta}\sigma_{\beta\alpha} + I_1^3\right). \tag{3.10}$$

Here, α, β, γ are summation indices denoting the x, y and z components. The solutions of (3.7) are the three principal stresses $\sigma_1, \sigma_2, \sigma_3$.

Similarly, the procedure described above can be also applied to the deviatoric stress tensor $s_{\alpha\beta}$, resulting in a different characteristic equation:

$$s^3 - J_1 s^2 - J_2 s - J_3 = 0, \tag{3.11}$$

where s denotes the principal stress for the transformed deviatoric stress tensor (s_1, s_2, s_3), and J_1, J_2 and J_3 are the three invariants of the deviatoric stress tensor, defined as

$$J_1 = s_{\alpha\alpha} = 0, \tag{3.12}$$

$$J_2 = \frac{1}{2}s_{\alpha\beta}s_{\alpha\beta}, \tag{3.13}$$

$$J_3 = \frac{1}{3}s_{\alpha\beta}s_{\beta\gamma}s_{\gamma\alpha}. \tag{3.14}$$

3.1.2 Plane strain condition

In the current work, attention is restricted to two-dimensional problems in the $x-y$ plane, where x is the horizontal axis and y is the vertical axis. The three-dimensional stress tensor can be approximated in two dimensions via the assumption of *plane stress* or *plane strain*. A material is in plane stress if all stress components along the normal axis (the z-axis) are zero. Zero normal stress means that there is no restriction on the material deformation in the z direction, and deformations can occur in the longitudinal (z) direction. Consequently, the ϵ_{zz} component of the strain tensor is non-zero. Conversely, a material is in plane strain if longitudinal deformations are prevented, and all deformations occur in the two-dimensional $(x-y)$ cross section. The normal component of the stress tensor in the longitudinal direction (σ_{zz}) is therefore non-zero. For the application to geotechnical problems, the plane strain condition is often a reasonable assumption and considerably simplifies the full three-dimensional analysis (Powrie, 2004; Bui et al., 2008). Therefore the plane strain

condition is assumed in the current work, where the stress and strain tensors reduce to

$$\sigma_{\alpha\beta} = \begin{pmatrix} \sigma_{xx} & \sigma_{xy} & 0 \\ \sigma_{xy} & \sigma_{yy} & 0 \\ 0 & 0 & \sigma_{zz} \end{pmatrix}, \quad \epsilon_{\alpha\beta} = \begin{pmatrix} \epsilon_{xx} & \epsilon_{xy} & 0 \\ \epsilon_{xy} & \epsilon_{yy} & 0 \\ 0 & 0 & 0 \end{pmatrix}. \tag{3.15}$$

3.2 Equations of motion

The equations of motion for a soil consist of the conservation of mass and momentum:

$$\frac{\partial \rho}{\partial t} = -\frac{1}{\rho}\frac{\partial u_\alpha}{\partial x_\alpha}, \tag{3.16}$$

$$\frac{\partial u_\alpha}{\partial t} = \frac{1}{\rho}\frac{\partial \sigma_{\alpha\beta}}{\partial x_\beta} + b_\alpha, \tag{3.17}$$

where ρ is the soil density, u_α is velocity, $\sigma_{\alpha\beta}$ is the total stress tensor and b_α denotes the external body forces. For the applications of relevance in this research, the external body force consists of gravity only.

3.3 Constitutive model

A constitutive equation is required to relate the soil stresses to the strain rates. As described in Chapter 2.2, the total stress in a soil is split up into an effective stress carried by the soil skeleton and a pore water pressure term (Terzaghi, 1936). Here, attention is restricted to a dry soil, and the total soil stress is therefore equal to the effective stress.

The total strain rate is defined in terms of the velocity gradients via the kinematic condition:

$$\dot{\epsilon}_{\alpha\beta} = \frac{1}{2}\left(\frac{\partial u_\alpha}{\partial x_\beta} + \frac{\partial u_\beta}{\partial x_\alpha}\right), \tag{3.18}$$

where the dot notation represents the derivative with respect to time. Recall that the total strain rate can be split up into an elastic $\dot{\epsilon}^e_{\alpha\beta}$ and a plastic component $\dot{\epsilon}^p_{\alpha\beta}$:

$$\dot{\epsilon}_{\alpha\beta} = \dot{\epsilon}^e_{\alpha\beta} + \dot{\epsilon}^p_{\alpha\beta}. \tag{3.19}$$

Equation (3.19) describes the underlying assumption of plasticity-based models. From here, descriptions are required for the behaviour of the elastic and plastic strain rates, as well as a yield function to distinguish between the two types of behaviour. In soil mechanics, the elastic strain rate is often related to the rate of stress via the *generalised Hooke's law* (Chen and Mizuno, 1990). For a full three-dimensional problem this is written as:

$$\dot{\sigma}_{\alpha\beta} = D^e_{\alpha\beta mn}\dot{\epsilon}^e_{mn}, \tag{3.20}$$

where $\alpha, \beta, m, n = x, y, z$, and $D^e_{\alpha\beta}$ is a fourth-order tensor consisting of 81 material constants. This tensor, the *elastic constitutive tensor*, is a function of Young's modulus E – a measure of material stiffness, and Poisson's ratio ν – the ratio of relative contraction strain to axial strain in the direction of the applied load. Equation (3.20) can be written in vector notation as

$$\dot{\boldsymbol{\sigma}} = \mathbf{D^e} : \dot{\boldsymbol{\epsilon}}^{\mathbf{e}}, \tag{3.21}$$

where the double dots denote a double tensorial contraction (Heeres, Suiker, and Borst, 2002). Equation (3.20) is the simplest expression of the stress-strain relationship in an elastic material, and states that the stress rate increases linearly with strain rate, as a function of the material properties (Chen and Mizuno, 1990). Equation (3.20) may also be rewritten for $\dot{\epsilon}^e_{\alpha\beta}$, which for an isotropic material is expressed as:

$$\dot{\epsilon}^e_{\alpha\beta} = \frac{\dot{s}_{\alpha\beta}}{2G} + \frac{1-2v}{3E}\dot{\sigma}_{\gamma\gamma}\delta_{\alpha\beta}, \tag{3.22}$$

where $G = \frac{E}{2(1+v)}$ is the shear modulus – describing a material response to shear, and $\dot{\sigma}_{\gamma\gamma} = \dot{\sigma}_{xx} + \dot{\sigma}_{yy} + \dot{\sigma}_{zz}$.

In plasticity-based models, the plastic strain rate is defined via the plastic flow rule:

$$\dot{\epsilon}^p_{\alpha\beta} = \dot{\lambda}\frac{\partial g}{\partial \sigma_{\alpha\beta}}, \tag{3.23}$$

where $\dot{\lambda}$ is the so-called *consistency parameter* and g is the *plastic potential function*. The consistency parameter defines the magnitude of plastic strain via the plastic multiplier λ, while the plastic potential function describes the direction of plastic flow as a function of the stress tensor. For a plastic potential function that is equal to the yield function, the flow rule is said to be associated. Otherwise, it is non-associated. Beyond this general framework, the elastoplastic and viscoplastic Perzyna models are derived under different approaches.

3.3.1 Yield criteria

Elastic and plastic material behaviour are distinguished according to a specified yield function f. Of relevance to the current work are the Von Mises and Drucker-Prager yield criteria. The Von Mises yield criterion is a function of the second invariant of the deviatoric tensor J_2:

$$f = \sqrt{3J_2} - f_c, \tag{3.24}$$

where f_c is a constant stress value. The criterion has the benefit of being simple, but is only relevant when modelling soils of a clay-type. It does not take the hydrostatic pressure of the material into account, which has been shown to play a role in the strength of granular materials (Chen, 2013). The Drucker-Prager criterion does include hydrostatic stress dependence, is an adapted version of the Mohr-Coulomb criterion. The Drucker-Prager criterion is defined in terms of the second deviatoric

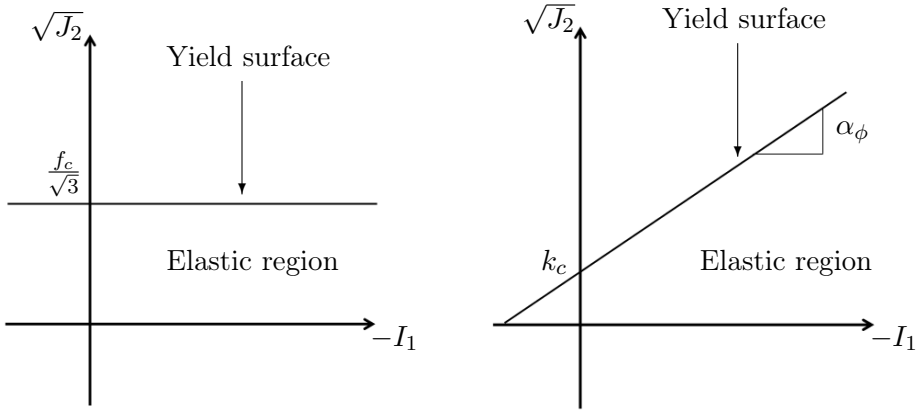

(A) The Von Mises yield criterion (B) The Drucker-Prager yield criterion.

FIGURE 3.2: Yield criteria in the $(-I_1, \sqrt{J_2})$ plane

stress invariant and the first invariant of the stress tensor I_1:

$$f = \sqrt{J_2} + \alpha_\phi I_1 - k_c = 0, \tag{3.25}$$

where α_ϕ and k_c are the model parameters. These are functions of the Coulomb material constants – the soil internal friction ϕ and cohesion c_{oh}:

$$\alpha_\phi = \frac{\tan\phi}{\sqrt{9 + 12\tan^2\phi}} \quad \text{and} \quad k_c = \frac{3c_{oh}}{\sqrt{9 + 12\tan^2\phi}}. \tag{3.26}$$

The Von Mises and Drucker-Prager yield criteria are illustrated in two dimensions in Figures 3.2a and 3.2b respectively. In each case, when the stress state does not lie within the elastic region, the material exhibits plastic strains.

Strain hardening and softening

Once plastic strains have occurred, if the size of the yield surface does not change the material is said to be *perfectly plastic*. Alternatively the size of the yield surface may vary according to a suitable hardening or softening law. Soils often exhibit strain softening behaviour, where the shear strength reduces with increasing plastic strain (Sluys, 1992). Strain softening can be described according to the following equation:

$$\frac{\partial Y_0}{\partial t} = H\frac{\partial \bar{\epsilon}^p}{\partial t}, \tag{3.27}$$

where Y_0 is the initial yield surface (Pa), H is a hardening modulus (Pa) and $\bar{\epsilon}^p$ is the deviatoric plastic strain (dimensionless). The deviatoric plastic strain represents the magnitude of plastic strain:

$$\bar{\epsilon}^p = \frac{1}{\sqrt{3}}\sqrt{2\left(\epsilon^p_{xx} + \epsilon^p_{yy} + \epsilon^p_{zz}\right) + \epsilon^p_{xy}}. \tag{3.28}$$

The size of the yield surface can also be defined to simply decrease or increase linearly with time, to approximate softening or hardening behaviour respectively.

3.3.2 Elastoplastic model

The elastoplastic constitutive model is derived under the theory of classic plasticity. To obtain a relationship between stress and strain, the equations defining the elastic and plastic strain rates (Equations (3.22) and (3.23)) are substituted into the equation for the total strain rate (Equation (3.19)). Furthermore, the stress tensor decomposition (3.3) is substituted into Equation (3.22) to rewrite the deviatoric stress in terms of the total stress. After rearranging, the result is an equation relating the stress rate to the strain rate:

$$\frac{\partial \sigma_{\alpha\beta}}{\partial t} = 2G\dot{e}_{\alpha\beta} + K\dot{\epsilon}_{\gamma\gamma}\delta_{\alpha\beta} - \dot{\lambda}\left(\left(K - \frac{2G}{3}\right)\frac{\partial g}{\partial \sigma_{mn}}\delta_{mn}\delta_{\alpha\beta} + 2G\frac{\partial g}{\partial \sigma_{\alpha\beta}}\right), \tag{3.29}$$

where m and n are dummy indices, $\dot{e}^{\alpha\beta} = \dot{\epsilon}_{\alpha\beta} - \frac{1}{3}\dot{\epsilon}^{\gamma\gamma}\delta_{\alpha\beta}$ is the deviatoric strain rate tensor and $K = \frac{E}{3(1-2v)}$ is the elastic bulk modulus. The first two terms on the right hand side of Equation (3.29) describe the elastic strain, while the latter term describes the plastic deformations (which is non-zero when plastic flow occurs).

In the elastoplastic model, the plastic multiplier λ must satisfy the following criteria:

$$\lambda = \begin{cases} 0, & \text{if } f < 0. \\ 0, & \text{if } f = 0 \text{ and } \mathrm{d}f < 0 \\ \lambda > 0, & \text{if } f = 0 \text{ and } \mathrm{d}f = 0, \end{cases} \tag{3.30}$$

where f is the yield function, and $\mathrm{d}f$ is the increment of the yield function after plastic loading or unloading. The stress state is not allowed to exceed the yield surface, and the yield function increment cannot be greater than zero. With the criteria defined by Equation (3.30), a zero plastic multiplier (and therefore a zero plastic strain rate) corresponds to elastic behaviour or plastic unloading. Plastic loading is characterised by a non-zero value of the plastic multiplier λ, which can be obtained via the consistency condition:

$$\mathrm{d}f = \frac{\partial f}{\partial \sigma_{\alpha\beta}}\mathrm{d}\sigma_{\alpha\beta} = 0. \tag{3.31}$$

Equation (3.31) ensures that the stress state remains on the yield surface during plastic loading, as

$$f(\sigma_{\alpha\beta} + \mathrm{d}\sigma_{\alpha\beta}) = f(\sigma_{\alpha\beta}) + \mathrm{d}f = f(\sigma_{\alpha\beta}). \tag{3.32}$$

To obtain the value of the plastic multiplier, Equation (3.29) is substituted into the consistency condition (3.31), and rearranged:

$$\dot{\lambda} = \frac{2G\dot{\epsilon}_{\alpha\beta}\frac{\partial f}{\partial \sigma_{\alpha\beta}} + \left(K - \frac{2G}{3}\right)\dot{\epsilon}_{\gamma\gamma}\frac{\partial f}{\partial \sigma_{\alpha\beta}}\delta_{\alpha\beta}}{2G\frac{\partial f}{\partial \sigma_{mn}}\frac{\partial g}{\partial \sigma_{mn}} + \left(K - \frac{2G}{3}\right)\frac{\partial f}{\partial \sigma_{mn}}\delta_{mn}\frac{\partial g}{\partial \sigma_{mn}}\delta_{mn}}. \tag{3.33}$$

Equation (3.33) can be solved upon substitution of the yield function f and potential function g, to close the model.

In the current work, the elastoplastic constitutive model is used in combination with a Drucker-Prager yield criterion, with a non-associated flow rule. Following Bui et al. (2008), the plastic potential function is defined as

$$g = \sqrt{J_2} + 3I_1 \sin\psi, \tag{3.34}$$

where ψ is the dilatancy angle, which is assumed to be zero in the current work (this assumption was also adopted by Bui et al. (2008)). Upon substitution of Equation (3.34) and the Drucker-Prager yield function (3.25) into Equations (3.29) and (3.33), the elastoplastic constitutive equation is

$$\frac{\partial \sigma_{\alpha\beta}}{\partial t} = 2G\dot{e}^{\alpha\beta} + K\dot{\epsilon}_{\gamma\gamma}\delta_{\alpha\beta} - \dot{\lambda}\left(9K\sin\psi\delta_{\alpha\beta} + \frac{G}{\sqrt{J_2}s_{\alpha\beta}}\right), \tag{3.35}$$

where

$$\dot{\lambda} = \frac{3\alpha_\phi\dot{\epsilon}^{\gamma\gamma} + (G/\sqrt{J_2})s^{\alpha\beta}\dot{\epsilon}^{\alpha\beta}}{27\alpha_\phi K\sin\psi + G}. \tag{3.36}$$

For further details on the derivation of Equations (3.35) and (3.36) the reader is referred to Chen and Mizuno (1990) and Bui et al. (2008).

3.3.3 Perzyna model

In the derivation of the Perzyna model, the stress decomposition defined by Equation (3.19) is rearranged in terms of the elastic strain:

$$\dot{\epsilon}^e_{\alpha\beta} = \dot{\epsilon}_{\alpha\beta} - \dot{\epsilon}^p_{\alpha\beta}, \tag{3.37}$$

and substituted into Equation (3.20):

$$\frac{\partial \sigma_{\alpha\beta}}{\partial t} = D^e_{\alpha\beta mn}\left(\dot{\epsilon}_{mn} - \dot{\epsilon}^p_{mn}\right). \tag{3.38}$$

To determine the plastic strain rate, the consistency parameter $\dot{\lambda}$ is defined as

$$\dot{\lambda} = \gamma\langle\phi(F)\rangle, \tag{3.39}$$

where γ is a fluidity parameter (acts as the reciprocal of viscosity) and $\phi(F)$ is a yield-type function. The $\langle ... \rangle$ symbol represents the Macaulay brackets:

$$\langle \phi \rangle = \begin{cases} \phi, & \phi \geq 0 \\ 0, & \phi < 0 \end{cases}.$$

The function $\phi(F)$ is therefore defined as

$$\phi(F) = \left(\frac{F - F_0}{F_0} \right)^N, \tag{3.40}$$

where N is a model parameter, F is a function of the stress state (related to the yield function), and F_0 defines a critical stress value for plastic strains. Plastic strains are non-zero when the function F exceeds the critical value F_0, such that

$$\langle \phi(F) \rangle = \begin{cases} 0, & \text{if } F \leq F_0 \\ \phi(F) > 0, & \text{if } F > F_0. \end{cases} \tag{3.41}$$

Plastic behaviour is determined according to a yield function f, in the same way as described in Section 3.3.2. However, for the viscoplastic Perzyna model, f is reformulated so that it can be written in terms of F and F_0, where F can be larger than zero. This feature is the main difference between the Perzyna model and the elastoplastic model – for the latter, the yield function is never greater than zero (see Equation (3.30)) and the stress state cannot exceed the yield surface. Conversely, the definition of $\phi(F)$ in Equation (3.41) allows the stress state to exceed the yield surface, producing an effect called 'overstress' (Heeres, Suiker, and Borst, 2002). Note that the Perzyna model includes additional parameters, γ and N, that introduce viscous effects to the constitutive equation. This is why the Perzyna model is referred to as *viscoplastic*, and the plastic strains are also often referred to as viscoplastic. In the current work, the term plastic is generally used to describe the inelastic, irreversible strains in both the elastoplastic and Perzyna models. In summary, the Perzyna constitutive model is defined as

$$\frac{\partial \sigma_{\alpha\beta}}{\partial t} = D^e_{\alpha\beta mn} \left(\dot{\epsilon}_{mn} - \gamma \frac{\partial g}{\partial \sigma_{mn}} \left(\frac{F - F_0}{F_0} \right)^N \right), \tag{3.42}$$

which is closed upon substitution of F, F_0 and g. For simplicity, Equation (3.42) is typically written in vector form as

$$\frac{\partial \boldsymbol{\sigma}}{\partial t} = \mathbf{D}^e : \left(\dot{\boldsymbol{\epsilon}} - \gamma \frac{\partial g}{\partial \boldsymbol{\sigma}} \left(\frac{F - F_0}{F_0} \right)^N \right), \tag{3.43}$$

Relevant to the current work is the implementation of the Von Mises yield criterion (defined by Equation (3.24)), with an associated flow rule ($f = g$). In terms of

F and F_0, the Von Mises yield criterion is defined as

$$F = \sqrt{3J_2} \quad \text{and} \quad F_0 = f_c. \tag{3.44}$$

Plastic flow therefore occurs when $\sqrt{3J_2} > f_c$, where f_c is a critical stress value that may vary according to a hardening or softening law. Upon substitution of Equation (3.44) and $g = \sqrt{3J_2} - f_c$ into Equation (3.42), the Perzyna constitutive model is

$$\frac{\partial \boldsymbol{\sigma}}{\partial t} = \mathbf{D}^e : \left(\dot{\boldsymbol{\epsilon}} - \gamma \frac{\partial \sqrt{3J_2}}{\partial \boldsymbol{\sigma}} \left(\frac{\sqrt{3J_2} - f_c}{f_c} \right)^N \right). \tag{3.45}$$

3.3.4 A generalised system of equations

The general elastoplastic and viscoplastic Perzyna constitutive equations are defined respectively as:

$$\frac{\partial \sigma_{\alpha\beta}}{\partial t} = 2G\dot{e}_{\alpha\beta} + K\dot{\epsilon}_{\gamma\gamma}\delta_{\alpha\beta} - \dot{\lambda}\left(\left(K - \frac{2G}{3} \right) \frac{\partial g}{\partial \sigma_{mn}} \delta_{mn}\delta_{\alpha\beta} + 2G \frac{\partial g}{\partial \sigma_{\alpha\beta}} \right), \tag{3.46}$$

$$\frac{\partial \sigma_{\alpha\beta}}{\partial t} = D^e_{\alpha\beta mn}\dot{\epsilon}_{mn} - D^e_{\alpha\beta mn}\gamma \frac{\partial g}{\partial \sigma_{mn}} \left(\frac{F - F_0}{F_0} \right)^N, \tag{3.47}$$

The first two terms on the right hand side of Equation (3.46) are equivalent to the first term on the right hand side of Equation (3.47):

$$2G\dot{e}_{\alpha\beta} + K\dot{\epsilon}_{\gamma\gamma}\delta_{\alpha\beta} = D^e_{\alpha\beta mn}\dot{\epsilon}_{mn}. \tag{3.48}$$

Furthermore, the final terms on the right hand side of Equations (3.46) and (3.47) are both functions of the plastic strain rate $\dot{\epsilon}^p_{\alpha\beta}$. Therefore, Equations (3.46) and (3.47) can be written in the following compact form:

$$\frac{\partial \sigma_{\alpha\beta}}{\partial t} = D^e_{\alpha\beta mn}\dot{\epsilon}_{mn} - g^{\epsilon^p}_{\alpha\beta}, \tag{3.49}$$

where $g^{\epsilon^p}_{\alpha\beta}$ is a function of the plastic strain. Depending on the choice of constitutive model,

$$g^{\epsilon^p}_{\alpha\beta} = \dot{\lambda}\left(\left(K - \frac{2G}{3} \right) \frac{\partial g}{\partial \sigma_{mn}} \delta_{mn}\delta_{\alpha\beta} + 2G \frac{\partial g}{\partial \sigma_{\alpha\beta}} \right) \text{ or } g^{\epsilon^p}_{\alpha\beta} = D^e_{\alpha\beta mn}\gamma \frac{\partial g}{\partial \sigma_{mn}} \left(\frac{F - F_0}{F_0} \right)^N. \tag{3.50}$$

For large deformation problems, the rate of stress must be adapted so that it is invariant with respect to large body rotations. The standard stress rate is replaced with the Jaumann stress rate $\dot{\tilde{\sigma}}_{\alpha\beta}$:

$$\dot{\tilde{\sigma}}_{\alpha\beta} = \dot{\sigma}_{\alpha\beta} - \sigma_{\alpha\gamma}\dot{\omega}_{\beta\gamma} - \sigma_{\gamma\beta}\dot{\omega}_{\alpha\gamma}, \tag{3.51}$$

where $\dot{\omega}$ is the spin rate tensor:

$$\dot{\omega}_{\alpha\beta} = \frac{1}{2}\left(\frac{\partial u_\alpha}{\partial x_\beta} - \frac{\partial u_\beta}{\partial x_\alpha}\right). \tag{3.52}$$

With this adaptation, Equation (3.49) becomes

$$\frac{\partial \sigma_{\alpha\beta}}{\partial t} = \sigma_{\alpha\gamma}\dot{\omega}_{\beta\gamma} - \sigma_{\gamma\beta}\dot{\omega}_{\alpha\gamma} + D^e_{\alpha\beta mn}\dot{\epsilon}_{mn} - g^{\epsilon^p}_{\alpha\beta}. \tag{3.53}$$

The governing equations describing soil behaviour under the theory of plasticity can therefore be summarised as

$$\text{Conservation of mass :} \quad \frac{\partial \rho}{\partial t} = -\frac{1}{\rho}\frac{\partial u_\alpha}{\partial x_\alpha}, \tag{3.54}$$

$$\text{Conservation of momentum :} \quad \frac{\partial u_\alpha}{\partial t} = \frac{1}{\rho}\frac{\partial \sigma_{\alpha\beta}}{\partial x_\beta} + b_\alpha, \tag{3.55}$$

$$\text{Constitutive equation :} \quad \frac{\partial \sigma_{\alpha\beta}}{\partial t} = \sigma_{\alpha\gamma}\dot{\omega}_{\beta\gamma} - \sigma_{\gamma\beta}\dot{\omega}_{\alpha\gamma} + D^e_{\alpha\beta mn}\dot{\epsilon}_{mn} - g^{\epsilon^p}_{\alpha\beta}. \tag{3.56}$$

3.4 Summary of the governing equations

For the numerical discretisation of Equations (3.54) - (3.56) described in the following chapter, it is convenient to write the governing system of equations in vector notation. In the plane strain condition, the elastic constitutive tensor can be written as a 4×4 matrix, defined as:

$$D^e_{pq} = \frac{E}{(1+v)(1-v)}\begin{pmatrix} 1-v & v & 0 & v \\ v & 1-v & 0 & v \\ 0 & 0 & (1-2v)/2 & 0 \\ v & v & 0 & 1-v \end{pmatrix}, \tag{3.57}$$

where $p, q = 1, 2, 3, 4$ denote the rows and columns of the matrix respectively. Furthermore, the stress and plastic strain rate tensors are reformulated as row vectors $\boldsymbol{\sigma}$ and $\dot{\boldsymbol{\epsilon}}^p$, containing the non-zero elements of the full tensors:

$$\boldsymbol{\sigma} = \begin{pmatrix} \sigma_{xx} \\ \sigma_{yy} \\ \sigma_{xy} \\ \sigma_{zz} \end{pmatrix}, \quad \dot{\boldsymbol{\epsilon}}^p = \begin{pmatrix} \dot{\epsilon}^p_{xx} \\ \dot{\epsilon}^p_{yy} \\ \dot{\epsilon}^p_{xy} \\ 0 \end{pmatrix}. \tag{3.58}$$

Therefore, in two dimensions with the plane strain condition, the system is governed by

$$\text{Conservation of mass :} \quad \frac{\partial \rho}{\partial t} = -\rho \nabla \cdot \boldsymbol{u}, \tag{3.59}$$

$$\text{Conservation of momentum :} \quad \frac{\partial \boldsymbol{u}}{\partial t} = \frac{1}{\rho} \nabla \cdot \mathbf{f}^{\sigma} + \boldsymbol{b}, \tag{3.60}$$

$$\text{Constitutive equation :} \quad \frac{\partial \boldsymbol{\sigma}}{\partial t} = \tilde{\boldsymbol{\sigma}} + \nabla \cdot \mathbf{f}^{u} - \mathbf{g}^{\epsilon^p}. \tag{3.61}$$

In Equations (3.59) - (3.61), the tensors $\mathbf{f}^u$ and $\mathbf{f}^\sigma$ have been introduced:

$$\mathbf{f}^u = \begin{pmatrix} D^e_{11} u_x & D^e_{12} u_y \\ D^e_{12} u_x & D^e_{22} u_y \\ D^e_{33} u_y & D^e_{33} u_x \\ D^e_{41} u_x & D^e_{42} u_y \end{pmatrix}, \quad \mathbf{f}^\sigma = \begin{pmatrix} \sigma_{xx} & \sigma_{xy} \\ \sigma_{xy} & \sigma_{yy} \end{pmatrix}, \tag{3.62}$$

which are functions of velocity and stress respectively. For completeness, the remaining vectors are defined as

$$\mathbf{x} = \begin{pmatrix} x \\ y \end{pmatrix}, \quad \boldsymbol{u} = \begin{pmatrix} u_x \\ u_y \end{pmatrix}, \quad \tilde{\boldsymbol{\sigma}} = \begin{pmatrix} 2\sigma_{xy}\omega_{xy} \\ 2\sigma_{xy}\omega_{yx} \\ \sigma_{xx}\omega_{yx} + \sigma_{yy}\omega_{xy} \\ 0 \end{pmatrix}, \quad \mathbf{g}^{\epsilon^p} = \begin{pmatrix} g^{\epsilon^p}_{xx}(\dot{\boldsymbol{\epsilon}}^p) \\ g^{\epsilon^p}_{yy}(\dot{\boldsymbol{\epsilon}}^p) \\ g^{\epsilon^p}_{xy}(\dot{\boldsymbol{\epsilon}}^p) \\ g^{\epsilon^p}_{zz}(\dot{\boldsymbol{\epsilon}}^p) \end{pmatrix}, \quad \boldsymbol{b} = \begin{pmatrix} b_x \\ b_y \end{pmatrix}. \tag{3.63}$$

Chapter 4

Stress-Particle SPH

4.1 Introduction

For the current purpose of modelling the failure and the post-failure behaviour of soil (with an application to landslides), the numerical method must be suitable for both small and large deformation problems. As discussed in Chapter 2.4, the meshless nature of SPH means that it can easily handle both large deformations and free surface flows, and it has been used with success to model a wide range of problems of this type (Shao and Lo, 2003; Fang et al., 2006; Bui et al., 2008; Peng et al., 2015; Minatti and Paris, 2015). However, there exist numerical instabilities that either arise due to the absence of a mesh, or are more complicated to eliminate than in mesh-based methods. The most significant of these instabilities with regards to predicting soil behaviour are: the problem of zero-energy modes, and the tensile instability. A detailed explanation of these instabilities along with available remedies to combat them within SPH was provided in Chapter 2.5. Of the available stabilising techniques, the addition of stress-points within SPH has a large number of benefits. First, the use of stress-points allows for the calculation and storage of stress and velocity at separate locations (Dyka, Randles, and Ingel, 1995). This can prevent the occurrence of the zero-energy modes, as their cause is directly linked to the fact that in Standard SPH the stress and velocity are calculated at the same location (Swegle et al., 1994). Furthermore, a stability analysis conducted by Belytschko et al. (2000) has shown that the threshold at which the tensile instability occurs can be significantly increased with the addition of stress-points. Moreover, the inclusion of stress-points within SPH acts to stabilise the scheme in a 'natural' way, avoiding the need for the tuning of non-physical parameters (Randles and Libersky, 2000). The role of stress-points within SPH is currently relatively unexplored and only simple configurations have been applied to a limited range of problems. Consequently, this research aims to develop an SPH model with stress-points, named *Stress-Particle SPH*, for application to the failure and post-failure behaviour of soil.

Motivated by the results of the stability analysis performed by Swegle et al. (1994) (described in Chapter 2.5.1), Dyka, Randles, and Ingel (1995) introduced stress-points to SPH to eliminate the tensile instability observed in an elastic bar subjected to tensile stress. In their one-dimensional set-up, two stress-points (x) were

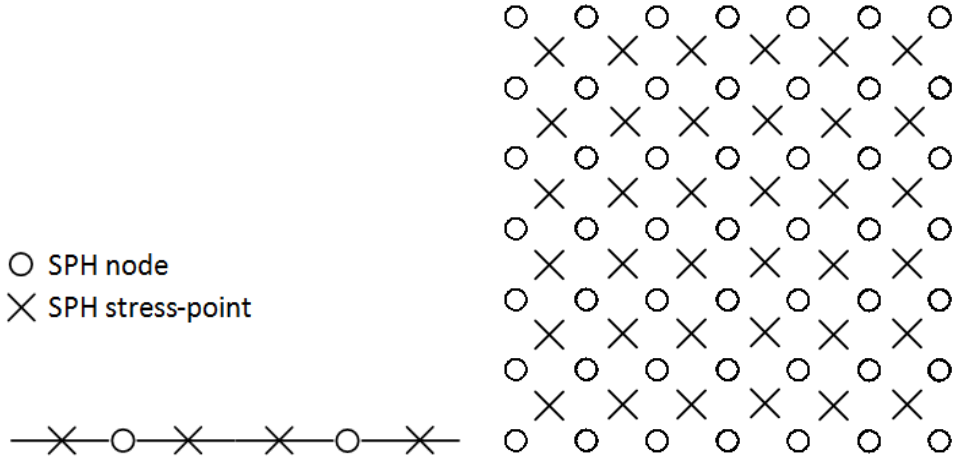

(A) One-dimensional set-up (B) Two-dimensional set-up

FIGURE 4.1: Stress-Particle SPH configurations in one and two dimensions.

positioned on either side of each node (o), as depicted in Figure 4.1a. The velocities were calculated at the SPH nodes, using the information from the surrounding stress-points to calculate the stress gradients at the nodes. Similarly, the stresses were calculated on the stress-points, utilising the nodes to calculate the velocity gradients. In standard SPH, the gradient of the smoothing kernel is equal to zero at the location of the node in question, and the stress at that node is not taken into account in the gradient calculation. Within the Stress-Particle method, splitting the stress and velocity over two sets of particles essentially includes the stress value of a particle itself within the calculation. This improves the accuracy of the gradient approximation, which can eliminate or reduce the effects of both the tensile instability and the zero-energy modes. Consequently, the application of Stress-Particle SPH in one dimension enabled the accurate prediction of the shock wave in the bar. The method was successfully applied to further problems in one dimension, including a bar in an initial state of alternating velocities (Dyka, Randles, and Ingel, 1997). This initial condition produces an alternating stress field within the bar, which was not possible to predict with standard SPH due to the zero-energy mode problem (Swegle et al., 1994). The Stress-Particle method was later extended to two dimensions by Randles and Libersky (2000) and Vignjevic, Campbell, and Libersky (2000), for the configuration shown in Figure 4.1b. It was applied to a number of benchmark cases with a low particle resolution, including the Taylor impact test of a metal cylinder impacting a rigid boundary (Taylor, 1948), and the impact of two rubber rings (Swegle et al., 1994).

With the aim of quantifying the instabilities observed in meshless particle methods, Belytschko et al. (2000) conducted a linear stability analysis and explored the stabilising effects of stress-points. An isothermal, adiabatic material was considered in one and two dimensions with a rate-independent constitutive law. The stresses and strains were linearly related via the material tangent modulus – this defines the

slope of the stress-strain curve and is equivalent to Young's modulus for elastic flow. A linear stability analysis was first conducted for the continuum equations, where an unstable solution was identified when the value of the tangent modulus was less than zero. The analysis was then performed for the discretised governing equations, for both SPH and an Element Free Galerkin method (EFGM) (Belytschko, Lu, and Gu, 1994), identifying the instabilities that are solely a result of the numerical discretisation. Numerical instabilities were found both in the absence of stress and when the material was in tension, corresponding to the zero-energy modes and the tensile instability respectively. These instabilities were explicitly related to the form of the smoothing kernel. The stress-points were first included in the stability analysis of SPH in one dimension, where they were placed centrally between each node as depicted in Figure 4.2a. With the inclusion of the stress-points the zero-energy modes were eliminated completely, while the threshold at which the tensile instability occurred was increased. In two dimensions, multiple patterns were explored where a number of stress-points were placed inside 'virtual quadrilaterals' or 'virtual triangles' as shown in Figure 4.2b. The addition of these extra interpolation points was shown to reduce the number of instabilities due to the zero-energy modes for all configurations, and with the hexagonal set-up they were completely eliminated. Belytschko et al. (2000) also investigated the effects of a Lagrangian kernel, and found that the combination of the Lagrangian kernel with stress-points was able to completely stabilise the linearised numerical system. The linear stability analysis was repeated for a hyperelastic material by Xiao and Belytschko (2005), where the role of stress-points and Lagrangian kernels were again evaluated. The conclusions from this analysis were the same as for the material considered by Belytschko et al. (2000): stress-points can eliminate the zero-energy modes and the combination of a Lagrangian kernel with stress-points removes the instability under tension. It is important to highlight that these stability analyses were performed for specific materials, and different results may arise for other materials.

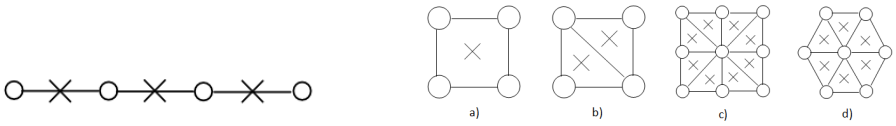

(A) One-dimensional set-up (B) Two-dimensional set-up

FIGURE 4.2: The node-stress-point arrangements considered in the stability analysis performed by Belytschko et al. (2000).

Following the work of Belytschko et al. (2000), stress-points have been included within meshless methods based on FEM (e.g. EFGM) to eliminate the zero-energy modes in the simulation of solid materials. This has been applied to a range of small deformation problems such as the shear band propagation in metals (Rabczuk, Belytschko, and Xiao, 2004; Rabczuk, Areias, and Belytschko, 2007), crack formation in concrete (Rabczuk and Belytschko, 2004; Rabczuk and Belytschko, 2007) and fluid-structure interaction (Rabczuk et al., 2010). Stress-points have also been

utilised within a Moving Least Squares (MLS) particle method in three dimensions by Sanchez and Randles (2012) and Sanchez and Randles (2013) to simulate quasi-static solid problems. These consisted of the formation of fractures in concrete and the compression of a hyperelastic cylinder. In all of the aforementioned studies, stress-points were implemented in meshless methods that are more complex and computationally expensive than SPH. In EFGM for example, a background grid is required for nodal integration, and hence the method is not truly meshless. Although Belytschko et al. (2000) examined various node-stress-point patterns in their stability analysis, all applications involving stress-points in two dimensions have used only the simplest configuration shown in Figure 4.2b. This arrangement, with one stress-point in the centre of a virtual quadrilateral, was in fact found to be the least stabilising of the different configurations investigated in the linear stability analysis. Similarly, the three-dimensional models utilised one stress-point in the centre of every virtual cube (although no investigations have been conducted on the stabilising role of stress-points in three dimensions). The problems that have previously been modelled with the aid of stress-points did not involve large deformations, which allowed the use of Lagrangian kernels (in addition to stress-points) to completely eliminate the tensile instability.

While it is acknowledged that stress-points may not be able to completely eradicate the effects of the tensile instability, it is widely believed that they bring significant improvements to numerical models. The results of linear stability analyses conducted by Belytschko et al. (2000) and Xiao and Belytschko (2005) provided valuable insight on the stabilising properties of the stress-points and highlighted that their quantity and arrangement is linked to the performance of particle methods with stress-points. However these analyses represent a highly idealised case for specific materials, and do not reveal how the nonlinear discretised system of equations will evolve in a general physical problem. Although a handful of physical problems have been numerically simulated using stress-points, there have been no quantitative or qualitative investigations on how they affect the material behaviour for these problems. There are no comparisons of the numerical solution with and without the addition of stress-points. Furthermore, these simulations have been confined to small deformation solid problems. This research therefore aims to apply Stress-Particle SPH to the failure and post-failure behaviour of soil for the first time, which involves extending the method to be applicable for large deformations and flow-type problems. Moreover, the role of stress-points are here quantified and analysed in further detail than has been done before. Note that in the literature the Lagrangian kernel has typically been employed alongside the stress-points to ensure the elimination of the tensile instability. The Lagrangian kernel is only suited for small deformation problems and it is therefore not applicable to the current research. However, the problems of interest relating to soil behaviour are expected to be subjected to lower stress states than those considered in the literature, where the stress-points were not able to completely remove the tensile instability (Rabczuk,

Belytschko, and Xiao, 2004). Therefore it is expected that Stress-Particle SPH is better suited for remedying the tensile instability in these problems. If effects of the tensile instability are still found to be significant, alternative methods (Monaghan, 2000; Xu and Yu, 2018) will be considered in addition to the stress-points.

The remainder of this chapter is structured as follows: first, the conventional SPH method is outlined and applied to discretise the mathematical model presented in Chapter 3. A selection of relevant stabilising techniques, such as the artificial stress and the particle shifting methods, are detailed. Then, the Stress-Particle SPH method is introduced and described, followed by details on its incorporation into a fourth order Runge-Kutta time discretisation scheme. A description of the extension of Stress-Particle SPH for large displacement problems is included. Finally, information is provided on the computational implementation of Stress-Particle and Standard SPH within the current research.

4.2 Standard SPH

The formulation of the SPH method consists of two fundamental approximations – the integral approximation and the particle approximation. The former involves representing a function $f(\mathbf{x})$ as an integral, which is motivated by the following expression:

$$f(\mathbf{x}) = \int_{\Omega} f(\mathbf{x}')\delta(\mathbf{x}-\mathbf{x}')\mathrm{d}\mathbf{x}', \tag{4.1}$$

where Ω denotes the integral domain and $\delta(\mathbf{x}-\mathbf{x}')$ is the Dirac delta function defined as

$$\delta(\mathbf{x}-\mathbf{x}') = \begin{cases} 1 & \mathbf{x} = \mathbf{x}', \\ 0 & \mathbf{x} \neq \mathbf{x}'. \end{cases} \tag{4.2}$$

For a function that is defined and continuous in Ω the integral representation given by (4.1) is exact. In the derivation of SPH, the integral approximation is obtained by replacing the Dirac delta in Equation (4.1) with a smoothing function W:

$$\langle f(\mathbf{x})\rangle = \int_{\Omega} f(\mathbf{x}')W(\mathbf{x}-\mathbf{x}', h_s)\mathrm{d}\mathbf{x}'. \tag{4.3}$$

Here, $\langle f(\mathbf{x})\rangle$ is the integral approximation of $f(\mathbf{x})$ and h_s is the smoothing length, which defines the region of influence of W. The smoothing length is defined in terms of the initial particle spacing, Δx. The smoothing function, or kernel, must satisfy three conditions. The first is the normalisation condition:

$$\int_{\Omega} W(\mathbf{x}-\mathbf{x}', h_s)\mathrm{d}\mathbf{x}' = 1. \tag{4.4}$$

The second condition requires that the kernel has compact support:

$$W(\mathbf{x}-\mathbf{x}', h_s) = 0 \quad \text{when} \quad |\,\mathbf{x}-\mathbf{x}'\,| > \kappa h_s, \tag{4.5}$$

where κ is a scale factor that multiplies the smoothing length. Lastly, the kernel should satisfy the Dirac delta function condition when the smoothing length approaches zero:

$$\lim_{h\to 0} W(\mathbf{x}-\mathbf{x}', h_s) = \delta(\mathbf{x}-\mathbf{x}'). \tag{4.6}$$

With these conditions for the smoothing kernel, the integral approximation given by Equation 4.3 is of second order accuracy, so that

$$f(\mathbf{x}) = \int_\Omega f(\mathbf{x}')W(\mathbf{x}-\mathbf{x}', h_s)\mathrm{d}\mathbf{x}' + O(h_s^2). \tag{4.7}$$

In the second step of deriving the SPH equations, the particle approximation is utilised to discretise the integral equation over a set of particles. This involves writing the integral approximation in discrete form using a summation approach:

$$\langle f(\mathbf{x})\rangle \approx \sum_{j=1}^{N} f(\mathbf{x}_j)W(\mathbf{x}-\mathbf{x}_j, h_s)V_j, \tag{4.8}$$

where V_j is the discrete volume at each point and N is the total number of particles within the region defined by W and h_s. Here, the function $f(\mathbf{x})$ is approximated by summing over all discrete particles j within the domain of influence at the position $\mathbf{x}$. Equation (4.8) can be expressed for a specific particle i as

$$f(\mathbf{x}_i) = \sum_{j=1}^{N} \frac{m_j}{\rho_j} f(\mathbf{x}_j)W(\mathbf{x}_i-\mathbf{x}_j, h_s), \tag{4.9}$$

where the mass m and density ρ are related to the volume at a point j as $V_j = \frac{m_j}{\rho_j}$. Equation (4.9) describes the SPH evaluation of a function or variable at a particle i.

It follows from (4.3) that the derivative of a function is approximated as

$$\left\langle \frac{\partial f(\mathbf{x})}{\partial \mathbf{x}} \right\rangle = \int_\Omega \frac{\partial f(\mathbf{x}')}{\partial \mathbf{x}'} W(\mathbf{x}-\mathbf{x}', h_s)\mathrm{d}\mathbf{x}'. \tag{4.10}$$

Upon integration by parts and the use of the divergence theorem, Equation (4.10) becomes

$$\left\langle \frac{\partial f(\mathbf{x})}{\partial \mathbf{x}} \right\rangle \approx \int_S f(\mathbf{x}')W(\mathbf{x}-\mathbf{x}', h_s)\cdot\mathbf{n}\mathrm{d}S - \int_\Omega f(\mathbf{x}')\frac{\partial W(\mathbf{x}-\mathbf{x}', h_s)}{\partial \mathbf{x}'}\cdot\mathbf{n}\mathrm{d}\mathbf{x}', \tag{4.11}$$

where $\mathbf{n}$ is the unit normal vector to the surface S. As the smoothing kernel has compact support, the first term on the right hand side of Equation (4.11) is equal to zero. The summation approach can then be applied in the same way as for Equation (4.8), to obtain the discrete derivative approximation:

$$\left\langle \frac{\partial f(\mathbf{x})}{\partial \mathbf{x}} \right\rangle \approx -\sum_{j=1}^{N} f(\mathbf{x}_j)\frac{\partial W(\mathbf{x}-\mathbf{x}_j, h_s)}{\partial \mathbf{x}_j} V_j, \tag{4.12}$$

which for a single particle i is written as

$$\frac{\partial f(\mathbf{x}_i)}{\partial \mathbf{x}} = -\sum_{j=1}^{N} \frac{m_j}{\rho_j} f(\mathbf{x}_j) \frac{\partial W(\mathbf{x}_i - \mathbf{x}_j, h_s)}{\partial \mathbf{x}_j}. \tag{4.13}$$

The derivative of the kernel can instead be expressed in terms of $\mathbf{x}_i$, where it follows from the chain rule that $\frac{\partial W(\mathbf{x}_i - \mathbf{x}_j, h_s)}{\partial \mathbf{x}_i} = -\frac{\partial W(\mathbf{x}_i - \mathbf{x}_j, h_s)}{\partial \mathbf{x}_j}$. With this change, the SPH approximation of a function and its derivative are written in compact form as

$$f(\mathbf{x}_i) = \sum_{j=1}^{N} \frac{m_j}{\rho_j} f(\mathbf{x}_j) W_{ij}, \tag{4.14}$$

$$\nabla f(\mathbf{x}_i) = \sum_{j=1}^{N} \frac{m_j}{\rho_j} f(\mathbf{x}_j) \nabla_i W_{ij}. \tag{4.15}$$

Here $W_{ij} = W(\mathbf{x} - \mathbf{x}_j, h_s)$ is the kernel, and ∇W_{ij} is the derivative of the kernel:

$$\nabla W_{ij} = \frac{\partial W_{ij}}{\partial \mathbf{x}_i} = \left(\frac{\mathbf{x}_i - \mathbf{x}_j}{r} \right) \frac{\partial W_{ij}}{\partial r}, \tag{4.16}$$

where $r = |\mathbf{x}_i - \mathbf{x}_j|$ is the distance between two particles. Equation (4.14) approximates the value of a function at a particle i as the average of the function values at all surrounding particles within the support domain, weighted by the kernel. Similarly, the gradient approximation in Equation (4.15) is expressed as the average of the surrounding function values weighted by the gradient of the kernel. Equation (4.15) is the simplest form of the gradient approximation and has a relatively low accuracy. In particular, it does not ensure that the gradient of a constant function field is equal to zero. Higher accuracy expressions can be derived by considering the difference in function values between the particle i and its neighbouring particles j. This can be achieved by considering the gradient approximation of unity:

$$\nabla 1 = \sum_{j=1}^{N} \frac{m_j}{\rho_j} \nabla W_{ij} = 0. \tag{4.17}$$

Multiplying Equation (4.17) by $f(\mathbf{x}_i)$ and subtracting it from the right hand side of Equation (4.15) gives

$$\nabla f(\mathbf{x}_i) = \sum_{j=1}^{N} \frac{m_j}{\rho_j} \left(f(\mathbf{x}_j) - f(\mathbf{x}_i) \right) \nabla W_{ij}, \tag{4.18}$$

which ensures that the gradient of a constant field vanishes. Similar expressions can be derived by applying the integral and particle approximations to vector identities involving function gradients (Monaghan, 1992). From Equation (4.18), the particle

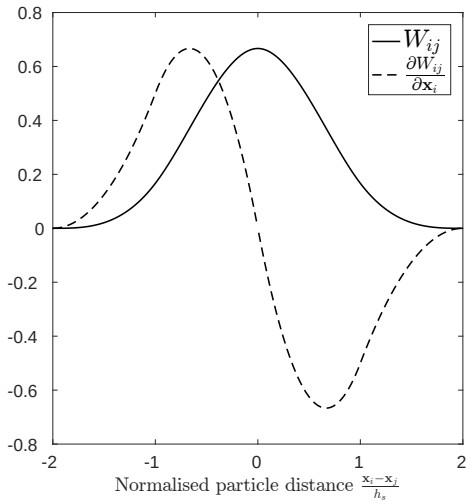

FIGURE 4.3: The cubic smoothing kernel and its first derivative.

approximation of the divergence of a vector $\mathbf{F}(\mathbf{x})$ is approximated as

$$\nabla \cdot \mathbf{F}(\mathbf{x}_i) = \sum_{j=1}^{N} \frac{m_j}{\rho_j} \left(\mathbf{F}(\mathbf{x}_j) - \mathbf{F}(\mathbf{x}_i)\right) \cdot \nabla W_{ij}, \tag{4.19}$$

In the SPH method, the particle approximations of functions and their derivatives are substituted into the governing equations of a system and discretised in time. This requires the definition of the kernel function, which directly impacts the integral approximation and the numerical simulation. A kernel with high accuracy is desirable, and in general this correlates positively with the order of the kernel. However, the computational time increases with the order of the kernel and therefore a compromise is sought between accuracy and computational cost. For this reason, the choice of kernel in this research is the cubic spline, defined in two dimensions as

$$W_{ij} = W(r, h_s) = \alpha_d \begin{cases} \frac{1}{2}q^3 - q^2 + \frac{2}{3} & 0 \leq q < 1 \\ \frac{1}{6}(2-q)^3 & 1 \leq q < 2 \\ 0 & q \geq 2 \end{cases} \tag{4.20}$$

where α_d is the normalisation factor which in two dimensions is $\frac{15}{7\pi h_s^2}$, and $q = r/h_s$ is the normalised distance between two particles. The cubic kernel and its first derivative are plotted together in Figure 4.3. The cubic spline is the most commonly used kernel in SPH (Monaghan, 1988; Shao and Gotoh, 2005; Bui et al., 2008), although higher order functions have also been implemented (Violeau and Issa, 2007; Xu, Stansby, and Laurence, 2009). Alternative forms of the smoothing function include Gaussian (Gingold and Monaghan, 1977), exponential (Monaghan, 1988) and quadratic (Johnson and Beissel, 1996).

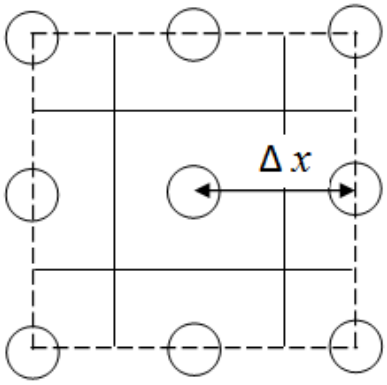

FIGURE 4.4: An illustration of the initial particle and mass distribution for SPH in two dimensions.

4.2.1 Particle and mass distribution

At the start of an SPH simulation, the particles are arranged in the initial shape of the material for the problem of interest. The particles can be distributed in a uniform arrangement, with the separation between adjacent nodes equal to Δx. The particles may also be distributed in a staggered arrangement.

The mass of each SPH particle is constant throughout the numerical simulation, and the sum of the mass of the individual particles is equal to the total mass of the system. The mass is calculated at each particle as

$$m_i = V_{0i}\rho_{0i}, \tag{4.21}$$

where V_{0i} and ρ_{0i} are the initial volumes and densities at particle i. Each SPH particle is assumed to occupy a finite section of the total volume of the material. For a two-dimensional, uniform particle distribution, the interior particles have a different initial volume to those that lie on the edges and the corners. The initial volume at an interior node can be calculated as

$$V_{0i} = \Delta x^2. \tag{4.22}$$

For a rectangular arrangement, the particles that are located on the edges and corners of the domain occupy one half and one quarter of the volume of an interior particle respectively. This is illustrated in the simple node configuration shown in Figure 4.4. The majority of problems considered at a later stage in this research have an initial rectangular arrangement, and the method described above is used to define the mass of the particles.

4.3 Discrete mathematical model

Under the framework described above, the SPH method can be applied to the mathematical model described in Chapter 3. Different discrete SPH equations arise depending on which operations are performed when applying the particle approximations to the analytical equations. Here, some common treatments for the discretisation of the equations of motion are discussed, and the discrete governing equations of soil behaviour are presented. The analytical equations are repeated for convenience:

$$\text{(Conservation of mass)} \quad \frac{\partial \rho}{\partial t} = -\rho \nabla \cdot \boldsymbol{u}, \tag{4.23}$$

$$\text{(Conservation of momentum)} \quad \frac{\partial \boldsymbol{u}}{\partial t} = \frac{1}{\rho} \nabla \cdot \mathbf{f}^{\sigma} + \boldsymbol{b}, \tag{4.24}$$

$$\text{(Constitutive equation)} \quad \frac{\partial \boldsymbol{\sigma}}{\partial t} = \tilde{\boldsymbol{\sigma}} + \nabla \cdot \mathbf{f}^{u} - \mathbf{g}^{\epsilon^p}, \tag{4.25}$$

where the tensors $\mathbf{f}^{\sigma}$ and $\mathbf{f}^{u}$ are defined according to Equation (3.62) (see Chapter 3.4), and $\mathbf{g}^{\epsilon^p}$ is a function of plastic strain (see Chapter 3.3.4). First, applying the conservation of mass at a particle gives

$$\frac{\partial \rho_i}{\partial t} = -\rho_i \left(\nabla \cdot \boldsymbol{u} \right)_i, \tag{4.26}$$

where the subscript i is written after the velocity divergence to denote that the calculation is required at the particle i. Equation (4.26) is solved to approximate the density, which is an important aspect of SPH as the density is a key component of the particle approximation. Applying Equation (4.19) to obtain the discrete divergence term results in

$$\frac{\partial \rho_i}{\partial t} = -\rho_i \sum_{j=1}^{N} \frac{m_j}{\rho_j} \left(\boldsymbol{u}_j - \boldsymbol{u}_i \right) \cdot \nabla_i W_{ij}. \tag{4.27}$$

A slightly different formulation of Equation (4.27) is derived by writing the right hand side term of Equation (4.23) as

$$-\rho \nabla \cdot \boldsymbol{u} = -\left(\nabla \cdot (\rho \boldsymbol{u}) - \boldsymbol{u} \cdot \nabla \rho \right), \tag{4.28}$$

and applying the SPH approximations described in the previous section to obtain

$$\frac{\partial \rho_i}{\partial t} = -\sum_{j=1}^{N} m_j \left(\boldsymbol{u}_j - \boldsymbol{u}_i \right) \cdot \nabla_i W_{ij}. \tag{4.29}$$

Equations (4.27) and (4.29) approximate the density according to the continuity equation in what is called the continuity density approach. An alternative way in which to calculate the density is to directly apply the SPH approximation of a function (4.14):

$$\rho_i = \sum_{j=1}^{N} m_j W_{ij}. \tag{4.30}$$

Equation (4.30) approximates the density as the weighted average of the densities of the surrounding particles, in the so-called summation density approach. This approach is less accurate than the continuity approach (particularly at the boundaries of the computational domain). However, the accuracy of the summation approach can be improved via a normalisation method (Randles and Libersky, 1996; Chen, Beraun, and Carney, 1999). Furthermore, unlike the continuity approach, the summation approach has the benefit of conserving mass exactly (Monaghan, 1992). Both of the methods described above are frequently used in the literature to calculate the density. It is important to note that in the simulation of fluids the density fluctuations are often used to determine the fluid pressure via an equation of state (Monaghan, 1994; Violeau and Issa, 2007; Gómez-Gesteira et al., 2010). As such, it is not possible to have a constant density for all particles, or the pressure would be calculated as zero. However, for problems in soil dynamics the pressure is calculated directly from the constitutive model and does not depend on the density. Therefore, it is not essential to update the density in incompressible soil dynamics problems and its value can be kept constant throughout the SPH simulation (Bui et al., 2008).

The conservation of momentum equation is written in discrete form as

$$\frac{\partial \boldsymbol{u}_i}{\partial t} = \frac{1}{\rho_i} \left(\nabla \cdot \mathbf{f}^{\sigma}\right)_i + \boldsymbol{b}_i. \tag{4.31}$$

Applying Equation (4.19) to approximate the divergence term in Equation (4.31) gives

$$\frac{\partial \boldsymbol{u}_i}{\partial t} = \frac{1}{\rho_i} \sum_{j=1}^{N} \frac{m_j}{\rho_j} \left(\mathbf{f}_j^{\sigma} - \mathbf{f}_i^{\sigma}\right) \cdot \nabla W_{ij} + \boldsymbol{b}_i. \tag{4.32}$$

While Equation (4.32) ensures that the stress gradients (defined by $\mathbf{f}^{\sigma}$) vanish in a constant stress field, it does not conserve momentum exactly. In the absence of external forces, two particles must have an equal and opposite force between them for the conservation of momentum to hold. This condition is not always satisfied when Equation (4.32) is used to determine the motion of SPH particles. Consider two isolated particles p_1 and p_2, with $\boldsymbol{b} = 0$. Applying Equation (4.32), the force $\mathbf{F}_{p1}$ at particle p_1 is calculated using Newton's second law as

$$\mathbf{F}_{p1} = m_{p1}\mathbf{a}_{p1} = \frac{m_{p1}m_{p2}}{\rho_{p1}\rho_{p2}} \left(\mathbf{f}^{\sigma}{}_{p2} - \mathbf{f}^{\sigma}{}_{p1}\right) \cdot \nabla W_{p1p2}, \tag{4.33}$$

where $\mathbf{a}$ is acceleration and the subscripts $p1$ and $p2$ denote the values at particles p_1 and p_2 respectively. The force at particle p_2 is

$$\mathbf{F}_{p2} = m_{p2}\mathbf{a}_{p2} = \frac{m_{p1}m_{p2}}{\rho_{p1}\rho_{p2}} \left(\mathbf{f}^{\sigma}{}_{,p1} - \mathbf{f}^{\sigma}{}_{,p2}\right) \cdot \nabla W_{p2p1} = F_{p1}, \quad \text{since} \quad \nabla W_{p1p2} = -\nabla W_{p2p1}. \tag{4.34}$$

Therefore, $\mathbf{F}_{p1} \neq -\mathbf{F}_{p2}$ unless $\mathbf{f}^{\sigma}{}_{p1} = \mathbf{f}^{\sigma}{}_{p2}$ and conservation of momentum is not always satisfied. To ensure momentum conservation, a symmetric form of the stress gradient can be employed (Monaghan, 1982; Monaghan, 1988; Monaghan, 1992).

This expression is derived by utilising the following identity:

$$\frac{1}{\rho}\nabla\mathbf{f}^{\sigma} = \nabla\left(\frac{\mathbf{f}^{\sigma}}{\rho}\right) + \frac{\mathbf{f}^{\sigma}}{\rho^2}\nabla\rho. \tag{4.35}$$

The SPH gradient approximation is applied to Equation (4.35) to obtain

$$\frac{1}{\rho_i}\left(\nabla\mathbf{f}^{\sigma}\right)i = \sum_{j=1}^{N} m_j \left(\frac{\mathbf{f}_i^{\sigma}}{\rho_i^2} + \frac{\mathbf{f}_j^{\sigma}}{\rho_j^2}\right)\nabla W_{ij}, \tag{4.36}$$

which is inserted into the momentum equation as follows:

$$\frac{\partial \boldsymbol{u}_i}{\partial t} = \sum_{j=1}^{N} m_j \left(\frac{\mathbf{f}_i^{\sigma}}{\rho_i^2} + \frac{\mathbf{f}_j^{\sigma}}{\rho_j^2}\right)\cdot\nabla W_{ij} + \boldsymbol{b}_i. \tag{4.37}$$

Two particles governed by Equation (4.37) can be shown to exert equal and opposite forces upon one another, and momentum is conserved exactly (Monaghan, 1982; Swegle, 2000). However it should be noted that this only applies when the kernel is the same at each particle. There are a number of kernel correction methods to improve the accuracy of the SPH particle approximation that have been developed in the literature (Chen, Beraun, and Carney, 1999; Li and Liu, 1999; Liu and Liu, 2006). A shortcoming of these methods is that the modification of the kernel can result in it being different for two interacting particles, meaning that momentum is not always conserved (Swegle, 2000).

The next governing equation to consider is the constitutive equation (4.25). Approximations of the velocity gradients are required to calculate this equation within SPH – the gradient approximation defined by Equation (4.18) is a common choice for this (Bui et al., 2008; Blanc and Pastor, 2012; Bui et al., 2014; Nguyen et al., 2017). In discrete form, the constitutive equation is expressed as

$$\frac{\partial \boldsymbol{\sigma}_i}{\partial t} = \tilde{\boldsymbol{\sigma}}_i + \left(\nabla\cdot\mathbf{f}^{u}\right)_i - \mathbf{g}_i^{\epsilon^p}. \tag{4.38}$$

The first term on the right hand side of Equation (4.38) results from the replacement of the standard stress rate with the Jaumann stress rate and is defined as

$$\tilde{\boldsymbol{\sigma}}_i = \begin{pmatrix} 2\sigma_{xy}\omega_{xy} \\ 2\sigma_{xy}\omega_{yx} \\ \sigma_{xx}\omega_{yx} + \sigma_{yy}\omega_{xy} \\ 0 \end{pmatrix}_i = \begin{pmatrix} 2\sigma_{xy,i}\omega_{xy,i} \\ 2\sigma_{xy,i}\omega_{yx,i} \\ \sigma_{xx,i}\omega_{yx,i} + \sigma_{yy,i}\omega_{xy,i} \\ 0 \end{pmatrix}, \tag{4.39}$$

with

$$\omega_{xy,i} = \frac{1}{2}\left(\frac{\partial u_{x,i}}{\partial y_i} - \frac{\partial u_{y,i}}{\partial x_i}\right), \qquad \omega_{yx,i} = \frac{1}{2}\left(\frac{\partial u_{y,i}}{\partial x_i} - \frac{\partial u_{x,i}}{\partial y_i}\right). \tag{4.40}$$

The partial derivatives in Equation (4.40) can be discretised using the SPH gradient approximation (4.18) as

$$\frac{\partial u_{x,i}}{\partial y_i} = \sum_{j=1}^{N} \frac{m_j}{\rho_j} \left(u_{x,j} - u_{x,i}\right) \frac{\partial W_{ij}}{\partial y_i}, \tag{4.41}$$

$$\frac{\partial u_{y,i}}{\partial x_i} = \sum_{j=1}^{N} \frac{m_j}{\rho_j} \left(u_{y,j} - u_{y,i}\right) \frac{\partial W_{ij}}{\partial x_i}, \tag{4.42}$$

where

$$\frac{\partial W_{ij}}{\partial x_i} = \left(\frac{x_i - x_j}{r}\right) \frac{\partial W_{ij}}{\partial r}, \quad \frac{\partial W_{ij}}{\partial y_i} = \left(\frac{y_i - y_j}{r}\right) \frac{\partial W_{ij}}{\partial r}. \tag{4.43}$$

Equations (4.41) and (4.42) are substituted into (4.39) to obtain the discrete term $\tilde{\boldsymbol{\sigma}}_i$. The SPH approximation of the divergence (Equation (4.19)) is applied to the second term on the right hand side of (4.38):

$$\left(\nabla \cdot \mathbf{f}^u\right)_i = \sum_{j=1}^{N} \frac{m_j}{\rho_j} \left(\mathbf{f}_j^u - \mathbf{f}_i^u\right) \cdot \nabla W_{ij}, \tag{4.44}$$

where $\mathbf{f}^u$ is a velocity-dependent tensor. The plastic term $\mathbf{g}_i^{\epsilon^p}$ is a function of stress and material parameters, and is calculated on each particle using the discrete stress values that are already stored on those particles. In this research two definitions of $\mathbf{g}_i^{\epsilon^p}$ are considered, which are based upon the classic plasticity and the Perzyna approaches. The two definitions of $\mathbf{g}_i^{\epsilon^p}$ are defined in Chapter 3.3.4.

In addition to the governing equations described above, SPH requires the solution of a displacement equation to update the particle positions. In discrete form, this equation is

$$\frac{\mathrm{d}\mathbf{x}_i}{\mathrm{d}t} = \boldsymbol{u}_i. \tag{4.45}$$

An alternative way in which to update the particle positions is via the XSPH method (Monaghan, 1989):

$$\frac{\mathrm{d}\mathbf{x}_i}{\mathrm{d}t} = \boldsymbol{u}_i + \epsilon_x \sum_{j=1}^{N} \frac{m_j}{\rho_j} \left(\boldsymbol{u}_j - \boldsymbol{u}_i\right) \nabla W_{ij}, \tag{4.46}$$

where ϵ_x is a tuning parameter ($0 \leq \epsilon_x \leq 1$). Equation (4.46) updates the position of a particle with a velocity that is representative of the average velocity in its neighbourhood, rather than its individual velocity. This acts to smooth the velocity field and ensure that particles do not become too close to one another, which is particularly useful in simulations with high velocity gradients. Equation (4.46) is frequently used in place of (4.45) to update the particle positions in SPH (Gómez-Gesteira and Dalrymple, 2004; Dalrymple and Rogers, 2006; Crespo, Gómez-Gesteira, and Dalrymple, 2008; Paiva et al., 2009).

To simplify the analysis of Standard and Stress-Particle SPH, a constant density

is considered in the numerical examples presented in the following two chapters. Therefore, the conservation of mass equation is neglected in the present SPH model for a single phase soil. The considered governing SPH equations are summarised as

$$\text{(Conservation of momentum)} \quad \frac{\partial \boldsymbol{u}_i}{\partial t} = \sum_{j=1}^{N} m_j \left(\frac{\mathbf{f}_i^{\sigma}}{\rho_i^2} + \frac{\mathbf{f}_j^{\sigma}}{\rho_j^2} \right) \cdot \nabla W_{ij} + \boldsymbol{b}_i, \tag{4.47}$$

$$\text{(Constitutive equation)} \quad \frac{\partial \boldsymbol{\sigma}_i}{\partial t} = \tilde{\boldsymbol{\sigma}}_i + \sum_{j=1}^{N} \frac{m_j}{\rho_j} \left(\mathbf{f}_j^{u} - \mathbf{f}_i^{u} \right) \cdot \nabla W_{ij} - \mathbf{g}_i^{\epsilon^p}, \tag{4.48}$$

$$\text{(Position update)} \quad \frac{\mathrm{d}\mathbf{x_i}}{\mathrm{d}t} = \boldsymbol{u}_i, \tag{4.49}$$

$$\text{or} \quad \frac{\mathrm{d}\mathbf{x_i}}{\mathrm{d}t} = \boldsymbol{u}_i + \epsilon \sum_{j=1}^{N} \frac{m_j}{\rho_j} \left(\boldsymbol{u}_j - \boldsymbol{u}_i \right) \nabla W_{ij}. \tag{4.50}$$

A time discretisation scheme is applied to Equations (4.47) - (4.49) or (4.50) to evolve the velocity, stress and particle positions in time.

4.3.1 Stress modification in computational plasticity

In this research two definitions of $\mathbf{g}_i^{\epsilon^p}$ are considered, which are based upon the elastoplastic and the Perzyna approaches. In both cases, $\mathbf{g}_i^{\epsilon^p}$ is non-zero only when the stress state reaches the yield surface. With regards to the elastoplastic framework, the stress state is not allowed to exceed the yield surface. However, this is not guaranteed in the numerical implementation unless a corrective treatment is applied. The stress must be checked at every calculation step and adapted if it does not lie within a valid range. This technique was developed by Chen and Mizuno (1990) for the numerical modelling of soil in an FEM model, and was also used within SPH by Bui et al. (2008) for the simulation of a soil with a Drucker-Prager yield surface. First, the stress state must be adapted if it moves outside the apex of the yield surface, which is known as tension cracking. This adaptation process is shown in Figure 4.5, in the movement of the stress state at point E to point F. Recall that the yield surface for a perfectly plastic Drucker-Prager material is defined as

$$f = \sqrt{J_2} + \alpha_\phi I_1 - k_c = 0. \tag{4.51}$$

Tension cracking occurs when

$$-\alpha_\phi I_1 + k_c < 0. \tag{4.52}$$

In such circumstances, the hydrostatic stress I_1 must be shifted back to the apex of the yield surface by adapting the normal stress components (Bui et al., 2008):

$$\hat{\sigma}_{xx} = \sigma_{xx} - \frac{1}{3} \left(I_1 - \frac{k_c}{\alpha_\phi} \right), \tag{4.53}$$

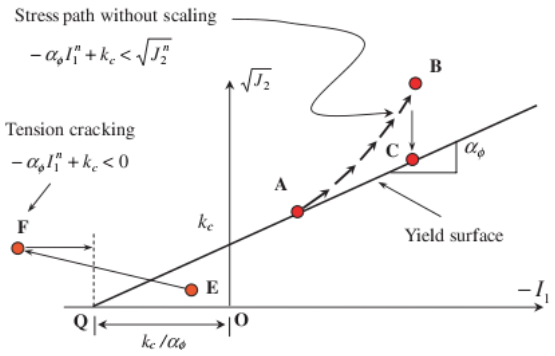

FIGURE 4.5: An illustration of the stress states in tension cracking (E ⇒ F) and imperfectly plastic behaviour (A ⇒ B), for a Drucker-Prager yield surface. The image is taken from Bui et al. (2008).

$$\hat{\sigma}_{yy} = \sigma_{yy} - \frac{1}{3}\left(I_1 - \frac{k_c}{\alpha_\phi}\right). \tag{4.54}$$

In Equations (4.53) and (4.54), $\hat{\sigma}$ is the stress value after the correction procedure.

The second corrective stress treatment must be performed when the stress state exceeds the yield surface during plastic loading, as shown by the path A to B in Figure 4.5. For the Drucker-Prager yield criterion, this occurs when

$$-\alpha_\phi I_1 + k_c < \sqrt{J_2}. \tag{4.55}$$

If the stress state satisfies Equation (4.55), it must be scaled back appropriately. For this, a scaling factor r_σ is introduced:

$$r_\sigma = \frac{-\alpha_\phi I_1 + k_c}{\sqrt{J_2}}. \tag{4.56}$$

The deviatoric shear stress $s_{\alpha\beta}$ is then reduced via this scaling factor for all components of the stress tensor:

$$\hat{\sigma}_{xx} = r_\sigma s_{xx} + \frac{1}{3}I_1, \tag{4.57}$$

$$\hat{\sigma}_{yy} = r_\sigma s_{yy} + \frac{1}{3}I_1, \tag{4.58}$$

$$\hat{\sigma}_{zz} = r_\sigma s_{zz} + \frac{1}{3}I_1, \tag{4.59}$$

$$\hat{\sigma}_{xy} = r_\sigma s_{xy}. \tag{4.60}$$

The procedure of applying Equations (4.57) to (4.60) is referred to as the stress-scaling back procedure (Bui et al., 2008), or stress modification. In the SPH implementation of the elastoplastic model, the two corrective treatments described above are applied to the nodes that have a stress state outside of the valid range.

4.4 Boundary treatment

It follows from the meshless nature of SPH that the treatment of boundary conditions is non-trivial. For methods that involve a mesh, the boundary condition can simply be applied to the relevant nodes. This can also be performed in SPH simulations when the node positions are not updated, or if the particle displacement is small (Blanc, 2011). However, in general, a different method of boundary treatment is required. Furthermore, SPH suffers from a deficiency of particles in the regions near the boundaries, which can affect the accuracy of the kernel approximation. Most relevant to the problems of interest in the current research are no-slip wall boundaries. The treatment of solid boundaries in SPH usually involves the application of virtual particles that are placed at the location of the boundary (Liu and Liu, 2010). The interaction between the interior and the virtual particles is then defined so as to ensure the interior particles do not penetrate the boundary, and that the correct boundary condition is applied to the material. For this, a number of different methods have been proposed (Takeda, Miyama, and Sekiya, 1994; Morris, Fox, and Zhu, 1997; Willemsen, Hoefsloot, and Iedema, 2000; Wang, Ge, and Li, 2006; Crespo, Gómez-Gesteira, and Dalrymple, 2007). In this research, the *dummy node* method is implemented, which consists of using layers of SPH particles to represent a no-slip wall. The method was introduced by Morris, Fox, and Zhu (1997) to model incompressible flows, and adapted by Bui et al. (2008) to be suitable for soil dynamics problems. Here, the adapted method is described.

The wall boundary is represented by three layers of dummy nodes, spaced apart by the initial particle spacing Δx, as shown in Figure 4.6. The first layer of dummy nodes can either be positioned at the location of the wall itself, or just behind the wall. Bui et al. (2008) placed the first layer at a distance of $\frac{\Delta x}{2}$ behind the virtual solid wall. For an interior particle A that contains a dummy node B within its domain of influence, the normal distance d_A of A to the wall is calculated. This distance is used to define a tangent plane at the boundary, from which the distance of the dummy node B is calculated (denoted as d_B). Note that for a straight boundary this tangent plane is the boundary plane itself. An artificial velocity $\mathbf{u}_B$ is then assigned to the dummy particle:

$$\mathbf{u}_B = -\frac{d_B}{d_A}\mathbf{u}_A, \tag{4.61}$$

where $\mathbf{u}_A$ is the velocity of the interior node. With this definition, the dummy nodes are assigned velocities that oppose the interior particle velocity, with the magnitude of the dummy velocity increasing with the distance from the wall. If the dummy particle is at an equal distance from the wall as the interior particle, its artificial velocity will be the negative of the interior particle velocity. Furthermore, the zero velocity condition is satisfied for particles that lie on the boundary. For moving boundaries, the velocity $\mathbf{u}_A$ should be replaced with the velocity of particle A relative to the moving wall. Furthermore, to account for extremely large values of the dummy node velocity when an interior particle approaches the boundary (and d_A approaches

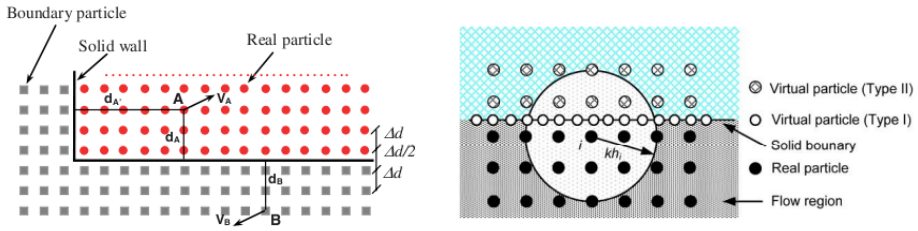

(A) Bui et al. (2008) (B) Liu and Liu (2010)

FIGURE 4.6: A schematic depiction of the dummy nodes and their interaction with the interior particles, taken from Bui et al. (2008) and Liu and Liu (2010).

zero), a parameter β is introduced:

$$\mathbf{u}_B = (1-\beta)\mathbf{u}_A + \beta\mathbf{u}_{wall}, \tag{4.62}$$

where $\mathbf{u}_{wall}$ is the velocity of the wall. The parameter β is defined as

$$\beta = \min\left(\beta_{\max}, 1 + \frac{d_B}{d_A}\right), \tag{4.63}$$

where optimum values of $\beta_{\max}$ have been found to be between 1.5 - 2 (Morris, Fox, and Zhu, 1997; Bui et al., 2008). The velocities of the dummy nodes are then included in the calculation of the velocity gradient at the interior particles to apply the no-slip effect. In the governing SPH equations described in Section 4.3, the velocity gradient is included in the constitutive law (through the $\mathbf{f}^u$ term), defined by Equation (4.48).

With the application of SPH to a rate-dependent soil as defined by Equations (4.47) and (4.48), it is also necessary to assign stress values to the dummy nodes. For a pair of interacting interior and dummy nodes (denoted as A and B respectively), Bui et al. (2008) defined the stress of the boundary particle to be equal to the stress of the interior node:

$$\boldsymbol{\sigma}_B = \boldsymbol{\sigma}_A. \tag{4.64}$$

This simple definition ensures that there is a uniform stress distribution for the nodes that are near the wall boundaries, and it contributes to smooth stress distributions in these areas. The boundary stress values defined by Equation (4.64) are included in the stress gradient calculations (through the $\mathbf{f}^\sigma$ term) on the interior nodes in the equation of momentum (Equation (4.47)). This method is utilised in the current research. An alternative technique for the interpolation of the stress from the interior nodes to the dummy nodes was developed by Randles and Libersky (1996).

An alternative way in which to prevent the SPH particles from penetrating the wall is to include a boundary repulsive force, which was first introduced into SPH by Monaghan (1994). Liu and Liu (2010) suggested that dummy nodes alone may not always prevent the interior particles from penetrating the boundary, and consequently

combined the repulsive force and the dummy node methods. In this approach a layer of repulsive particles are positioned on the boundary itself, in addition to three layers of dummy nodes behind the wall boundary (see Figure 4.6b). The particles on the boundary are spaced apart by $\frac{\Delta x}{2}$, and are utilised to apply a repulsive force on the interior particles when they approach the boundary. The particles that compose this layer do not contribute to the gradient calculations on the interior nodes. However, in the classic repulsive force method, the force is highly repulsive, which can cause unrealistic disturbances in the flow. A 'soft' repulsive force was later introduced, that prevents particle penetration without obviously disturbing the interior particles (Liu, Shao, and Chang, 2012). The repulsive force $\hat{\mathbf{F}}_{ij}$ is applied to all nodes that interact with the repulsive boundary particles, and is included in the SPH momentum equation:

$$\frac{\partial \boldsymbol{u}_i}{\partial t} = \sum_{j=1}^{N} m_j \left(\frac{\mathbf{f}_i^{\sigma}}{\rho_i^2} + \frac{\mathbf{f}_j^{\sigma}}{\rho_j^2} + \Pi_{ij}\mathbf{I} \right) \nabla \cdot W_{ij} + \hat{\mathbf{F}}_{ij} + \boldsymbol{b}_i, \tag{4.65}$$

The force is defined by the following equations:

$$\hat{\mathbf{F}}_{ij} = \sum_{j=1} 0.01c^2 \chi \cdot \hat{f}(\gamma) \frac{\mathbf{x}_{ij}}{r^2}, \tag{4.66}$$

$$\chi = \begin{cases} 1 - \frac{r}{1.5\Delta x}, & 0 \leq r < 1.5\Delta x \\ 0, & r \geq 1.5\Delta x, \end{cases} \tag{4.67}$$

$$\gamma = \frac{r}{0.75 h_{ij}}, \tag{4.68}$$

$$\hat{f}(\gamma) = \begin{cases} \frac{2}{3}, & 0 < \gamma \leq \frac{2}{3} \\ (2\gamma - 1.5\gamma^2), & \frac{2}{3} < \gamma \leq 1 \\ 0.5(2-\gamma)^2, & 1 < \gamma < 2 \\ 0, & \gamma \geq 2. \end{cases} \tag{4.69}$$

In Equation (4.66), c is the numerical speed of sound (see Section 4.5.1). The soft repulsive force defined by Equations (4.66) to (4.69) was combined with dummy nodes and applied to simulations of water flow (Liu, Shao, and Chang, 2012) and the propagation of a Bingham material (Hu et al., 2015).

In the current research, the dummy node method described above is used to approximate no-slip walls when relevant. The first layer of dummy nodes is positioned at a distance of Δx behind the outermost layer of the interior particles (in their interior position). If dummy nodes alone are not able to prevent the penetration of interior particles through the boundary, the soft repulsive force is also applied from the top layer of particles on the neighbouring nodes. In this case, the top layer of particles are spaced apart by $\frac{\Delta x}{2}$ (as opposed to Δx).

4.4.1 Free surface detection

The absence of a mesh allows the simple detection of the free surface in SPH simulations. The free surface detection method used in the current work was introduced by Marrone et al. (2010), and extended by Blanc (2011). The method consists of approximating the unit normal vector at each particle. A scan region is then defined for each particle, and an algorithm is applied that detects whether there are other particles located in the scan region. If there are no other particles within the scan region, then the particle at which the scan region is defined is a free surface particle. Otherwise, it does not lie on the free surface. A full description of the algorithm can be found in Blanc (2011).

4.5 SPH improvement techniques

Within the literature there are a variety of techniques that are employed to improve the SPH method. Many of these are included in order to combat the pitfalls of SPH that were outlined in Chapter 2.5, and to improve the accuracy and stability of the method. Here a selection of the relevant techniques are detailed.

4.5.1 Artificial viscosity

The concept of artificial viscosity was introduced by Von Neumann and Richtmyer (1950) to calculate flows with shocks. The Von Neumann-Richtmyer artificial viscosity was defined to act only when material is under compression in order to smooth over shocks and solve the system of equations without the need for any complex shock boundary treatment. Artificial viscosities based on this work were initially implemented and established in FDM (Roache, 1972), before being applied to SPH. The meshless nature of SPH means that the effects of shocks are more severe than for mesh-based methods – they induce irregular particle motions on the length scale of the initial particle separation, and result in large pressure fluctuations. An adapted artificial viscosity was implemented within SPH to dampen the irregular particle motion and pressure fluctuations, and to prevent the non-physical collisions of two approaching particles (Monaghan, 1989). The artificial viscosity term Π_{ij} is included in the SPH momentum equation as:

$$\frac{\partial \boldsymbol{u}_i}{\partial t} = \sum_{j=1}^{N} m_j \left(\frac{\mathbf{f}_i^{\sigma}}{\rho_i^2} + \frac{\mathbf{f}_j^{\sigma}}{\rho_j^2} + \Pi_{ij}\mathbf{I} \right) \nabla \cdot W_{ij} + \boldsymbol{b}_i, \tag{4.70}$$

where $\mathbf{I}$ is the identity matrix. The most widely used form of artificial viscosity is

$$\Pi_{ij} = \begin{cases} \frac{-\alpha_{\Pi} c_{ij} \phi_{ij} + \beta_{\Pi} \phi_{ij}^2}{\rho_{ij}}, & \boldsymbol{u}_{ij} \cdot \mathbf{x}_{ij} < 0 \\ 0, & \boldsymbol{u}_{ij} \cdot \mathbf{x}_{ij} \geq 0 \end{cases} \tag{4.71}$$

$$\phi_{ij} = \frac{h_{sij}\boldsymbol{u}_{ij} \cdot \mathbf{x_{ij}}}{|\mathbf{x_{ij}}^2| + 0.01h_{ij}^2}, \quad c_{ij} = \frac{c_i + c_j}{2}, \quad \rho_{ij} = \frac{\rho_i + \rho_j}{2}, \tag{4.72}$$

$$h_{sij} = \frac{h_{si} + h_{sj}}{2}, \quad \mathbf{x}_{ij} = \mathbf{x}_i - \mathbf{x}_j, \quad \boldsymbol{u}_{ij} = \boldsymbol{u}_i - \boldsymbol{u}_j. \tag{4.73}$$

where α_Π and β_Π are problem dependent tuning parameters and c is the speed of the sound (Monaghan and Gingold, 1983; Monaghan, 1989; Monaghan, 1992). The parameter α_Π is associated with the speed of sound, while β_Π is associated with the square of the velocity and has little effect in problems where the flow velocity is not comparable to the speed of sound. The speed of sound is dependent upon the material under consideration, which for a soil lies between $450-600$ m s^{-1} (Flammer et al., 2001; Adamo et al., 2004). The term $0.01h_{sij}^2$ is included to prevent numerical divergence when two particles approach one another. Note that the pressure fluctuations discussed above should be distinguished from the instabilities associated with the zero-energy modes and tensile instability. While the artificial viscosity is also able to reduce the effects of these instabilities, it is unable to eliminate them fully. Furthermore, a high value of artificial viscosity can produce excessive material shear strength and non-physical stiffness (Swegle et al., 1994). However, artificial viscosity may still be essential to remove irregular particle motions and pressure oscillations, even if the zero-energy modes and tensile instability are eliminated via alternative methods.

Alternative damping terms

A disadvantage of using the artificial viscosity is that parameter tuning may be required to obtain the optimal values of α_Π and β_Π, which are not directly associated with any physical properties. Alternative damping terms can be used instead of the artificial viscosity that have more physical relevance to the problem, or require less calibration. The following velocity-dependent damping term can be included as a body force in the equation of the momentum:

$$-\mu_d \mathbf{u}, \tag{4.74}$$

where μ_d is the damping factor. This term has been utilised in the application of SPH to problems within soil mechanics. It was included in the Node-Element SPH method by Blanc (2011) and Blanc and Pastor (2013), where parameter tuning was performed to define the value of μ_d. Similar damping terms have also been included within standard SPH methods, where the damping factor has been defined according to relevant numerical parameters (such as the Young's modulus) (Bui and Fukagawa, 2013; Nguyen et al., 2017).

4.5.2 Corrective Smoothed Particle Method

To improve the accuracy of the smoothing kernel (and consequently the SPH approximation), it can be multiplied by a corrective term (Liu, Jun, and Zhang, 1995; Li

and Liu, 1999). The Corrective Smoothed Particle Method (CSPM) (Chen, Beraun, and Carney, 1999) increases the accuracy of the kernel via a normalisation procedure, which is based on a Taylor series expansion of the SPH equations. In one dimension, the Taylor series expansion of a function $f(x)$ around a discrete point x_i is

$$f(x) = f_i + (x - x_i)\frac{\partial f_i}{\partial x} + \frac{(x - x_i)^2}{2!}\frac{\partial^2 f_i}{\partial x^2} + \ldots, \tag{4.75}$$

where $f_i = f(x_i)$. To derive the corrective term for CSPM, Equation (4.75) is multiplied by the SPH kernel and integrated over the whole domain:

$$\int f(x)W_i(x)dx = f_i \int W_i(x)dx + \frac{\partial f_i}{\partial x}\int (x - x_i)W_i(x)dx + \frac{1}{2}\frac{\partial^2 f_i}{\partial x^2}\int (x - x_i)^2 W_i(x)dx + \ldots. \tag{4.76}$$

The differential terms are then neglected, and Equation (4.76) is rearranged to obtain the CSPM integral approximation for f_i:

$$f_i = \frac{\int f(x)W_i(x)dx}{\int W_i(x)dx}. \tag{4.77}$$

This corrected integral approximation has a higher accuracy than the classic SPH approximation in the regions of the boundary. It is also more accurate for interior particles that are uniformly distributed (if the particle distribution is non-uniform, Equation (4.77) has the same accuracy as standard SPH (Liu and Liu, 2010)). In two dimensions, the particle approximation of a function according to the CSPM is

$$f_i = \frac{\sum_{j=1}^{N} \frac{m_j}{\rho_j} f(\mathbf{x}_j)W_{ij}}{\sum_{j=1}^{N} \frac{m_j}{\rho_j} W_{ij}}. \tag{4.78}$$

The CSPM form of the derivative of a function is obtained by replacing the kernel by the kernel derivative in Equation (4.76), and neglecting the derivatives that are of second order and higher. The resulting equation is then rearranged in terms of the gradient of f. In two dimensions, the derivation of the corresponding particle approximation requires the inversion of a 2×2 matrix. The final result is

$$\left(\frac{\partial f}{\partial x}\right)_i = A^{-1}_{11,i}\sum_{j=1}^{N}\frac{m_j}{\rho_j}\left(f(\mathbf{x}_j) - f(\mathbf{x}_i)\right)\frac{\partial W_{ij}}{\partial x} + A^{-1}_{12,i}\sum_{j=1}^{N}\frac{m_j}{\rho_j}\left(f(\mathbf{x}_j) - f(\mathbf{x}_i)\right)\frac{\partial W_{ij}}{\partial y}, \tag{4.79}$$

$$\left(\frac{\partial f}{\partial y}\right)_i = A^{-1}_{21,i}\sum_{j=1}^{N}\frac{m_j}{\rho_j}\left(f(\mathbf{x}_j) - f(\mathbf{x}_i)\right)\frac{\partial W_{ij}}{\partial x} + A^{-1}_{22,i}\sum_{j=1}^{N}\frac{m_j}{\rho_j}\left(f(\mathbf{x}_j) - f(\mathbf{x}_i)\right)\frac{\partial W_{ij}}{\partial y}, \tag{4.80}$$

where

$$\mathbf{A}_i = \begin{pmatrix} \sum_{j=1}^{N}\frac{m_j}{\rho_j}(x_j - x_i))\frac{\partial W_{ij}}{\partial x} & \sum_{j=1}^{N}\frac{m_j}{\rho_j}(x_j - x_i))\frac{\partial W_{ij}}{\partial y} \\ \sum_{j=1}^{N}\frac{m_j}{\rho_j}(y_j - y_i))\frac{\partial W_{ij}}{\partial x} & \sum_{j=1}^{N}\frac{m_j}{\rho_j}(y_j - y_i))\frac{\partial W_{ij}}{\partial y}. \end{pmatrix} \tag{4.81}$$

In small deformation problems, the appropriate boundary conditions can be applied directly onto the SPH nodes and the CSPM can be included to improve the accuracy of the calculation in this area. This method of treating the boundaries was used in the Node-Element method to simulate a range of soil behaviour (with small deformations) (Blanc, 2011; Blanc and Pastor, 2012; Blanc and Pastor, 2013).

4.5.3 Artificial stress

The concept of an artificial force within SPH was first introduced by Monaghan (2000) to combat the tensile instability problem, and later extended to elastic materials by Gray, Monaghan, and Swift (2001). The artificial force was defined to introduce a short-range repulsive force between two particles, that increases as the distance between them decreases. This process has the purpose of preventing two particles from clumping together, and was shown to introduce minimal long-wavelength errors. The development of the method was motivated by the idea that SPH particles behave as atoms, with the artificial force acting as an atomic force. In the extension to elastic materials, an *artificial stress* is activated in the regions that are subject to a tensile stress. In the same way as for the artificial force, the artificial stress acts to prevent particles from becoming too close to one another. The artificial stress is included in the SPH momentum equation:

$$\frac{\partial \boldsymbol{u}_i}{\partial t} = \sum_{j=1}^{N} m_j \left(\frac{\mathbf{f}_i^{\sigma}}{\rho_i^2} + \frac{\mathbf{f}_j^{\sigma}}{\rho_j^2} + \Pi_{ij}\mathbf{I} + f_{ij}^{n}(\mathbf{R}_i + \mathbf{R}_j) \right) \nabla \cdot W_{ij} + \boldsymbol{b}_i, \tag{4.82}$$

where f_{ij} is the repulsive term, defined as

$$f_{ij} = \frac{W_{ij}}{W(\Delta x, h_s)}. \tag{4.83}$$

Equation (4.83) was defined to ensure that the artificial stress decreases as the particle separation increases, where $W(\Delta x, h_s)$ is constant for a constant smoothing length. The exponent n in Equation (4.82) is a model parameter. Bui et al. (2008) used a value of $n = 2.5$ in the application of the artificial stress method to an elasto-plastic soil. The term $\mathbf{R}$ in Equation (4.82) is the artificial stress tensor, which is defined as follows:

$$R_{xx} = R'_{xx}\cos^2\theta + R'_{yy}\sin^2\theta \tag{4.84}$$

$$R_{yy} = R'_{xx}\sin^2\theta + R'_{xx}\cos^2\theta \tag{4.85}$$

$$R_{xy} = \left(R'_{xx} - R'_{yy}\right)\sin\theta\cos\theta, \tag{4.86}$$

where θ is defined as

$$\tan 2\theta = \frac{2\sigma_{xy}}{\sigma_{xx} - \sigma_{yy}}. \tag{4.87}$$

In Equations (4.84) - (4.86), $R'_{\alpha\beta}$ is the artificial stress tensor in the principle coordinate system (x', y') (corresponding to zero shear stress components). The principle

artificial stress term is defined according to the components of the principle stress:

$$R'_{xx} = \begin{cases} -\epsilon \frac{\sigma'_{xx}}{\rho^2} & \text{if} \quad \sigma'_{xx} > 0 \\ 0 & \text{if} \quad \sigma'_{xx} \leq 0, \end{cases} \tag{4.88}$$

where $0 < \epsilon < 1$ is a constant parameter defining the magnitude of the repulsive force acting on the particles. Gray, Monaghan, and Swift (2001) found $\epsilon = 0.3$ to provide optimum results in the simulations of elastic solids, while Bui et al. (2008) found that a value of $\epsilon = 0.5$ was essential to remove the instabilities in a cohesive elastoplastic soil. The terms R'_{yy} and R'_{xy} are defined by replacing the subscript xx with yy or xy in Equation (4.88). The principle stress $\boldsymbol{\sigma'}$ is related to the reference stress $\boldsymbol{\sigma}$ as

$$\sigma'_{xx} = \cos^2\theta\sigma_{xx} + 2\cos\theta\sin\theta\sigma_{xy} + \sin^2\theta\sigma_{yy} \tag{4.89}$$

$$\sigma'_{yy} = \sin^2\theta\sigma_{xx} - 2\cos\theta\sin\theta\sigma_{xy} + \cos^2\theta\sigma_{yy}. \tag{4.90}$$

The artificial stress term defined by Equations (4.83) - (4.90) is implemented within Standard SPH in the current research and applied to certain problems. When included, the parameter n is defined to be 2.5, to coincide with Bui et al. (2008). The tuning parameter ϵ is investigated and defined when relevant. The artificial stress is included within Standard SPH to provide a point of comparison for the performance of the Stress-Particle SPH model.

4.5.4 Particle shifting method

An alternative method to remove the effects of the tensile instability within SPH is the particle shifting method. This was first developed for SPH by Xu, Stansby, and Laurence (2009), and extended to free surface flows by Lind et al. (2012). An improvement of the technique was recently proposed by Xu and Yu (2018), and applied to the simulations of viscoelastic fluids. The method acts to remove voids in a simulated material (such as those resulting from the tensile instability) by shifting the SPH particles from regions of high concentration to low concentration. The particles are assigned a shifting vector, which is governed by Fick's law of diffusion (Lind et al., 2012). The shifting vector $\mathbf{r}$ is defined at each particle as

$$\mathbf{r}_i \propto D\nabla C_i \Delta t, \tag{4.91}$$

where D is a diffusion coefficient and ∇C_i is the particle concentration gradient. Lind et al. (2012) determined the diffusion coefficient by a linear stability analysis of the advection-diffusion equation, The resultant term was a function of the global time step, and required the definition of an upper shifting limit. Xu and Yu (2018) modified this definition of D by considering the Courant-Friedrichs-Lewy (CFL) condition of stability for the local time step Δt, and defined the particle shifting

vector as

$$\mathbf{r}_i = -5h_s|\boldsymbol{u}_i|\nabla C_i \Delta t, \tag{4.92}$$

where $|\boldsymbol{u}_i|$ is the velocity magnitude. The upper shifting limit is not required when Equation (4.92) is used to define the shifting vector. The particle concentration C_i and its gradient are defined as

$$C_i = \sum_{j=1}^{N} \frac{m_j}{\rho_j} W_{ij}, \quad \nabla C_i = \sum_{j=1}^{N} \frac{m_j}{\rho_j} \nabla W_{ij}. \tag{4.93}$$

Special treatment is needed for the shifting of particles at the free surface, due to the large concentration gradients there. This involves the detection of free surface particles, the calculation of their normal vectors and the subsequent reduction of diffusion in the normal direction. Particles that are detected as being on the free surface are assigned the following shifting vector

$$\mathbf{r}_i = -5h_s|\boldsymbol{u}_i|(\mathbf{I} - \mathbf{n}_i \otimes \mathbf{n}_i)\nabla C_i \Delta t. \tag{4.94}$$

Xu and Yu (2018) calculated the normal vector as

$$\mathbf{n}_i = \frac{\mathbf{M}_i \cdot \nabla C_i}{|\mathbf{M}_i \cdot \nabla C_i|}, \tag{4.95}$$

where $\mathbf{M}$ is a corrective matrix that improves the accuracy of the kernel approximation:

$$\mathbf{M}_i = \sum_{j=1}^{N} \frac{m_j}{\rho_j} \nabla W_{ij} \otimes (\mathbf{x}_j - \mathbf{x}_i). \tag{4.96}$$

The free surface treatment is also applied to the particles that are within the domain of influence as those directly on the free surface. After the particles have been shifted according to Equation (4.92) or (4.94), the variables are corrected according to the Taylor series:

$$\phi_{i'} = \phi_i + \mathbf{r}_{ii'} \cdot (\nabla \phi)_i + O(\mathbf{r}_{ii'}^2). \tag{4.97}$$

In Equation (4.97), ϕ is a general variable, the subscripts i and i' denote the old (before shifting) and new (after shifting) particles respectively, and $\mathbf{r}_{ii'}$ is the position vector between the old and the updated particle positions.

The particle shifting method described above was applied to remove the effects of the tensile instability in the SPH simulation of a viscoelastic drop impacting a rigid wall (Xu and Yu, 2018). Without the particle shifting technique, the drop exhibited severe non-physical fractures due to the tensile instability. When the particle shifting was included within SPH, the fractures were removed completely. The artificial stress method was also utilised, which was not able to fully eliminate the fractures. The particle shifting method has been implemented within the current Standard SPH model, in addition to the artificial stress method, to provide another point of comparison for the results of the Stress-Particle method.

4.6 Time discretisation

A fourth order Runge-Kutta (RK4) scheme is implemented to increment Equations (4.47) and (4.48) in time. The RK4 scheme has been chosen due to its fourth order accuracy and relatively simple implementation. Consider a general ordinary differential equation for a variable ϕ with an initial condition ϕ^0 at an initial time t^0:

$$\dot{\phi} = f(t, \phi), \quad \phi(t^0) = \phi^0,$$

where f is a function of ϕ and time t. The RK4 method is employed to increment ϕ by a time step Δt to obtain the solution at time $t = t + \Delta t$:

$$\phi^{t+\Delta t} = \phi^t + \frac{\Delta t}{6}(k_1 + 2k_2 + 2k_3 + k_4). \tag{4.98}$$

$$k_1 = f(\phi_1), \quad k_2 = f(\phi_2), \quad k_3 = f(\phi_3), \quad k_4 = f(\phi_4), \tag{4.99}$$

$$\phi_1 = \phi^t, \quad \phi_2 = \phi^t + \frac{\Delta t}{2}k_1, \quad \phi_3 = \phi^t + \frac{\Delta t}{2}k_2, \quad \phi_4 = \phi^t + \Delta t k_3. \tag{4.100}$$

Here, the RK4 scheme is applied to Equations (4.47) and (4.48), which are repeated here as

$$\frac{\partial \boldsymbol{u}_i}{\partial t} = \sum_{j=1}^{N} m_j \left(\frac{\mathbf{f}_i^\sigma}{\rho_i^2} + \frac{\mathbf{f}_j^\sigma}{\rho_j^2} \right) \cdot \nabla W_{ij} + \boldsymbol{b}_i, \tag{4.101}$$

$$\frac{\partial \boldsymbol{\sigma}_i}{\partial t} = \tilde{\boldsymbol{\sigma}}_i + \sum_{j=1}^{N} \frac{m_j}{\rho_j} \left(\mathbf{f}_j^u - \mathbf{f}_i^u \right) \cdot \nabla W_{ij} - \mathbf{g}_i^{\epsilon^p}, \tag{4.102}$$

where the tensors $\mathbf{f}^\sigma = \mathbf{f}^\sigma(\boldsymbol{\sigma})$ and $\mathbf{f}^u = \mathbf{f}^u(\boldsymbol{u})$ are functions of stress and velocity respectively (defined by Equation (3.62) in Chapter 3). It is convenient to write Equations (4.101) and (4.102) as

$$\frac{\partial \boldsymbol{u}_i}{\partial t} = F_1(\boldsymbol{\sigma}), \tag{4.103}$$

$$\frac{\partial \boldsymbol{\sigma}_i}{\partial t} = F_2(\boldsymbol{u}, \boldsymbol{\sigma}), \tag{4.104}$$

where

$$F_1(\boldsymbol{\sigma}) = \sum_{j=1}^{N} m_j \left(\frac{\mathbf{f}_i^\sigma}{\rho_i^2} + \frac{\mathbf{f}_j^\sigma}{\rho_j^2} \right) \cdot \nabla W_{ij}, + \boldsymbol{b}_i \tag{4.105}$$

$$F_2(\boldsymbol{u}, \boldsymbol{\sigma}) = \tilde{\boldsymbol{\sigma}}_i + \sum_{j=1}^{N} \frac{m_j}{\rho_j} \left(\mathbf{f}_j^u - \mathbf{f}_i^u \right) \cdot \nabla W_{ij} - \mathbf{g}_i^{\epsilon^p}. \tag{4.106}$$

Note that F_2 is a function of both stress and velocity. This is because as well as $\mathbf{f}_i^u$, Equation (4.102) involves the term $\tilde{\boldsymbol{\sigma}}_i$ (arising from the Jaumann stress transformation) and the plastic term $\mathbf{g}_i^{\epsilon^p}$ (which is a function of the stress state). Using the RK4 method, Equations (4.103) and (4.104) are incremented in time at each SPH node as

$$\boldsymbol{u}_i{}^{t+\Delta t} = \boldsymbol{u}_i{}^t + \frac{\Delta t}{6}\left(F_1(\boldsymbol{\sigma}_1) + 2F_1(\boldsymbol{\sigma}_2) + 2F_1(\boldsymbol{\sigma}_3) + F_1(\boldsymbol{\sigma}_4)\right), \tag{4.107}$$

$$\boldsymbol{\sigma}_i{}^{t+\Delta t} = \boldsymbol{\sigma}_i^t + \frac{\Delta t}{6}\left(F_2(\mathbf{u}_1, \boldsymbol{\sigma}_1) + 2F_2(\mathbf{u}_2, \boldsymbol{\sigma}_2) + 2F_2(\mathbf{u}_3, \boldsymbol{\sigma}_3) + F_2(\mathbf{u}_4, \boldsymbol{\sigma}_4)\right), \tag{4.108}$$

where

$$\mathbf{u}_1 = \mathbf{u}^t \qquad \boldsymbol{\sigma}_1 = \boldsymbol{\sigma}^t \tag{4.109}$$

$$\mathbf{u}_2 = \mathbf{u}^t + \frac{\Delta t}{2}(F_1(\boldsymbol{\sigma}_1)) \qquad \boldsymbol{\sigma}_2 = \boldsymbol{\sigma}^t + \frac{\Delta t}{2}(F_2(\mathbf{u}_1, \boldsymbol{\sigma}_1)) \tag{4.110}$$

$$\mathbf{u}_3 = \mathbf{u}^t + \frac{\Delta t}{2}(F_1(\boldsymbol{\sigma}_2)) \qquad \boldsymbol{\sigma}_3 = \boldsymbol{\sigma}^t + \frac{\Delta t}{2}(F_2(\mathbf{u}_2, \boldsymbol{\sigma}_2)) \tag{4.111}$$

$$\mathbf{u}_4 = \mathbf{u}^t + \Delta t(F_1(\boldsymbol{\sigma}_3)) \qquad \boldsymbol{\sigma}_4 = \boldsymbol{\sigma}^t + \Delta t(F_2(\mathbf{u}_3, \boldsymbol{\sigma}_3)). \tag{4.112}$$

In Standard SPH, Equations (4.109) - (4.112) are spatially resolved at each calculation step by applying Equations (4.105) and (4.106) at each node. This involves summing over the surrounding SPH nodes to obtain the terms involving the velocity and stress gradients.

In addition to the velocity and stress, the position vectors of each node $\mathbf{x}_i$ are updated at the end of each time step as

$$\mathbf{x}_i^{t+\Delta t} = \mathbf{x}_i^t + \Delta t \mathbf{u}_i^{t+\frac{\Delta t}{2}}, \tag{4.113}$$

where $\mathbf{u}_i^{t+\frac{\Delta t}{2}}$ is the average of the velocity at the current time and the previous time:

$$\mathbf{u}_i^{t+\frac{\Delta t}{2}} = \frac{1}{2}\left(\boldsymbol{u}_i^{t+\Delta t} + \boldsymbol{u}_i^t\right). \tag{4.114}$$

Alternatively, the discretised XSPH equation is

$$\mathbf{x}_i^{t+\Delta t} = \mathbf{x}_i^t + \Delta t\left(\boldsymbol{u}_i^{t+\Delta t} + \epsilon_x \sum_{j=1}^{N} \frac{m_j}{\rho_j}\left(\boldsymbol{u}_j - \boldsymbol{u}_i\right)\nabla W_{ij}\right). \tag{4.115}$$

The accuracy of the numerical solution is dependent upon the size of the time step Δt, which must be small enough to resolve the problem dynamics and provide numerical stability. The time step can be determined according to the Courant number C_o:

$$C_o = \frac{\hat{u}\Delta t}{\Delta x}, \tag{4.116}$$

where $\hat{u}$ represents a characteristic velocity and Δx is the spatial resolution (Courant, Friedrichs, and Lewy, 1967). For explicit time integration schemes, the Courant

number should be less than 1 for numerical stability. Although the RK4 method described above is implicit, the Courant number guideline is applied in this investigation nonetheless. In SPH, the Courant number can instead be written in terms of the material speed of sound c and the smoothing length h_s as

$$C_o = \frac{c\Delta t}{h_s}. \tag{4.117}$$

Equation (4.117) defines the CFL condition for SPH. Following Bui et al. (2008), in this research the time step is chosen to satisfy Equation (4.117) with a Courant number of $C_o = 0.2$, unless stated otherwise.

4.7 Nearest neighbouring particle searching

Each SPH particle requires a list of neighbouring particles in order to extract the information required for the numerical calculations. The neighbours may vary as the particle positions are updated, and therefore the list of neighbours must be updated. In this research, a linked-list method is utilised to search for the neighbours of each particle. The linked-list algorithm was first introduced by Hockney, Goel, and Eastwood, 1973, and is a popular choice of method for updating neighbouring particle lists in SPH (Liu and Liu, 2010). In the linked-list technique, a temporary mesh is utilised to find the nearest neighbours. The mesh has the same resolution as that of the compact support of the kernel function (κh). For a particle i, the nearest neighbours can only be found within the same cell of the mesh that it lies in. For n particles with a constant smoothing length, this technique has a computational complexity of $O(n)$. For comparison, searching through every particle in the domain, for each particle, requires n^2 calculations. A description of the linked-list method can be found in further detail in Simpson (1995).

4.8 Stress-Particle SPH

In the Stress-Particle SPH method there are two sets of particles – nodes and stress-points. The velocity is calculated on the SPH nodes and the stress is updated on the stress-points. As discussed in Section 4.1 (and Chapter 2.5), there are a number of benefits associated with splitting up the velocity and stress. In this section the Stress-Particle SPH method is described in detail, with respect to the equations governing soil behaviour. The discretised SPH equations describing a soil are here

repeated:

$$\text{(Conservation of momentum)} \quad \frac{\partial \boldsymbol{u}_i}{\partial t} = \sum_{j=1}^{N} m_j \left(\frac{\mathbf{f}_i^{\sigma}}{\rho_i^2} + \frac{\mathbf{f}_j^{\sigma}}{\rho_j^2} \right) \cdot \nabla W_{ij} + \boldsymbol{b}_i, \tag{4.118}$$

$$\text{(Constitutive equation)} \quad \frac{\partial \boldsymbol{\sigma}_i}{\partial t} = \tilde{\boldsymbol{\sigma}}_i + \sum_{j=1}^{N} \frac{m_j}{\rho_j} \left(\mathbf{f}_j^{u} - \mathbf{f}_i^{u} \right) \cdot \nabla W_{ij} - \mathbf{g}_i^{\epsilon^p}. \tag{4.119}$$

In the Standard SPH method the velocity and stress are solved at each node, utilising the information from the neighbouring nodes. In Equations (4.118) and (4.119) the subscript i denotes the node where the variables are calculated, and j denotes the neighbours of that node.

In Stress-Particle SPH, Equations (4.118) and (4.119) are instead written as

$$\text{(Calculated on node } i\text{)} \quad \frac{\partial \boldsymbol{u}_i}{\partial t} = \sum_{j=1}^{N} m_j \left(\frac{\mathbf{f}_i^{\sigma}}{\rho_i^2} + \frac{\mathbf{f}_j^{\sigma}}{\rho_j^2} \right) \cdot \nabla W_{ij} + \boldsymbol{b}_i, \tag{4.120}$$

$$\text{(Calculated on stress-point } j\text{)} \quad \frac{\partial \boldsymbol{\sigma}_j}{\partial t} = \tilde{\boldsymbol{\sigma}}_j + \sum_{i=1}^{N} \frac{m_i}{\rho_i} \left(\mathbf{f}_i^{u} - \mathbf{f}_j^{u} \right) \cdot \nabla W_{ji} - \mathbf{g}_j^{\epsilon^p}, \tag{4.121}$$

where now the subscript i denotes the SPH nodes, and the subscript j represents the SPH stress-points. Equation (4.120) is solved at each node i, using the stress values (in the form of $\mathbf{f}^{\sigma}$) from the neighbouring stress-points j. Similarly, Equation (4.121) is solved at each stress-point j, utilising the velocity information (in the form of $\mathbf{f}^{u}$) from the neighbouring nodes i.

The discrete variable gradient terms on the right hand side of Equations (4.120) and (4.121) involve the value of that variable at the particle itself. For example, the divergence of $\mathbf{f}^{\sigma}$ at node i in Equation (4.120) is approximated as:

$$\left(\nabla \cdot \mathbf{f}^{\sigma} \right)_i = \sum_{j=1}^{N} m_j \left(\frac{\mathbf{f}_i^{\sigma}}{\rho_i^2} + \frac{\mathbf{f}_j^{\sigma}}{\rho_j^2} \right) \cdot \nabla W_{ij}, \tag{4.122}$$

which requires the value of $\mathbf{f}^{\sigma}$ at node i (in addition to the values of $\mathbf{f}^{\sigma}$ at the surrounding stress-points j). The tensor $\mathbf{f}^{\sigma}$ is a function of stress, which is stored on the stress-points. Therefore, in order to calculate $\mathbf{f}^{\sigma}$ at the nodes, the stress must be transferred from the surrounding stress-points. Similarly, values of $\mathbf{f}^{u}$ (which is a function of velocity) are required at the stress-points to approximate the divergence of $\mathbf{f}^{u}$ in Equation (4.121). Thus, the velocity must be transferred from the nodes to the stress-points. The method in which the stress and velocity are interpolated onto the nodes and stress-points is a key aspect of Stress-Particle SPH.

In the one-dimensional Stress-Particle set-up introduced by Dyka, Randles, and Ingel (1995) (depicted in Figure 4.1a), the stress at each node is approximated as

being the average of the two stress-points on either side. Meanwhile, the velocity of each pair of stress-points is defined to be equal to that of their intermediate node. In two dimensions, the transfer of the stress to the nodes and the velocity to the stress-points is more complex. In all previous particle-based methods with the implementation of stress-points, the variable interpolation was performed via an MLS approximation (Belytschko et al., 2000; Randles and Libersky, 2000; Vignjevic, Campbell, and Libersky, 2000; Rabczuk and Belytschko, 2004; Rabczuk, Areias, and Belytschko, 2007). MLS approximations are shape functions, that attempt to minimise the sum of the squared deviations of a function from existing data points. It is linearly consistent, but considerably more complex to construct than the SPH smoothing kernel.

In this section, three different options are described for the interpolation of the stress and the velocity onto the nodes and the stress-points within the Stress-Particle SPH method. The three interpolation methods are denoted as the 'Average', 'SPH-CSPM' and 'MLS' methods. The SPH-CSPM method is used to interpolate the variables in the majority of Stress-Particle SPH applications in this research. This is because of the compromise between the accuracy and simplicity of the method. The alternative techniques are also explored, which will be stated when relevant.

4.8.1 Average method

The simplest way to update the velocity on the stress-points and the stress on the nodes is to average over the surrounding values within the domain of influence defined by the kernel:

$$\boldsymbol{u}_j \approx \frac{1}{N_i} \sum_{i=1}^{N_i} \boldsymbol{u}_i, \tag{4.123}$$

$$\boldsymbol{\sigma}_i \approx \frac{1}{N_j} \sum_{j=1}^{N_j} \sigma_j^{\alpha\beta}, \tag{4.124}$$

where N_i is the number of nodes within the domain of influence of a stress-point j, and N_j is the number of stress-points within the domain of influence of a node i. This method does not including any distance-dependent weighting effect, and is therefore the least accurate of the possible techniques.

4.8.2 SPH-CSPM method

A straightforward way in which to interpolate the stress and velocity is to utilise the SPH function approximation. To reduce the interpolation errors near the material boundaries, as well as to eliminate the dependency of the interpolation procedure on the particle mass, the SPH approximation should also be normalised using the

CSPM. The SPH interpolation method, with CSPM, is defined as

$$\boldsymbol{u}_j \approx \frac{\sum_{i=1}^{N_i} \frac{m_i}{\rho_i} \boldsymbol{u}_i W_{ij}}{\sum_{i=1}^{N_i} \frac{m_i}{\rho_i} W_{ij}}, \tag{4.125}$$

$$\boldsymbol{\sigma}_i \approx \frac{\sum_{j=1}^{N_j} \frac{m_j}{\rho_j} \boldsymbol{\sigma}_j W_{ij}}{\sum_{j=1}^{N_j} \frac{m_j}{\rho_j} W_{ij}}. \tag{4.126}$$

Of the different available interpolation techniques, the SPH-CSPM method is preferable for implementation in the current research. As opposed to the averaging method, the SPH approximation places a higher influence on particles that are closer to the node or stress-point in question. Furthermore, the technique is relatively simple. The simplicity of Standard SPH is one of its major benefits. While there are interpolation procedures that have a higher degree of accuracy than the SPH approximation (dependent on the choice of kernel function), they are associated with an increase in complexity and computational time.

4.8.3 MLS method

The MLS approximation involves more computation steps than the SPH approximation. The velocity at a stress-point j is approximated via the linear MLS method as

$$\mathbf{u}_j = \mathbf{a} + \mathbf{b} \cdot \mathbf{x}_{ij}, \tag{4.127}$$

where $\mathbf{a}$ is a constant vector, $\mathbf{b}$ is a constant second order tensor and $\mathbf{x}_{ij}$ is the relative distance between the stress-point and surrounding nodes:

$$\mathbf{x}_{ij} = \mathbf{x}_i - \mathbf{x}_j. \tag{4.128}$$

The MLS method is based upon the minimisation of the weighted residual function. For velocity, the residual function is

$$R(\mathbf{u}_j) = \frac{1}{2} \sum_{i=1}^{N_i} (\mathbf{u}_j - \mathbf{u}_i) \cdot (\mathbf{u}_j - \mathbf{u}_i) w_{ij}. \tag{4.129}$$

where, as in the SPH kernel approximation, w_{ij} is the weight function. In this research, the MLS weight function is defined to be the same as the SPH kernel function. Equation (4.129) is minimised by solving the following equations:

$$\frac{\partial R(\mathbf{u}_j)}{\partial \mathbf{a}} = 0, \quad \frac{\partial R(\mathbf{u}_j)}{\partial \mathbf{b}} = 0. \tag{4.130}$$

Equations (4.127), (4.129) and (4.130) are combined to obtain the solutions for $\mathbf{a}$ and $\mathbf{b}$, which are substituted back into Equation (4.127) to obtain the velocity approximation:

$$\mathbf{u}_j = \left(\sum_{i=1}^{Ni} w_{ij}\right)^{-1} \left(\left(\sum_{i=1}^{Ni} w_{ij}\right) - \mathbf{S}(\mathbf{u},\mathbf{x}) \cdot \mathbf{S}_j(\mathbf{x},\mathbf{x})^{-1} \cdot \left(\sum_{i=1}^{Ni} w_{ij}\mathbf{x}_{ij}w_{ij}\right)\right), \quad (4.131)$$

$$\mathbf{S}_j(\mathbf{x},\mathbf{x}) = \left(\sum_{i=1}^{N_i} (\mathbf{x}_{ij} : \mathbf{x}_{ij})\, w_{ij} \left(\sum_{i=1}^{N_i} w_{ij}\right) - \left(\sum_{i=1}^{N_i} \mathbf{x}_{ij} w_{ij}\right) : \left(\sum_{i=1}^{N_i} \mathbf{x}_{ij} w_{ij}\right)\right), \quad (4.132)$$

$$\mathbf{S}(\mathbf{u},\mathbf{x}) = \left(\sum_{i=1}^{N_i} (\mathbf{u}_{ij} : \mathbf{x}_{ij})\, w_{ij} \left(\sum_{i=1}^{N_i} w_{ij}\right) - \left(\sum_{i=1}^{N_i} \mathbf{u}_{ij} w_{ij}\right) : \left(\sum_{i=1}^{N_i} \mathbf{x}_{ij} w_{ij}\right)\right). \quad (4.133)$$

With regards to the stress approximation on the nodes, this is assumed to be of the form

$$\boldsymbol{\sigma}_i = \mathbf{a} + \mathbf{b} \cdot \mathbf{x}_{ij}, \quad (4.134)$$

where $\mathbf{a}$ is a constant second order tensor and $\mathbf{b}$ is a constant third order tensor. The weighted residual function for the stress is minimised, and the final form of the stress approximation is

$$\boldsymbol{\sigma}_i = \left(\sum_{j=1}^{Nj} w_{ij}\right)^{-1} \left(\left(\sum_{j=1}^{Nj} w_{ij}\right) - \mathbf{S}(\boldsymbol{\sigma},\mathbf{x}) \cdot \mathbf{S}_i(\mathbf{x},\mathbf{x})^{-1} \cdot \left(\sum_{j=1}^{Nj} w_{ij}\mathbf{x}_{ij}w_{ij}\right)\right), \quad (4.135)$$

$$\mathbf{S}_i(\mathbf{x},\mathbf{x}) = \left(\sum_{j=1}^{N_j} (\mathbf{x}_{ij} : \mathbf{x}_{ij})\, w_{ij} \left(\sum_{j=1}^{N_j} w_{ij}\right) - \left(\sum_{j=1}^{N_j} \mathbf{x}_{ij} w_{ij}\right) : \left(\sum_{i=1}^{N_j} \mathbf{x}_{ij} w_{ij}\right)\right), \quad (4.136)$$

$$\mathbf{S}(\boldsymbol{\sigma},\mathbf{x}) = \left(\sum_{j=1}^{N_j} (\boldsymbol{\sigma}_{ij} : \mathbf{x}_{ij})\, w_{ij} \left(\sum_{j=1}^{N_j} w_{ij}\right) - \left(\sum_{j=1}^{N_j} \boldsymbol{\sigma}_{ij} w_{ij}\right) : \left(\sum_{j=1}^{N_j} \mathbf{x}_{ij} w_{ij}\right)\right). \quad (4.137)$$

The derivation of Equations (4.131) and (4.135) is provided in further detail by Sanchez and Randles (2012). The tensors $\mathbf{S}_j(\mathbf{x},\mathbf{x})$ and $\mathbf{S}_i(\mathbf{x},\mathbf{x})$ defined by Equations (4.132) and (4.136) are functions of the local geometry at a particle, and are sensitive to the surrounding particle distribution. In areas where the particle neighbourhood is truncated, i.e. at the material boundaries, the terms can become singular (Sanchez and Randles, 2012). To avoid this, the tensors are adapted at boundary particles to include reflections of the internal particles. This process is quite elaborate, and differs for the particles located at the edges and at the corners of the material. A full description of how the reflective tensors are incorporated can be found in the literature (Sanchez and Randles, 2012).

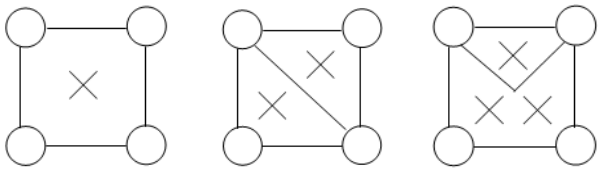

(A) SP1 (B) SP2 (C) SP3

FIGURE 4.7: Examples of different node-stress-point arrangements, with one, two and three stress-points inside each virtual quadrilateral.

4.8.4 Node-stress-point arrangement

The benefits that stress-points bring to SPH in terms of stability are dependent on the initial node-stress-point arrangement (Belytschko et al., 2000). Despite this, all previous applications with stress-points have been restricted to having one stress-point in the centre of every virtual quadrilateral, as depicted in Figure 4.1b. Belytschko et al. (2000) considered alternative arrangements (shown in Figure 4.2) in a linear stability analysis. However, no numerical simulations were conducted with these arrangements. In the current research, multiple node-stress-points configurations are considered. First, these configurations consist of a specified number of stress-points placed inside virtual quadrilaterals. This method of arranging the nodes and stress-points is denoted the *inside approach*, and example arrangements are shown in Figure 4.7. The different configurations depicted in Figure 4.7 consist of one, two and three stress-points placed inside every virtual quadrilateral, denoted SP1, SP2 and SP3 respectively. To describe in further detail the locations of the stress-points, the four nodes are labelled 1,2,3 and 4 – starting from the bottom left node and moving clockwise to the bottom right node. The stress-point in configuration SP1 is simply placed in the centre of nodes 1,2,3 and 4. The SP2 configuration includes two stress-points, with each one placed in the centre of the two 'virtual triangles' that are created by connecting the nodes 2 and 4. The SP3 configuration includes three stress-points that are positioned as follows. One is placed in the centre of the virtual triangle made by connecting nodes 1,2 and 4. The second stress-point is placed in the centre of the virtual triangle made by connecting nodes 1, 3 and 4. Finally, the third stress-point is positioned in the centre of the triangle created by connecting nodes 2 and 3 with the centre of the quadrilateral. The majority of SPH simulations conducted with the inside approach will compare the results from SP1, SP2 and SP3, although other configurations are also considered.

An alternative approach in which to arrange the nodes and stress-points is to assign a specified number of stress-points to each SPH node. Examples of such configurations are provided in Figure 4.8, for one, two, three and four stress-points per node. With this method, each individual SPH node is associated with one or more stress-points, in what is denoted as the *outside approach*. The stress-points are each positioned a horizontal distance r_x and a vertical distance r_y away from the node, as shown in Figure 4.8a. For simplicity, unless stated otherwise, the distances

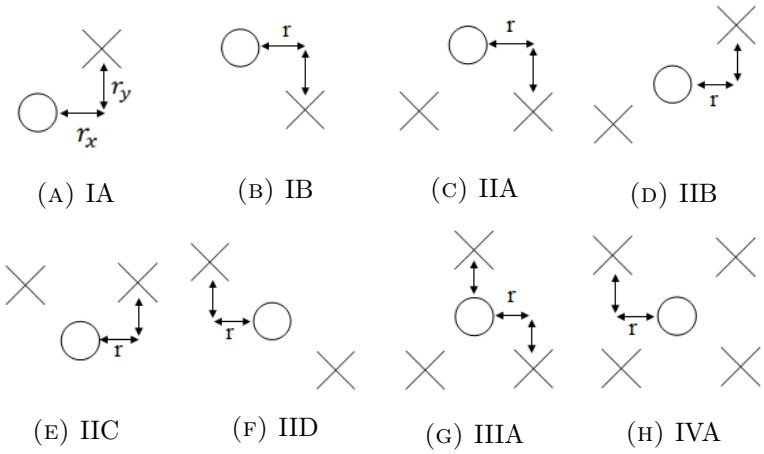

(A) IA (B) IB (C) IIA (D) IIB

(E) IIC (F) IID (G) IIIA (H) IVA

FIGURE 4.8: A depiction of the Stress-Particle outside approach.

r_x and r_y are defined to be equal and are labelled as r. For all of the configurations displayed in Figure 4.8a, the stress-points are placed from their corresponding node at a horizontal and vertical distance of r, in either the positive or negative direction. The distance r is a function of the initial particle spacing, such that

$$r = l\Delta x, \quad 0 < l \leq \frac{1}{2}. \tag{4.138}$$

For the majority of applications in this research, r is defined to be equal to $\Delta x/3$. For this definition of r, the initial, interior node-stress-point arrangement for configuration IIB (shown in Figure 4.8d) is equal to the inside approach configuration SP2 (shown in Figure 4.7b). There are a number of benefits to having stress-points associated with individual nodes – namely, the stress-points can be manipulated for specific nodes if required. The results from simulations conducted with the outside approach are presented in Chapter 6.

Mass distribution

As the calculations on the SPH nodes utilise information from the stress-points only (as opposed to both nodes and stress-points), the total mass of the stress-points must equal the total mass of the nodes:

$$\text{Total Mass} = \sum m_{\text{Nodes}} = \sum m_{\text{Stress-Points}}. \tag{4.139}$$

For the Stress-Particle inside approach, the stress-points are initially assigned the same mass as the interior SPH nodes. This is then divided by the respective number of stress-points per virtual quadrilateral. Recall that the mass of the boundary nodes is different to the mass of the interior nodes. Therefore in the inside approach, the total mass of the stress-points is not exactly equal to the total mass of the nodes. In the outside approach, the stress-points are assigned the same mass as their associated

node, divided by the number of stress-points per node. Thus, in the outside approach the total mass of the stress-points is exactly equal to the total mass of the nodes.

4.8.5 Stress-point position update procedure

To ensure that the calculations within the Stress-Particle method are accurate and stable, a sufficient number of stress-points is required in the neighbourhood of the nodes. Therefore the positions of the stress-points must be updated along with the nodes. This is not straightforward, because the material velocity is not calculated on the stress-points. However, the stress-points do have a velocity that is interpolated from the surrounding nodes, as required for the calculation of the velocity gradient on the stress-points. Hence, one way in which to update the stress-point positions is according to this interpolated velocity. Equation (4.49) or (4.50) can be applied to move the stress-points in the same way as for the nodes. This method has been used to update the stress-point positions in all existing stress-point schemes in the literature. As all applications of the Stress-Particle method have been confined to small displacement problems, this position update method has been sufficient. However, updating the stress-point positions according to an interpolated velocity is likely to be unsuitable for problems involving rapid velocities and large displacements (Vignjevic, Campbell, and Libersky, 2000).

An advantage of having stress-points associated with individual nodes in the outside approach is that the positions of the stress-points can be determined by their corresponding node. The stress-points can be assigned to follow their associated nodes for the duration of the numerical simulation, as depicted in Figure 4.9 for configuration IIB. In this way it is ensured that every node always has at least one (in the case of one stress-point following each node) stress-point in its neighbourhood.

The stability analysis performed by Belytschko et al. (2000) highlighted the importance of the node-stress-point arrangement on the performance of Stress-Particle methods. The analysis was performed for stationary particles, and the behaviour of the Stress-Particle method for transient problems is unexplored. Furthermore, the particle configuration changes as the node and particle positions are updated. One of the aims of the current research is to investigate the capabilities of the Stress-Particle method when applied to problems with large deformations and displacements.

4.8.6 Boundary treatment

The boundaries of the material domain can be composed of either nodes or stress-points. In the existing literature, both of these options have been employed (Randles and Libersky, 2000; Vignjevic, Campbell, and Libersky, 2000). In the first extension of the Stress-Particle method to two dimensions, Randles and Libersky (2000) used stress-points to define the boundaries of the material in order to simplify the explicit application of a stress-free boundary condition. In later work, the material boundaries were composed of SPH nodes (Sanchez and Randles, 2012; Sanchez and

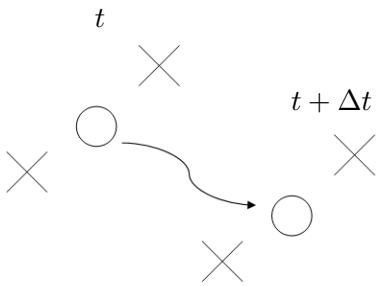

FIGURE 4.9: A sketch depicting the stress-points following their associated node in the Stress-Particle outside approach.

Randles, 2013). Vignjevic, Campbell, and Libersky (2000) also used SPH nodes as boundary particles, and updated the positions of the boundary nodes in a way that reduced the stress of its neighbouring stress-points, thereby implicitly applying a stress-free condition at the free surface.

Here, simulations conducted with the Stress Particle inside approach are initialised so that the boundaries of the material domain are composed of SPH nodes. All stress-points lie within the boundaries. Conversely, in the outside approach, some stress-points will lie outside of the material domain. However, it is possible to remove these stress-points from the simulation if necessary. The problems considered in the following chapters consist of both small and large displacements, and two different methods of treating the boundaries are required for this. First, for the small displacement problems, the boundary conditions are explicitly applied to the nodes that compose the domain boundaries. The CSPM method described in Section 4.5.2 is included in the SPH gradient approximations to reduce the error associated with the kernel truncation at the boundaries.

For the problems involving large displacements, dummy nodes are implemented to simulate a no-slip wall as outlined in Section 4.4. The implementation is slightly different when applied to the Stress-Particle method, than for Standard SPH. In Standard SPH, the velocity of the dummy nodes is included in the gradient calculation on the interior SPH nodes, which implicitly enforces a no-slip condition on the interior nodes. In the Stress-Particle method, the velocity gradient is calculated on the stress-points and the no-slip effect is therefore applied to the stress-points, and not the nodes. The no-slip condition will influence the nodes nonetheless, as the nodes utilise the stress information from the surrounding stress-points. However, the application of the no-slip condition is less direct than for Standard SPH, and it may not be sufficient to ensure that nodes do not penetrate the boundary. This could be particularly problematic when the nodes are located closer to the wall boundaries than the stress-points. Therefore, the soft repulsive force defined by Equations (4.66) - (4.69) is also applied to the SPH nodes when necessary.

A further benefit of the outside approach set-up is that it is straightforward to adapt the stress-points in the regions next to the boundary, as shown in Figure

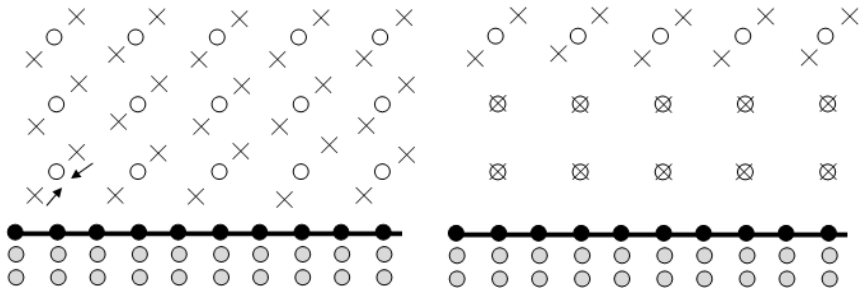

(A) Before stress-point adaptation at the boundaries (B) After stress-point adaptation at the boundaries

FIGURE 4.10: A depiction of the nodes and stress-points in the outside approach, in the proximity of the wall boundary.

4.10. This process – denoted as stress-point adaptation – could be beneficial if the presence of stress-points interferes with the intended purpose of the dummy nodes. The technique is explored in Chapter 6.

4.9 A summary of Stress-Particle SPH

The RK4 method outlined in Section 4.6 is implemented to solve the governing equations of motion for Stress-Particle SPH. This consists of four steps to temporally integrate the equations from time t to time $t+\Delta t$ – the process is the exact same for Stress-Particle SPH as for Standard SPH, and is detailed by Equations (4.101) - (4.149). However for Stress-Particle SPH, the spatial derivatives within each integration step are calculated with the Stress-Particle method. For completeness, the RK4 scheme is rewritten here, in the framework of Stress-Particle SPH.

The equation of momentum and constitutive equation are written compactly as

$$\frac{\partial \boldsymbol{u}_i}{\partial t} = F_1(\boldsymbol{\sigma}), \tag{4.140}$$

$$\frac{\partial \boldsymbol{\sigma}_j}{\partial t} = F_2(\boldsymbol{u}, \boldsymbol{\sigma}), \tag{4.141}$$

where the velocity is updated on the nodes, denoted by i, and the stress is updated on the stress-points, denoted by j. The right hand side terms F_1 and F_2 are functions of stress and velocity:

$$F_1(\boldsymbol{\sigma}) = \sum_{j=1}^{N} m_j \left(\frac{\mathbf{f}_i^{\sigma}}{\rho_i^2} + \frac{\mathbf{f}_j^{\sigma}}{\rho_j^2} \right) \cdot \nabla W_{ij} + \boldsymbol{b}_i, \tag{4.142}$$

$$F_2(\boldsymbol{u}, \boldsymbol{\sigma}) = \tilde{\boldsymbol{\sigma}}_j + \sum_{i=1}^{N} \frac{m_i}{\rho_i} \left(\mathbf{f}_i^u - \mathbf{f}_j^u \right) \cdot \nabla W_{ji} - \mathbf{g}_j^{\epsilon^p}, \tag{4.143}$$

where F_1 and F_2 are calculated on the nodes and stress-points respectively. With the RK4 scheme, Equation (4.140) is incremented in time at each SPH node as

$$\boldsymbol{u}_i{}^{t+\Delta t} = \boldsymbol{u}_i{}^{t} + \frac{\Delta t}{6}\left(F_1(\boldsymbol{\sigma}_1) + 2F_1(\boldsymbol{\sigma}_2) + 2F_1(\boldsymbol{\sigma}_3) + F_1(\boldsymbol{\sigma}_4)\right). \tag{4.144}$$

Additionally, Equation (4.141) is incremented in time at each SPH stress-point:

$$\boldsymbol{\sigma}_j{}^{t+\Delta t} = \boldsymbol{\sigma}_j^{t} + \frac{\Delta t}{6}\left(F_2(\mathbf{u}_1, \boldsymbol{\sigma}_1) + 2F_2(\mathbf{u}_2, \boldsymbol{\sigma}_2) + 2F_2(\mathbf{u}_3, \boldsymbol{\sigma}_3) + F_2(\mathbf{u}_4, \boldsymbol{\sigma}_4)\right). \tag{4.145}$$

The variables $\boldsymbol{u}$ and $\boldsymbol{\sigma}$ are updated at each integration step:

$$\mathbf{u}_1 = \mathbf{u}^t \qquad \boldsymbol{\sigma}_1 = \boldsymbol{\sigma}^t \tag{4.146}$$

$$\mathbf{u}_2 = \mathbf{u}^t + \frac{\Delta t}{2}(F_1(\boldsymbol{\sigma}_1)) \qquad \boldsymbol{\sigma}_2 = \boldsymbol{\sigma}^t + \frac{\Delta t}{2}(F_2(\mathbf{u}_1, \boldsymbol{\sigma}_1)) \tag{4.147}$$

$$\mathbf{u}_3 = \mathbf{u}^t + \frac{\Delta t}{2}(F_1(\boldsymbol{\sigma}_2)) \qquad \boldsymbol{\sigma}_3 = \boldsymbol{\sigma}^t + \frac{\Delta t}{2}(F_2(\mathbf{u}_2, \boldsymbol{\sigma}_2)) \tag{4.148}$$

$$\mathbf{u}_4 = \mathbf{u}^t + \Delta t(F_1(\boldsymbol{\sigma}_3)) \qquad \boldsymbol{\sigma}_4 = \boldsymbol{\sigma}^t + \Delta t(F_2(\mathbf{u}_3, \boldsymbol{\sigma}_3)). \tag{4.149}$$

Within each integration step, the Stress-Particle method is applied to obtain the spatial derivatives required for F_1 and F_2, and to update the stress and the velocity. To demonstrate this, the first step of the RK4 integration process for Stress-Particle SPH is summarised in the following points. At the start of the first step, the values of $\mathbf{u}_1$ and $\boldsymbol{\sigma}_1$ are defined as $\mathbf{u}^t$ and $\boldsymbol{\sigma}^t$ respectively.

1. **Interpolate the stress and the velocity**

   The stress $\boldsymbol{\sigma}_1$ is interpolated from the stress-points onto the nodes, and the velocity $\mathbf{u}_1$ is interpolated from the nodes onto the stress-points. For the SPH-CSPM interpolation method, this is defined as

   $$\boldsymbol{u}_{1j} \approx \frac{\sum_{i=1}^{N_i} \frac{m_i}{\rho_i} \boldsymbol{u}_{1i} W_{ij}}{\sum_{i=1}^{N_i} \frac{m_i}{\rho_i} W_{ij}}, \tag{4.150}$$

   $$\boldsymbol{\sigma}_{1i} \approx \frac{\sum_{j=1}^{N_j} \frac{m_j}{\rho_j} \boldsymbol{\sigma}_{1j} W_{ij}}{\sum_{j=1}^{N_j} \frac{m_j}{\rho_j} W_{ij}}. \tag{4.151}$$

   The terms $\mathbf{f}^\sigma$ and $\mathbf{f}^u$ (which are functions of stress and velocity respectively) are then defined at the nodes and stress-points.

2. **Update boundary conditions/Adapt the stress**

   If the boundary conditions are applied directly to the SPH boundary nodes, then the relevant components of the stress and velocity are updated.

   If the material is described with an elastoplastic rheological model, the stress state is adapted to ensure that it lies on the yield surface (see Section 4.3.1).

3. **Calculate the gradient terms**

The SPH gradient approximation term is applied to calculate the gradients of the stress and velocity (and hence $\mathbf{f}^\sigma$ and $\mathbf{f}^u$) on the nodes and stress-points respectively:

$$(\nabla \cdot \mathbf{f}^\sigma)_i = \sum_{j=1}^{N} m_j \left(\frac{\mathbf{f}_i^\sigma}{\rho_i^2} + \frac{\mathbf{f}_j^\sigma}{\rho_j^2} \right) \cdot \nabla W_{ij}, \tag{4.152}$$

$$(\nabla \cdot \mathbf{f}^u)_j = \sum_{i=1}^{N} \frac{m_i}{\rho_i} \left(\mathbf{f}_i^u - \mathbf{f}_j^u \right) \cdot \nabla W_{ji}. \tag{4.153}$$

If the CSPM normalisation is included, the gradient terms are normalised as described in Section 4.5.2. If dummy nodes are used, then they are included in the gradient calculations.

4. **Calculate the additional terms for the momentum equation**

   The body force $\mathbf{b}$ is updated on the nodes. In this research, gravity is the only physical body force that is considered. If included, the artificial viscosity is also calculated on the nodes, using information from the neighbouring nodes.

5. **Calculate the additional terms for the constitutive equation**

   The plastic strain function $\mathbf{g}^{\epsilon^p}$ is calculated on the stress-points. At each particle, the stress state is checked to see if the yield criterion has been met. If the stress state lies within the elastic range, then $\mathbf{g}^{\epsilon^p} = 0$. Otherwise, the plastic term is calculated and $\mathbf{g}^{\epsilon^p}$ is non-zero. The plastic term is a function of stress and velocity gradients, which are known at the stress-points.

   For large deformation problems, the Jaumann stress rate $\tilde{\boldsymbol{\sigma}}$ is also updated on the stress-points, according to Equations (4.39) and (4.40). This involves gradients of the velocity, which are already stored on the stress-points.

6. **Compute F_1 and F_2**

$$F_1(\boldsymbol{\sigma}) = (\nabla \cdot \mathbf{f}^\sigma)_i + \boldsymbol{b}_i \quad \text{on nodes,} \tag{4.154}$$

$$F_2(\boldsymbol{u}, \boldsymbol{\sigma}) = \tilde{\boldsymbol{\sigma}}_j + (\nabla \cdot \mathbf{f}^u)_j - \mathbf{g}_j^{\epsilon^p} \quad \text{on stress-points.} \tag{4.155}$$

7. **Calculate $\boldsymbol{u}_2$ and $\boldsymbol{\sigma}_2$**

$$\mathbf{u}_2 = \mathbf{u}^t + \frac{\Delta t}{2}(F_1(\boldsymbol{\sigma}_1)) \qquad \boldsymbol{\sigma}_2 = \boldsymbol{\sigma}^t + \frac{\Delta t}{2}(F_2(\mathbf{u}_1, \boldsymbol{\sigma}_1)) \tag{4.156}$$

8. **Update boundary conditions/Adapt the stress**

   If necessary, the boundary conditions and stress state are again updated.

The same process described by Steps 1 - 8 is followed to obtain $\boldsymbol{u}_3, \boldsymbol{u}_4, \boldsymbol{\sigma}_3$ and $\boldsymbol{\sigma}_4$. Then, Equations (4.144) and (4.145) are applied to update the velocity and the stress at the subsequent time step. Once the variables have been updated, the positions of the nodes are updated according to Equation (4.113) or (4.115). The stress-point positions are also advanced – either according to Equation (4.113) or (4.115), or by following their associated node as described in Section 4.8.5.

4.10 Computational implementation

The Stress-Particle SPH method has been written in Fortran 90, and implemented by the author of this research. Additionally, a Standard SPH technique has also been developed by the author, for comparison with the Stress-Particle method. Select routines have been recycled from the numerical code that was written in the development of the Node-Element method. This code was kindly provided to the author by Professor Manuel Pastor, of the Technical University of Madrid. The Node-Element SPH code was written by Thomas Blanc and Manuel Pastor as part of the PhD thesis of Thomas Blanc (Blanc, 2011), supervised by Professor Pastor. A description of the specific routines that have been recycled from the Node-Element method, and those that have been written by the author, is here provided.

To obtain the neighbours within the domain of influence of each particle, the same linked-list algorithm has been used that was implemented by Blanc (2011) (described in Section 4.7). The numerical algorithm produces a list of all neighbouring particles, in the form of a *linked list*. Each member of the list contains information regarding an interacting pair of particles, with a pointer to the next pair of interacting particles in the list. The relevant pair information is the type of particle (i.e. node or element, identified by an index), and the values of the kernel and the kernel gradient. This algorithm has been utilised by the current author to find the neighbouring particles, and to determine the type of particle-particle interaction. In the current research the possible particle interactions are node-node, stress-point-stress-point, node-stress-point, node-dummy node and stress-point-dummy node. In addition to the linked list algorithm, the Stress-Particle method uses the same kernel calculation routine as for the Node-Element method (the cubic spline), and the same free surface detection algorithm (see Section 4.4.1). Furthermore, the Node-Element method includes an implementation of the CSPM (see Section 4.5.2), which has been used for certain problems in this research.

The Node-Element method utilises a viscoplastic Perzyna model to describe a soil, with a Von Mises yield surface. This description has also been included in the Stress-Particle SPH method. In addition to this, an elastoplastic Drucker-Prager model has been implemented by the author, so that the soil can be modelled with either the Perzyna or the elastoplastic model. This also required the implementation of the stress modification procedure, described in Section 4.3.1. There are some aspects of the Node-Element code that were edited and adapted by the author of this research

TABLE 4.1: A summary of the various numerical routines and features (written in Fortran 90) of Stress-Particle SPH and Standard SPH. The column headers detail the authors of the routines.

Routines written and implemented by the current author (in full)	Routines recycled from the Node-Element method (written by Thomas Blanc and Prof Pastor)	Routines adapted from the Node-Element method by the current author
Addition of stress-points	Linked-list	RK4 scheme
Node-stress-point interactions	Cubic spline kernel	GiD output
Node-stress-point configuration	Free surface detection	
Stress-point position update	Perzyna model	
Elastoplastic model	CSPM	
Dummy nodes		
Repulsive boundary nodes		
Artificial viscosity		
Stress modification		
XSPH position update		
ParaView output		
Artificial stress		
Particle shifting		

for use in the Stress-Particle method. In the Node-Element method, the governing equations of motion are split into two, consisting of an advective equation and an ordinary differential equation (ODE). The ODE is solved using an RK4 integration scheme, which has been adapted for the current research to solve the full system of equations. Moreover, the Node-Element method contains a routine that outputs data in a format that can be inserted into the post-processing software GiD. This was adapted by the current author to allow the Stress-Particle SPH results to be visualised in GiD. Additionally, a routine was developed for the Stress-Particle SPH code to enable to post-processing of results in ParaView.

The computational implementation of the Stress-Particle SPH method required the development of numerous new Fortran routines to describe the stress-point behaviour, including their quantity and arrangement, the gradient calculations between the nodes and stress-points, the transfer of information between the nodes and stress-points, and the position update of the stress-points. Furthermore, additional routines were implemented within the Standard SPH code, such as the artificial stress and particle shifting methods. A summary of the relevant routines that were implemented in both Stress-Particle SPH and Standard SPH is provided in Table 4.1, where it is highlighted which ones were originally developed by the authors of the Node-Element method.

4.11 Conclusion

In the following chapters, Stress-Particle SPH is applied to a number of problems regarding soil behaviour, using both a viscoplastic Perzyna model and an elasto-plastic constitutive model. The majority of the problems are also simulated in the literature. First, the Stress-Particle inside approach is applied to a range of problems that are relevant to soil failure (and therefore landslide initiation), that exhibit instabilities. The effect of the stress-point quantity and position are analysed with regards to the performance and stabilising qualities of the numerical method, and the results are compared with those from the literature. The inside approach is also applied to a problem involving the post-failure behaviour of soil, which exhibits large displacements. The method is not expected to be able to handle this type of problem, due to the way in which the stress-point positions are updated. Following the assessment of the inside approach, the novel outside approach is also applied to a range of problems. It is expected that the outside approach is better suited for large displacement problems. The performance of both approaches are assessed in terms of the ability to eliminate the effects of zero-energy modes and the tensile instability. Furthermore, it is observed how the presence of stress-points affect the overall dynamics of the problem (if at all). The Standard SPH model is also used to compare against the Stress-Particle SPH results.

Chapter 5

Stress-Particle inside approach results

5.1 Introduction

In this chapter the results of the Stress-Particle SPH method with the inside approach are presented. First, the method is applied to simulate the propagation of a shock wave in a one-dimensional bar. This problem was simulated by Dyka, Randles, and Ingel (1995) and Dyka, Randles, and Ingel (1997) to validate the original Stress-Particle method. For this problem, the current Stress-Particle SPH method is identical to the one-dimensional method introduced by Dyka, Randles, and Ingel (1995). The simulations are conducted to ensure that the basic structure of the Stress-Particle approach is implemented correctly. Following this, the two-dimensional Stress-Particle SPH method is applied to problems regarding soil failure – that are relevant to landslide initiation – with the purpose of validating the model and assessing its capabilities in this area. These problems consist of the strain localisation in a two-dimensional soil sample (Mabssout and Herreros, 2013), an elastic and viscoplastic vertical slope (Blanc, 2011; Blanc and Pastor, 2013), and the collapse of a cohesive soil (Bui et al., 2008). The effect of the quantity and arrangement of the stress-points is analysed in the simulation of these problems. Furthermore, the inside approach is employed to simulate the collapse of a non-cohesive soil (Bui et al., 2008). The non-cohesive soil exhibits large displacements and is representative of landslide propagation (of the flow-type). The purpose of this simulation is to determine the capabilities of the inside approach, with regards to large displacement problems. The following results of the Stress-Particle SPH method are compared with the selected solutions from the literature, in addition to those computed with Standard SPH (that has been developed for this purpose). The reader is referred to Sections 4.9 and 4.10 of Chapter 4 for details on the numerical implementation of the Stress-Particle SPH and Standard SPH methods.

5.2 Shock wave in a one-dimensional bar

Dyka, Randles, and Ingel (1995) developed the one-dimensional Stress-Particle method to model the stress and velocity evolution in a solid elastic bar that is subjected to an initial tensile stress. The results of velocity, stress and displacement at a specified point in the bar over time were presented. The authors also simulated the same problem with a comparable Finite Element model (ABAQUS (Cook et al., 2001)) in order to validate the results of Stress-Particle SPH in one dimension. The profiles of velocity, stress and displacement obtained with the two different techniques were in close agreement with one another, with minimal differences. As a result, "An approach for tension instability in smoothed particle hydrodynamics (SPH)" concluded that the Stress-Particle approach provided a promising solution to the problem of the tensile instability within SPH. The problem has been recreated here with the purpose of validating the current Stress-Particle SPH model. The results are also compared with those obtained using the Standard SPH method. The problem is comprised of a solid bar of length 0.1333 m, of which one quarter is subjected to an initial velocity of -5 m/s, thereby creating a state of tensile stress. The constitutive behaviour of the material is assumed to be purely elastic, with a Young's modulus of $E = 200 \times 10^9$ Pa and density of $\rho = 7833$ kg m^{-3}. Previous authors have stated that it is not possible to model this problem with Standard SPH, due to the problem of the tensile instability (Dyka, Randles, and Ingel, 1995; Dyka, Randles, and Ingel, 1997; Blanc and Pastor, 2013).

The one-dimensional elastic bar was described with 41 SPH nodes and 82 stress-points, with an inter-particle spacing of $\Delta x = 0.0033325$ m. A time step of $\Delta t = 4 \times 10^{-7}$ s was defined, with a smoothing length equal to the node spacing. No artificial viscosity was included. All model parameters were chosen to agree with those used in the literature. For this low displacement problem, the positions of the nodes and stress-points were not updated. The evolution of the velocity at the first node in the bar is shown in Figure 5.1, for the results presented by Dyka, Randles, and Ingel (1995) and the current Stress-Particle and Standard SPH models. The results of the current Stress-Particle SPH model closely coincide with the results of the original Stress-Particle method. The shock wave is shown to be travelling back and forth through the bar. The Standard SPH model is incapable of capturing the propagation of the shock wave for the duration of the simulation.

Dyka, Randles, and Ingel (1997) analysed the one-dimensional bar problem further, using 81 SPH nodes with a particle spacing of $\Delta x = 0.00166625$ m and a time step of $\Delta t = 2.5 \times 10^{-7}$ s. Artificial viscosity was this time included, with parameters $\alpha_\Pi = 0.5$, $\beta_\Pi = 1$ and a speed of sound of $c_s = 5053.02$ m s^{-1}. This simulation has also been recreated in the current work. The time evolution of the stress (σ_{xx}) at $x = 0.035$ m (node 21) is shown in Figure 5.2, comparing the results of Stress-Particle SPH and Standard SPH with the results from the literature. The results show that both Stress-Particle SPH and Standard SPH are capable of simulating the shock

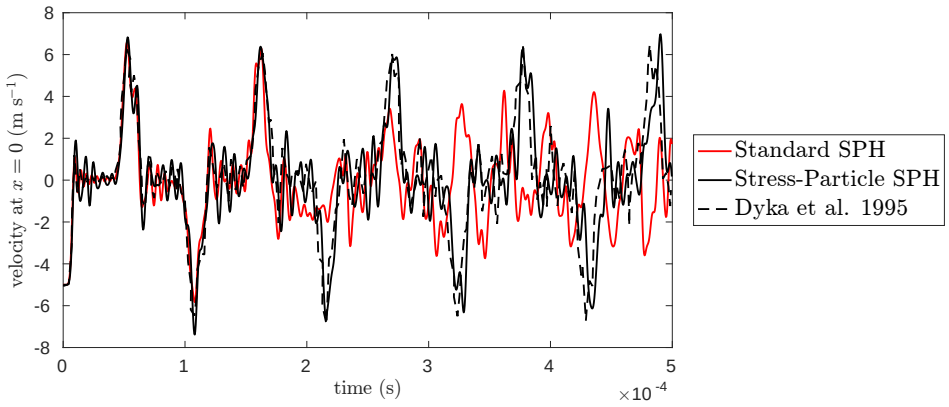

FIGURE 5.1: The velocity u_x evolution at $x = 0$ m in a one-dimensional bar subjected to a tensile stress. The Standard SPH and Stress-Particle SPH results are compared with those of Dyka, Randles, and Ingel (1995).

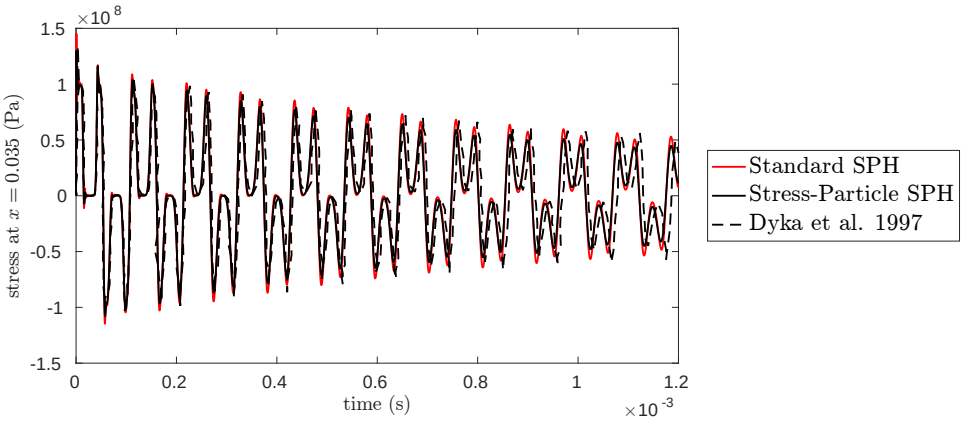

FIGURE 5.2: The stress σ_{xx} evolution at $x = 0.035$ m in a one-dimensional bar subjected to a tensile stress. The Standard SPH and Stress-Particle SPH results are compared with those of Dyka, Randles, and Ingel (1997).

wave when artificial viscosity is included. This contrasts with the claim of Dyka, Randles, and Ingel (1997) – that the addition of artificial viscosity would not enable Standard SPH to model the problem of the elastic bar under tension. In fact, for this particularly problem, artificial viscosity is sufficient to stabilise the model. However, the artificial viscosity is also responsible for the non-physical stress damping that can be seen in Figure 5.2. The results of the one-dimensional bar confirm that the Stress-Particle SPH method has been implemented correctly in one dimension.

5.3 Vertical slope

The vertical slope problem consists of an initial soil square with sides of 10 m that is allowed to deform due to the effects of gravity. This problem was simulated by Blanc (2011) and Blanc and Pastor (2013) with the Node-Element SPH method, 441 SPH nodes spaced apart by $\Delta x = 0.5$ m, and a time step of $\Delta t = 0.001$ s.

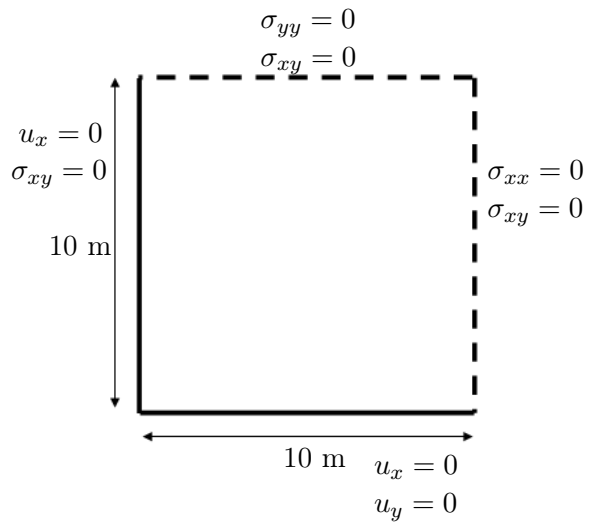

FIGURE 5.3: A schematic diagram of the vertical slope.

TABLE 5.1: Perzyna model parameters for the elastic and viscoplastic vertical slope problems.

	E (Pa)	ν	ρ (kg m^{-3})	Y_0 (Pa)	γ (s^{-1})	N
Elastic	8×10^7	0.3	2000	n/a	n/a	n/a
Viscoplastic	8×10^7	0.3	2000	2×10^5	2	1

Blanc (2011) described the material with both an elastic and a viscoplastic Perzyna model, with a Von Mises yield criterion for the latter. A damping coefficient of $\mu_d = 50$ was applied to the gravity force, in order to completely eliminate stress and velocity oscillations. Due to the relatively low displacement observed in the problem, Blanc (2011) did not update the positions of the nodes and the boundary conditions were explicitly enforced on the boundary nodes. The top and right boundaries were assigned to be stress-free and the bottom boundary had zero velocity. The horizontal velocity and shear stress were enforced to be zero on the nodes on the left boundary, to simulate a free-slip condition. A schematic diagram of the model is provided in Figure 5.3. The Stress-Particle SPH and Standard SPH methods have been used to model both the elastic and viscoplastic problems, in an attempt to recreate the results from the literature. To coincide with the literature, the positions of the nodes and stress-points were not updated and the boundary conditions were explicitly enforced on the boundary particles. The same number of SPH nodes were employed, with the same time step value. Normalisation via the CSPM was included in the stress and velocity gradient approximations, to eliminate the kernel truncation error near material boundaries. A damping factor of 50 was included in the momentum equation and artificial viscosity was not used. The material parameters for both the elastic and viscoplastic case are provided in Table 5.1.

5.3.1 Elastic slope

In addition to the damping force, Blanc (2011) progressively applied the gravity force to the elastic slope over 1 second to avoid instabilities. This progressive application has also been included in the current Stress-Particle SPH and Standard SPH simulations. The smoothing length is defined as $h_s = 0.8\Delta x$. Contours of stress and displacement after 2 seconds of simulation are provided in Figure 5.4, comparing the results from the literature with Standard SPH and the Stress-Particle inside approach. The simulations were performed with the SP1, SP2 and SP3 configurations, with the SPH-CSPM interpolation method to transfer the required information between the nodes and stress-points. The vertical stress profile provided by Blanc (2011) exhibits the expected behaviour of an increase in compressive stress with sample depth. The profile is disturbed in the region close to the right boundary due to the interaction between the stress-free nodes and the no-slip bottom layer. The horizontal stresses are negative in the bottom left corner and increase towards a positive value at the top of the sample, due to the gradual horizontal movement under the effects of gravity. The total displacement is largest at the top of the sample, and smoothly decreases to a value of zero at the bottom, where the SPH nodes have an imposed zero velocity. This general behaviour is captured with both Stress-Particle SPH and Standard SPH. With regards to the Stress-Particle method, the SP2 and SP3 results show some differences to the literature in the areas close to the boundaries. Namely, there is a small discontinuity at the left boundary in the stress profiles, which is not present in the SP1 or the literature results. Furthermore, the SP3 results show extra discontinuities in the vertical stress profile at the bottom boundary. As the stress-points lie closer to the boundaries in the SP2 and SP3 set-ups than in SP1, it is suggested that the close proximity of stress-points to the boundaries contributes to these discrepancies. The Standard SPH results suffer from severe singularities in stress and displacement which has caused noisy variable profiles with reduced accuracy. These singularities are typical manifestations of the zero-energy modes, and have been completely eliminated with the Stress-Particle method with the SP2 and SP3 configurations. While the singularities are not observed in the stress profiles of the SP1 method, the contours of displacement show some small oscillations. This indicates that the zero-energy modes were not completely eliminated with the SP1 set-up. The simulation was repeated for Standard SPH with the inclusion of artificial viscosity, with parameters $\alpha_\Pi = 1$, $\beta_\Pi = 0$. As can be observed in Figure 5.5, the addition of artificial viscosity is not able to eliminate the instability causing the noisy stress and displacement profiles.

Figure 5.6 shows the vertical stress profiles computed with SP3 with the SPH-CSPM interpolation method, compared against the SPH-Average and SPH-MLS methods. As evident from Figure 5.6, the choice of the interpolation technique has little effect on the elastic slope problem results.

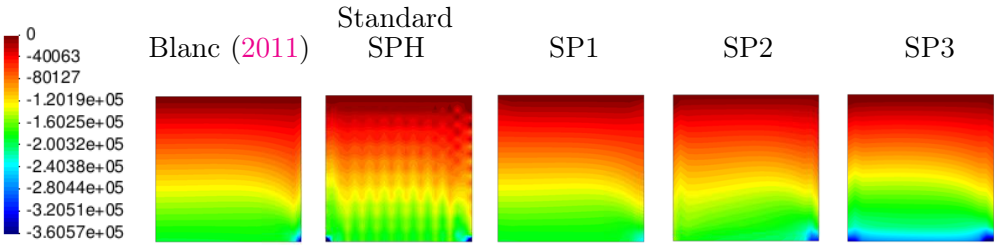

(A) Vertical stress σ_{yy} (Pa)

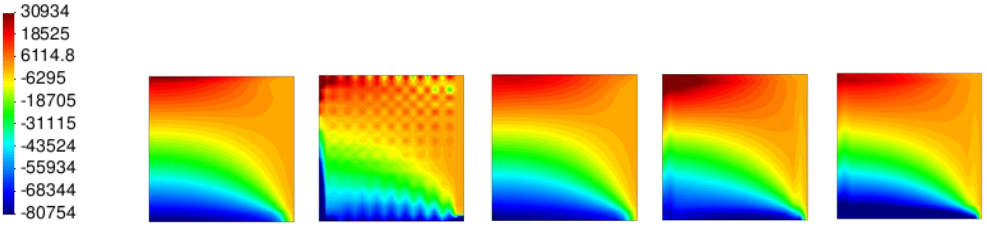

(B) Horizontal stress σ_{xx} (Pa)

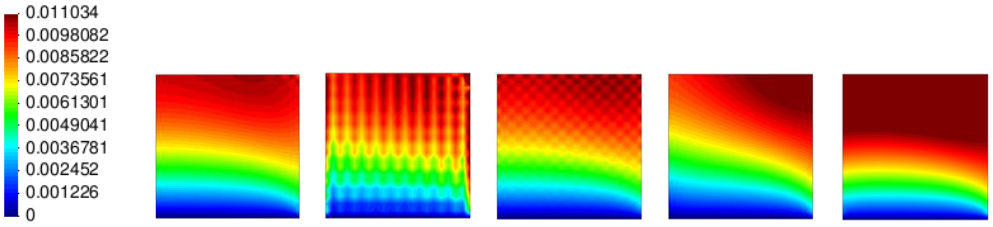

(C) Total displacement $|s| = \sqrt{s_x^2 + s_y^2}$ (m)

FIGURE 5.4: Contours of stress and velocity in the elastic slope at $t = 2$ s, comparing the Standard SPH and Stress-Particle SPH results with those of Blanc (2011).

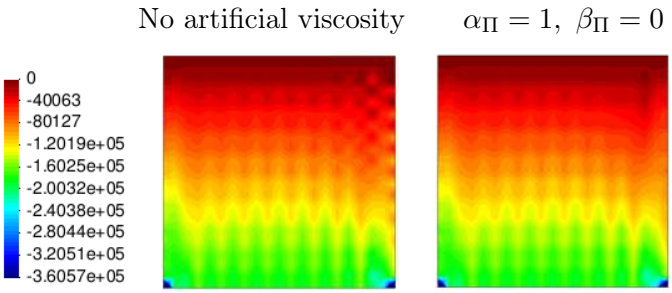

(A) Vertical stress σ_{yy} (Pa)

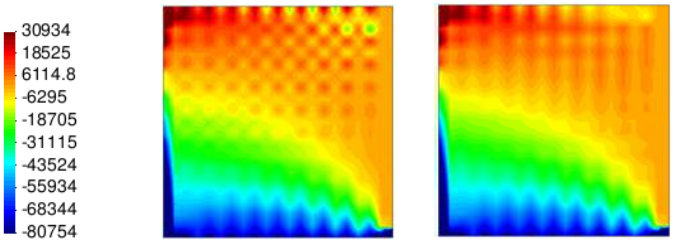

(B) Horizontal stress σ_{xx} (Pa)

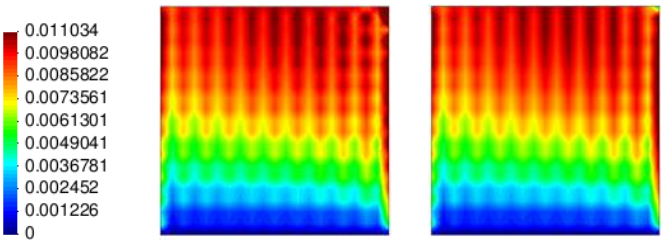

(C) Total displacement $|s| = \sqrt{s_x^2 + s_y^2}$

FIGURE 5.5: A comparison of the stress and displacement profiles at $t = 2$ s for the elastic slope problem for Standard SPH, with and without artificial viscosity.

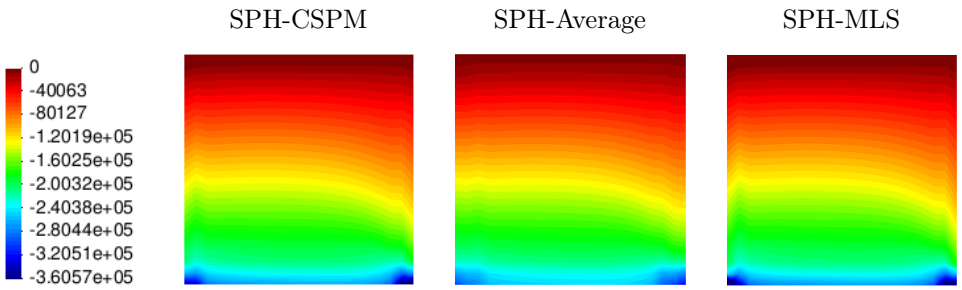

FIGURE 5.6: Profiles of vertical stress σ_{yy} (Pa) for the elastic slope problem at $t = 2$ s for Stress-Particle SP3, comparing the results from different node-stress-point interpolation methods.

5.3.2 Viscoplastic slope

The vertical slope is more representative of actual slope failure mechanisms when the material is modelled as viscoplastic, which undergoes irreversible deformations in the form of plastic strains. Blanc (2011) and Blanc and Pastor (2013) modelled the behaviour of the viscoplastic slope with a Von Mises yield surface, and reduced the shear strength of the material with time. All other material properties were the same as for the elastic slope. The size of the yield surface Y was defined to decrease as

$$Y = (1 - 0.1t)Y_0. \tag{5.1}$$

With this enforced yield strength reduction, it is possible to calculate the factor of stability (FoS) of the slope, which for a Von Mises material is defined as

$$\text{FoS} = \frac{Y_{failure}}{\sqrt{3}\rho g H}, \tag{5.2}$$

where $Y_{failure}$ is the value of the yield function at failure and H is the height of the slope (Chen, 2013). Viscoplastic (or plastic) strains first originated in the bottom right corner of the slope due to the interaction between the lower and stress-free side boundary, which localised in the form of a shear band. Material failure was assumed to have occurred when the viscoplastic strains reached the top left of the sample (at $\mathbf{x} = (1, 10)$). Blanc (2011) calculated the FoS as 0.26, which is close to the analytical solution of 0.25 provided by Taylor (1937). As opposed to the problem of the elastic slope, the gravity force was applied in full at the beginning of the simulation.

The problem has been simulated with Standard SPH, SP1, SP2 and SP3. Results of deviatoric plastic strain and total displacement are plotted against time in Figure 5.7, for the nodes positioned at $\mathbf{x} = (1, 10)$ and $\mathbf{x} = (9.5, 9.5)$ respectively. As the choice of interpolation method did not significantly affect the stress results for the elastic slope, only the SPH-CSPM technique has been used for the viscoplastic problem. The results are plotted alongside those provided by Blanc (2011) and Blanc and Pastor (2013). In each case, two different smoothing lengths of $h_s = 0.8\Delta x$ and $h_s = \Delta x$ were used and a time step of $\Delta t = 0.0001$ s was required for model stability. The results were found to be suitably independent of this time step when it was decreased. For all configurations of Stress-Particle SPH, the plastic strains reach the top left node at approximately the same time as for the Node-Element model, resulting in a similar factor of safety to that calculated by Blanc (2011). However the behaviour of the viscoplastic strain evolution after failure is strongly dependent on the smoothing length. When calculated with SP1, the magnitude of the plastic strain increases at a much lower rate than for the Node-Element method (Figure 5.7b). With regards to SP2 and SP3, the growth rate of the irreversible strain is comparable to that of the Node-Element model with a smoothing length of $h_s = \Delta x$. When a smoothing length of $h_s = 0.8\Delta x$ is used, the solution becomes rapidly unstable once failure has occurred for SP2, but results in the smallest growth rate of plastic strain

for SP3. Both the magnitude and behaviour of the displacement calculated with SP1 and SP3 are similar to the Node-Element results. The displacement calculated with SP2 exhibits a higher rate than the literature results. The Standard SPH model results differ from the others in that the viscoplastic strains reach the node at $\mathbf{x} = (1, 10)$ at an earlier time, producing a FoS value that is different to that obtained by Blanc and Pastor (2013). Additionally the rate of increase of this quantity varies sporadically, due to the instabilities caused by the zero-energy modes.

The same problem was repeated with the SP1 method, with the addition of extra stress-points on the material boundaries, as depicted in Figure 5.8a. With these extra stress-points, the SP1 method was able to closely recreate the Blanc and Pastor (2013) results with a smoothing length of $h_s = 0.8\Delta x$. The evolution of the viscoplastic strain and displacement at $\mathbf{x} = (1, 10)$ and $\mathbf{x} = (9.5, 9.5)$ are shown in Figure 5.8b. This highlights that accurate results are dependent on there being a sufficient number of stress-points in the neighbourhood of each SPH node. This is particularly relevant for nodes at the boundaries, which have a reduced neighbourhood than for interior nodes.

5.4 Strain localisation in a soil sample with strain softening

The Stress-Particle SPH inside approach has been applied to model the strain localisation in a two-dimensional soil sample with the viscoplastic Perzyna model. The material was described with a Von Mises yield criterion that varied according to the softening law defined by Equation (3.27) (see Section 3.3.1), for the material parameters provided in Table 5.2. Half of a square sample with a 1 m side was considered, where a symmetry condition was assigned to the left boundary as shown in Figure 5.9. A tensile force was applied by imposing a vertical velocity on the upper boundary. This created a shock wave that travelled through the sample and produced irreversible deformations, which localised as a shear band. The same problem was also considered by Mabssout and Herreros (2013) with the Node-Element SPH method, although in a plane stress condition. The shear band evolution presented by Mabssout and Herreros (2013) is shown in Figure 5.10, which propagated at an inclination angle of 35°. This agrees with the theoretical solution for the inclination angle in a material with a Von Mises yield function in plane stress conditions (Sluys, 1992). In the current application a plane strain condition is considered, for which the theoretical angle is calculated to be 45°.

The soil sample is instantly subjected to a tensile state of stress, which makes the SPH model highly susceptible to the tensile instability. Within the Node-Element SPH model, Mabssout and Herreros (2013) employed a Lagrangian kernel to ensure that the tensile instability was eliminated. Here the Stress-Particle SPH method has been applied to solve the problem and reduce any numerical instabilities. The boundary conditions shown in Figure 5.9 were applied directly to the SPH nodes that

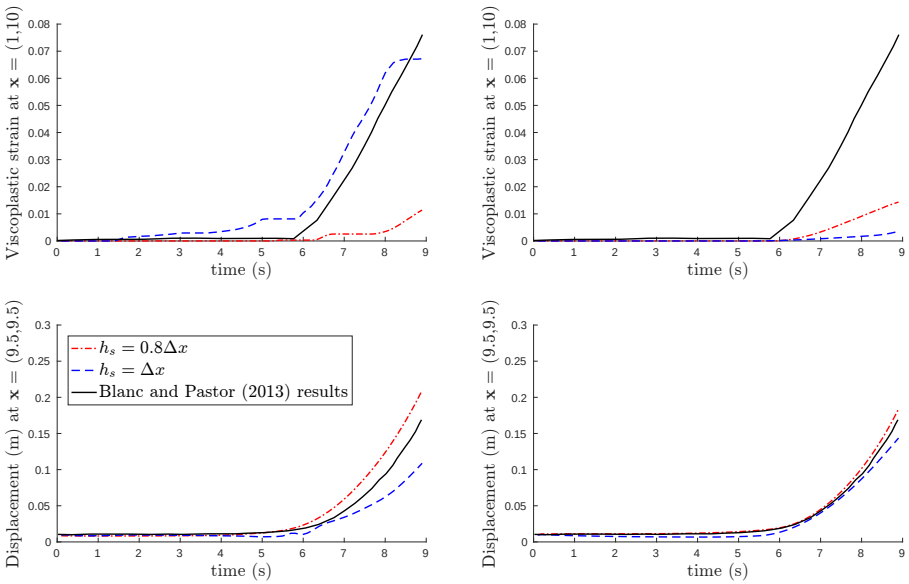

(A) Standard SPH (B) SP1

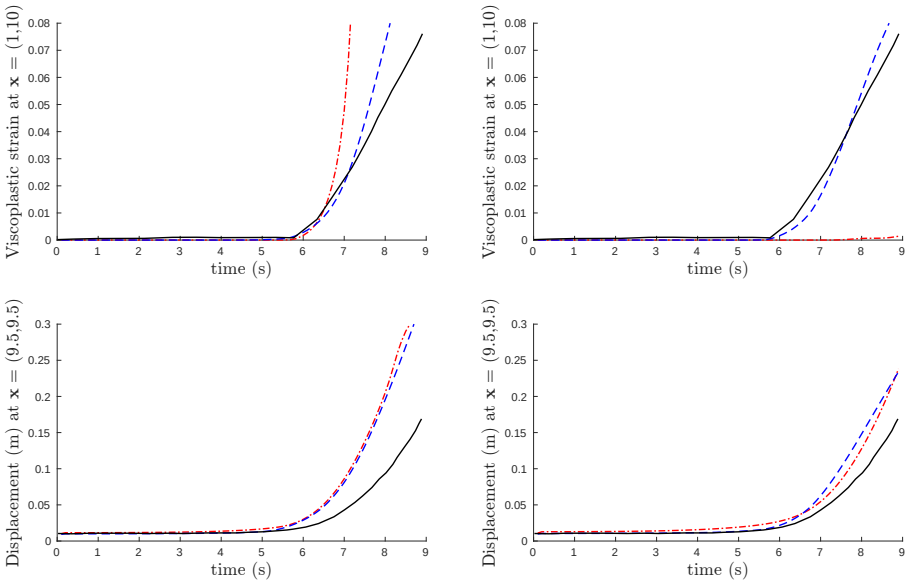

(C) SP2 (D) SP3

FIGURE 5.7: A comparison of the evolution of deviatoric plastic strain $\bar{\epsilon}^p$ (dimensionless) and total displacement $|s|$ (m) between the current Stress-Particle SPH model, a Standard SPH model, and the results presented by Blanc and Pastor (2013), for the viscoplastic vertical slope failure

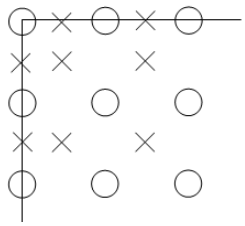

(A) A depiction of Stress-Particle SP1, with extra boundary stress-points

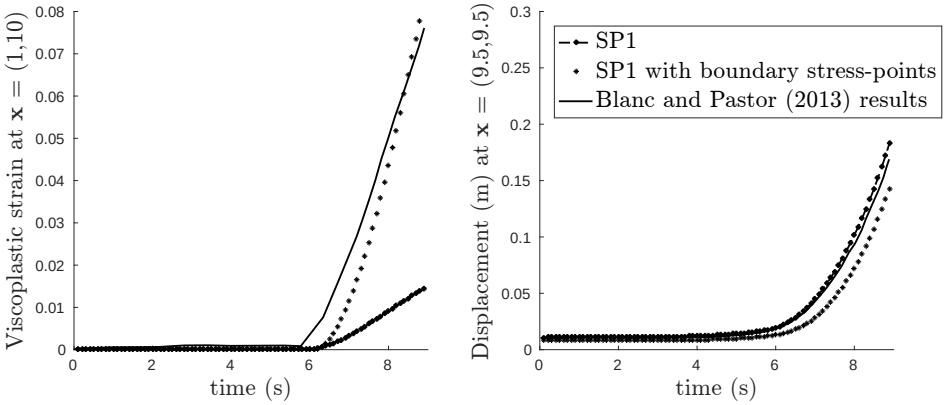

(B) Deviatoric viscoplastic strain and displacement against time

FIGURE 5.8: The deviatoric plastic strain $\bar{\epsilon}^p$ (dimensionless) and total displacement $|s|$ (m) evolution in the viscoplastic slope, calculated with SP1 with and without extra boundary stress-points (as highlighted in the figure legend), compared against the results of Blanc and Pastor (2013).

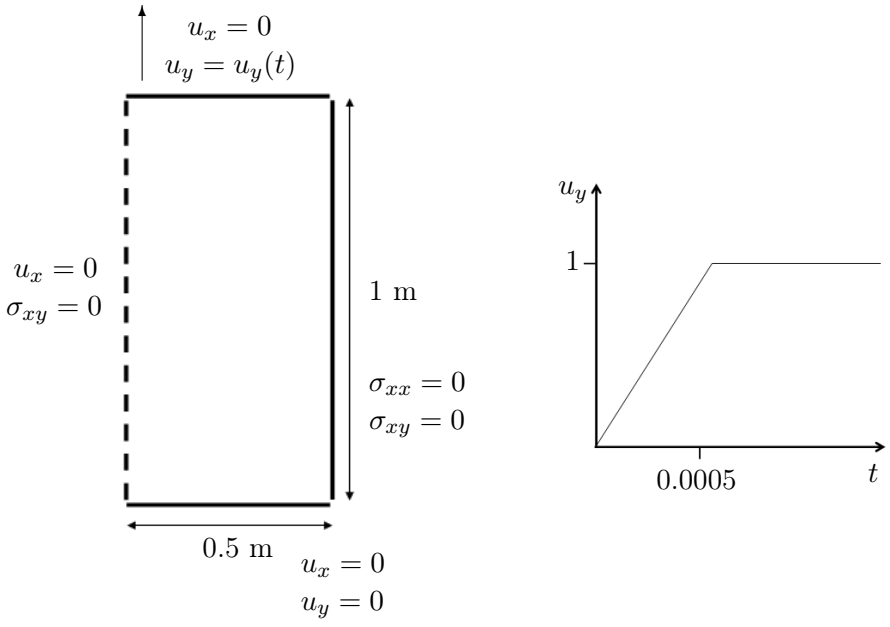

FIGURE 5.9: A schematic diagram of the strain localisation problem.

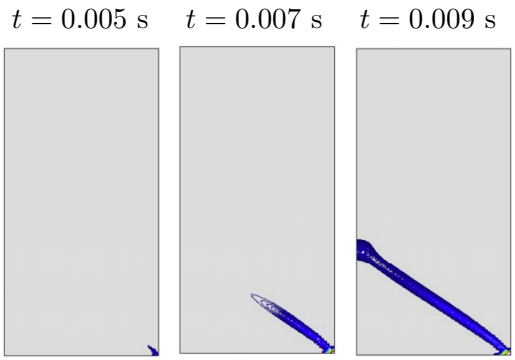

FIGURE 5.10: The strain localisation in the soil sample presented by Mabssout and Herreros (2013).

TABLE 5.2: Perzyna model parameters for the strain localisation problem.

E (Pa)	ρ (kg m^{-3})	Y_0 (Pa)	H (Pa)	γ (s $^{-1}$)	N
8 $\times 10^7$	2000	5 $\times 10^5$	-8 $\times 10^6$	50	1

lay on the boundaries, and the CSPM was employed to reduce the error in this area. The chosen time step was $\Delta t = 1 \times 10^{-5}$ s, with 3321 particles spaced $\Delta x = 0.0125$ m apart. No artificial viscosity was included in the literature or in the Stress-Particle SPH model implemented here. The results are also compared with those obtained with the Standard SPH model, both with and without artificial viscosity.

The first appearance of localised viscoplastic strains in the soil sample and the subsequent evolution as a shear band is provided in Figure 5.11 for Stress-Particle SPH and Standard SPH. The SPH-CSPM method was used to interpolate the variables onto the nodes and stress-points. To align with the method outlined in the literature the positions of the nodes and stress-points have initially not been updated. The smoothing length was chosen to be equal to the particle spacing. Viscoplastic strains first occurred in the bottom right corner as the shock wave created by the imposed velocity reached the lower boundary, and spread according to the material softening law. The shear band propagation has been captured in all cases, although there is extra diffusion exhibited by both the Stress-Particle and Standard SPH results than with those presented by Mabssout and Herreros (2013). Contours of localised deviatoric plastic strain, stress and vertical velocity are provided in Figure 5.12 after 0.02 seconds of simulation time. As seen in the results of the vertical slope problem analysed in Section 5.3, the stress and velocity of Standard SPH show singularities that have contributed to noisy profiles of stress, velocity and plastic strain. This is particularly evident at the right boundary of the soil sample where the Standard SPH results show excessive plastic strain, in an area where there should not be any. The noisy stress profiles have been smoothed considerably with all configurations of the Stress-Particle method, and the shear band at $t = 0.02$ s is well-defined. Although the singularities in the velocity profiles have not been completely eliminated, they have been significantly reduced, with the SP3 profile showing the most

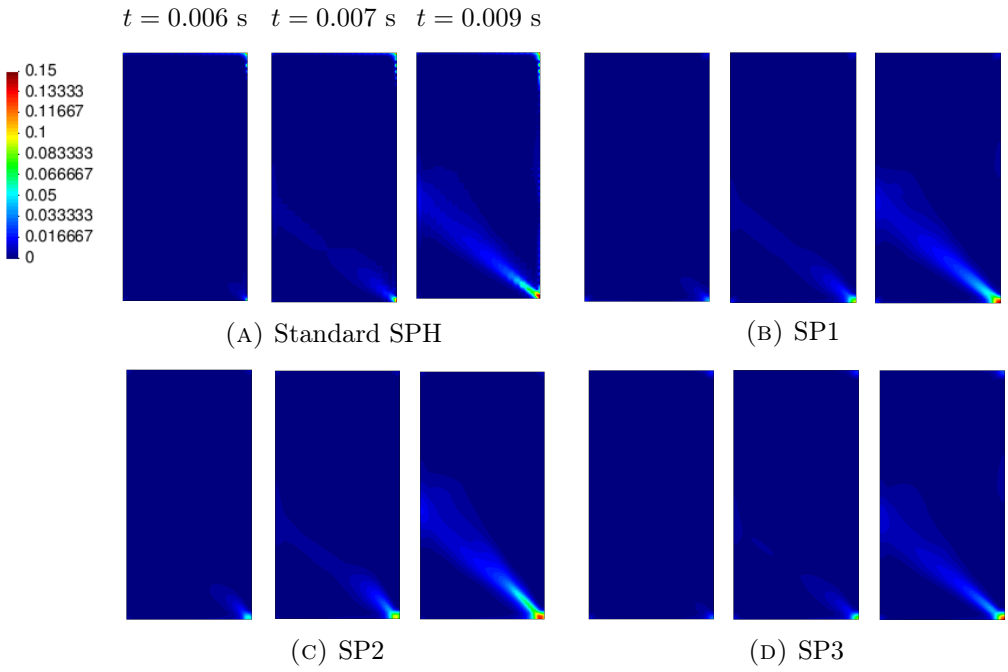

FIGURE 5.11: The evolution of deviatoric plastic strain $\bar{\epsilon}^p$ (dimensionless) in the soil sample, computed with the Stress-Particle SPH inside approach and Standard SPH.

reduction. While the overall profile of deviatoric plastic strain is smooth for the SP2 results, there is a discontinuity in the lower half of the sample where the shear band divides into two.

The results in Figure 5.12 show a second, upper shear band that formed due to the interaction of the velocity wave with the upper boundary. The theoretical solution predicts the two shear bands to meet exactly half way along the left boundary as this coincides with an inclination angle of 45° (Sluys, 1992). The SP1 and Standard SPH profiles show shear band inclinations of approximately 45°, while the shear bands calculated with SP2 and SP3 exhibit inclination angles that are visibly different to this. A similar sensitivity to the numerical discretisation configuration is found in FEM simulations of shear band formation in softening soils. Sluys (1992) showed that it was essential to align the diagonals of the triangular elements in FEM to the theoretical shear band inclination angle, in order to predict it. To explore this further, additional node-stress-point geometries have been considered. The SP2 configuration can be visualised in Figure 5.13a, where the nodes and stress-points form a pattern that contains lines aligned in different directions at different angles. When the stress-point positions are horizontally reflected, so are the lines created by the node-stress-point geometry. Combining the two configurations so that there are 4 stress-points positioned in between every 4 connected nodes (denoted as SP4), forms a pattern where the lines are horizontally symmetric. These geometric configurations are displayed in Figure 5.13a, with the respective shear band profiles at $t = 0.02$ s presented in Figure 5.13b. For the reflected SP2 configuration, the discontinuity in the lower shear band is reduced and the inclination angles of the upper and

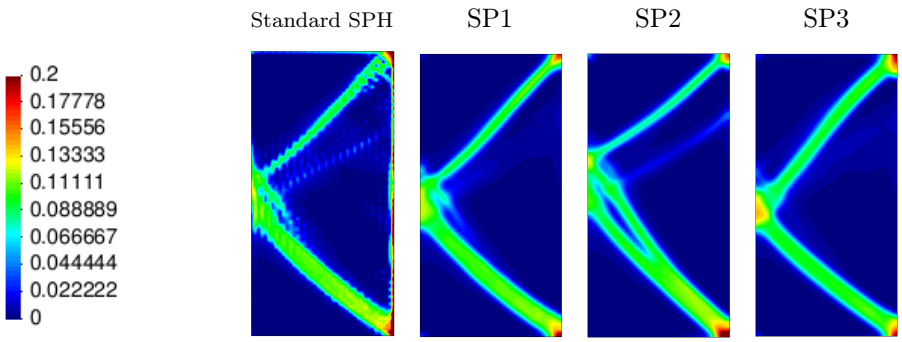

(A) Deviatoric plastic strain $\bar{\epsilon}^p$ (dimensionless)

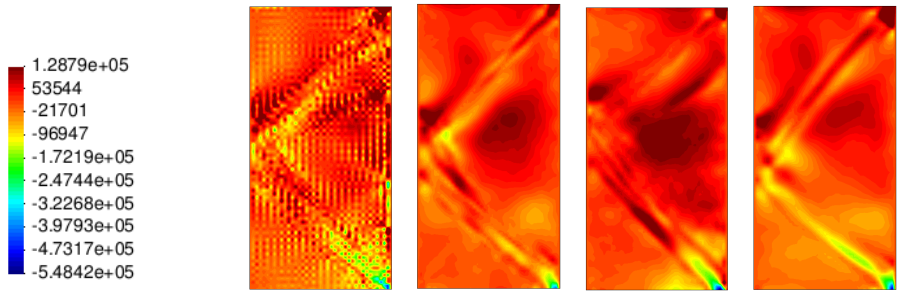

(B) Shear stress σ_{xy} (Pa)

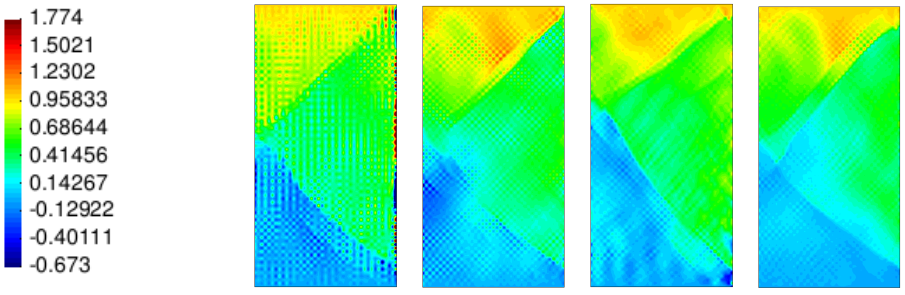

(C) Vertical velocity u_y (Pa)

FIGURE 5.12: A comparison of deviatoric plastic strain, stress and velocity profiles for the strain localisation problem at $t = 0.02$ s, for Standard SPH, SP1, SP2 and SP3. The node and stress-point positions were not updated.

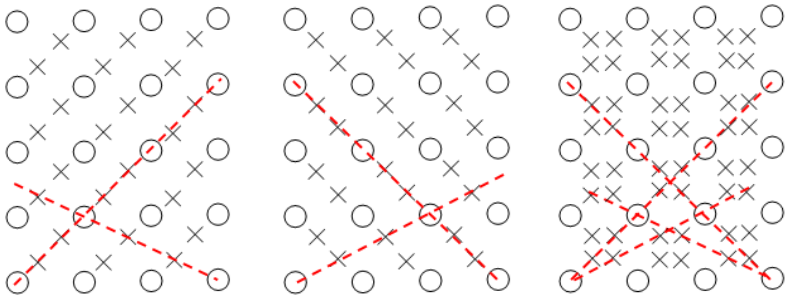

(A) Alternative node-stress-point configurations (SP2, a horizontal reflection of SP2, SP4)

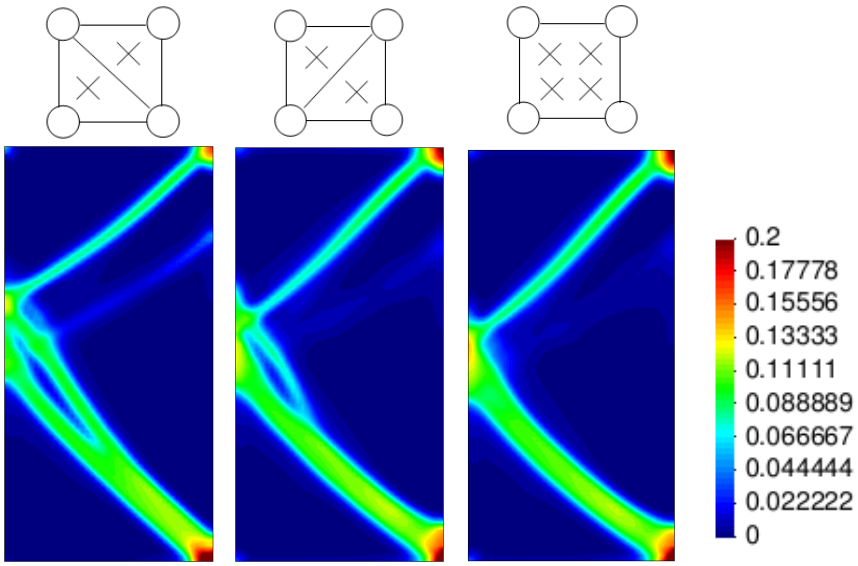

(B) Localised deviatoric plastic strain $\bar{\epsilon}^p$ (dimensionless), for alternative configurations of the inside approach

FIGURE 5.13: The dependency of the shear band profile on the node-stress-point configuration, in the strain localisation problem.

lower shear bands are different to the shear band predicted with SP2. The results computed with 4 stress-points inside every 4 nodes exhibit smooth lower and upper shear bands that meet half way along the sample. Note that the SP4 configuration contains lines that are aligned with both the lower and upper shear bands. These results highlight that the mesh sensitivity found in FEM shear band predictions is also relevant in Stress-Particle SPH.

Next, the positions of the nodes and stress-points were updated according to Equation (4.113) (see Section 4.6). These results are provided in Figure 5.14 for Standard SPH, SP1, SP2 and SP3. In this case the smoothing length was defined as $h_s = 1.2\Delta x$, while the other conditions were the same as described above. With the position update, all three configurations of the Stress-Particle inside approach display smooth stress profiles and well-defined shear bands at $t = 0.02$ s. Particularly, the discontinuities observed in the SP2 results when the particle positions were not updated are no longer present. This suggests that the particle position update adds stability to Stress-Particle SPH. A possible explanation for this is related to the result dependency on the alignment of the nodes and stress-points discussed above.

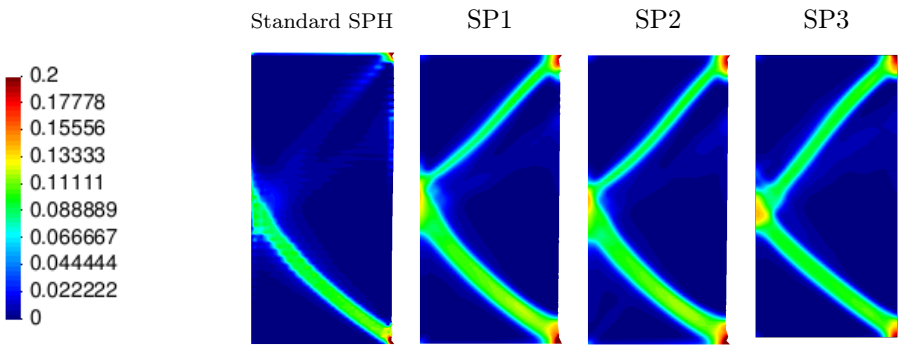

(A) Deviatoric plastic strain $\bar{\epsilon}^p$ (dimensionless)

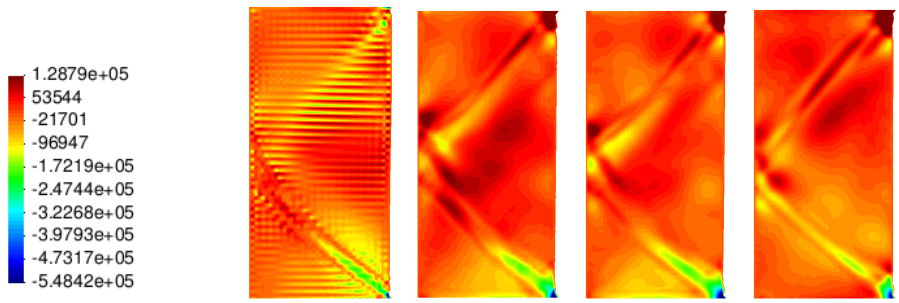

(B) Shear stress σ_{xy} (Pa)

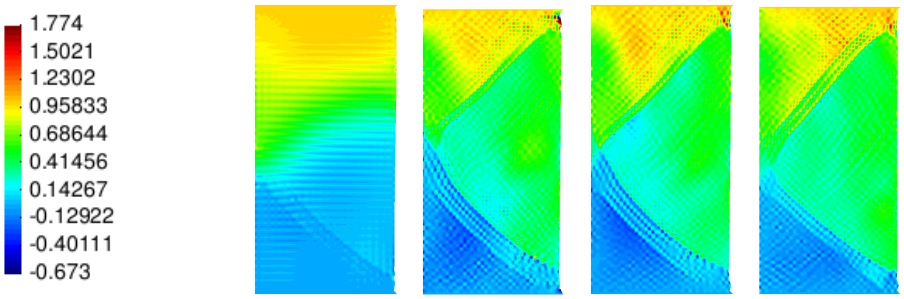

(C) Vertical velocity u_y (Pa)

FIGURE 5.14: A comparison of deviatoric plastic strain, stress and velocity profiles for the strain localisation problem at t = 0.02 s, for Standard SPH (with artificial viscosity), SP1, SP2 and SP3 (with no artificial viscosity). The node and stress-point positions were updated.

As the shear band represents the area where most deformation has occurred, the particle displacement is highest in this area. When the nodes and stress-points are allowed to move, they naturally align themselves in the direction of the propagating region of localised strain.

While the particle position update improved the Stress-Particle SPH results, the opposite effect was observed for the Standard SPH method. For this case the simulation became rapidly unstable, even with a decrease in time step. In order to obtain a solution, it was necessary to include artificial viscosity with parameters $\alpha_\Pi = \beta_\Pi = 1$ (with a speed of sound of $c_s = \sqrt{E/\rho} = 200$ m s^{-1}). These results are shown in Figure 5.14, where the stress and velocity oscillations have been reduced and the lower half of the shear band propagation has been captured. However, the profiles exhibit signs of excessive, artificial shear strength, which is indicated by

the horizontal stripes in the contour plots. It was first identified by Swegle et al. (1994) in the simulation of two impacting metal plates that the artificial viscosity can produce effects of artificial shear strength. The artificial viscosity acts to ensure particles do not fluctuate relative to one another. Swegle et al. (1994) discovered that this inhibition of relative particle motion caused the SPH particles to form ordered chains, which provided the metal plates with extra, unrealistic strength. In addition to the visible chain structures in the Standard SPH profiles in Figure 5.14, the fact that the viscoplastic strains have not formed a defined shear band throughout the top of the sample also indicates that the artificial viscosity has given the material an excessive, non-physical strength.

The strain localisation problem was also simulated with the SPH-Average and the SPH-MLS interpolation methods, for the SP1 configuration. These results are shown in Figure 5.15. It can be seen that there is little difference between the three interpolation techniques. The SPH-CSPM method is employed to transfer information between the nodes and stress-points in all subsequent simulations in the remainder of this research.

The strain localisation problem was repeated with the same geometry as depicted in Figure 5.9. Instead of a symmetry condition, the left boundary was assigned to be a free surface in the same way as for the right boundary. Additionally, the vertical velocity on the upper boundary was decreased to zero after $t = 0.02$ s. The positions of the nodes and stress-points were updated. Shear band profiles at $t = 0.035$ s are shown in Figure 5.16 for Stress-Particle SPH with the SPH-CSPM interpolation method. The SP1, SP2 and SP3 results are provided in Figures 5.16a, 5.16b and 5.16c respectively, where two shear bands have originated from the bottom corners and spread diagonally across the sample. An inclination angle of 45° is shown via the dashed line, where only the SP1 results have produced shear bands with this angle. Those calculated with SP3 have a lower inclination angle, while the two shear bands in the SP2 results have inclined at different angles to one another. This unexpected anti-symmetry can be attributed to the node-stress-point configuration in the SP2 method. Figure 5.16d shows the solution when the stress-points were reflected horizontally, where the inclination angles of the two lower shear bands are opposite to those calculated with SP2. The shear band profile obtained with the SP4 configuration is provided in Figure 5.16e. With the SP4 set up, the lower shear bands have propagated at the same angle, which is lower than the theoretical solution of 45°. Additionally, the bands are thicker than those computed with the SP1 set-up. These results support the findings that the shear band evolution is dependent upon the stress-point arrangement, and show that a symmetry amongst the stress-points is desirable. They also suggest that while more stress-points equates to higher stability, this may reduce solution accuracy. This idea is investigated with further examples in the following sections.

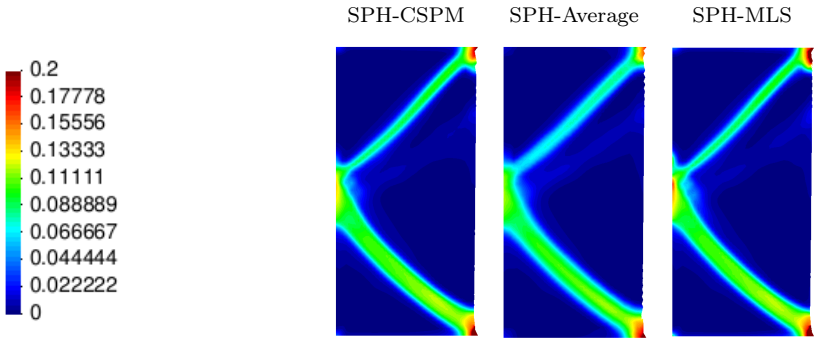

(A) Deviatoric plastic strain $\bar{\epsilon}^p$ (dimensionless)

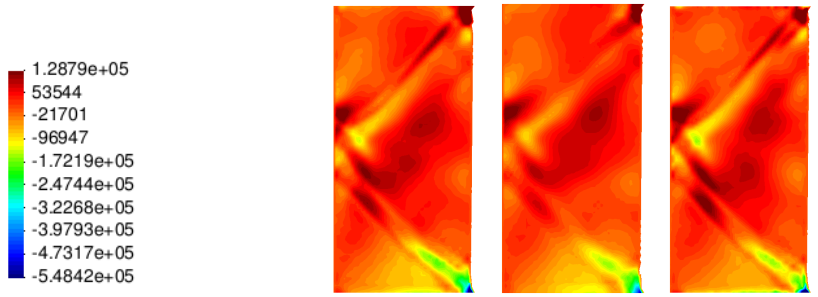

(B) Shear stress σ_{xy} (Pa)

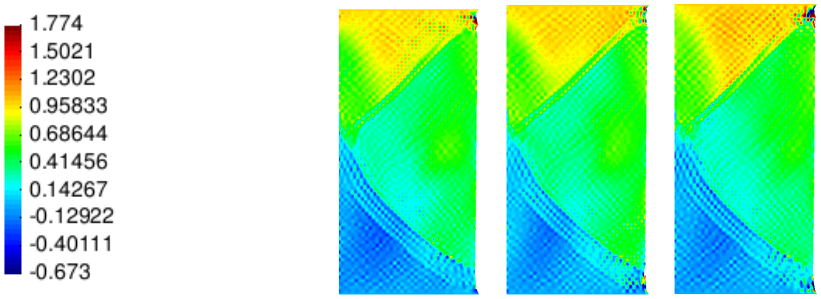

(C) Vertical velocity u_y (Pa)

FIGURE 5.15: Deviatoric plastic strain, stress and velocity profiles at $t = 0.02$ s in the strain localisation problem. Results were calculated with Stress-Particle SPH with configuration SP1, comparing three different node-stress-point interpolation methods. The node and stress-point positions were updated.

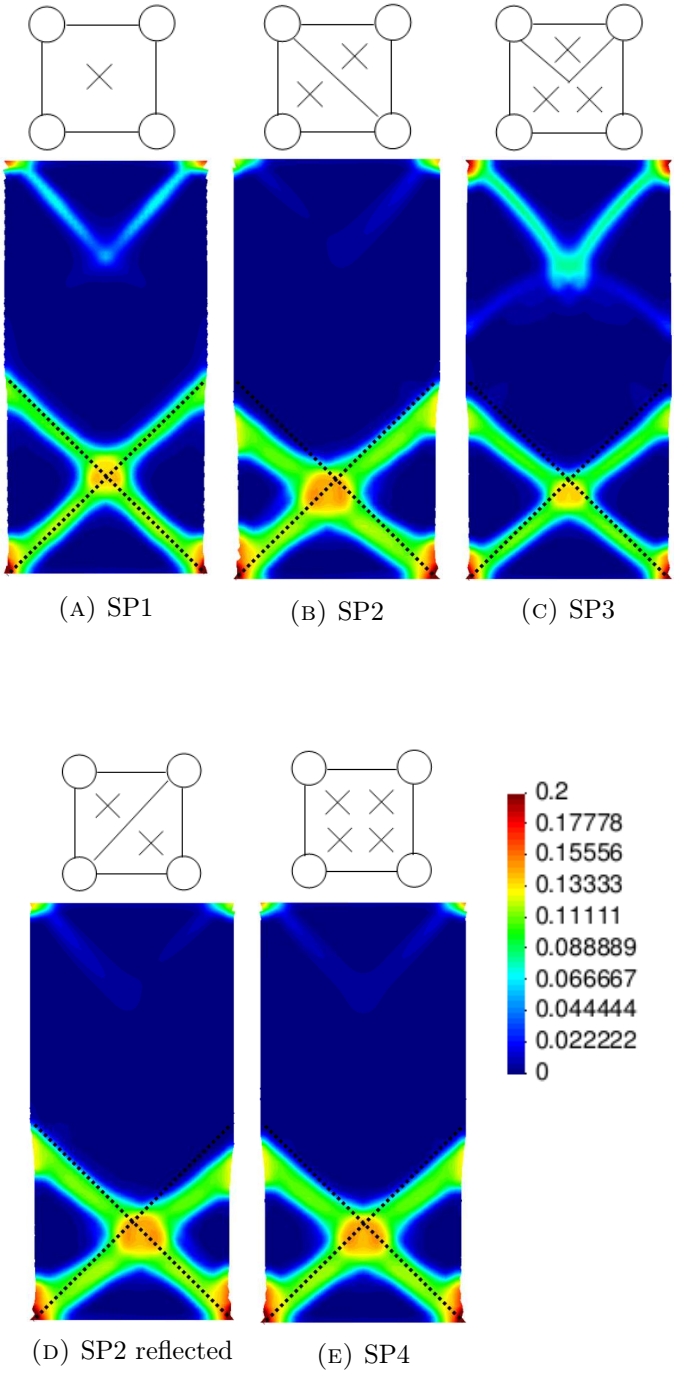

(A) SP1 (B) SP2 (C) SP3

(D) SP2 reflected (E) SP4

FIGURE 5.16: Profiles of deviatoric plastic strain $\bar{\epsilon}^p$ (dimensionless) at $t = 0.035$ s in the triaxial test simulation, comparing the results from different node-stress-point configurations. The imposed dashed line represents an inclination angle of 45°.

TABLE 5.3: Drucker-Prager material parameters for the cohesive and non-cohesive soil failure.

	E (Pa)	ρ (kg m^{-3})	c_{oh} (Pa)	ϕ (°)
Cohesive soil	1.8 $\times 10^6$	1850	5000	25
Non-cohesive soil	1.8 $\times 10^6$	1850	0	25

5.5 Soil failure

In this section the soil failure problem introduced by Bui et al. (2008) is recreated. The problem consists of a perfectly plastic Drucker-Prager material that is allowed to collapse and deform under the effects of gravity. The material has an initial rectangular area of 4 m in length and 2 m in height and is constrained by no-slip walls behind the left and bottom boundaries, which were created using dummy nodes. The problem was described with a non-associated flow rule and both a cohesive and a non-cohesive soil were considered, which were modelled by Bui et al. (2008) using SPH. The material parameters for both cases are provided in Table 5.3. When cohesion was included the material exhibited severe non-physical fractures due to the tensile instability unless a stabilisation technique was employed. To improve the simulation, the artificial repulsive force proposed by Monaghan (2000) was included (described in Section 4.5.3), with a tuning parameter of $\epsilon = 0.5$, The results of the cohesive soil failure provided by Bui et al. (2008) are shown in Figure 5.17a. With regards to the non-cohesive soil, no effects of the tensile instability were observed and no artificial repulsive force was included in the SPH model. The non-cohesive material behaviour was purely frictional and it propagated further than when cohesive strength was added, exhibiting fluid-like behaviour. The results of the non-cohesive soil simulation are shown in Figure 5.17b. In both the cohesive and non-cohesive cases, the material was described using 5000 SPH nodes, with an initial spacing of $\Delta x = 0.04$ m and a smoothing length of $h_s = 1.2\Delta x$. The time step was defined as $\Delta t = 1.5 \times 10^{-5}$ s to satisfy the CFL condition with a Courant number of 0.2. Bui et al. (2008) included artificial viscosity with parameters $\alpha_\Pi = \beta_\Pi = 0.1$ and a sound speed of $c = 600$ m s^{-1} (which is the maximum sound speed in soil).

The Stress-Particle method has been applied to model the soil failure problem to assess its capabilities at remedying the severe effects of the tensile instability in the case of the cohesive material. Furthermore the simulation of the non-cohesive material provides a test of how Stress-Particle SPH can simulate flow-type problems involving rapid propagation and large displacements, for which the method has not previously been applied to. The same problems have also been modelled using Standard SPH to compare against the Stress-Particle method. Both the artificial stress (Monaghan, 2000) and particle shifting methods (Xu and Yu, 2018) are implemented within Standard SPH to eliminate the tensile instability in the cohesive soil. The majority of the input parameters used by Bui et al. (2008) were employed in the current application, in order to attempt to recreate the literature results as closely as possible. The exceptions are as follows. Bui et al. (2008) used a second order

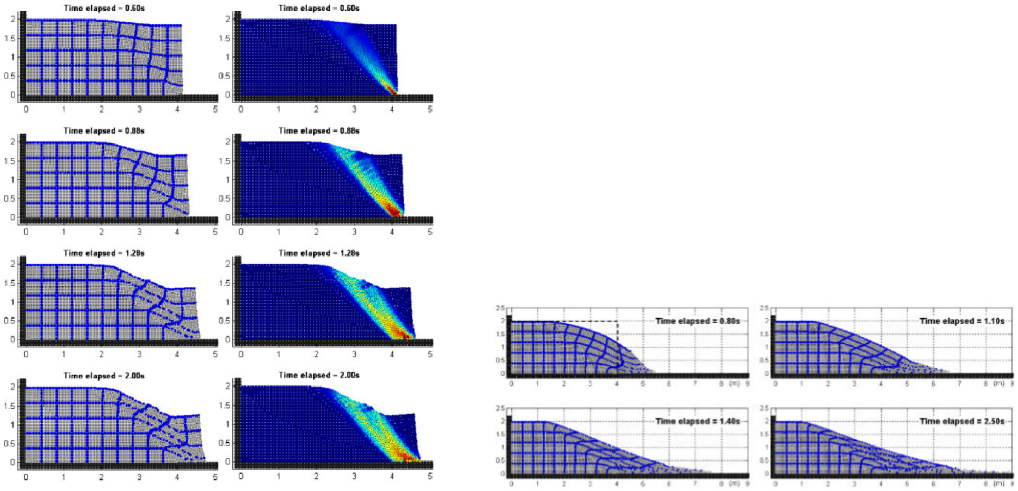

(A) Cohesive soil (B) Non-cohesive soil

FIGURE 5.17: The evolution of the cohesive and the non-cohesive soil failure, provided by Bui et al. (2008). The contours show deviatoric plastic strain (no scale is provided in the literature).

leapfrog time integration scheme, while the current SPH model utilises a fourth order Runge-Kutta scheme. Furthermore, Bui et al. (2008) updated the soil density according to the continuity equation, whereas here a constant density has been employed. However, it is shown in the next section that having a constant density has little effect on the SPH results. Lastly, for the inside approach simulations, it was essential to include repulsive particles along the wall boundary (spaced apart by a distance of $\Delta x/2$). This is to prevent the penetration of the interior nodes through the wall, as discussed in Section 4.8.6.

5.5.1 Cohesive soil

The cohesive soil failure problem has first been recreated with the Standard SPH model, along with the inclusion of the artificial stress (Monaghan, 2000) and the particle shifting method (Xu and Yu, 2018). The results are provided in Figure 5.18. To recreate the literature results, the tuning parameter in the artificial stress was chosen to be $\epsilon = 0.5$. Plastic strains first appear in the bottom right corner of the material due to the interaction between the moving nodes and the no-slip boundary. The slope progressively fails as the region of irreversible deformation localises as a shear band and propagates through the sample, forming the failure surface. Without any treatment for the tensile instability, Figure 5.18a shows that fractures are apparent in the soil at $t = 0.6$ s, which spread throughout the material with time. As also shown by Bui et al. (2008), the use of the artificial repulsive force suppresses the effects of the tensile instability, and the results provided in Figure 5.18b do not exhibit any non-physical fractures. The particle shifting method was shown by Xu and Yu (2018) to perform better than the artificial force method at removing the tensile instability in the simulation of a viscoelastic droplet impacting a

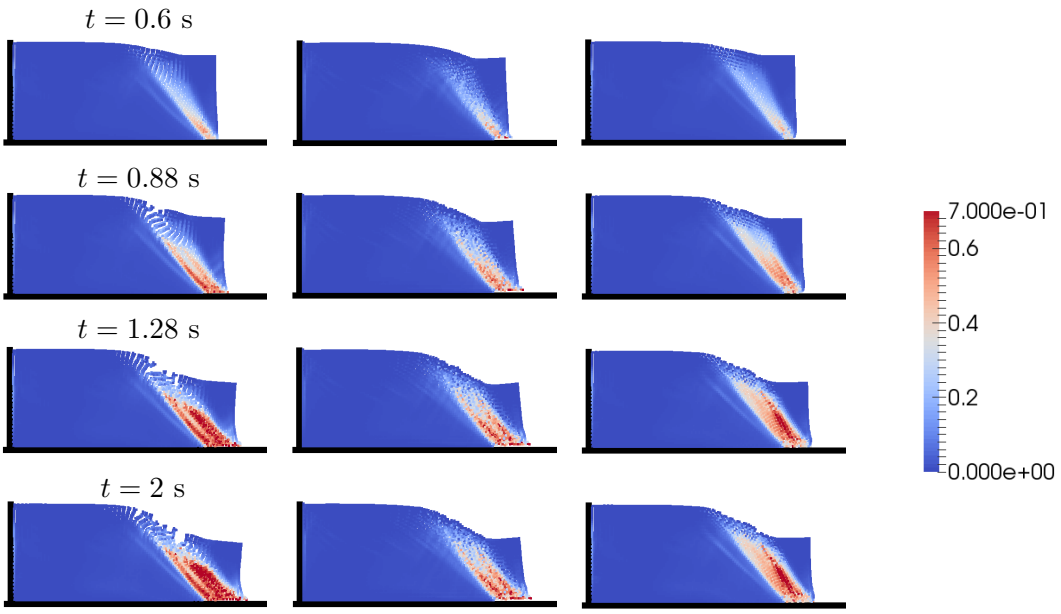

(A) Standard SPH (B) Standard SPH with artificial repulsive force (C) Standard SPH with particle shifting

FIGURE 5.18: Snapshots of the progressive failure of the cohesive soil, for Standard SPH with no treatment for the tensile instability, Standard SPH with the artificial stress (Monaghan, 2000), and Standard SPH with the particle shifting method (Xu and Yu, 2018). The material is coloured by values of deviatoric plastic strain $\bar{\epsilon}^p$ (dimensionless).

solid boundary. For the cohesive soil failure problem, the shifting method was able to eliminate the effects of the instability at interior particles, but it did not completely remove the non-physical fracturing at the free surface (see Figure 5.18c). The nodes that are in the vicinity of the free surface are shifted in a different way to the interior particles due to the large concentration gradients in that area (see Section 4.5.4). As a result, the free surface nodes that exhibit clumping and subsequent separation due to the tensile instability may not be assigned a sufficient shifting vector to prevent the clumping. However, it is evident that the results obtained with particle shifting (Figure 5.18c) exhibit smoother contours of deviatoric plastic strain than for the artificial force results (Figure 5.18b).

The free surface profiles of the cohesive soil failure obtained using Standard SPH with the artificial stress are compared against the results from the literature in Figure 5.19. Also shown are the results calculated with the artificial stress method, with the employment of the continuity equation to update the soil density. For Standard SPH with the artificial stress, the final height of the front of the material once it has stopped moving is approximately 1.321 m. This is slightly higher than the results from the literature, as shown in Figure 5.19d, which exhibit a final front height of 1.299 m. The final horizontal position of the front of the material in the literature is approximately 0.068 m greater than for the current Standard SPH results

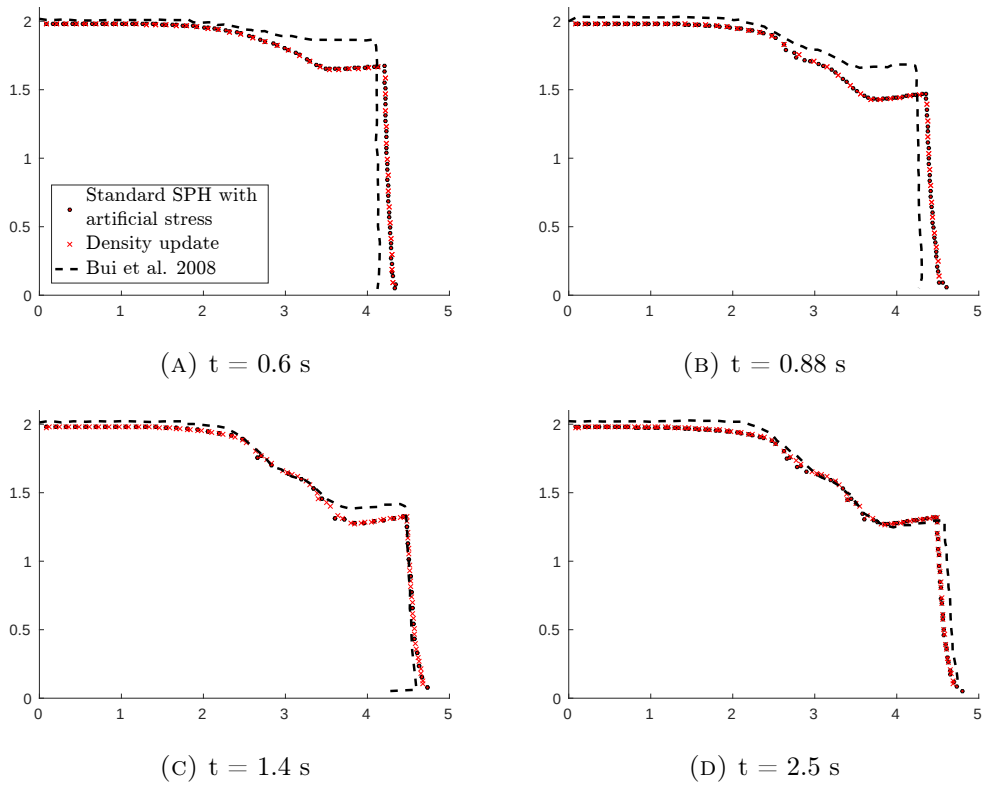

(A) t = 0.6 s (B) t = 0.88 s

(C) t = 1.4 s (D) t = 2.5 s

FIGURE 5.19: Free surface profiles for the cohesive soil problem. The markers denote the results from the current Standard SPH model, while the dashed line represents the results provided by Bui et al. (2008).

with the artificial repulsive force. Also, with the latter model the material deforms and propagates more rapidly than in the literature, which is evident in Figures 5.19a - 5.19c. In the current model, the material stopped moving at approximately $t = 1.4$ s, whereas in the literature this occurred at $t = 2$ s. It can be seen that updating the density has little effect on the material behaviour and it is therefore not responsible for the differences between the models. A possible reason for the discrepancies between the rate of the material movement is the difference in the numerical implementation of the governing equations – in the current application a fourth order accurate RK4 scheme is employed, while Bui et al. (2008) utilised a second order Leap From method. Alternatively, the literature results behave as if more numerical damping has been included than in the current model, such as the progressive application of the gravity term. However, what is most significant is that the current Standard SPH model is able to eliminate the non-physical fractures with the artificial repulsive force, and that the material profile generally aligns with the literature once it has stopped deforming. Therefore, the current Standard SPH model with the artificial stress method is used to compare the Stress-Particle SPH results against for the cohesive soil failure problem.

Snapshots of the node positions in the cohesive soil failure problem, computed with the SP2 configuration of Stress-Particle SPH, are shown in Figure 5.20a. In the

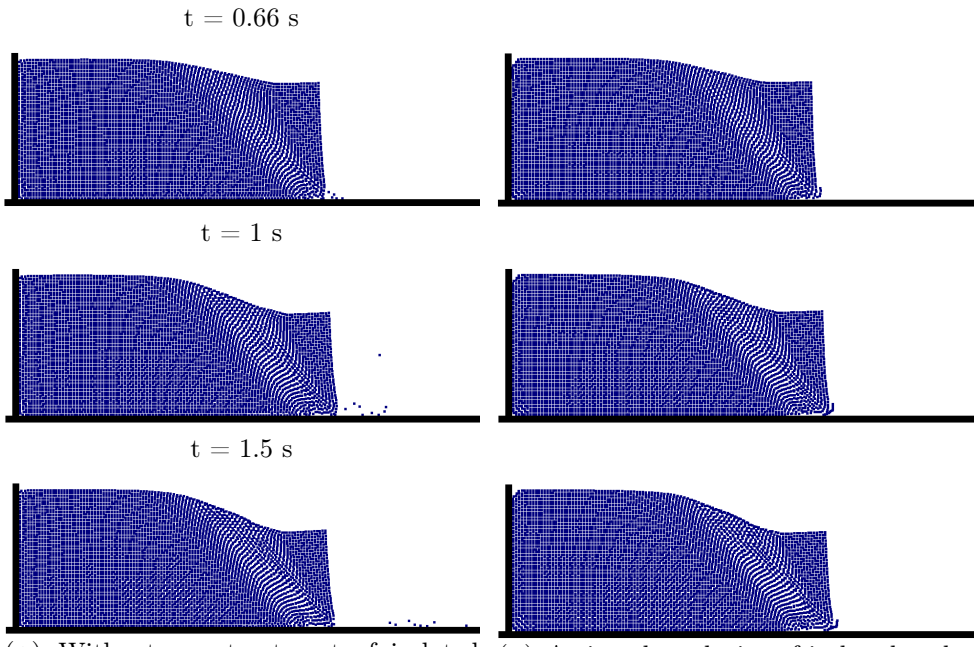

(A) Without any treatment of isolated nodes

(B) Assign the velocity of isolated nodes to be zero

FIGURE 5.20: Particle positions at different times for the cohesive soil failure, calculated with SP2. The results compare the node behaviour with and without the treatment of isolated SPH nodes – note the behaviour of the isolated nodes when no treatment is included.

same way as for Standard SPH, the material in the Stress-Particle method stopped moving at approximately $t = 1.4$ s. There are no fractures in the material due to the tensile instability. However, the nodes exhibit peculiar behaviour at the very front of the deforming soil, in the region next to the wall boundary. At $t = 0.66$ s, the nodes in this area have detached from the rest of the material. This is possibly an effect of the boundary repulsive force, which is required in the inside approach to prevent the penetration of SPH nodes through the boundary. Furthermore, there are fewer stress-points at the material boundaries, which results in less accurate calculations. At later times, the isolated nodes continue to travel separately from the main bulk of material, which can be seen at times $t = 1$ s and $t = 1.5$ s in Figure 5.20a. Therefore as a remedy for this unrealistic behaviour, the inside approach method is adapted so that the isolated nodes (those that do not interact with any stress-points) are assigned a zero velocity. The results of the Stress-Particle SP2 method with this treatment of the isolated nodes are provided in Figure 5.20b, where it can be observed that the treatment prevents the isolated nodes from separating completely from the bulk of the material. This method of tending to isolated nodes is included in the remainder of the inside approach simulations.

The material evolution coloured by contours of deviatoric plastic strain is provided in Figure 5.21 for SP1, SP2 and SP3. The unrealistic particle clumping and subsequent material fracture is not evident in the results for any of the node-stress-point configurations. In the plastic strain profiles provided by Bui et al. (2008)

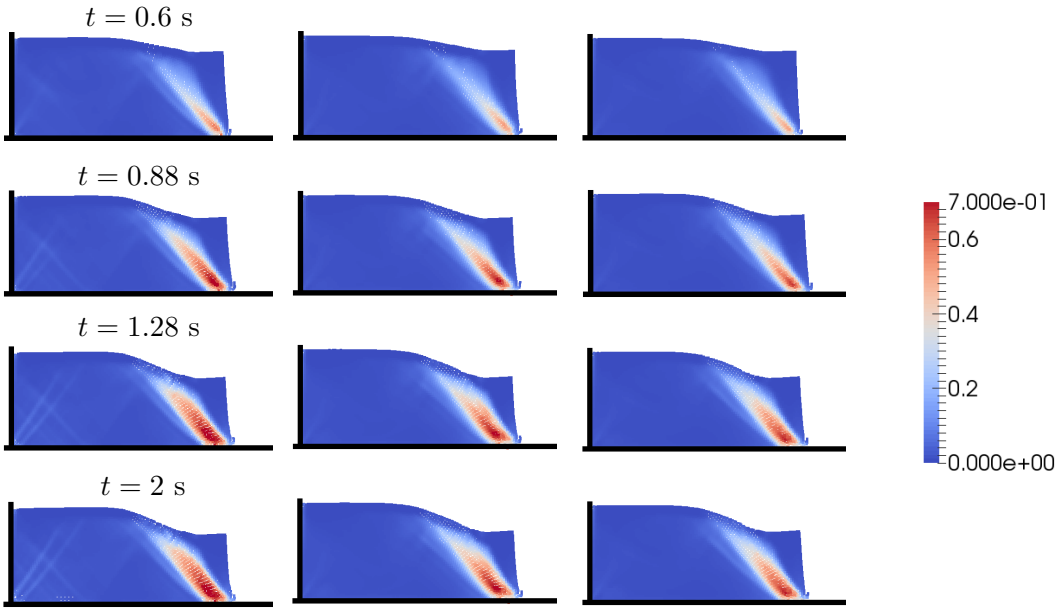

(A) SP1 (B) SP2 (C) SP3

FIGURE 5.21: Snapshots of the progressive failure of the cohesive slope, for SP1, SP2 and SP3. The material is coloured by values of deviatoric plastic strain $\bar{\epsilon}^p$ (dimensionless).

displayed in Figure 5.17, the shear band is composed of two thinner bands that both originate from the bottom right corner. These two separate bands are not as distinguished in the Stress-Particle results, indicating that the method has smoothed over this detail. The SP1 results show some additional regions of localised plastic strain close to the intersection between the two walls, suggesting that the material has slipped along the wall. An explanation for this is that there are not enough stress-points to interact with the dummy nodes behind the boundaries, to simulate the no-slip effect. The node positions are shown in closer detail in Figure 5.22 after 2.5 seconds of simulation. Here it can be seen that there are in fact very small fractures at the material free surface in the SP1 results (see Figure 5.22a), which are not present for the SP2 or SP3 methods (shown in Figures 5.22b and 5.22c respectively).

The material free surface obtained with Stress-Particle SPH is compared with the results of Standard SPH with the artificial stress and the particle shifting methods in Figure 5.23. The results of SP1, SP2 and SP3 differ slightly from one another. In the non-deformed region of the material (adjacent to the left wall), the height of the material in the SP1 model is lower than for the other models, indicating that it has compressed in this region. This can be seen at all times shown in Figures 5.23a - 5.23d, where the red, filled diamond pointers represent the SP1 results. In the deformed region of the material, the SP1 and SP2 profiles align closely. The SP3 results exhibit some extra stiffness than for SP1 and SP2, and the free surface profile (represented by the blue diamond pointers) is slightly higher than for SP1 and SP2 in Figures 5.23b – 5.23d. The final height of the material front modelled with the SP3 configuration is approximately 1.395 m, whereas for SP1 and SP2 it is 1.366

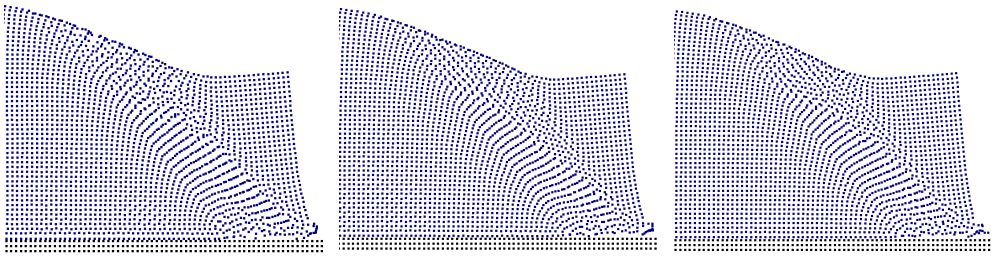

(A) SP1 (B) SP2 (C) SP3

FIGURE 5.22: The node positions at the front of the material at $t = 2.5$ s for the cohesive soil problem, calculated with configurations SP1, SP2 and SP3 of the inside approach. Note the small fractures that are present at the free surface for the SP1 configuration, which are not present in the SP2 and SP3 configurations.

m. For Standard SPH with the artificial stress this value is approximately 1.319 m, which is around 0.076 m less than for the SP3 results. With regards to Standard SPH with the particle shifting method, the results are in close agreement with those of the artificial stress method. The overall material behaviour is qualitatively similar for all of the SPH models used to produce the results in Figure 5.23. In the region of the material where plastic strains have occurred, the Standard SPH results exhibit an uneven free surface, whereas for the Stress-Particle method the free surface is smooth.

The free surface profiles presented in Figure 5.23 show that there are slight differences in the behaviour of the cohesive material when modelled with the five different SPH methods. Particularly, the final height of the front of the material differs between the models, with the results from SPH with artificial stress exhibiting the lowest height. Although it is plausible to dismiss these differences as being insignificant, it is useful to analyse why the results do not completely coincide with one another. A possible explanation for the Stress-Particle SPH results exhibiting extra stiffness than for Standard SPH in Figure 5.23 is that the tensile instabilities were not completely eliminated in the Stress-Particle method. If the particle clumping has not been fully removed then this could prevent the nodes from 'spreading out' as much as they would in the absence of the particle clumping. However, the results provided in Figure 5.18c show that the particle shifting method is not able to completely eliminate the effects of the tensile instability in the cohesive soil problem, yet the free surface profiles align overall between the particle shifting and artificial stress methods. Furthermore, the results of the Stress-Particle SP2 and SP3 methods presented in Figure 5.22 do not exhibit any obvious effects of the instability. The disparities in the free surface profiles could also simply be a result of the different processes that are performed to calculate the variables and variable gradients in the Standard SPH and Stress-Particle methods. It is important to highlight that the behaviour of the material modelled with SPH with the artificial stress method is dependent on the value of the tuning parameter ϵ, which defines the magnitude of the inter-particle repulsive force. Figure 5.24 shows the free surface profiles of the

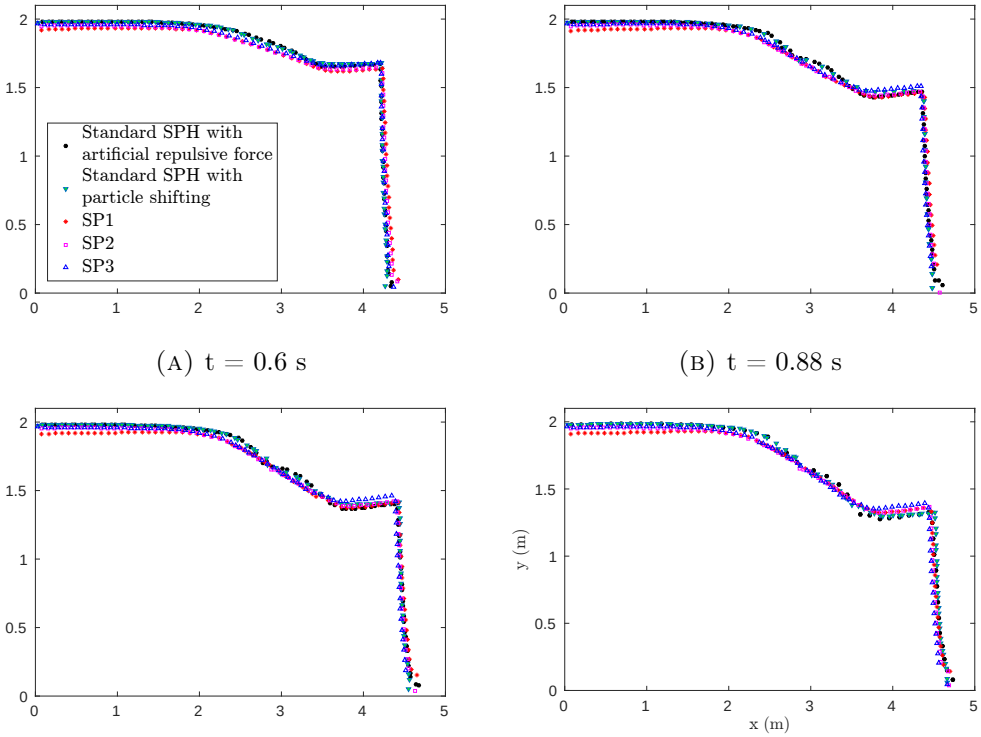

(A) t = 0.6 s

(B) t = 0.88 s

(C) t = 1 s

(D) t = 1.28 s

FIGURE 5.23: Free surface profiles for the cohesive soil failure problem. The different markers correspond to the results calculated with Standard SPH with the artificial stress, Standard SPH with particle shifting, SP1, SP2 and SP3.

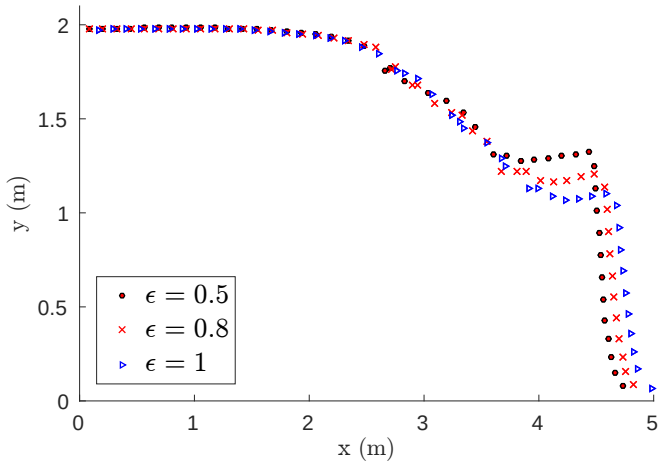

FIGURE 5.24: Free surface profiles of the cohesive soil at $t = 1.28$ s, calculated with Standard SPH with the artificial stress. The different markers correspond to different values of the tuning parameter ϵ.

cohesive soil for Standard SPH with different values of ϵ. It can be seen that as ϵ is increased, the SPH nodes spread further apart and contribute to a change in material behaviour. This demonstrates that the artificial stress method can produce an excessive repulsive force between particles, causing the SPH nodes to spread apart in an unrealistic manner.

To gain further understanding of the alternative SPH stabilisation techniques, the final node positions are compared in Figure 5.25 for Standard SPH with the artificial repulsive force, Standard SPH with the particle shifting method and the Stress-Particle SP3 method. The material is coloured by values of vertical stress, and the nodes in the region where the tensile instability occurs are shown in detail. The results of the artificial stress method shown in Figure 5.25a exhibit a noisy stress profile, particularly along the region of the shear band. The stress profile obtained with the particle shifting method is smoother (Figure 5.25b), due to the variable update of the stress that is performed when the particles have been shifted (see Section 4.5.4). Notably, the Stress-Particle SP3 method has produced the smoothest stress profiles with no obvious fluctuations. Concerning the structure of the particles, the nodes from the artificial force and the particle shifting methods have an isotropic configuration. The isotropy of the particles is an inherent feature of both the artificial stress force and particle shifting methods, which act to avoid voids in the material. It is this elimination of material voids that prevents the effects of the tensile instability from occurring. On the contrary, the particle positions in the SP3 method have formed structures that align with the trajectories of the soil movement. The presence of such structures is an indication of the accuracy of the scheme – the more accurate a meshless method is, the more likely that the particles will accurately follow the flow trajectories (Oger et al., 2016). These results highlight that, unlike with the artificial repulsive force and particle shifting methods, the Stress-Particle method reduces the errors associated with the tensile instability in a more natural way than

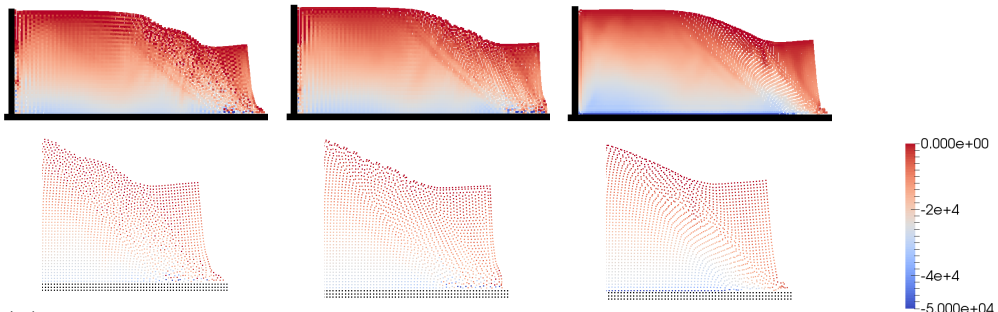

(A) Standard SPH with artificial stress (B) Standard SPH with particle shifting (C) SP3

FIGURE 5.25: Node positions at the end of the cohesive soil failure problem, for Standard SPH with the artificial stress, Standard SPH with particle shifting and Stress-Particle SPH with the SP3 configuration. The nodes are coloured by values of vertical stress σ_{yy} (Pa).

for alternative methods.

In Standard SPH, the presence of anisotropic structures (such as those observed in Figure 5.25c) has been linked to a decrease in accuracy and stability of the numerical method. The accuracy of the SPH kernel approximation strongly depends on the distribution of the particles, and can significantly decline in areas where there is high particle disorder (Quinlan, Basa, and Lastiwka, 2006; Antuono et al., 2014). Oger et al. (2016) showed for a range of fluid flow problems that the presence of anisotropic structures can lead to strong particle disordering, which was detrimental to the performance of SPH. In the considered examples, the deterioration of the SPH simulation was mainly associated with noisy pressure fields. However, the Stress-Particle SPH method naturally smooths the pressure (or stress), thereby potentially counteracting the problems that anisotropic particle structures can bring. Furthermore, it is expected that the structures will be less problematic for the Stress-Particle method than for Standard SPH, as the gradient calculations are split up over the nodes and the stress-points. It is clear from the results shown in Figure 5.25 that the presence of the anisotropic structures have not reduced the quality of the cohesive soil simulation. Nonetheless, the presence of particle structures should be analysed in subsequent simulations to ensure that they have not affected the simulation quality.

Particle position update

The SPH nodes in the Stress-Particle method have been shown to form coherent structures that follow the material trajectories (see Figure 5.25c). As discussed above, this is an indication of the accuracy of the method, but it also has the potential to eventually reduce the quality of the simulations (Oger et al., 2016). Although a significant reduction in quality has not been obvious in the Stress-Particle method thus far, it is beneficial nonetheless to include a technique that can prevent the deterioration of the Stress-Particle method in the presence of anisotropic structures. The XSPH method (Monaghan, 1992) is employed to update the particle positions in a way that smooths the velocity field and ensures that the particles do not become too

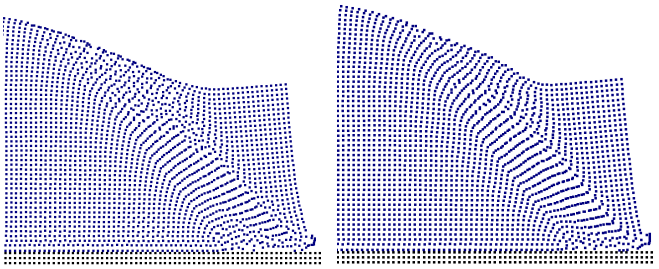

(A) SP1 – without XSPH (B) SP1 – with XSPH

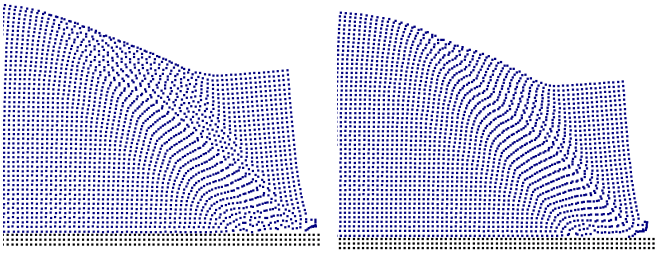

(C) SP2 – without XSPH (D) SP2 – with XSPH

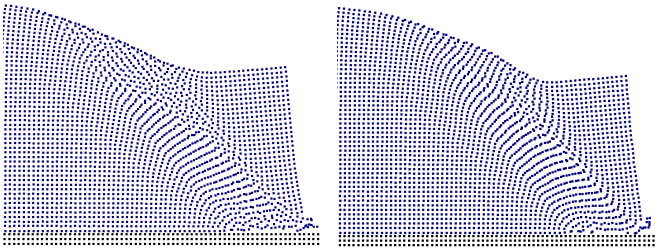

(E) SP3 – without XSPH (F) SP3 – with XSPH

FIGURE 5.26: The node positions at the front of the material at $t = 2.5$ s, for the cohesive soil failure problem. The results show the effect of updating the node and stress-point positions via the XSPH method, for SP1, SP2 and SP3.

close to one another (see Section 4.3). This assists in avoiding the strong disordering of particles which is often associated with anisotropic particle structures. The cohesive soil problem was therefore modelled with Stress-Particle SPH with the XSPH position update, with a tuning parameter of $\epsilon_x = 0.5$. Figure 5.26 shows the particle positions at $t = 2.5$ s for SP1, SP2 and SP3, updated with and without the XSPH method. When the particle positions were updated without XSPH, some particle disordering is present in the SP1 configuration in the upper half of the shear band (see Figure 5.26a). This region is also where the small fractures occur in the SP1 method, suggesting that the values of stress and velocity in this area are not accurate. When the XSPH method was used to update the SP1 node positions, Figure 5.26b shows that the particles form smooth trajectories throughout the material. Similar results are also obtained for the SP2 and SP3 configurations in Figures 5.26c - 5.26f (although the particle disordering without the XSPH method is not as obvious for the SP2 and SP3 configurations than for SP1).

The XSPH technique has also been used to update the node positions in both the Standard SPH method and SPH with the artificial stress. A comparison of the node

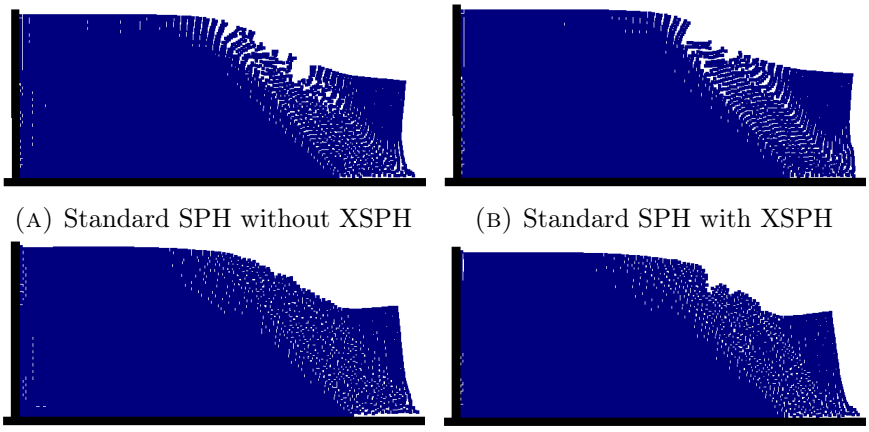

(A) Standard SPH without XSPH

(B) Standard SPH with XSPH

(C) Standard SPH with the artificial repulsive force, without XSPH

(D) Standard SPH with the artificial repulsive force, with XSPH

FIGURE 5.27: Profiles of the cohesive soil when the material had stopped deforming. Compared are the results of Standard SPH with and without the XSPH particle update method.

positions with and without XSPH is provided in Figure 5.27. Although the inclusion of the XSPH method is not sufficient to remove the effects of the tensile instability, it appears to somewhat reduce the non-physical material fractures. For Standard SPH, the particles updated with the XSPH method, shown in Figure 5.27b, exhibit less disordering than when XSPH was not used. Conversely, the performance of the artificial stress method is impaired when the XSPH technique is included. With the combination of the artificial stress and the XSPH method, non-physical fractures are observed near the material free surface in Figure 5.27d. The artificial stress term is included in the momentum equation to repel particles when they clump together in a state of tensile stress. The XSPH method updates the node positions according to an averaged velocity, as opposed to their discrete velocities. The results shown in Figures 5.27c and 5.27d suggest that this counteracts the ability of the artificial stress method to eliminate the tensile instability effects.

5.5.2 Non-cohesive soil

The non-cohesive material collapsed and propagated downstream at a rapid rate, exhibiting flow-type behaviour. The implementation of stress-points within SPH has not been applied to this type of problem before, and extending the Stress-Particle method to model such problems is one of the key challenges of the current research. Although no tensile instability was observed by Bui et al. (2008) in the collapse of the non-cohesive soil, recreating the results has the purpose of assessing how the Stress-Particle method can deal with high displacement problems that are relevant to the post-failure behaviour of landslides. First, the problem has been modelled with Standard SPH to determine how closely the current model can recreate the results of Bui et al. (2008). Snapshots of the material free surface are provided in Figure 5.28, for the current Standard SPH model and the results from the literature.

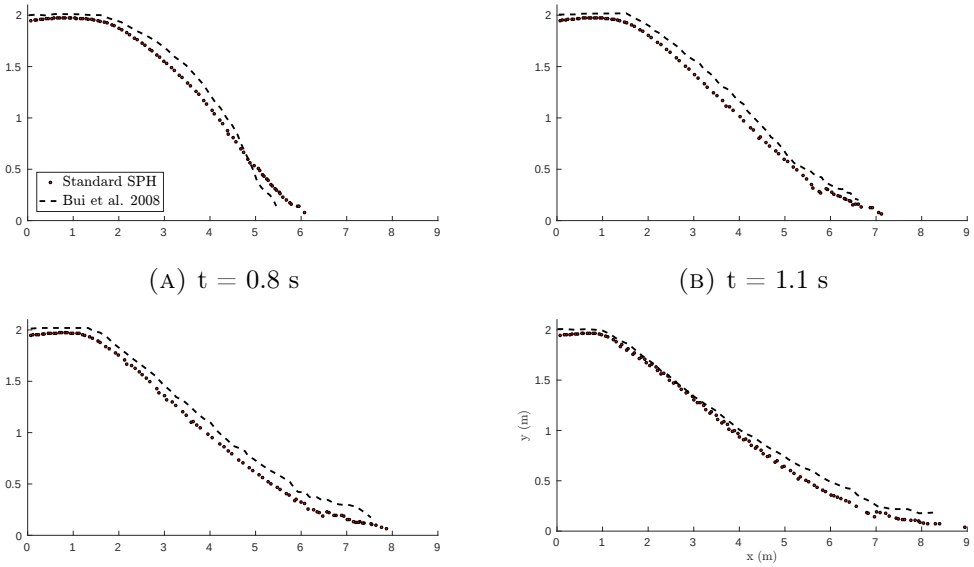

(A) t = 0.8 s (B) t = 1.1 s

(C) t = 1.4 s (D) t = 2.5 s

FIGURE 5.28: Free surface profiles for the non-cohesive soil problem. The markers denote the results of the current Standard SPH model, while the dashed line represents the results provided by Bui et al. (2008).

The overall behaviour of the Standard SPH results coincides well with those from the literature, and the free surface profiles align within a reasonable degree at all times. The small differences in the profiles are attributed to the differences in the numerical implementation between the current model and the literature model.

The Stress-Particle method, with its current set-up, is unable to capture the dynamics of the non-cohesive soil problem. This is evident in the results provided in Figure 5.29a, which show the node (depicted by the black dots) and stress-point (depicted by the red dots) positions at $t = 2.5$ s for SP1, SP2 and SP3. The nodes and stress-points exhibit highly unstable behaviour at the front of the material. It can be seen that the stress-points are relatively sparse in this area for all node-stress-point configurations, which contributes to the deterioration of the simulation. The lack of stress-points at the material front is due to the fact that in high velocity problems, updating the position of the stress-points with an interpolated velocity does not ensure that there will always be a sufficient number of them in the support domain of an SPH node. Additionally, with the Stress-Particle inside approach it is essential to include a repulsive boundary force that acts on the SPH nodes to prevent them from penetrating the boundary. This is also likely to interfere with the material behaviour, particularly when the material layer above the boundary is thin. The simulations were not improved when the nodes and stress-points were updated according to the XSPH method, shown in Figure 5.29b.

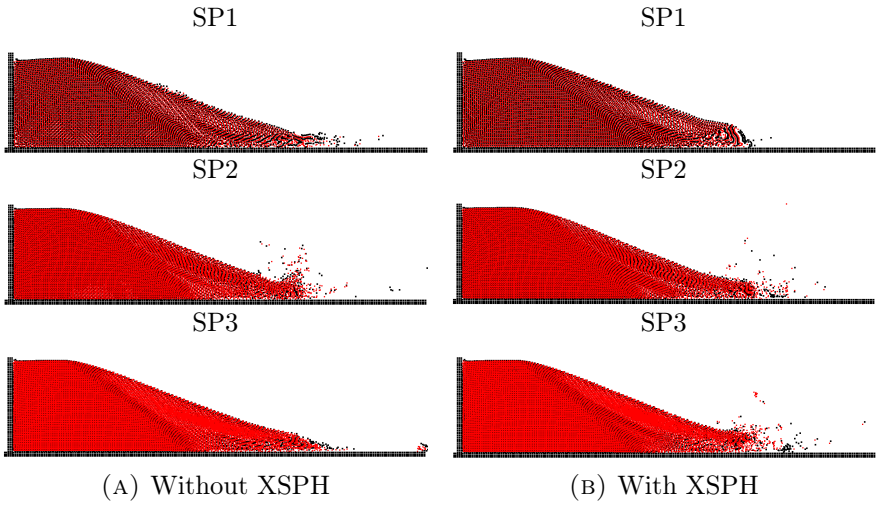

(A) Without XSPH (B) With XSPH

FIGURE 5.29: Particle positions at $t = 2.5$ s for the non-cohesive soil failure problem, calculated with the SP1, SP2 and SP3 configurations. The nodes are represented by the black points, while the stress-points are denoted by the smaller, red points.

5.6 Conclusion

This chapter has been dedicated to the application of Stress-Particle SPH (developed and implemented by the author) to problems involving the behaviour of soil, that are relevant to landslide initiation and propagation mechanisms. Furthermore, the role of the stress-points has been analysed and assessed in more detail than has been done before. This analysis has not only been focussed on how the stress-points combat the instabilities that are prevalent in SPH (the zero-energy modes and the tensile instability), but also to how they affect the numerical solution in general. The underlying procedure was first validated in one dimension by recreating the results of a shock wave in a bar, introduced by Dyka, Randles, and Ingel (1995). The Stress-Particle method was then considered in two dimensions, with the 'inside approach' arrangement of the nodes and stress-points. The inside approach has been applied to a range of problems involving soil dynamics from the literature, with the implementation of both a viscoplastic Perzyna and an elastoplastic mathematical model. These problems consist of: the vertical slope, strain localisation in a soil sample and the failure of cohesive and non-cohesive soil. From the results presented in this chapter, a number of conclusions can be made regarding the role of stress-points within SPH.

To compare with the Stress-Particle SPH model, Standard SPH was also employed to obtain a solution of the considered problems. In all cases, the Standard SPH results exhibited noisy stress profiles with singularities as a result of the zero-energy modes. The Stress-Particle method was able to drastically reduce the effects of the zero-energy modes for all configurations, and produce smooth stress profiles. In general, the Stress-Particle results support the conclusion that the higher the node-stress-point ratio, the higher the quality of the SPH simulation. This was observed

in all of the problems, where smoother stress profiles were produced when more stress-points were included. This conclusion was also supported with regards to the tensile instability – small non-physical fractures were present in the SP1 results for the cohesive soil failure problem, which appeared to be completely eliminated with the SP2 and SP3 configurations. However, the performance of the Stress-Particle method is not completely determined by the stress-point quantity. The arrangement of the stress-points was also shown to affect the quality of the SPH simulation. This was particularly evident in the results of the strain localisation in the soil sample, presented in Section 5.4. It was observed that the inclination of the shear band was affected by the stress-point composition, and the results were favourable when the configuration was symmetric about the vertical axis. Moreover, a higher node-stress-point ratio produced a thicker, less defined shear band. Therefore, the SP1 configuration produced the most satisfactory results for this problem.

The stress-points have been shown to pose problems in the boundary regions. This is unsurprising, as it is well known that the Standard SPH method suffers from accuracy-related issues at the boundaries. However with regards to Stress-Particle SPH, it is difficult to pinpoint the stress-point related boundary issues. In the elastic vertical slope problem (Section 5.3.1), having more stress-points near the boundaries contributed to discontinuities in the stress profiles in this region. For the SP1 configuration, with less stress-points near the boundaries, the discontinuities were not present. However, for the viscoplastic case (Section 5.3.2) it was essential to include extra boundary stress-points to accurately predict the evolution of plastic strain in the boundary region. Furthermore, when dummy nodes were employed for the simulations of the cohesive and non-cohesive soil failure in Section 5.5, a sufficient number of stress-points was required to accurately simulate the no-slip condition at the wall boundaries. It is suggested that future work involves developing a more sophisticated treatment of boundary conditions within Stress-Particle SPH.

A notable result in this chapter is the ability of the Stress-Particle method to eliminate the severe effects of the tensile instability in the problem of the cohesive soil failure. Although stress-points were originally introduced within SPH by Dyka, Randles, and Ingel (1995) to combat the tensile instability, the results of a linear stability analysis performed by Belytschko et al. (2000) suggested that they can only increase the stress threshold at which they occur. Following this publication, stress-points were not utilised in the literature with the purpose of alleviating the tensile instability. In Section 5.5, the non-physical fracturing in the cohesive soil was completely eliminated with a sufficient node-stress-point ratio. Additionally, further insight was provided on the mechanism of how the stress-points act to improve SPH. In the Stress-Particle SPH results, the SPH nodes closely followed the flow trajectories, indicating the accuracy of the scheme. It is this increase in accuracy, combined with the stability associated with splitting the numerical integration over two sets of particles, that prevents the onset of the tensile instability. What's more, unlike the artificial stress method that is commonly used to remove the effects of the

TABLE 5.4: The computational time taken (hours, to one decimal place) to simulate 2.5 seconds of the cohesive soil problem, comparing Standard SPH, SP1, SP2 and SP3

	Standard SPH	SP1	SP2	SP3
Without XSPH	5.3	10.6	18.3	28.5
With XSPH	7.8	15.9	23.9	33.5

tensile instability, no parameter tuning is required for Stress-Particle SPH.

A drawback of using the Stress-Particle SPH method over Standard SPH is the increase in computational expense. Table 5.4 shows the time taken in hours to simulate 2.5 seconds of cohesive soil failure, for Standard SPH and Stress-Particle SPH (with and without the XSPH method). For the SP1 configuration, the computational time is approximately double that of Standard SPH, regardless of whether or not XSPH is included. With an increase in the node-stress-point ratio from configuration SP1 to SP2, the computational time increases by a factor of approximately 1.7 when XSPH is not included, and 1.6 when XSPH is included. From SP2 to SP3, the increase in computational time is approximately 1.5 and 1.4, with and without XSPH respectively. Therefore, simulations performed with Stress-Particle SPH provide a compromise between accuracy and stability, and computational time. With added model complexity, such as the extension from two to three dimensions, the computational expense will increase further and the use of Stress-Particle SPH may not be viable in terms of computational efficiency. However, methods such as parallel computing and the implementation of graphics processing units could be utilised to increase the efficiency of Stress-Particle SPH significantly. Such improvements in computational efficiency are beyond the scope of the current investigation. The two-dimensional problems of interest in the current work are simulated within a reasonable time frame.

Despite there being certain features of the Stress-Particle method that require further attention, the method has been shown to bring significant benefits to the majority of the problems presented in this chapter. These problems are relevant to the behaviour of soil upon failure (and therefore landslide initiation), and are limited to those that do not undergo rapid velocities and large displacements. In Section 5.5.2, the Stress-Particle method was applied to model the failure of a non-cohesive soil, which exhibited flow-type behaviour. The method broke down for this problem, and the technique of updating the stress-point position was not sufficient to ensure that there were enough stress-points in the vicinity of each node. At the front of the propagating material, where velocities were highest, the node-stress-point distribution became highly irregular and resulted in the deterioration of the numerical simulation. For application to the post-failure behaviour of landslides, Stress-Particle SPH must be extended to be able to capture the dynamics of flow-type problems. Consequently, the next chapter of this research is devoted to improving the Stress-Particle method for application to the post-failure stage of landslides.

Chapter 6

Stress-Particle SPH for large displacement problems

6.1 Introduction

In the previous chapter, the role of stress-points in SPH was explored with regards to problems involving soil behaviour. For this, different numbers and patterns of stress-points were examined, where they were initially arranged inside every 'virtual quadrilateral' of nodes. In the current research, this method of arranging the stress-points has been denoted the 'inside approach'. While Stress-Particle SPH with the inside approach was able to eliminate the effects of the zero-energy modes and the tensile instability in most of the problems considered, it could not accurately predict the rapid collapse of a non-cohesive soil. This shortcoming was attributed to the method by which the stress-point positions were updated. As the velocity is not stored on the stress-points, the velocity used to update the stress-point positions was interpolated from surrounding nodes. This method becomes inaccurate for problems involving large displacements and high velocities, as it does not ensure that there is a sufficient number of stress-points in the vicinity of each node. Therefore this chapter focusses on extending the capabilities of Stress-Particle SPH to model problems with large displacements, which stress-points have not been applied to before. To fulfil the primary aim of the current research – the development of a stable numerical tool that is applicable for general landslide behaviour – Stress-Particle SPH must be capable of capturing large displacements that are relevant to landslide propagation. All previous applications of stress-points have been confined to problems exhibiting relatively low displacements (Randles and Libersky, 2000; Rabczuk and Belytschko, 2004; Sanchez and Randles, 2012).

Rather than having the stress-points initially placed inside virtual quadrilaterals, for the application to large displacements they are arranged with respect to each node, where a predefined number of stress-points are assigned to every node. This method of arranging the nodes and stress-points is referred to as the 'outside approach' and examples of different configurations are provided in Figure 6.1. Arranging the stress-points in this way offers a number of potential benefits for large displacement problems: as each node is associated with one or more stress-points,

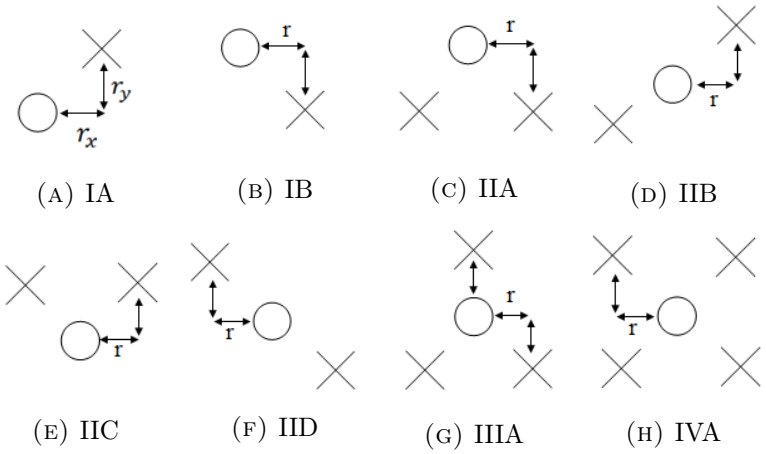

(A) IA (B) IB (C) IIA (D) IIB

(E) IIC (F) IID (G) IIIA (H) IVA

FIGURE 6.1: A depiction of the Stress-Particle outside approach.

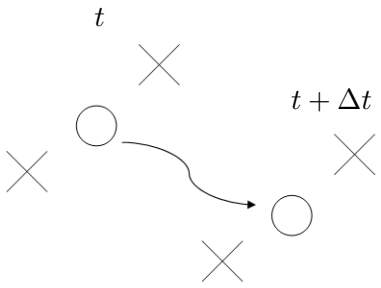

FIGURE 6.2: A sketch depicting the stress-points positions following their associated node in the Stress-Particle outside approach.

the stress-point positions can be updated according to the position of the node. The stress-points can therefore follow the node for the duration of the simulation as shown in Figure 6.2, which ensures that there are always enough stress-points in the domain of influence of each node. With this method of updating the stress-point positions, it is no longer necessary to apply the boundary repulsive force that prevents the penetration of nodes through the boundaries. Furthermore, in the outside approach it is possible to remove the influence of the stress-points in areas where they may pose problems for the numerical calculations. This is achieved by assigning the positions of the problematic stress-points to be equal to the position of their associated node. In the outside approach this technique of reassigning the stress-point position is applied in two cases. First, the stress-points that are associated with nodes moving along the wall boundary are reassigned, as depicted in Figure 6.3. Moving the positions of these stress-points to align with their corresponding node is useful, as the addition of stress-points complicates the interaction between the interior SPH particles and the dummy nodes. Secondly, the stress-points that are connected to nodes with a low number of neighbours are also shifted, to ensure the momentum conservation of the system. Further details on the stress-point reassignment method are provided later in this chapter.

In this chapter, Stress-Particle SPH with the outside approach is utilised to model

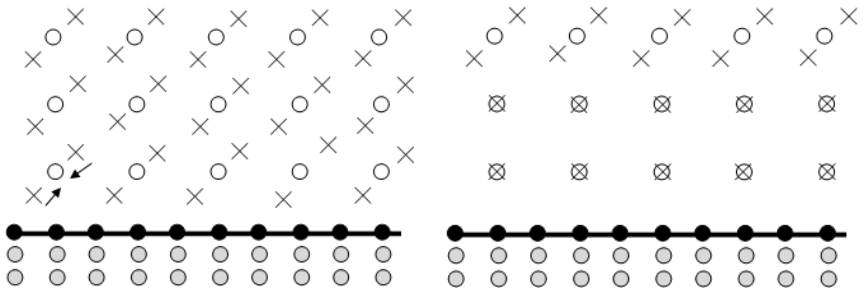

(A) Before stress-point adaptation at the boundaries (B) After stress-point adaptation at the boundaries

FIGURE 6.3: A depiction of the nodes and stress-points in the outside approach, in the proximity of the wall boundary.

three problems regarding soil behaviour. First, it is applied to the same problem of the non-cohesive soil failure described in Section 5.5, which involves large displacements that could not be accurately modelled with the inside approach. The second problem considered is the failure of the cohesive soil, also introduced in Section 5.5, which exhibits effects of the tensile instability. This problem is simulated to verify whether the outside approach is as efficient as the inside approach at combating the tensile instability. The third problem is the collapse and propagation of a Von Mises material, with a Perzyna rheological model. This problem exhibits both the tensile instability and large displacements, thus it serves as a good test of the capabilities of the outside approach in terms of removing the instability and capturing the large displacements. The effects of the node-stress-point arrangement and the procedure in which the stress-point positions are updated are analysed in all three problems. The different arrangements will be referred to via the labels given in Figure 6.1. Due to the benefits outlined in the previous chapter, the SPH particle positions have been updated with the XSPH method (Monaghan, 1989) (with $\epsilon_x = 0.5$) in all of the following examples.

6.2 Non-cohesive soil failure

The Stress-Particle SPH method with the outside approach has been first employed to predict the failure of the non-cohesive soil, originally modelled with Standard SPH by Bui et al., 2008. A full problem description is provided in Section 5.5. No tensile instability was observed in this problem and therefore no technique is required for its removal. However, the simulation provides an indication of the accuracy of the Stress-Particle method in the absence of the instability, and its ability at capturing large displacements. For comparison, also presented are the results computed with Standard SPH. Unless stated otherwise, the positions of the stress-points were updated by ensuring that they followed their associated node for the duration of the simulation. Dummy nodes were used to simulate the no-slip walls and no boundary repulsive force was included. In the outside approach, the

positions of certain stress-points are reassigned to coincide with the positions of their associated nodes, as discussed above. The effect of this adaptation of the stress-points is detailed in Section 6.2.1, for the non-cohesive soil failure problem.

Figure 6.4 displays the particle positions at $t = 2.5$, for the node-stress-point configurations given in Figure 6.1. Figures 6.4b and 6.4c show the results for configurations IA and IB respectively, where one stress-point is attached to each node. In these cases, the final node positions are extremely different both from those of Standard SPH and from one another. For configuration IA the nodes have not reached the end of the run-out surface, while the nodes have exceeded this length for configuration IB. Depending on which side of the node the stress-point is positioned, both the value and the sign of the gradient of the smoothing kernel are different. With only one stress-point, the influence of the kernel is weighted towards one side, explaining the difference between Figures 6.4b and 6.4c. When more stress-points are attached to each node, as for Figures 6.4d - 6.4h, the results exhibit the same behaviour as for Standard SPH. Having more stress-points per node provides a wider range of interpolation points and a more accurate representation of the average flow field.

It is important to note that for this particular example, the influence of the stress-point is strongly dependent on whether it is placed on the left or the right hand side of the node, and not on its vertical position. This is because in this case the horizontal velocity gradient is stronger than the vertical, as the material rapidly flows downstream. In problems where the vertical velocity gradient is comparable to, or greater than, the horizontal, it is expected that the vertical position of the stress-point would have a larger influence on the material behaviour. The free surface profiles calculated with two stress-points per node and three stress-points per node are compared directly with the results of Bui et al., 2008 in Figure 6.5. The profiles agree for all three node-stress-point configurations, showing that the Stress-Particle SPH method is capable of capturing the large displacements in soil flow problems, provided an appropriate node-stress-point arrangement.

Contour plots of vertical stress at $t = 2.5$ s are provided in Figure 6.6, for configurations IIA, IIB, IIC, IID and IIIA. The stress profile for Standard SPH exhibits noisy areas due to stress fluctuations resulting from the zero-energy modes. Noisy stress profiles were also observed by Nguyen et al., 2017 when simulating the collapse of a non-cohesive soil. There the stress profiles were smoothed via an MLS interpolation every specified number of time steps. Here, the Stress-Particle SPH method has also succeeded in smoothing the stress profiles for the configurations shown. However, the results produced with configuration IIC (with two stress-points above each node on either side) differ significantly from the stress profiles for the other configurations. In the former case, the stress magnitude is lower in the bottom left region of the material than for the other results. With regards to the other configurations, the contour plots computed with the outside approach are considerably smoother than those of Standard SPH. This is because the stress on the nodes is calculated

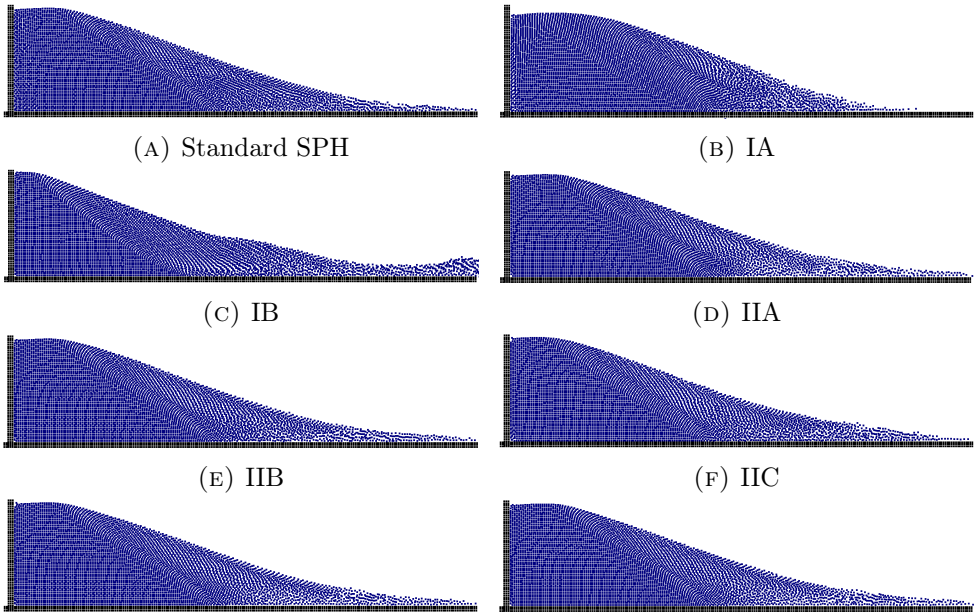

(A) Standard SPH (B) IA

(C) IB (D) IIA

(E) IIB (F) IIC

(G) IID (H) IIIA

FIGURE 6.4: Node positions at $t = 2.5$ s for the non-cohesive soil failure problem. The different outside approach configurations are shown in Figure 6.1.

by smoothing over the stress values of the surrounding stress-points within each time step, and the Stress-Particle method therefore has the inherent advantage of producing smooth stress profiles. It was shown in the previous chapter that a high number of stress-points resulted in smoother stress profiles (albeit at the expense of an increase in computational time). In Figure 6.6 the stress profiles calculated with configuration IIIA are not evidently smoother than for the configurations with two stress-points per node.

6.2.1 Adaptation at the boundaries

The results provided in Section 6.2 were calculated with the outside approach with the adaptation of the stress-points near the wall boundary – for moving nodes that interacted with the dummy nodes defining the boundary, their associated stress-points were reassigned to have the same position as the node itself, as depicted in Figure 6.3. The reasoning behind the adaptation of stress-points at the wall boundaries is as follows. The stress-points use information from the dummy nodes in the calculation of the velocity gradient in order to prevent the particles from penetrating the boundary. Therefore, the no-slip effect results from the interactions between the stress-points and dummy nodes, as opposed to the node-dummy node interaction. In consequence, the number of stress-points and their position with respect to the nodes affects the interaction between the material and the boundary. It is not essential to implement the adaptation of the stress-points in the proximity of the wall. However, the interaction between the wall and the interior particles can vary depending on the node-stress-point configuration, as discussed above. Furthermore,

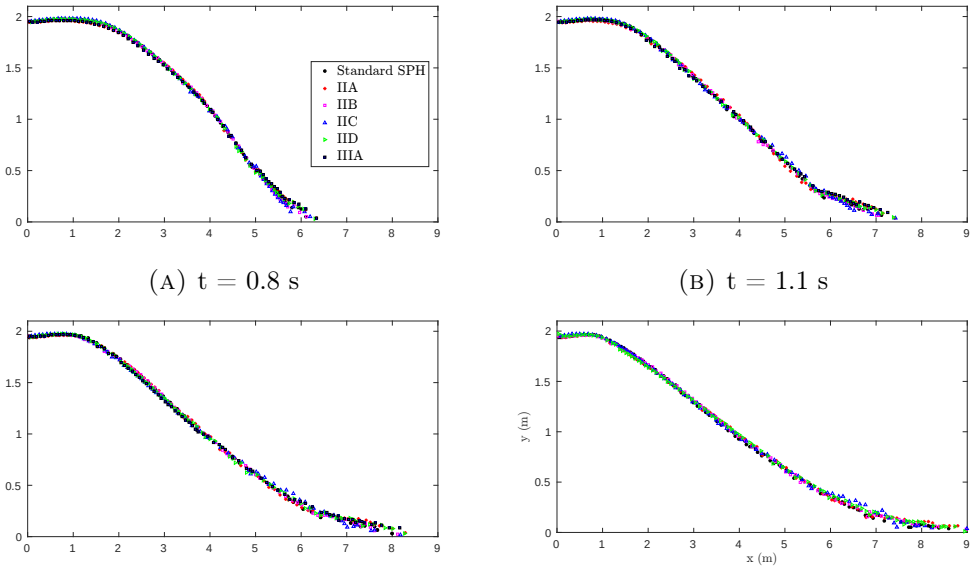

(A) t = 0.8 s (B) t = 1.1 s

(C) t = 1.4 s (D) t = 2.5 s

FIGURE 6.5: Free surface profiles for the non-cohesive soil problem. The black circle markers denote the results from the current Standard SPH model with the artificial stress, while the other markers represent the outside approach results.

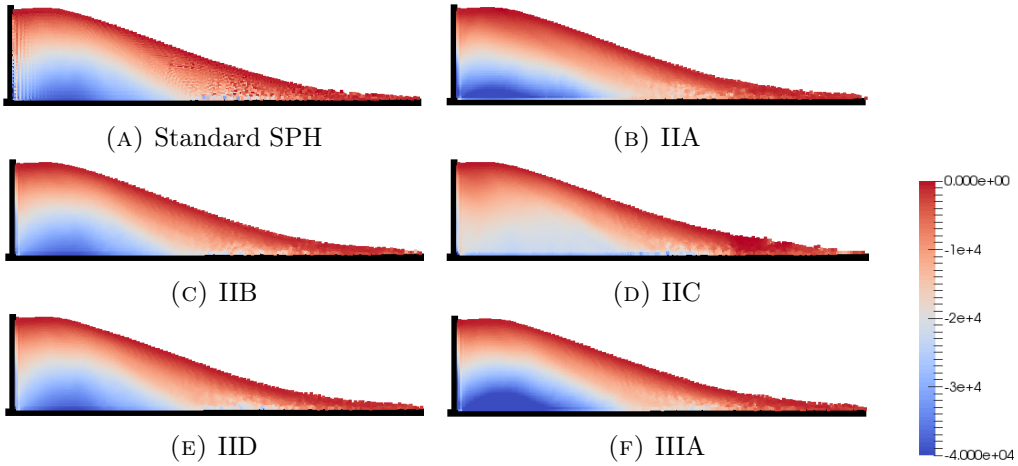

(A) Standard SPH (B) IIA

(C) IIB (D) IIC

(E) IID (F) IIIA

FIGURE 6.6: Node positions at $t = 2.5$ seconds for the non-cohesive soil failure problem, coloured by vertical stress σ_{yy} (Pa). Note the noisy areas of the stress profile for the Standard SPH results.

when two stress-points are placed above each node in configuration IIC, there are not a sufficient number of stress-points near the boundary to ensure that the nodes don't penetrate the wall. Thus the inclusion of the stress-point treatment at the boundaries is preferable, to reduce the inconsistencies between the performance of the different configurations and to eliminate the need for any repulsive force to prevent particle penetration into the boundary. Also, the adaptation technique has been found to improve the model performance only in areas where the material is propagating along the boundary. In areas where the overall material behaviour is stationary, adapting the stress-points can actually interfere with the development of a smooth stress profile. Therefore the stress-points are adapted for nodes in the proximity of the boundary that have an absolute velocity that is greater than a threshold value $\mathbf{u}_{tol}$. In this research, the technique of adapting the stress-point position near the walls has been included in all simulations with the outside approach, with $\mathbf{u}_{tol} = 0.4$ m s^{-1}.

6.2.2 Adaptation at isolated nodes

The method of shifting the stress-points to coincide with the positions of their associated nodes is also performed for isolated nodes. Consider an isolated particle i with two stress-points attached at the same distance from it. Note that here the term isolated refers to the interaction between nodes, and not nodes and stress-points. The velocities on the stress-points are identical because they are calculated by interpolating over the single node (since the kernel function is symmetric with respect to absolute distance). Therefore, in the absence of any external force, the stresses of the stress-points are zero since they depend on the node-stress-point velocity difference. Consequently, the stress gradient at the node is zero, and it travels with a constant velocity. However, if one of the stress-points is subjected to an external force, such as an interaction with a dummy node, then the stresses at the two nodes will be different which will cause a non-zero stress-gradient at the node. As a result, the node will accelerate in a non-physical manner and the conservation of momentum will not hold. As a result, in the outside approach the stress-points that are associated with isolated nodes are shifted so that they have the same position as the node. This ensures a zero stress gradient at the isolated node, since the value of the kernel gradient is zero at the position of the node itself. To employ the stress-point adaptation for isolated nodes, the number of node-node interactions, n_{int}, is recorded at each calculation step, and the shifting method is performed if $n_{int} \leq 2$. This threshold for n_{int} is chosen because these particles are more likely to become isolated than those with a higher number of neighbours. Furthermore, the Stress-Particle method is most effective when there are a sufficient amount of stress-points for the nodes to interact with.

The procedure of reassigning the position of certain stress-points is not possible to include in the inside approach as the stress-points are not connected to individual

nodes. In the remainder of this research, the procedure is employed within the outside approach for all simulations.

6.2.3 Updating the stress-point positions

In the Stress-Particle inside approach, the positions of the stress-points are updated according to their interpolated velocity. As discussed in Section 5.5.2, this method of updating the stress-points is unsuitable for problems with large displacements. Despite this, it has here been applied within the outside approach and used to simulate the non-cohesive soil problem. However, unlike in the inside approach, certain stress-points have been shifted according to the conditions described above in Sections 6.2.1 and 6.2.2. That is, the stress-points associated with nodes at the boundaries (for $|\mathbf{u}| > 0.4$), as well as those associated with isolated nodes ($n_{int} < 2$), are reassigned to have the same position as their corresponding node. The purpose of updating the stress-points in this way is to check if it is sufficient to move them according to their interpolated velocities if the stress-point shifting is also performed, or if it is essential that all stress-points follow their associated nodes.

Snapshots of the nodes are shown in Figure 6.7 for the IIB node-stress-point configuration, where the stress-point positions were updated as described above. Compared are the results with and without the reassignment of specific stress-points. Figure 6.7a shows the results obtained when all of the stress-points were updated according to their interpolated velocities. At $t = 1.1$ s, some nodes at the front have started to propagate away from the rest of the material, and at $t = 1.4$ s the behaviour is visibly unstable in this region. When the specified stress-points were adapted (see Figure 6.7b), the node behaviour is considerably more stable up until $t = 1.4$ s. However, their are discontinuities in the node profile and at $t = 2.5$ s the nodes at the material front exhibit unrealistic behaviour. Therefore, even with the mechanism of adapting certain stress-points, it is not appropriate to update the majority of the stress-points with their interpolated velocities for large displacement flows.

6.3 Cohesive soil failure

In addition to being able to model flow-type problems, the Stress-Particle outside approach must retain the stabilising effects of the inside approach in order to fulfil the original purpose of including stress-points within SPH. That is, to remedy the effects of the tensile instability and the zero-energy modes. The smooth stress profiles presented in Figure 6.6 show that the outside approach is capable of reducing stress fluctuations associated with zero-energy modes. To determine the abilities of the method at eliminating the effects of the tensile instability, it has been applied to the problem of the cohesive soil failure introduced by Bui et al., 2008. It was shown in Section 5.5 that this problem suffers from severe tensile instabilities unless a stabilisation technique is employed. A selection of the configurations shown in Figure

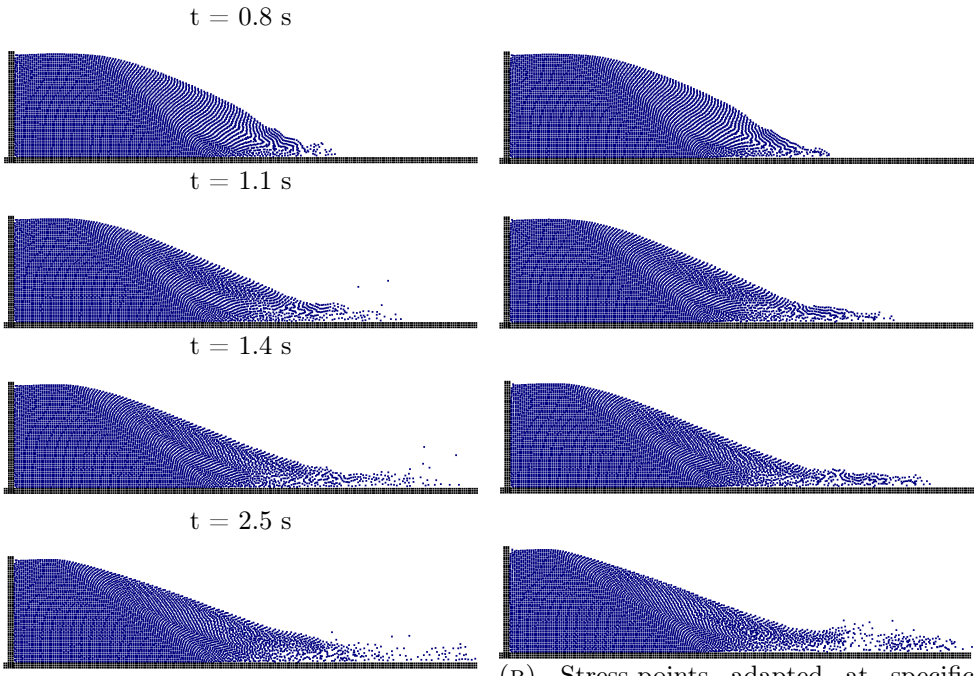

(A) No stress-point adaptation

(B) Stress-points adapted at specific nodes

FIGURE 6.7: The node evolution for the non-cohesive soil failure with configuration IIB. Compared are the results where all of the stress-points were moved via their interpolated velocities, against when certain stress-points were adapted as described in Sections 6.2.1 and 6.2.2.

6.1 have been used to model the problem, and the results are compared with those of Standard SPH with the inclusion of the artificial stress. Following the results presented in Section 6.2, the considered configurations consist of two and three stress-points per node. Unless stated otherwise, the stress-point positions are updated by ensuring that they follow their associated nodes throughout the simulation.

The deformed material at the end of the simulation is shown in Figure 6.8, coloured by values of deviatoric plastic strain. The contour plots calculated with the Stress-Particle method are significantly smoother than the Standard SPH results, both with and without the inclusion of the artificial stress. The effects of the tensile instability have been considerably reduced with the outside approach in comparison to the Standard SPH results with no artificial stress (see Figure 6.8a). However, the Stress-Particle method with the outside approach has not completely removed the effects of the instability for all of the implemented node-stress-point configurations. Small fractures are present in the region of the soil under tension for both the IIB and IIIA configurations. The latter configuration consists of three stress-points per node, which shows that the performance of the outside approach is not solely dependent on the quantity of the stress-points. Furthermore, the shape of the deformed material differs considerably between the different configurations. Differences of this magnitude were not observed in the results of the inside approach, where the stress-points were updated according to their interpolated velocity (see Section 5.5.1). The differences between the results are a consequence of ensuring that the stress-points follow their associated nodes. The relative position of the stress-points with respect to their corresponding nodes is constant throughout the numerical simulation. These stress-points influence the kernel approximation at the node, which will be different depending on the location of the stress-points. It is important to highlight that of the results displayed in Figure 6.8, those produced with configuration IID bear the closest resemblance with the Standard SPH profile (with the artificial stress). Configuration IID consists of two stress-points positioned diagonally around each node, as depicted in Figure 6.1. This configuration aligns most closely with the direction of the flow in the cohesive soil failure.

The inability of the Stress-Particle outside approach to completely remove the tensile instability in the cohesive soil is related to the method by which the stress-point positions are updated. The results displayed in Figure 6.8 were computed with the stress-points defined to follow their associated node, as shown in Figure 6.2. This means that the stress-point positions were updated with the same velocity as their corresponding node, and not with their actual, interpolated velocity. Figure 6.9 shows the positions of the nodes and the stress-points at $t = 2.5$ s of the cohesive soil failure simulation, for configuration IIB. Compared are the particle positions when the stress-points followed their assigned node, against when the stress-point positions were updated via their interpolated velocity. It can be seen that the latter method of updating the stress-point positions produces more accurate results than the former, and there is no effect of the instability. For this method, the stress-point

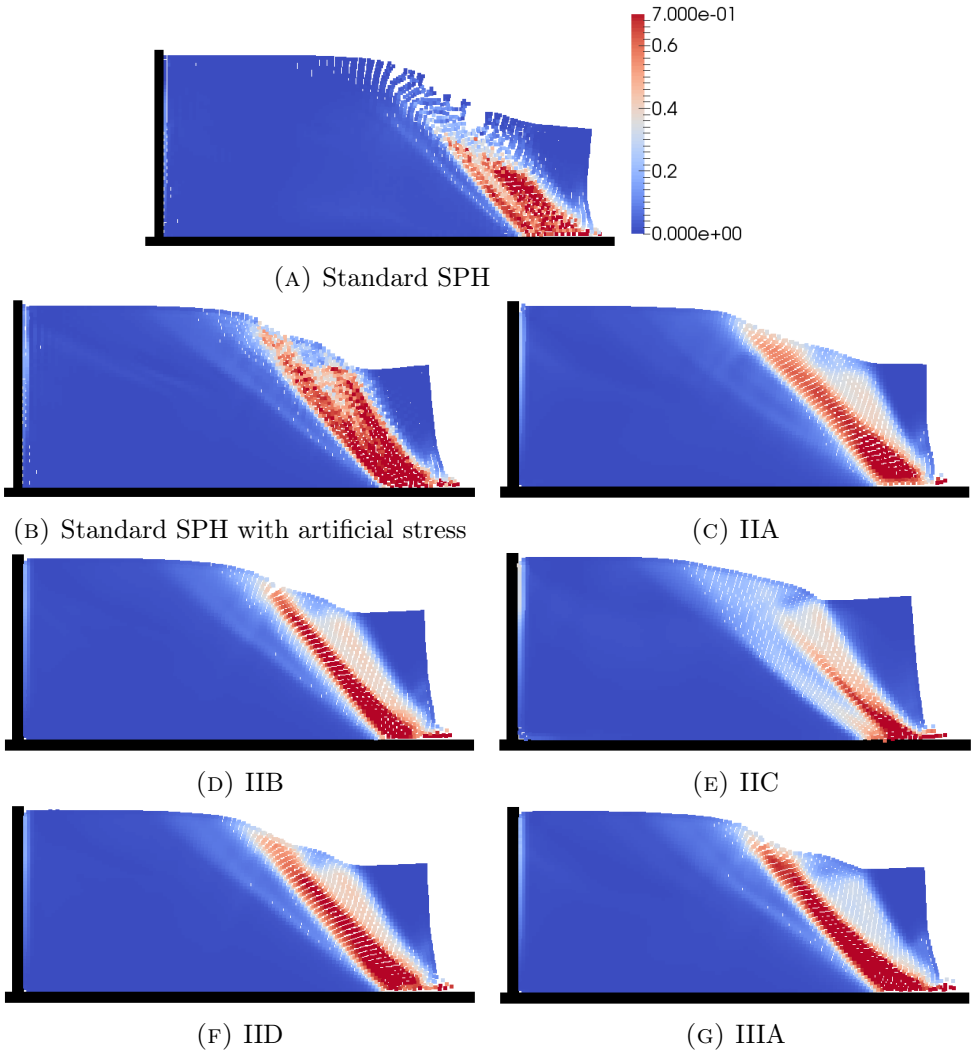

(A) Standard SPH

(B) Standard SPH with artificial stress

(C) IIA

(D) IIB

(E) IIC

(F) IID

(G) IIIA

FIGURE 6.8: The deformed material at $t = 2.5$ s in the cohesive soil failure problem, coloured by values of deviatoric plastic strain $\bar{\epsilon}^p$ (dimensionless). Displayed are the results computed with Standard SPH and different configurations of the outside approach.

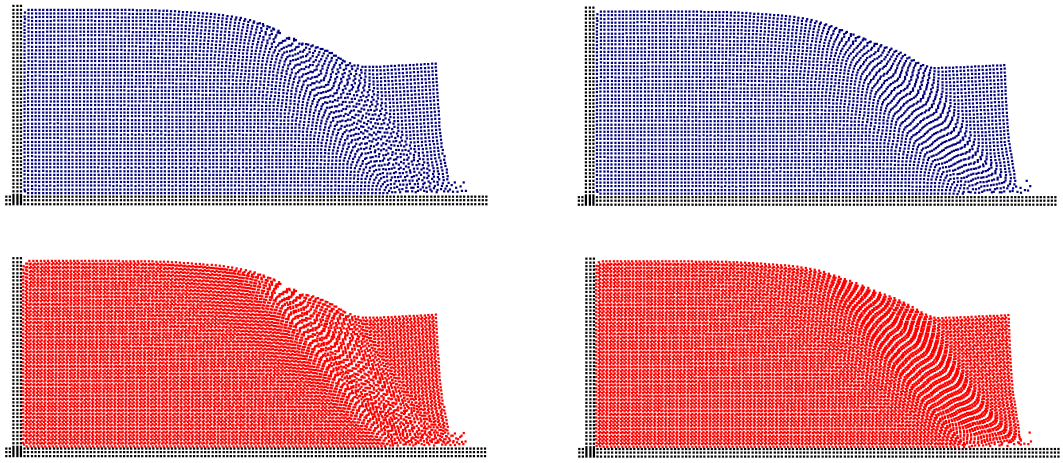

(A) Results where the stress-points were assigned to follow their associated node

(B) Results where the stress-point positions were updated according to their interpolated velocities

FIGURE 6.9: Node (blue) and stress-point (red) positions at $t = 2.5$ s for the cohesive soil problem with the Stress-Particle outside approach, configuration IIB. Compared are the results where the positions of the stress-points were updated according to their interpolated velocity, against those where the stress-points were assigned to follow their associated node.

velocity profile is smooth as it is calculated by interpolating over the velocities of the surrounding nodes. This is reflected in the stress-point positions displayed in Figure 6.9b, which are aligned with the streamlines of the soil movement. In contrast, there are discontinuities in the stress-point positions shown in Figure 6.9a, which were updated with a velocity that was not smoothed.

The difference in the results provided in Figure 6.9 shows that there are benefits to moving the stress-points according to a smoothed velocity, as opposed to a velocity that has not been smoothed. When the velocity profile of the stress-points is smooth, the stress calculations on the stress-points are likely to be more stable. In turn, this reduces the risk of stress fluctuations and discontinuities across the nodes and they are less susceptible to the tensile instability. Furthermore, when the stress-points are updated according to their interpolated velocity they naturally become aligned with the flow field. When the stress-points are defined to follow their associated nodes throughout the entire simulation, they are always aligned according to their initial placement (with respect to the nodes). It is possible to initially align the stress-points in the predicted general direction of the flow, such as for configuration IID in the cohesive soil problem. However, this approach would require some trial and error, not to mention that the flow field is not constant throughout most simulations.

6.4 The outside approach: improvements

The results presented in Sections 6.2 and 6.3 show that the current outside approach set-up is not as effective as the inside approach at removing the tensile instability in

the cohesive soil problem. However, the inside approach is not suitable for problems involving large displacements, such as the non-cohesive soil failure. Consequently, the outside approach is here extended to be better suited for both problems involving the tensile instability and large displacement problems. Two different techniques to improve the outside approach are here presented. Both techniques have been written in Fortran 90 and computationally implemented by the author of this investigation.

6.4.1 Concentration criteria approach

The results of the cohesive and non-cohesive soil failure problems suggest that the way in which the stress-points should be updated is different depending on the problem under consideration. For problems involving large displacements, such as the non-cohesive soil failure, it is essential that the stress-points are defined to follow their associated nodes to ensure that there are enough stress-points within the region of each node. However, for problems that exhibit the tensile instability (such as the cohesive soil failure), the stress-points were found to be most effective when they were moved according to a smoothed velocity, that was interpolated from the surrounding nodes. Therefore, the outside approach is here adapted so that the stress-point positions are updated according to their interpolated velocity, and shifted back to their original position (with respect to their associated node) when required.

This approach of updating the stress-point positions requires a criterion to determine when the stress-point positions are adapted. An appropriate criterion to consider is the stress-point concentration at each node. Particle concentration, C_i, is defined as (Xu and Yu, 2018)

$$C_i = \sum_{j=1}^{N} \frac{m_j}{\rho_j} W_{ij}. \tag{6.1}$$

In the Stress-Particle method, the stress-point concentration is determined by applying Equation (6.1) to each node and summing over the surrounding stress-points. A contour plot of the initial stress-point concentration is provided in Figure 6.10 for configuration IIB of the outside approach. The concentration at the interior nodes is approximately equal to 1. The nodes at, and in close proximity to, the material boundaries have a lower concentration than this due to the truncation error associated with the kernel approximation. The stress-point concentration at the material edges is approximately 0.5, and the lowest concentration values at the corners of the material are approximately 0.25. The method of adapting the stress-points according the node-stress-point concentration is as follows. The stress-points are initially positioned with respect to each node in the usual way for the outside approach. At each time step the node and stress-point positions are both updated according to their velocities, which for the stress-points is an interpolated velocity. The concentration defined by Equation (6.1) is then calculated on the nodes after the position update, to obtain the stress-point concentration at every node. For the nodes that have

FIGURE 6.10: A contour plot of initial stress-point concentration (dimensionless), for the cohesive soil problem with configuration IIB of the outside approach.

a stress-point concentration lower than a threshold value C_{tol}, their corresponding stress-points are moved to their original position with respect to the node. For the remaining nodes, the position of their associated stress-points is left unchanged.

The node positions at $t = 2.5$ s for the cohesive and non-cohesive soil failure problems are provided in Figure 6.11, for configuration IIB of the outside approach. The stress-point positions were adapted according to the stress-point concentration at the nodes, as described above. The concentration threshold was defined as a percentage of the initial concentration C_0. Figures 6.11a and 6.11b show the node positions when the concentration threshold C_{tol} was defined as $0.9C_0$ and $0.8C_0$ respectively. For both of these threshold values, the behaviour of the non-cohesive material is well captured. Shifting the stress-points according to these criteria was sufficient to ensure that there were enough stress-points in the vicinity of each node. For the cohesive soil problem, a small fracture is present at the free surface when a concentration threshold of $C_{tol} = 0.9C_0$ was used (see Figure 6.11a). This was eliminated when the threshold for adapting the stress-points was decreased to $C_{tol} = 0.8C_0$, as shown in Figure 6.11b. This suggests that the stress-point concentration at each node never exceeds 80 percent of its initial value in the cohesive soil problem.

6.4.2 Velocity vector approach

The stress-point concentration criterion described above provides a useful way in which to adapt the stress-point positions according to a relevant numerical parameter. However, it is unlikely to be applicable for all problems – such as those that exhibit severe effects of the tensile instability as well as large deformations. An alternative way in which to extend the method of updating the stress-point positions is by considering the velocity vector at each node. In this method, the stress-points follow their associated node throughout the simulation, yet their orientation is adapted to align with the velocity vector of that node. This is motivated by the results acquired when all stress-points were assigned to follow their associated nodes, presented in Section 6.3. The most realistic results were obtained when the stress-points were roughly aligned with the direction of the flow (for configuration IID).

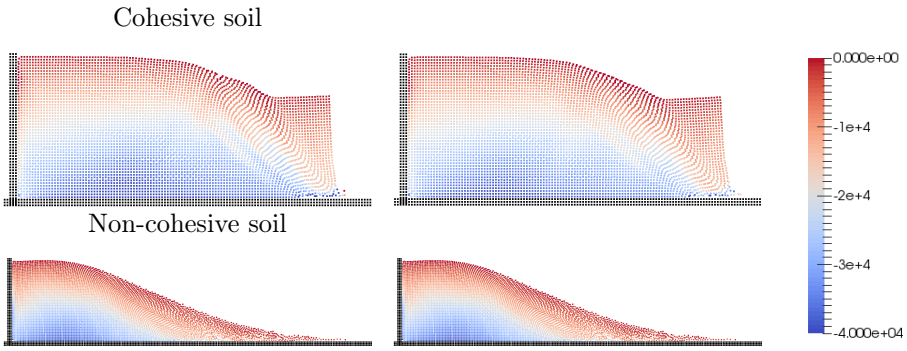

(A) $C_{tol} = 0.9C_0$ (B) $C_{tol} = 0.8C_0$

FIGURE 6.11: Node positions at $t = 2.5$ s for the cohesive and non-cohesive soil failure problems, calculated with configuration IIB of the outside approach. The material is coloured by values of vertical stress σ_{yy} (Pa). The interior stress-points were adapted for the nodes that had a the stress-point concentration less than C_{tol}.

A description of the method is given as follows. The stress-points are initially positioned with respect to each node in the usual way for the outside approach. At each time step, the components of the velocity are utilised to calculate the angle of direction of the velocity vector θ_u:

$$\cos\theta_u = u_x/|\boldsymbol{u}|, \quad \sin\theta_u = u_y/|\boldsymbol{u}|. \tag{6.2}$$

The stress-points are then positioned to align with that vector at a specified distance r from the node. The horizontal and vertical components of the position vector of each stress-point, denoted by r_x and r_y respectively, are calculated as

$$r_x = r\cos\theta_u, \quad r_y = r\sin\theta_u. \tag{6.3}$$

At each node with position vector (x_i, y_i), two stress-points are placed with the position vectors $(x_i + r_x, y_i + r_y)$ and $(x_i - r_x, y_i - r_y)$, as depicted in Figure 6.12. This ensures that each node is associated with two stress-points that are both aligned with the velocity vector of that node. Additionally, the stress-point distribution at each node is symmetric with respect to the normal velocity, and the influence of the stress-point is not weighted towards one side. It was shown in Section 6.2 that the outside approach does not perform well with only one stress-point attached to each node.

An area where the method described above may be ineffective is when the velocity is dominant in either the vertical or horizontal direction. For example, if the horizontal velocity is negligible, the angle θ_u is approximately zero and the stress-points will be aligned with the nodes in vertical structures. In general, a staggered node-stress-point arrangement is preferable (Belytschko et al., 2000). Therefore, the method is adapted so that the horizontal and vertical distances are increased if they

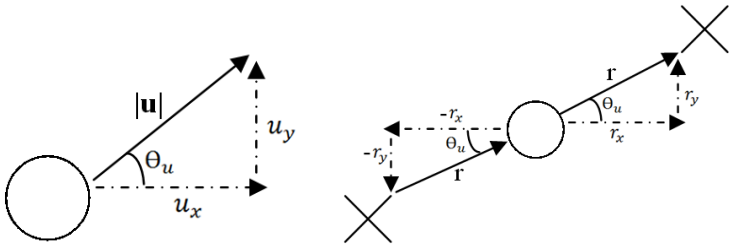

(A) The velocity vector at a node (B) The corresponding stress-point placement

FIGURE 6.12: A depiction of updating the stress-point positions according to the velocity vector at each node.

are below a threshold value. In this work a sufficient threshold is assumed to be $\frac{\Delta x}{5}$, and is implemented as follows.

$$\text{if } |r_x| < \frac{\Delta x}{5},\ |r_x| = |r_x| + \frac{\Delta x}{3}, \tag{6.4}$$

$$\text{if } |r_y| < \frac{\Delta x}{5},\ |r_y| = |r_y| + \frac{\Delta x}{3}. \tag{6.5}$$

Applying Equations (6.4) and (6.5) still ensures that the stress-points are orientated in the direction of the node velocities – they are simply shifted horizontally or vertically to also allow a staggered node-stress-point arrangement.

The results of the cohesive and non-cohesive problems when the stress-point positions were updated to align with the velocity vectors are provided in Figure 6.13. In both cases, the expected material behaviour has been predicted well, and there are no signs of the tensile instability in the cohesive soil. The nodes are coloured by values of vertical stress, where it can be seen that the profile is not completely smooth throughout the material. The stress profile is noisy in certain areas of the material, particularly in the regions where the overall displacement is minimal. This is attributed to small scale fluctuations of the nodes in this area, which can cause the stress-point orientation to change rapidly. Small node oscillations are often inevitable in meshless methods, even with the implementation of stabilising techniques. Here, they are only significant in areas where the overall material behaviour is almost stationary, yet they have a significant impact on the stress-point positions. The method described above is independent of the velocity magnitude at each node – the stress-point placement is identical for two nodes travelling in the same direction at different speeds.

To remove the problems associated with the node oscillations, the method is only applied to the nodes that are in motion. This requires the calculation of the relative displacement s_{rel} at a specified number of time steps n_t, for each node. If the value of s_{rel} at a node is greater than a threshold value s_{tol} then the stress-points associated with that node are positioned according to its velocity vector, as described above. Otherwise, the stress-point positions are not adapted and they are updated

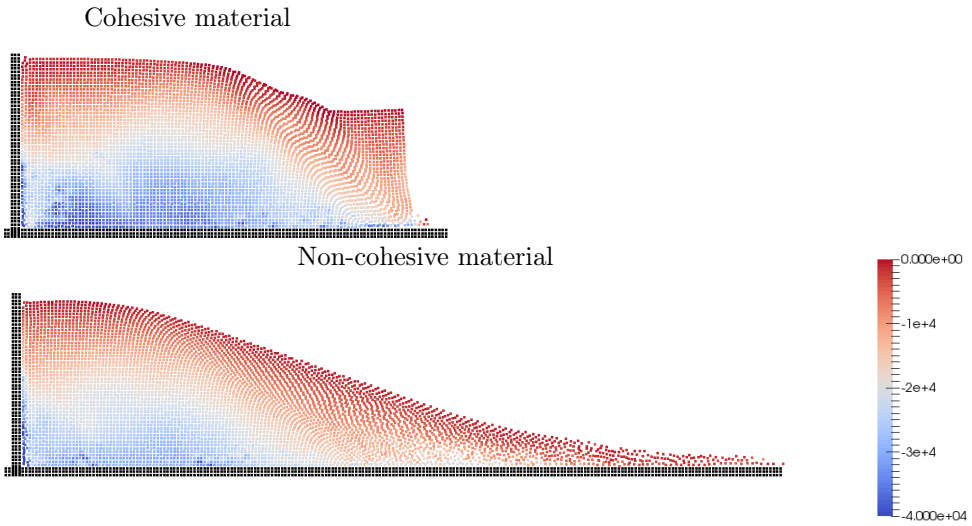

FIGURE 6.13: Node positions at $t = 2.5$ s with contour plots of vertical stress σ_{yy} (Pa), where all stress-point positions were updated to align with the velocity vector at each node.

according to their interpolated velocity. Alternatively, if $s_{rel} < s_{tol}$ the distances r_x and r_y can simply not be updated, rather than updating the stress-point according to the interpolated velocity. In this research, the differences between the two latter method was found to be insignificant if a sufficiently small value of n_t was chosen. Note that the values of s_{tol} and n_t must be large enough to remove the effects of the velocity fluctuations, but still ensure that the stress-point positions are updated for mobile nodes. For the cohesive and non-cohesive soil problems, suitable values of the two parameters were found to be $s_{tol} = 0.125\Delta x$ ($= 0.005$ m) and $n_t = 1000$ ($= 0.015$ s). Contour plots of stress are provided in Figure 6.14 for the cohesive and non-cohesive soil problems, where the stress-points were defined to align with the node velocity vectors for nodes with a displacement greater than s_{tol} every n_t time steps. With this adaptation, the velocity profiles are smooth throughout the material for both problems.

6.5 Collapse of a Von Mises material

Here the collapse of a viscoplastic Von Mises material is investigated. The material is initially positioned in a rectangular shape with a width of 4 m and a height of 2 m, as shown in Figure 6.15. It is horizontally unconstrained to allow the propagation in both the positive and negative x directions. The material is described with a viscoplastic Perzyna rheology, with a Von Mises yield function. The model parameters are provided in Table 6.1. A total of 3321 SPH nodes initially spaced apart by a distance of $\Delta x = 0.05$ m were used to model the material, with a smoothing length of $h_s = 1.2\Delta x$ and a time step of $\Delta t = 5 \times 10^{-5}$ s. Dummy nodes were employed to model the no-slip wall beneath the material, and artificial viscosity was included with parameters $\alpha_\Pi = \beta_\Pi = 0.1$. First, the results of a Standard SPH

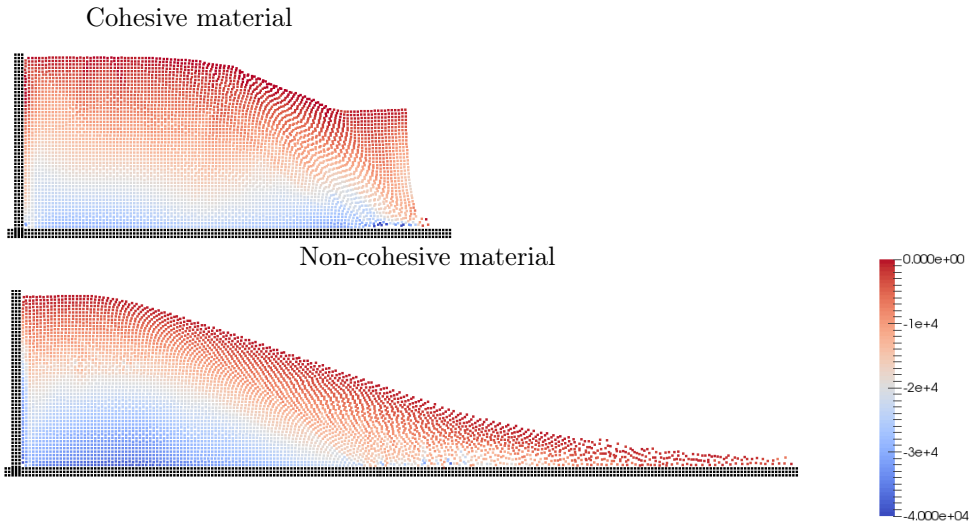

FIGURE 6.14: Node positions at $t = 2.5$ s with contour plots of vertical stress σ_{yy} (Pa), where the stress-point positions were updated to align with the velocity vector at each node. The method was only applied to the nodes that had displaced more than $s_{tol} = 0.125\Delta x$ every $n_t = 1000$ time steps.

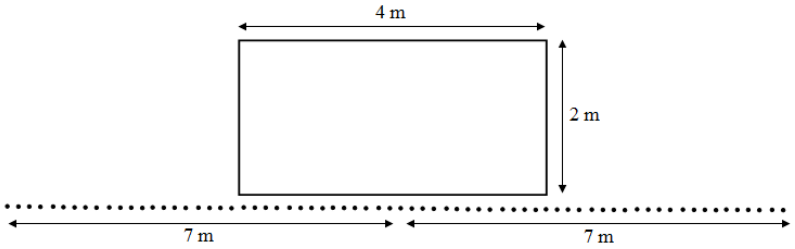

FIGURE 6.15: A schematic diagram of the Von Mises material collapse problem.

simulation are presented to show that the problem exhibits typical effects of the tensile instability. The Stress-Particle outside approach is then applied to this problem in order to examine further its capabilities of resolving the numerical instabilities. The effects of the stress-point arrangement and stress-point position update are also investigated. The artificial stress (Monaghan, 2000) and particle shifting (Xu and Yu, 2018) methods are also applied to the problem, for comparison with the outside approach results.

The evolution of the Von Mises material is shown in Figure 6.16a for Standard SPH. The material deformation is symmetric about the vertical axis. At $t = 0.8$ s, it can be seen that particles have started to clump together along the free surface.

TABLE 6.1: Perzyna model parameters for the Von Mises material collapse.

E (Pa)	ν	ρ (kg m^{-3})	F_0 (Pa)	γ (s^{-1})	N
1.5×10^6	0.3	1850	2×10^4	5	1

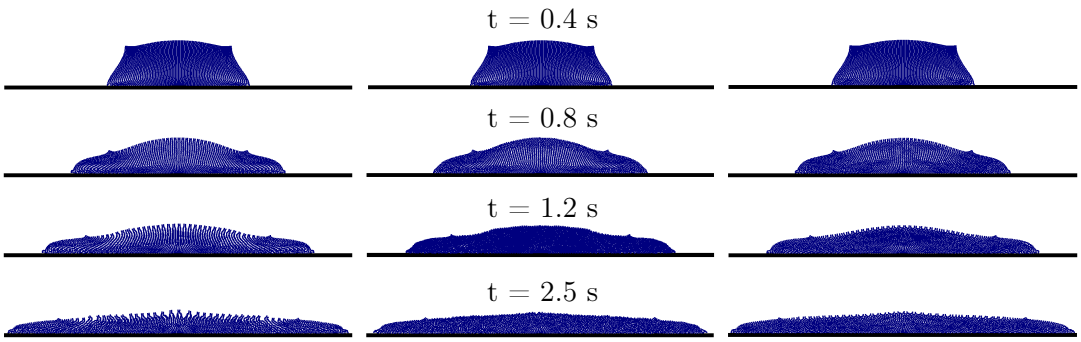

(A) Standard SPH (B) Standard SPH with artificial repulsive force (C) Standard SPH with particle shifting

FIGURE 6.16: Snapshots of node positions for the collapse of the Von Mises material: displayed are the results calculated with Standard SPH, along with the inclusion of the artificial stress and the particle shifting technique.

This results in the formation of fractures throughout the material, which become more severe as the material spreads and deforms. These features occur in the region where the material is under tensile stress, and are typical manifestations of the tensile instability (Swegle et al., 1994; Monaghan, 2000; Xu and Yu, 2018). The simulation was also performed with the inclusion of two remedies from the literature for the tensile instability – the artificial stress (Monaghan, 2000) and the particle shifting technique (Xu and Yu, 2018). These results are shown in Figures 6.16b and 6.16c respectively. With the artificial stress (with a tuning parameter of $\epsilon = 0.7$), the fractures have been eliminated. However, the nodes on the free surface at $t = 2.5$ s exhibit a bumpy profile. As was the case for the cohesive soil problem, the particle shifting method has failed to eliminate the material fractures at the free surface, which can be observed from time $t = 0.8$ s onwards in Figure 6.16c.

Snapshots of the propagation of the Von Mises material simulated with the outside approach are provided in Figure 6.17a, for configuration IIA. The material is coloured by values of vertical stress. The stress-points were assigned to follow their associated nodes throughout the simulation. The non-physical fractures that are evident in the Standard SPH results (see Figure 6.16a) appear to have been eliminated completely. The results of Standard SPH with the artificial repulsive force are provided for comparison in Figure 6.17b. The stress-profiles for the outside approach results are significantly smoother than for Standard SPH, which exhibit an excessive amount of noise.

To investigate further the effect that the stress-point placement has on the simulation results, different configurations of the outside approach were utilised to model the collapse of the Von Mises material. The results are displayed in Figure 6.18 at $t = 1.2$ s and $t = 2.5$ s. The stress-points were assigned to follow their corresponding nodes. At $t = 1.2$ s, the flow streamlines are orientated slightly in the positive $x-$direction for configuration IIB, which results in a discontinuity to the

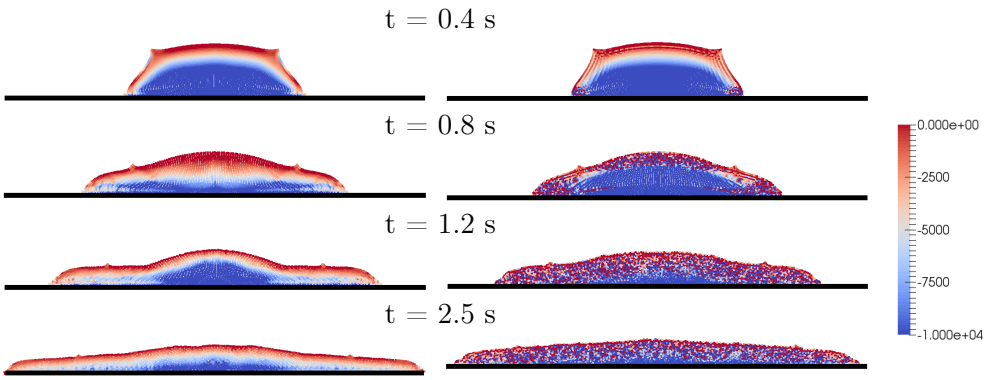

(A) Stress-Particle outside approach, configuration IIA

(B) Standard SPH with the artificial stress

FIGURE 6.17: Snapshots of the material evolution for the Von Mises material collapse, comparing the Stress-Particle SPH and Standard SPH results. The nodes are coloured by contours of vertical stress σ_{yy} (Pa).

right of the material centre at $t = 2.5$ s (see Figure 6.18b). Similarly, for configuration IID, the streamlines are aligned towards the negative $x-$direction at $t = 1.2$ s, and a discontinuity to the left of the material centre is exhibited at $t = 2.5$ s (see Figure 6.18d). This observed behaviour corresponds to the stress-point orientation for configurations IIB and IID: IIB consists of two stress-points positioned diagonally on either side of each node, where the upper stress-point is to the right of the node and the lower is to the left. Configuration IID is the opposite of this – the upper stress-point is to the left of the node and the lower is to the right. For configuration IIA, with two stress-points placed below each node on either side, the material deformation is symmetric about the y-axis, as expected for this problem (Figures 6.17 and 6.18a). This corresponds to the fact that the stress-point positions in IIA are symmetric about the $y-$axis, unlike in configurations IIB and IID. These results provide another example of how the material behaviour is sensitive to the stress-point arrangement, and suggest that for a symmetric flow, the stress-point orientation should also be symmetric about the line of symmetry. Moreover, these results support the proposition that the stress-point arrangement should be aligned with the general direction of the flow. The most stable results were obtained using configuration IIA, which bears the closest resemblance to the general flow field.

Figure 6.18c shows the Von Mises material collapse at $t = 1.2$ s and $t = 2.5$ s for configuration IIC. As for IIA, configuration IIC is symmetric about the $y-$axis, where two stress-points are positioned above each node at either side. For this configuration the numerical simulation becomes unstable and by $t = 2.5$ s the material behaviour is extremely non-physical. There is a dramatic difference between these results, and those computed with configuration IIA (Figures 6.17a and 6.18a). The only difference between the numerical models is that in configuration IIC the stress-points are placed above each node, as opposed to below each node in IIA. However, the local node-stress-points arrangement in configuration IIC is such that both of the stress-points

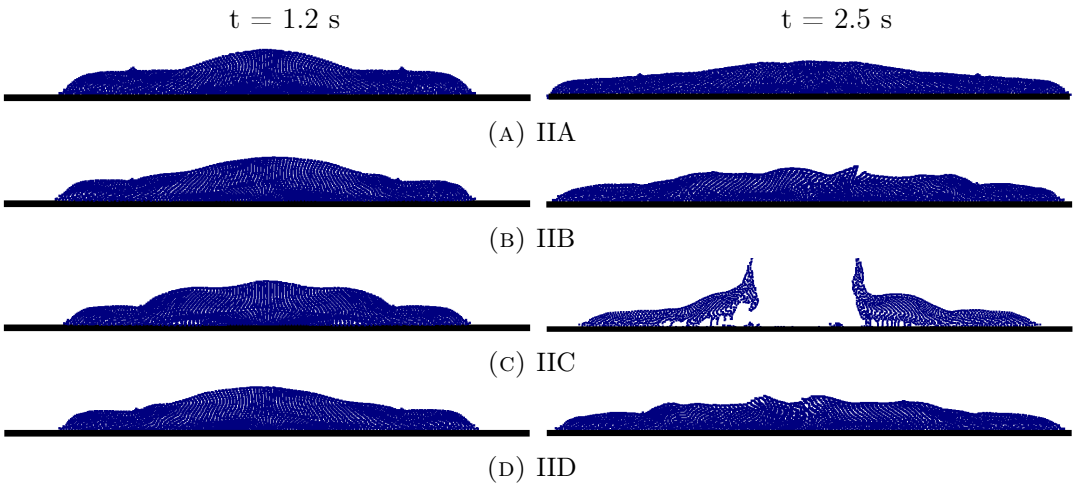

FIGURE 6.18: Node positions at $t = 1.2$ s and $t = 2.5$ s of the Von Mises material collapse, for the different node-stress-point configurations shown in Figure 6.1.

oppose the direction of the flow motion. Furthermore, it is of potential significance that for configuration IIC the free surface is always composed of stress-points, and not nodes. The calculations on the free surface stress-points are less accurate than for interior stress-points, as there are fewer surrounding nodes for the SPH calculations. Hence, it is likely that the abundance of free surface stress-points in configuration IIC contributes to the unstable behaviour shown in Figure 6.18c. Problems associated with free surface stress-points could also be partly responsible for the instabilities observed in Figures 6.18b and 6.18d. The location of the instabilities for these results coincides with the location of free surface stress-points in both cases (which is on opposite sides of the $y-$axis for the two configurations).

In Section 6.3 it was shown that with regards to removing the effects of the tensile instability, the outside approach performed well when the stress-point positions were updated according to their interpolated velocity. However this method of updating the stress-points was not sufficient when applied to the non-cohesive soil failure, which exhibited large displacements. Consequently, in Section 6.4 the outside approach was extended so that the stress-point shifting could be determined by the stress-point concentration at each node. The stress-points associated with nodes with a stress-point concentration lower than a threshold value were shifted back to their original position (with respect to the nodes), and all other stress-points were updated according to their interpolated velocity. An appropriate threshold value was found to be 80 percent of the initial stress-point concentration. The Von Mises problem was modelled with this method of updating the stress-point positions, for configuration IIA of the outside approach. The material at $t = 2.5$ s is shown in Figure 6.19b, compared against the results where all stress-points were assigned to follow their associated nodes (Figure 6.19a). With the concentration threshold method the material deformation is not symmetric about the vertical axis, and displays additional stiffness around the centre. This section is shown in closer detail,

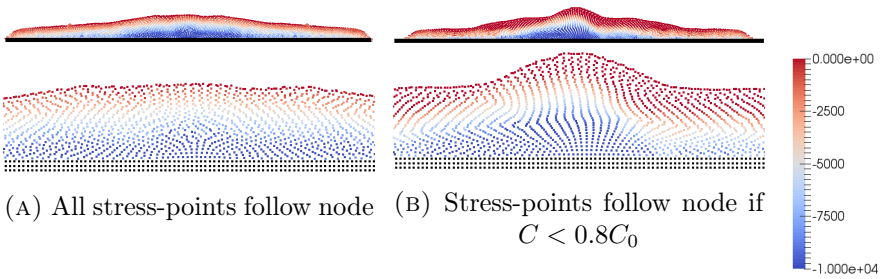

(A) All stress-points follow node (B) Stress-points follow node if $C < 0.8C_0$

FIGURE 6.19: Node positions at $t = 2.5$ s for the Von Mises material collapse, with configuration IIA of the outside approach. The nodes are coloured by values of vertical stress σ_{yy} (Pa).

where it can be seen that the nodes have formed anisotropic structures that follow the flow trajectories. Such structures were observed in the results of the cohesive soil failure in Sections 5.5.1 and 6.3, where it was suggested that they were an indication of the accuracy of the Stress-Particle method. However for the Von Mises problem, as a consequence of these structures the nodes in the centre of the material are unable to compress beyond a certain amount (or the SPH nodes would overlap). Therefore the trajectories have instead shifted towards one side. Errors associated with the formation of anisotropic structures have been documented previously in the SPH literature (Oger et al., 2016).

Another extension of the outside approach was developed earlier in this chapter, which involved assigning the stress-point positions to align with the velocity vectors at each node. This method is described in Section 6.4.2, and it was shown to be capable of removing the tensile instability in the cohesive soil and predicting the large displacements in the non-cohesive soil. This method has here been applied to the Von Mises material collapse (with the parameter $r = \frac{\Delta x}{2}$). Due to the rapid propagation of the material, the displacement threshold s_{tol} was defined to be equal to $0.025\Delta x$, and the relative displacement s_{rel} was calculated every $n_t = 500$ time steps. As described in Section 6.4.2, the stress-points were assigned to align with the velocity vectors for the nodes with $s_{rel} > s_{tol}$. The material propagation is shown in Figure 6.20 along with the Standard SPH results (with the artificial stress), where the nodes are coloured by values of vertical stress. There are no obvious effects of the tensile instability with the Stress-Particle method, nor any other instabilities that were observed for other stress-point configurations (see Figure 6.18). The free surface profiles obtained with this extension of the outside approach are compared directly with those of Standard SPH in Figure 6.21. The shape of the material as it deforms aligns closely between the two models at $t = 0.4$ s and $t = 0.8$ s. At later times, the profiles differ somewhat from one another, particularly in the centre of the material. The final run-out distances coincide – the material reaches a distance of approximately 6.727 m in both the positive and negative horizontal direction. Recall that for the cohesive soil problem, the free surface profile varied according to the tuning parameter ϵ in the artificial stress method (see Section 5.5.1). The effect of this parameter is not investigated here, but is likely to affect the Standard SPH

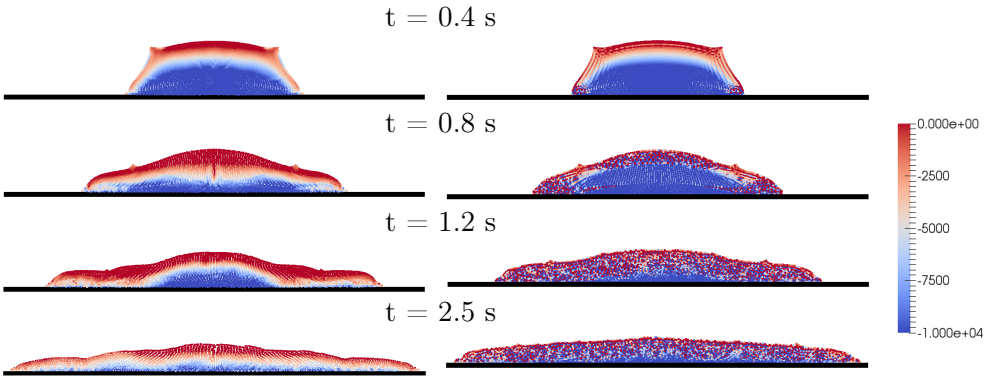

(A) Stress-Particle outside approach, with the stress-points aligned with the velocity vectors

(B) Standard SPH with the artificial repulsive force

FIGURE 6.20: Snapshots of the material evolution for the Von Mises material collapse, comparing Stress-Particle SPH and Standard SPH. The nodes are coloured by contours of vertical stress σ_{yy} (Pa).

results.

6.6 Conclusion

Following the promising results of Stress-Particle SPH when applied to soil failure mechanisms (see Chapter 5), this chapter has been devoted to the extension of the method (using the outside approach) for problems involving the post-failure behaviour of soil. These type of problems represent landslide propagation of the flow-type, and feature large displacements. While the inside approach is capable of eliminating the tensile instability and zero-energy modes, it is unable to model flow-type problems due to the way in which the stress-point positions are updated (see Section 5.5.2). Here, the outside approach was first applied to model the failure and propagation of a non-cohesive soil, that displayed flow-type behaviour. The stress-points were initially defined to follow their assigned nodes throughout the duration of the simulation, which eliminates the problems encountered in the inside approach. With more than one stress-point per node, the method was able to capture the large displacements of the non-cohesive soil, and the free surface profiles compared well between the outside approach and Standard SPH (see Figure 6.5). Furthermore, in the previous chapter the inside approach was shown to encounter problems in the boundary regions, and a boundary repulsive force was required to prevent the nodes from penetrating walls. By having stress-points associated with individual nodes in the outside approach, it is possible to 'turn off' the stress-points for the nodes at the boundary to reduce the complications in this region. With this, no repulsive force is required at the boundary, eliminating a second problem encountered in the inside approach.

In addition to capturing large displacements, Stress-Particle SPH with the outside approach must be capable of eliminating the effects of the tensile instability. To

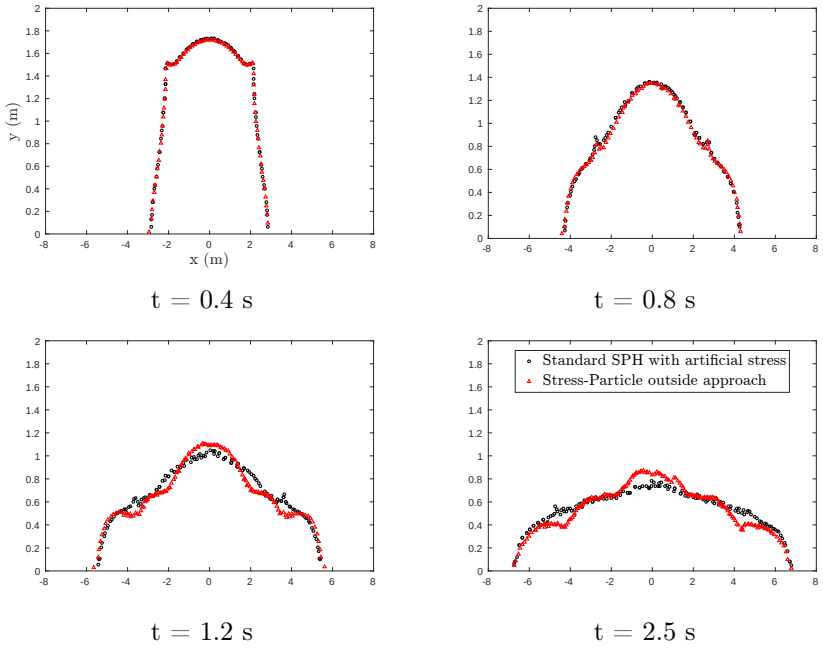

FIGURE 6.21: Free surface profiles for the Von Mises material collapse. The black markers represent the results from Standard SPH with the artificial stress, while the red markers represent the results from the outside approach, where the stress-points were defined to align with the node velocity field

check this, the outside approach was next applied to simulate the problem of the cohesive soil failure (which exhibits severe fractures due to the tensile instability). When the stress-points were assigned to follow their associated nodes, the performance of the outside approach was dependent on the node-stress-point arrangement. For certain configurations, the effects of the tensile instability were not completely eliminated (despite having two or three stress-points per node). Moreover, the general soil behaviour was affected by the stress-point arrangement, and different material profiles were obtained for the different configurations (see Figure 6.8). The most accurate results were achieved when the stress-points were approximately aligned with the general flow direction. An explanation for these observations is given as follows. When the stress-points follow their assigned nodes, the stress-point locations relative to the node are constant throughout the entire simulation. Although the stress-points are generally thought of as interpolation points (as opposed to being a part of the material), the stress calculation on the node is strongly dependent on the stress-point. Namely, the calculation is dependent on the value of the smoothing kernel, which is constant between the node and its associated stress-point for the duration of the calculation. Thus, the stress-point placement clearly influences the flow. It is unnatural to have stress-points positioned in areas where there would not usually be a material point to influence the stress calculations on a node. Therefore, it can be concluded that the stress-points should be aligned with the material motion. This conclusion was verified in the application of the outside approach to

the final problem considered in this chapter – the propagation of a viscoplastic Von Mises material. When two stress-points were positioned above each node on either side (in the opposite direction of the general material propagation), the flow calculation became unstable which lead to the complete degradation of the simulation (see Figure 6.18c). When the stress-points approximately aligned with the flow motion (for configuration IIA), the simulation results were stable and exhibited the expected material behaviour (see Figure 6.17).

Motivated by the conclusion that the Stress-Particle method is most effective when the stress-points align with the direction of motion, two techniques to improve the outside approach were explored in this chapter. This first was to specify a stress-point concentration threshold at each node which defined how the stress-point positions were updated. Those associated with nodes with a concentration lower than the threshold value were assigned to follow that node. Otherwise, the stress-points were moved according to their interpolated velocity. This method worked well for the cohesive and non-cohesive soil problems, but it is not a universal solution. A more universal technique to improve the outside approach consisted of aligning two stress-points with the velocity vector at each node, and assigning them to follow the node. The stress-point orientation therefore evolved with the flow. This method provided a way in which to capture the dynamics of large deformations, while not affecting the material propagation in an unrealistic way. With this technique the outside approach was able to eliminate the fractures in the cohesive soil problem, and accurately capture the large displacements in the non-cohesive soil (see Figure 6.14). The method also performed well for the Von Mises problem, where the final material run-out distance was the same as the results from Standard SPH (see Figure 6.21). These results confirm that the stress-points should be orientated in the direction of the flow field, for the optimum performance of Stress-Particle SPH.

The results presented in this chapter show that the Stress-Particle SPH model is capable of bridging the gap between the numerical modelling of the failure and post-failure behaviour of soil. The model is applicable to landslide triggering mechanisms (i.e. the formation of slip surfaces in the cohesive soil), in addition to rapid propagation of the flow-type (such as the behaviour exhibited by the non-cohesive soil and Von Mises material). Therefore, the Stress-Particle SPH model is able to simulate the broad range of behaviour exhibited by landslides with accuracy and stability – fulfilling the primary aim of this research. Moreover, the developments to the Stress-Particle method offer the potential for SPH to tackle a much broader range of problems than it is currently capable of – until now, SPH was not able to adequately eliminate all numerical instabilities in a way that still allows the simulation of large displacements. From here, the Stress-Particle SPH method is applied to another problem involving landslide behaviour. In the following chapter, a small scale experiment of a debris flow is presented. The Stress-Particle method is then utilised to model these results, which exhibit complex two-phase behaviour and high velocities. This provides a new type of problem in which to assess the performance

of Stress-Particle SPH.

Chapter 7

Spatial and temporal evolution of an experimental debris flow, exhibiting coupled fluid and particulate phases

7.1 Introduction

Following material failure, granular matter can propagate at rapid rates, exhibiting fluid-like behaviour. Examples of this were presented in the previous chapter, where SPH was used to model the post-failure behaviour of a non-cohesive soil, and a viscoplastic Perzyna material. These problems consisted of a single granular phase. In reality, granular material often becomes mixed with water post-failure, and develops into a *debris flow* – a gravity-driven flow where the interaction of both solid and fluid phases govern the dynamics (Iverson, 1997). Debris flows exhibit extremely complex and destructive behaviour, and significant research has been dedicated to the development of mathematical and numerical models to predict their dynamics (Pitman and Le, 2005; Pudasaini, 2012; Iverson and George, 2014; Pastor et al., 2015b). However, by nature, the occurrence of debris flows is unpredictable and their behaviour is dependent on a number of physical conditions, such as terrain and material composition (Iverson, 1997). Therefore, repeatable, physical models of debris flows are invaluable for the validation and development of mathematical and numerical models. In this chapter the results of a small scale experimental debris flow are presented. The Stress-Particle SPH method is then applied to model the experiment in Chapter 8, to provide further validation of the novel, numerical technique. The experimental debris flow reaches high velocities, which allows further testing of the capabilities of Stress-Particle SPH at capturing high displacements (see Chapter 6). Furthermore, simulating the experiment allows the analysis of the capabilities of SPH at modelling granular flows at a small scale.

There are various experimental methodologies that are dedicated to the investigation of one or more aspects of debris flow behaviour, under controlled conditions. Experiments have been performed within a wide range of physical scales, from those

with lengths of the order of 100 metres (Iverson et al., 2010; Johnson et al., 2012) to small scale laboratory flumes (Sanchez and Randles, 2012; Paleo Cageao, 2014; Turnbull, Bowman, and McElwaine, 2015). Large scale experiments have the benefit of being comparable to realistic debris flows. Dimensionless scaling analyses have shown that the stresses in debris flows cannot be accurately reproduced in standard small scale experiments – they exhibit disproportionately large effects of viscosity and yield strength, while the effects of pore water pressure are disproportionately small (Iverson, 2015). This is determined by considering the dimensionless parameters that characterise the force balances in debris flows (see Iverson (1997) for a detailed description of the dimensionless parameters). However, small scale experiments have the advantage of being simple and repeatable, allowing the investigation of multiple parameters. Moreover, they have been shown to be capable of reproducing key debris flow features, such as the formation of a distinct granular 'head' and fluid-like 'body' (Paleo Cageao, 2014; Turnbull, Bowman, and McElwaine, 2015), which are commonly observed in the field (Iverson, 1997). Additionally, small scale flume experiments allow the accessible observation of the internal dynamics of the flow (Sanvitale and Bowman, 2012).

An insight into the internal dynamics of debris flows is vital for understanding the mechanisms that are responsible for their motion. Qualitatively, observing the internal behaviour of individual grains provides an indication of the forces that dominate in different areas within the flow (Sanvitale and Bowman, 2012). Furthermore, information on internal flow dynamics is crucial for the development of debris flow models. The structure of the internal velocity and shear rate provides an indication of the rheological behaviour of the mixture, which is required for the governing equations of motion in mathematical and numerical models. Of the typical rheological models, there are distinct, corresponding velocity profiles that are derived when considering a simplified landslide model (see the caption of Figure 7.1 for further details). In simple analyses, the local flow shear rate is approximated as being equal to the ratio of the mean velocity to flow height (Savage and Hutter, 1989; Iverson, 1997). This corresponds to a velocity profile that is assumed to increase linearly from the flow bed. Measurements of vertical velocity profiles in steady granular flows have shown that this assumption is unrealistic (Kaitna, Dietrich, and Hsu, 2014; Paleo Cageao, 2014; Sanvitale and Bowman, 2017). Typical debris flow models often assume a viscoplastic rheology, where a yield stress is introduced to distinguish between plug regions and viscous fluid behaviour. Examples of this include the Bingham, Herschel-Bulkley and Perzyna models. In the simplified landslide assumption, the expected velocity profile for viscous-type fluid takes the shape of a half-parabola, governed by the following equation:

$$u(y) \propto H^2 - (H - y)^2, \tag{7.1}$$

where H is the height of the flow. This profile is shown in Figure 7.1, where it is depicted by the dashed-dotted line. For viscoplastic plug-type flows such as those described by the Herschel-Bulkley and Perzyna models, the profile is represented by

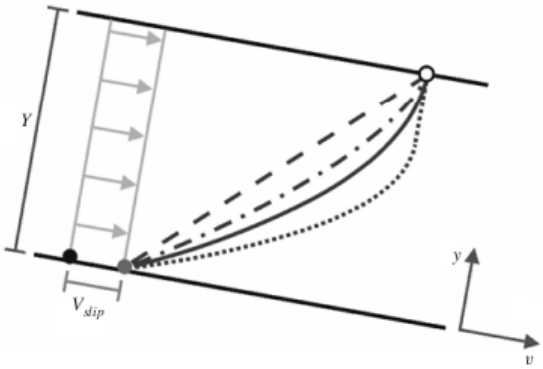

FIGURE 7.1: The different velocity profile shapes expected in an idealised water-granular free surface steady flow, from Kaitna, Dietrich, and Hsu (2014). The horizontal axis is horizontal velocity and the vertical is flow height. The profiles were derived under the assumption of a wide flow with uniform cross-stream conditions, constant flow height and a non-erodible bed. The types of profile are linear (dashed line), granular-type (dashed-dotted line), half-parabolic viscous-type (solid line) and a viscoplastic plug-type (dotted line).

Equation (7.1) in the sheared region, with a constant value in the plug region. This expected shape is given by the dotted line in Figure 7.1. Viscous and viscoplastic profiles have been observed in the steady, body region of experimental debris flow models (Kaitna, Dietrich, and Hsu, 2014; Kaitna et al., 2016; Sanvitale and Bowman, 2017). Alternatively, for flows where granular collisions dominate over viscous forces, the expected velocity profile derived in the infinite landslide assumption is

$$u(y) \propto H^{\frac{3}{2}} - (H - y)^{\frac{3}{2}}. \tag{7.2}$$

The derivation of Equation 7.2 is based upon the findings of Bagnold (1954), who determined two regimes in a suspension of non-cohesive grains – viscous and collisional. Internal velocity profiles of steady, experimental debris flows have also been found to exhibit a granular-type profile (Kaitna, Dietrich, and Hsu, 2014; Kaitna et al., 2016; Sanvitale and Bowman, 2017). Although Equations (7.1) and (7.2) are derived from idealised conditions, they give an indication of the dominant behaviour in granular flows and provide some basis for assumptions regarding rheological models.

In the present research, experiments were performed in a small scale Perspex flume, allowing the observation of the internal dynamics through the side wall of the flume. A mixture of realistic, granular material was released from behind a lock gate in a dam break scenario. This method of flow initiation provides excellent comparative for the numerical implementation with SPH. The mixture consisted of a high water to solid ratio (with a solid volume fraction of $\phi_s = 0.44$), to achieve a rapid granular flow that travelled along the entire length of the flume before depositing on a flat run-out area. This value of the solid volume fraction was determined by performing numerous tests with different solid-water ratios, and observing the flow behaviour. As mentioned previously, one of the aims of the current research

is to assess the roles of Standard SPH and Stress-Particle SPH with regards to the behaviour of granular material. The experimental debris flow represents an extreme case of post-failure behaviour in terms of material velocity, for the simulation with both Standard and Stress-Particle SPH. The experimental flow was recorded with a high speed camera, from which material velocities and shear rates were obtained using a Particle Image Velocimetry (PIV) technique. From this, conclusions can be drawn regarding the rheological behaviour of the flow, and the appropriate way in which to implement the problem numerically. The experimental methodology is explained in further detail in Section 7.2, including a description of the PIV method. The results are then presented in Section 7.3, before a discussion on the observed behaviour of the water-granular mixture. Finally, a conclusion is made regarding the appropriate steps for modelling the experiment with SPH.

7.2 Experimental methodology

A mixture of water and sediment was manually released from behind a lock gate in a rectangular flume of dimension $1.9 \times 0.2 \times 0.1$ m, at an inclination of $31°$ (see Figure 7.2). This angle of inclination corresponds to that of large scale flume experiments at the United States Geological Survey debris flow flume (Iverson et al., 2010). The mixture consisted of 2.177 kg of sediment and 1.5 l of water, resulting in a total volume of 0.0026775 m^3. The sediment phase was composed of multicoloured, crushed glass grit with an angular shape, to represent natural granular material. The particle size distribution is shown in Figure 7.3. The mean particle size is $d_{50} = 0.917$ mm, where d_x denotes the percentage passing by area. The coefficient of uniformity $C_U = \frac{d_{60}}{d_{10}}$ represents the particle size variety, where $d_{60} = 1$ mm, $d_{10} = 0.1928$ mm and $C_U = 5$ (to the nearest integer). The finer particles are expected to contribute to the viscous effects that are frequently observed in granular flows (Iverson, 1997). Sediment of the same grade was permanently fixed onto the flume bed to generate roughness which would produce a no-slip flow. It was found that due to the friction created by the bed roughness, mixtures with a volume fraction less than $\phi_s = 0.44$ did not propagate along the length of the flume.

A shear box test was conducted to determine the mechanical properties of the granular material. In this test, a sample of the material is placed inside a brass box that is split into two halves. A constant vertical stress is applied to the top of the sample, and the two halves of the box are sheared relative to one another. The shear load acting on the sample is recorded, along with the displacement of the material inside the box. From this, the evolution of the shear stress against strain can be obtained, and the peak value of shear stress corresponds to the shear strength of the material. The tests are repeated at different vertical loads, to obtain the relationship between the normal stress and the peak shear stress values. The data obtained for the saturated glass grit are provided in Figure 7.4, for normal stress values of 30 kPa, 60 kPa, 100 kPa and 130 kPa. A linear fit is applied to the relationship between the

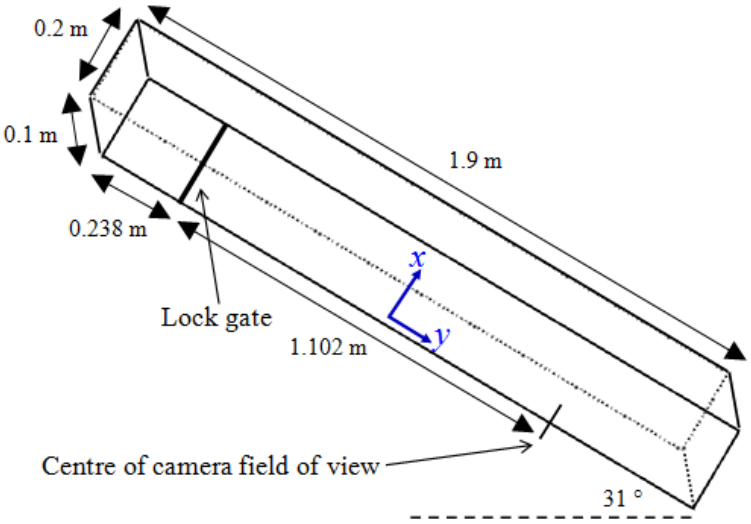

FIGURE 7.2: A schematic depiction of the experimental flume.

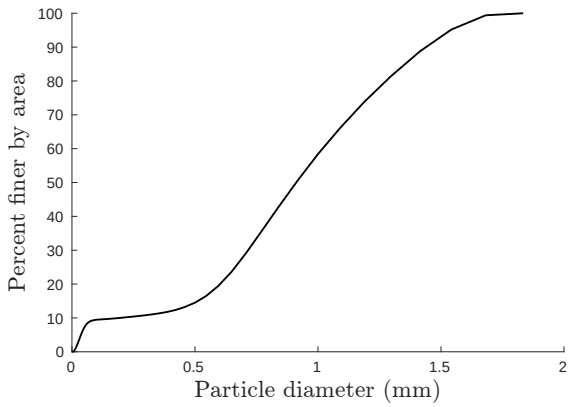

FIGURE 7.3: Particle size distribution for the glass grit.

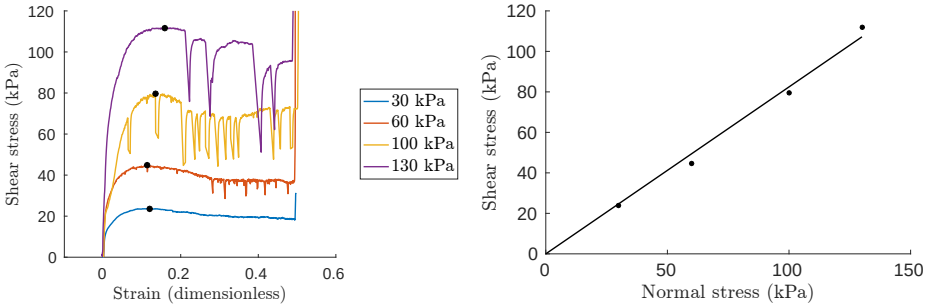

(A) Stress-strain relationship (B) Yield surface

FIGURE 7.4: Shear box test data.

normal stress and the peak shear stress, as shown in Figure 7.4b. The gradient and the $y-$intercept of this fit correspond to the internal friction angle ϕ and the cohesion c_{oh} of the material respectively. The glass grit was found to be non-cohesive, with an internal friction angle of $\phi = 39°$. The shear modulus K of the material can be approximated as the gradient of the strain-stress curve before the peak values. From this the elastic modulus E can be calculated (which is required for model input), which was approximated to be 6.916×10^5 Pa. See Powrie (2004) for further details on shear box tests.

At the beginning of each experimental run, 2.177 kg of glass grit was placed behind a lock gate with a cross-sectional area in the shape of a trapezoid, occupying a volume of 0.0017255 m^3. Subsequently, 1.5 l of water was added slowly to minimise the disturbance to the top of the sediment. The porosity of the sediment was large enough to ensure that it was fully saturated with water. The initial placement of the sediment and water is depicted in Figure 7.5, where the bottom layer consists of a mixture of water and glass grit, while the top layer is composed of water only. The total volume fraction of the water ϕ_w over both layers is calculated as the ratio of the total volume of water V_w and the total volume occupied by the water-granular mixture V_m:

$$\phi_w = \frac{V_w}{V_m} = \frac{0.0015}{0.0026775} = 0.56 \text{ (to 2 decimal places).}$$

The volume fraction of the sediment ϕ_s in the total mixture is then determined according to the following relation:

$$\phi_f + \phi_s = 1 \Rightarrow \phi_s = 1 - \phi_f = 0.44.$$

The density of the sediment phase can be approximated by considering the material in the bottom layer. The total volume of water in the bottom layer is 0.000548 m^3 (which is the difference between the total volume of water and the volume of the upper layer). The void ratio of water in the bottom layer only is therefore $\frac{0.000548}{0.0017255} = 0.32$ (to 2 decimal places), and the void ratio of the sediment is consequently 0.68 in this layer. Furthermore, the density of the mixture ρ_m in the bottom layer is the

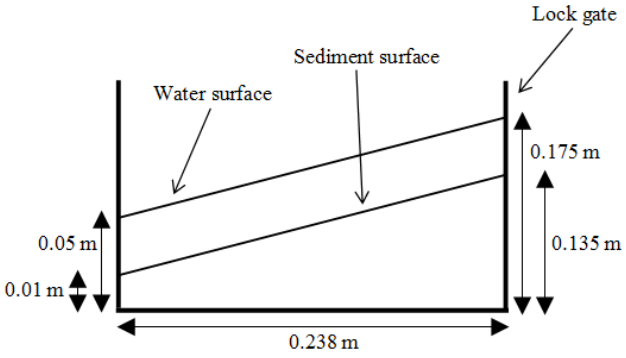

FIGURE 7.5: The initial placement of the water-granular mixture behind the lock gate.

TABLE 7.1: Properties of the material used in the debris flow experiments.

E (Pa)	ϕ (°)	c_{oh} (Pa)	ρ_w (kg m^{-3})	ρ_s (kg m^{-3})	ϕ_s
6.916 $\times 10^5$	39	0	997	1851	0.44

total mass of the mixture contained in the layer, divided by the total volume:

$$\rho_m = \frac{2.1777 + 0.548}{0.0017255} = 1580 \text{ kg m}^{-3} \text{ (to the nearest integer)}.$$

The sediment phase can then be approximated by assuming that the density of the mixture in the bottom layer is the sum of the densities of the two phases multiplied by their respective volume fractions:

$$\rho_m = \phi_s \rho_s + \phi_f \rho_f,$$

where the subscripts m, s and f denote the mixture, sediment and fluid respectively. To the nearest integer, the sediment density is calculated to be 1851 kg m^{-3} (where the density of water is 997 kg m^{-3}). A summary of the relevant material parameters is provided in Table 7.1.

To check for repeatability the debris flow experiments were performed three times. The surface of the sediment phase was marked onto the flume, to ensure that it was placed in the same initial position for each experimental run. Upon release of the lock gate, and coeval triggering of the high speed camera, the mixture propagated downstream along the length of the flume and onto the run-out area. To observe the propagation of the flow, a high speed camera was positioned with its centre 1.102 m downstream from the lock gate, with the front of the lens 0.19 m from the flume. The respective make and model of the camera are Vision Research, Miro M120 Colour. The lens is a Zeiss, 50 mm F1.4 ZF2 Planar. In order to capture the rapid flow dynamics, the images were taken at a rate of 1200 frames per second, with an exposure time of 200 μs and a resolution of 1280 $\times$ 800 pixels. This short exposure time required the addition of extra lighting to obtain a suitable image

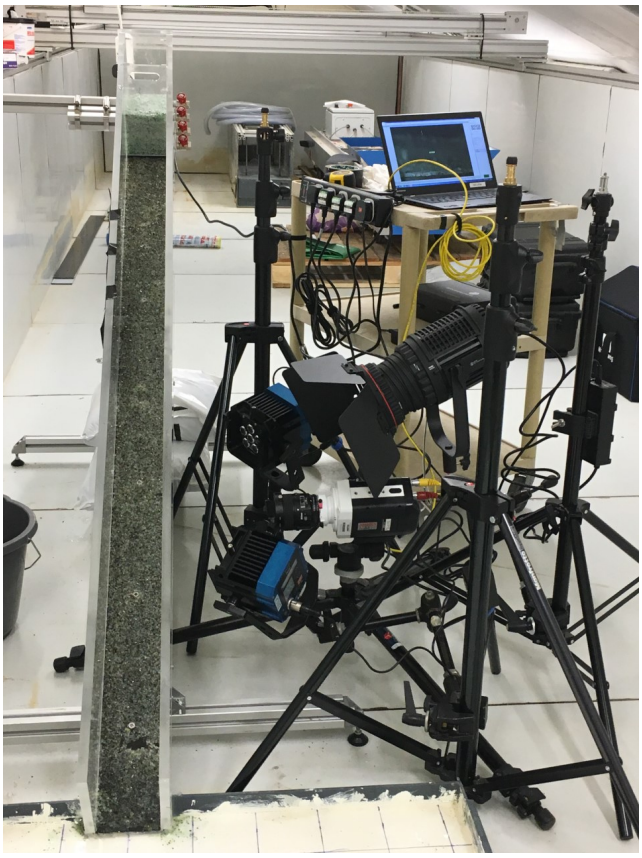

FIGURE 7.6: A photograph of the experimental set-up just prior to flow initiation. The set-up consists of a perspex channel with a roughened bed, that runs out onto a broader surface (at the bottom of the picture). A high speed camera and multiple LED lamps are used to visualise the flow.

quality. For this, two Nila LED lights (model Zaila) were placed on either side of the camera, and one NanGuang LED light (model CN-60F) was positioned above it. The three lights were directed to optimise the light conditions in front of the camera. A photograph of the experimental set-up is shown in Figure 7.6. Water was poured along the flume bed before and after each experimental run to ensure the removal of any loose sediment that had stuck to the bed. Furthermore, a wet bed typically provides more realistic conditions than a completely dry bed.

7.2.1 Particle Image Velocimetry (PIV)

A Particle Image Velocimetry (PIV) processing method was applied to the images obtained with the high speed camera. This is an experimental technique used within fluid dynamics, where instantaneous velocity fields are determined by tracking the displacements of individual particles, or groups of particles, within a flow (Adrian and Westerweel, 2011). The method (in two dimensions) involves splitting each image frame into a number of interrogation areas, within which the movement of particles is tracked between subsequent frames. The displacement is obtained by estimating the cross-correlation between the particle positions within each interrogation area,

where the true displacement of each particle group must be separated from the noise created by particles overlapping between frames. This is achieved by applying statistical correlation methods to the data, to determine the most likely 'true' particle displacement. An algorithm is then applied to obtain an estimate of the velocity vector field from the displacement values, where certain features of the camera used to obtain the images are taken into consideration. An extensive description of the PIV method can be found in Adrian and Westerweel (2011).

The size of each interrogation area should be optimised so that it is large enough to contain a sufficient number of particles to track the flow movement, yet not so large that there is an excessive amount of spatial averaging. Typically, the size of the area is chosen to be 32×32 or 64×64 pixels. In this research, the frames from the camera were processed with the DynamicStudio image processing software to obtain the velocity vectors. The 'Adaptive PIV' option was utilised within DynamicStudio, which automatically adjusts the interrogation area at each frame according to the local particle densities and velocity gradients. This requires the definition of the minimum and maximum values of interrogation areas, which were defined as 32×32 and 64×64 pixels respectively. The reader is referred to the DynamicStudio user manual for further details on the adaptive PIV method (Dynamics, 2018). The PIV method often requires the addition of seeding particles to track the fluid movement within each interrogation area of the flow images. This is not necessary in the current application as the granular mixture under consideration is multicoloured, and individual grains are easily distinguished. Note that the method relies on particle detection, and therefore won't produce accurate results in regions where particles are lacking.

The PIV analysis was applied to the images of the flow along the side wall, under the assumption of a two-dimensional flow. This is subject to error as the propagating material is not completely uniform across the width of the channel. Furthermore, the flow dynamics are likely to differ somewhat at the flow margin than in the centre, due to the influence of the wall. An alternative option is to use a laser sheet to illuminate a plane in the flow centre, and capture the images in this region for the PIV analysis. This method requires the combination of clear particles and a fluid that is refractive index matched, and has been applied recently by Sanvitale and Bowman (2017) to capture the internal dynamics of a granular-fluid mixture in an inclined flume. While the flow dynamics along the flume centre are less influenced by wall effects, the technique did not allow the tracking of the flow head, or the top 2 - 4 mm of the flow.

The rate at which the flow images are captured for analysis with the PIV method must be high enough to capture the local movement of particles. For accurate velocity measurements, the particle displacement between two consecutive frames should not be larger than one quarter of the interrogation area (Adrian and Westerweel, 2011). For this reason, a frame rate of 1200 frames per second was chosen. Time averaged velocity profiles were obtained by averaging the velocity vectors over 30 successive

frames, corresponding to a time interval of 0.025 s. This time internal was chosen following similar investigations in the literature, where averages were taken over time intervals of 0.02 s (Paleo Cageao, 2014), and 0.027 s (Sanvitale and Bowman, 2017). The initial flow time ($t = 0$) was defined to be when the front of the flow first reached the field of view of the camera, and the frames were cropped so that the first frame corresponded to $t = 0$. For each considered flow time, the velocities were averaged over the 30 surrounding frames. For example, the velocities at the sixtieth frame ($t = 0.05$ s) were time averaged by averaging over frames 45 to 75.

The velocity data obtained with DynamicStudio are provided in matrix form, where horizontal and vertical velocity components are output in separate matrices at each time frame. The location of the velocity values in each grid correspond to that of the spatial grid, which contains the x and y data. Before data post-processing, the matrix dimensions are constant at each frame as the spatial grid does not vary throughout the PIV analysis. For the experimental debris flow, the number of rows of each matrix must be cropped at each frame, to align with the free surface of the flow. This was conducted manually by inspecting the free surface position at each snapshot from the high speed camera. The flow free surface is therefore approximated as a horizontal line. In the current work, the post-processing of the PIV data was performed in Matlab.

7.3 Results

Once released from the lock gate, the soil-water mixture rapidly propagated downstream onto a horizontal run-out area, reaching front velocities in the range of $1-1.2$ m s^{-1}. The main bulk of the flow deposited onto the run-out area, although a thin layer of the granular material was deposited along the bed of the flume. The granular material was fully saturated throughout the flow. In the following results, the time $t = 0$ corresponds to when the front of the material first reached the field of view of the camera – the centre of which is located 1.102 m downstream from the lock gate. For the three experimental runs (Run 1, Run 2 and Run 3), the front of the flow reached this position at approximate times of 0.43 s, 0.79 s and 1.275 s, plus or minus any small scale variations due to the synchronisation of the lock gate release and the triggering of the high speed camera. The flow evolution relative to the time at which the flow reached the camera field of view is more relevant and comparable between runs. A snapshot from the high speed camera at 0.035 s after the material reached the field of view is shown in Figure 7.7, showing the area that was recorded throughout the flow (0.05×0.03 m^2).

Snapshots of the propagating mixture captured with the high speed camera are provided in Figure 7.8, for one of the experimental runs. The front part of the flow consists of a dilute and turbulent mixture, with a large void ratio. This region is shown at times $t = 0.035$ s and $t = 0.07$ s in Figure 7.8. Following this, the height of the flow increases and consists of two visible layers of material, which can be seen

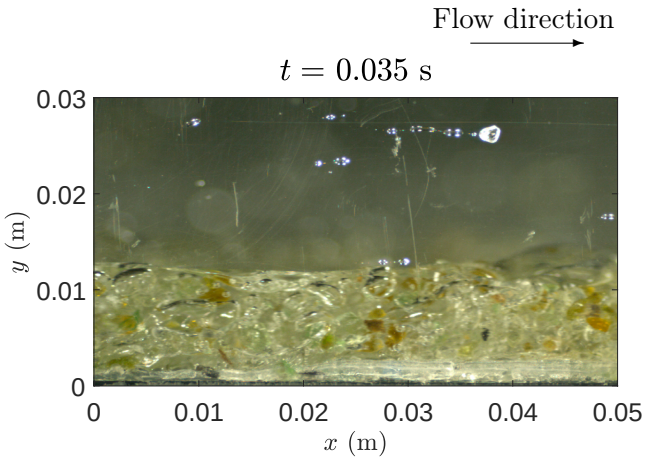

FIGURE 7.7: An snapshot of the water-granular mixture for Run 1, at $t = 0.035$ s after reaching the field of view of the camera.

clearly at $t = 0.3$ s. The bottom layer is composed of what appears to be a uniform water-granular mixture, while the main constituent of the upper layer is water, along with entrained grains with a large void ratio. The presence of the two layers persists for a short while, although the upper layer becomes less dilute with time as the large void ratios allow the rapid dissipation of the water. The distinction of the two separate layers diminishes as the flow progresses, and the material continues to propagate as a uniform mixture with a constant height. After approximately 1.4 seconds, the flow gradually decreases in height as the material velocity decreases. The mixture comes to a complete rest after 3 seconds, leaving a deposit approximately 0.5 mm in height along the flume.

As described in Section 7.2, average velocity profiles were obtained from the PIV data by calculating the mean velocity over 30 successive frames. The flow behaviour can thus be characterised by considering the standard deviation $\bar{e}$ of the velocity from the local average, within that interval:

$$\bar{e} = \sqrt{\frac{\sum_{i=1}^{N}(u'_x - \bar{u}_x)^2}{N-1}}, \tag{7.3}$$

where $\bar{u}_x$ is the average velocity over N frames, and u'_x is the instantaneous velocity. Low values of standard deviation equate to small variations in instantaneous velocity from the local mean, indicating that the flow has not changed significantly over the time interval. This type of behaviour is referred to as 'non-fluctuating'. Conversely, a high standard deviation demonstrates that the averaged velocity profile is not representative of the overall behaviour within the interval, as the flow is rapidly changing. With regards to granular flows, high standard deviations of velocity from the local average correspond to 'collisional' behaviour, which is dominated by fluid turbulence and particle collisions (Bagnold, 1954; Johnson and Jackson, 1987). A series of small scale debris flow experiments were performed by Paleo Cageao (2014), where sufficiently low deviation from the average was defined as being less than 0.15

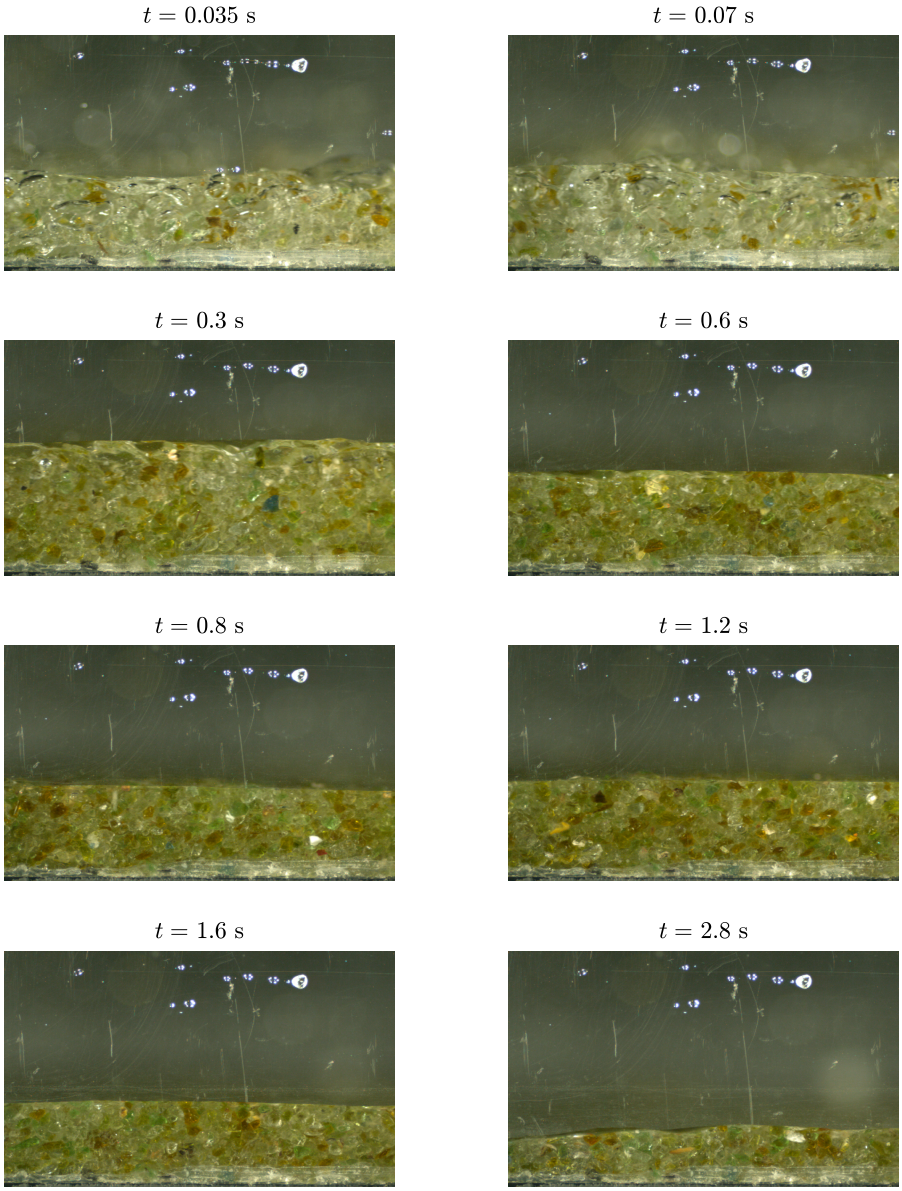

FIGURE 7.8: Snapshots of the propagating soil-water mixture for the experimental flow, Run 1. The area of the camera field of view is 0.05 $\times$ 0.03 m^2.

m s^{-1}. Non-fluctuating behaviour was characterised by a standard deviation less than this value, while above this value, the behaviour was collisional. This threshold value was chosen because it clearly distinguished the flow into two distinct regions, which displayed differences in behaviour.

Rather than choose a constant threshold value to distinguish between non-fluctuating and collisional behaviour, the deviations of velocity herein are instead considered as a percentage of the local average velocity at each time frame. Contour plots of the standard deviation as a percentage are provided in Figure 7.9 for Run 1, which is calculated as $100 \times \frac{\bar{e}}{\bar{u}_x}$. The upper limit of the contour scale is defined as 20%, which has been chosen as the cut-off value to differentiate between the two types of behaviour. The yellow regions in Figure 7.9 correspond to areas of the flow that have a standard deviation that is greater than 20% of the local time-averaged velocity, and are assumed to be collisional. The blue areas in Figure 7.9 represent a flow with a velocity deviation that is less than 20% of the average velocity, and can be assumed to be non-fluctuating. A threshold percentage of 20% was chosen because it clearly separates the flow into the two regions that are evident in the flow snapshots shown in Figure 7.8. The results in Figure 7.9 show that collisional behaviour is exhibited throughout the depth of the flow at $t = 0.035$ s, $t = 0.07$ s and $t = 0.3$ s. At $t = 0.6$ s, a non-fluctuating layer with a thickness of approximately 6 mm has developed at the flume bed. The height of this layer increases with time, and by $t = 1.2$ s the majority of the flow is non-fluctuating. However, the results in Figure 7.9 show that the experimental flow exhibits high deviations with respect to the local average velocity at the free surface and along the left horizontal boundary, for all times presented. The velocity values at the horizontal boundaries are subject to error due to the truncation of the PIV interrogation area. Regarding the flow free surface, a thin, watery layer is present at all times (see Figure 7.8). The PIV method relies on particle detection over subsequent frames, and therefore produces unreliable results in regions lacking particles. Consequently, the velocity values at the flow free surface are also subject to error.

To compare with the method of Paleo Cageao (2014), a constant value of $\bar{e} = 0.15$ m s^{-1} is also used to distinguish between non-fluctuating and collisional behaviour. Contour plots of the velocity standard deviation for Run 1 of the experimental flow are provided in Figure 7.10. The plots in Figure 7.10 are scaled so that the lower limit is equal to $\bar{e} = 0.15$ m s^{-1}. Accordingly, the dark blue areas in Figure 7.10 are assumed to correspond to non-fluctuating regions of the flow, while the lighter colours are assumed to represent the collisional regions. As also shown in Figure 7.9, the flow transforms from being purely collisional to non-fluctuating, with a layered transition at $t = 0.6$ s and $t = 0.8$ s. However, with a constant threshold value of $\bar{e} = 0.15$ m s^{-1}, the results in Figure 7.10 fail to highlight the high velocity deviations from the local average from $t = 0.3$ s onwards.

The averaged velocity vectors obtained from the PIV analysis are superimposed onto the flow snapshots in 7.11 (the vectors are represented by red arrows). The

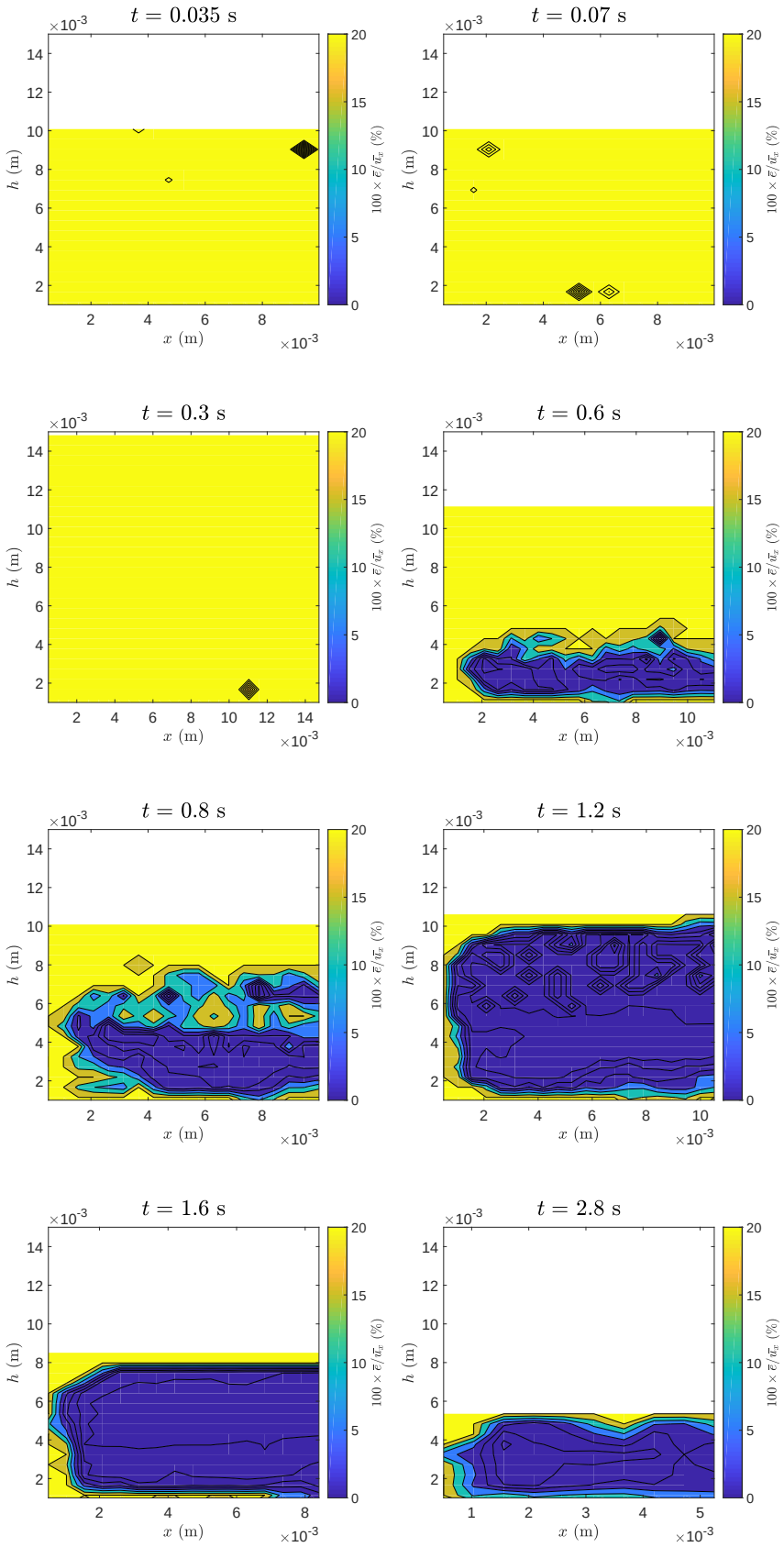

FIGURE 7.9: Contour plots of standard deviation as a percentage of the average velocity $100 \times \frac{\bar{e}}{\bar{u}_x}$ at different times of flow for Run 1 of the experiment. The upper limit on the scale bar is defined as 20% of the velocity average.

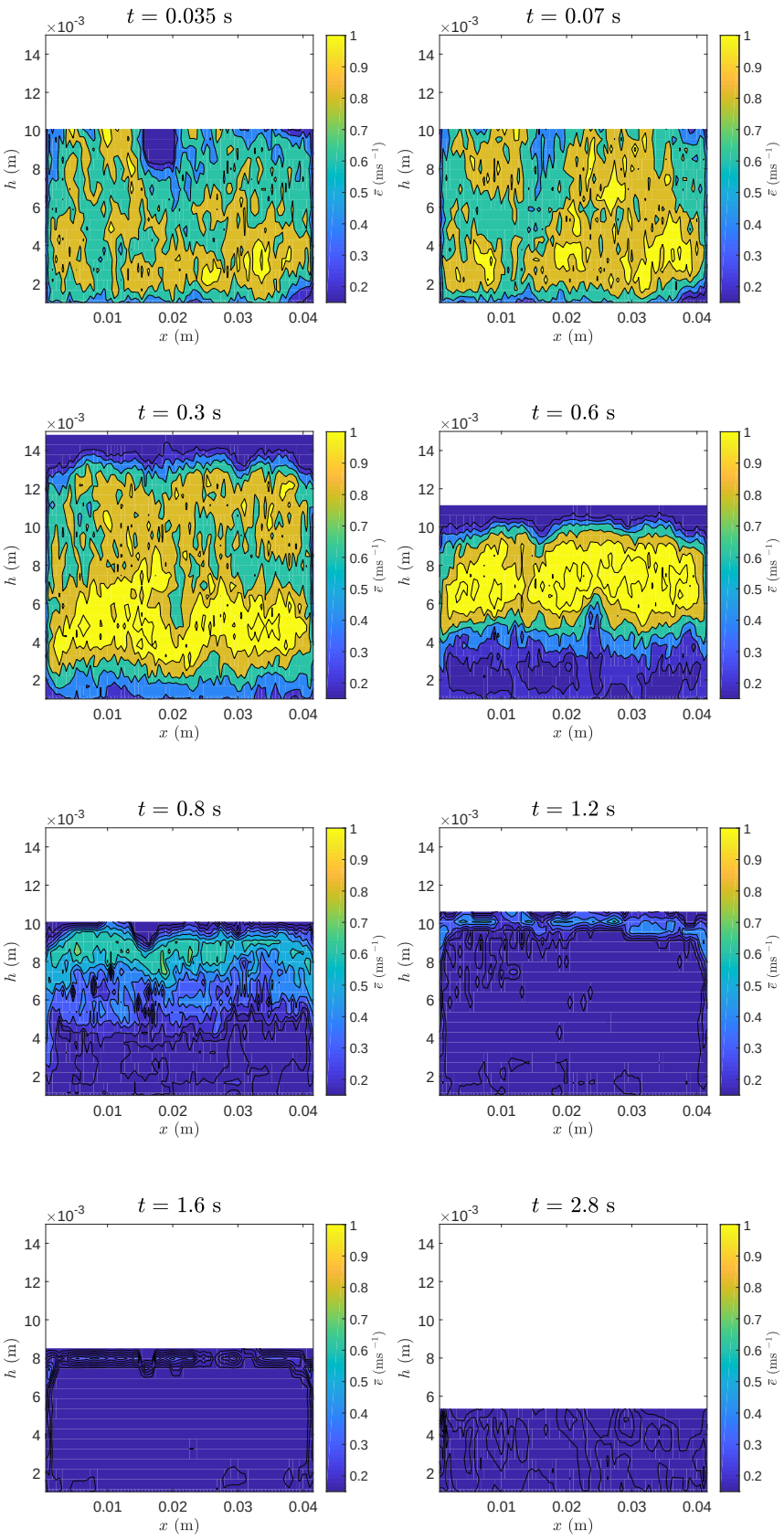

FIGURE 7.10: Contour plots of standard deviation $\bar{e}$ at different times of flow for the experimental water-granular mixture, Run 1. The lower limit on the scale bar is defined as $\bar{e} = 0.15$ m s^{-1}, which is the suggested cut-off between fluctuating and non-fluctuating behaviour used in the experiments of Paleo Cageao (2014).

velocity profiles align with the qualitative behaviour of the water-granular mixture described above. At times of $t = 0.035$ s and $t = 0.07$ s, the entire mixture is collisional and the PIV velocity vectors exhibit random and fluctuating behaviour throughout the majority of the flow depth. Most of the vectors are orientated in the negative direction which does not represent the physical behaviour of the flow. The spurious vectors show that there is not a sufficient correlation between particles in successive frames for the PIV method to produce robust velocity vectors. Although these vectors do not represent the true velocity, they indicate the high turbulence of the flow. At $t = 0.3$ s, while the majority of the velocity vectors exhibit similar turbulent behaviour to the earlier flow times, the vectors near the base of the flow are uniformly aligned in the downstream direction. The highest velocities are located in this lower, non-fluctuating region. Subsequently, the height of the non-fluctuating region increases from $t = 0.3$ s to $t = 0.6$ s, and the velocity vectors correspond to the presence of the two distinct layers discussed above (see Figures 7.9 and 7.10). The velocity magnitude increases with distance from the bed, and the maximum is located at the top of the non-fluctuating layer. The intensity of the turbulent vector distribution observed between $t = 0.035$ s and $t = 0.6$ s decreases with time. There are a number of negatively orientated vectors in the region between the non-fluctuating and collisional layers at $t = 0.6$ s, indicating the shearing that occurs in this area. At all subsequent times shown, the velocity vectors display linear behaviour throughout the flow depth. Moreover, at $t = 0.8$ s, the two material layers are no longer distinguished, and the height of the velocity maximum is located closer to the free surface. Above the height of the maximum, the velocity decreases towards the flow surface. At $t = 1.2$ s the height of the maximum velocity has increased further, and the same profile is also observed at $t = 1.6$, with a lower overall velocity magnitude. By $t = 2.8$ s the velocity has decreased significantly, and the mixture is almost stationary.

The corresponding contour plots for the PIV velocity data are shown in Figure 7.12. After the initial, fully collisional region of the flow, there is a concentrated area of high velocity at the base at $t = 0.3$ s. Above this, the upper, collisional layer exhibits some negative velocities. As discussed above, these negative velocities are not physical, but are useful in highlighting turbulent and rapidly varying flow regions. Similar behaviour is observed at $t = 0.6$ s, where the height of the concentrated, high velocity region has increased. Between times of $t = 0.8$ s and $t = 1.6$ s, the velocity contours are positive everywhere, and show an increase with height from the flume bed up to a maximum region. Above this region the profiles decrease to approximately zero at the flow free surface, due to the lack of particles detected with the PIV method. In reality, the velocity at the top of the flow is likely to be approximately equal to the velocities in the layer directly beneath it.

Profiles of horizontal velocity u_x against height h are provided in Figure 7.13 for twelve times ranging between $t = 0.035$ s and $t = 2.8$ s, comparing the results from the three different experimental runs. To analyse the error of the time-averaging

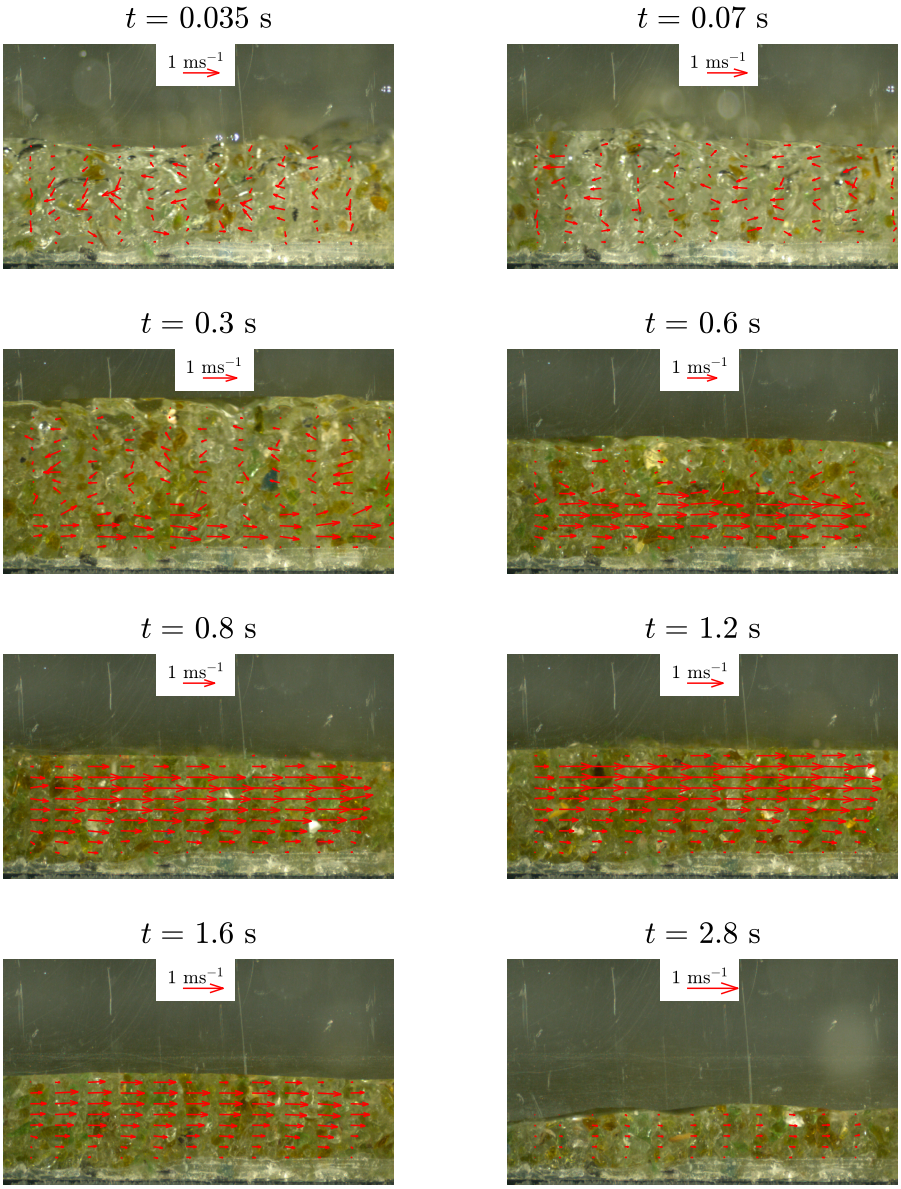

FIGURE 7.11: Snapshots of the propagating soil-water mixture for Run 1 of the experimental flow, with the overlaid time-averaged PIV velocity vectors. The area of the camera field of view is 0.05×0.03 m^2.

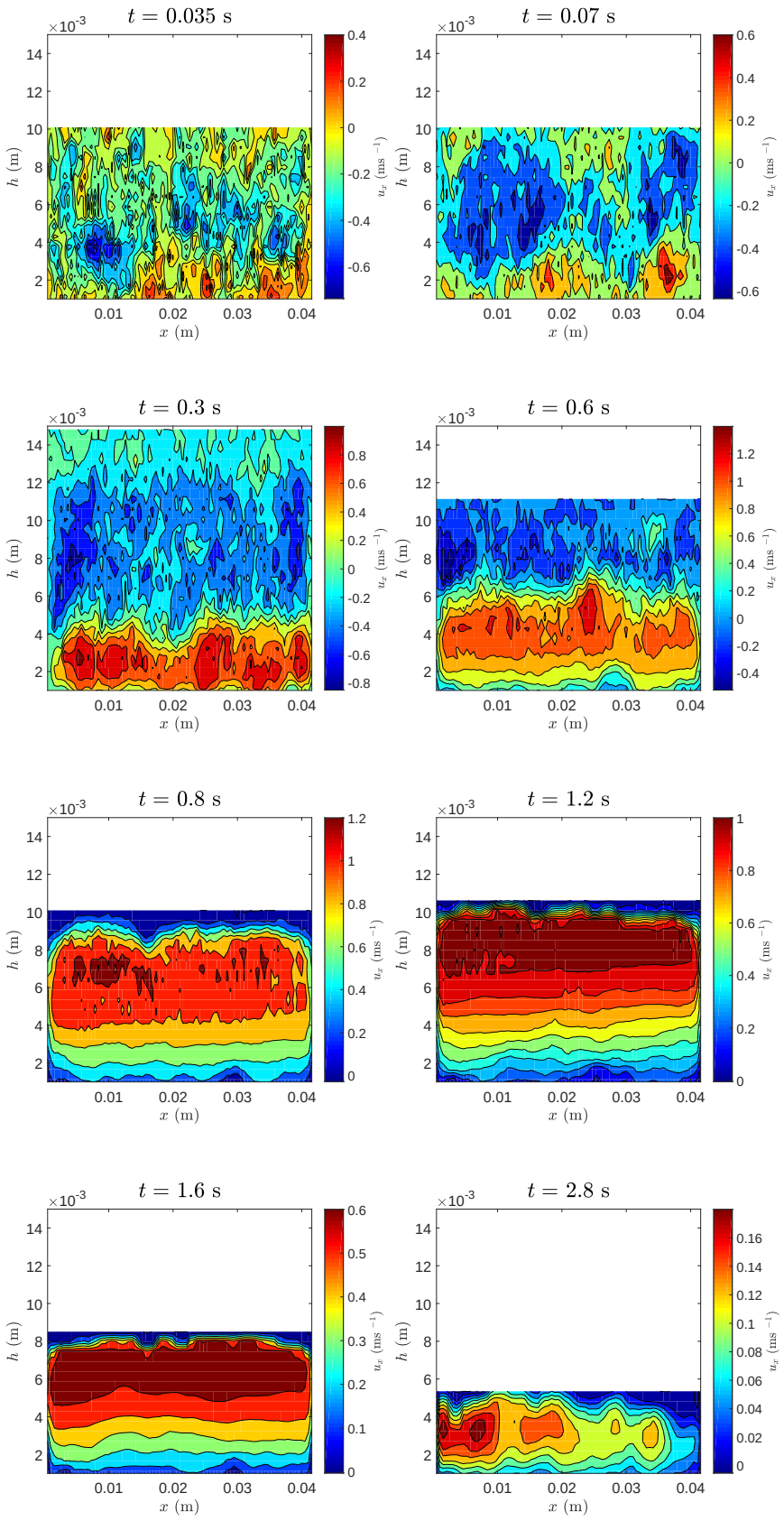

FIGURE 7.12: Contour plots of horizontal velocity u_x at different times for Run 1 of the experimental flow. Note the difference in scale for each image.

process, an autoregressive (AR) model was fit to the instantaneous data over the 30 frames that were averaged. AR models are used to represent a value in a time series as a weighted sum of previous values in the series, and can be used for forecasting purposes (Brockwell, Davis, and Calder, 2002; Box et al., 2015). A time series X_n is defined as a linear combination of past observations X_{n-1} and white noise error terms ϵ_n:

$$X_n = \sum_{i=1}^{p} \alpha_i X_{n-1} + \epsilon_n, \tag{7.4}$$

where α_i are the model parameters, and p is the number of past observations that used in the expression of X_n. An AR model is applicable only for a stationary time series – that has a time-independent mean and variance. The error terms are assumed to follow a normal distribution with a zero mean. For the current purpose, the parameter p was assumed to be one, so that each term in the AR model is based on the previous term, and the white noise. The optimum values for the coefficients α_i should minimise the error term. These were determined using the Matlab ARIMA (autoregressive-integrated-moving-average) function, which uses a maximum likelihood method to estimate the model parameters. The error in the experiment can be assessed by considering the residuals between the data and the AR model fit, which are plotted as error bars in Figure 7.13. Up to $t = 0.3$ s, the error bars are relatively large, indicating that the data cannot be satisfactorily modelled as a first order AR model. The data are unlikely to be stationary in this area, due to the rapidly varying velocities. The error bars are also large in the upper region of the flow at $t = 0.6$ s, where the behaviour is turbulent and collisional. Despite this, the collisional behaviour is consistent between the three different runs, even in the regions that exhibit non-physical negative velocities (between $t = 0.035$ s to $t = 0.6$ s). From $t = 0.8$ s onwards, the residual errors are insignificant. The overall flow behaviour for the three different runs is in good agreement, at each time shown in Figure 7.13 . There are some small differences in the height and velocity at certain times, namely at $t = 1.2$ s, and from $t = 1.6$ s to $t = 2.8$ s. A number of factors could contribute to such differences, such as the wetness of the bed, a delay in the lock gate release or variable composition between the granular material. Nonetheless, the shape of the velocity profiles align well at all times presented, showing that the experiments are repeatable in terms of the overall flow behaviour. For each run, it can be observed that the height of the velocity maximum steadily increases with time up to $t = 1$ s. From $t = 1.2$ s onwards, the location of the velocity maximum decreases with height. Considering the large errors and high quantity of negative velocities observed from $t = 0.035$ s to $t = 0.3$ s, attention is subsequently focused on the flow behaviour from $t = 0.6$ s onwards.

The velocity profiles at different times from $t = 0.6$ s to $t = 2.8$ s are plotted together in Figure 7.14a, for each experimental run. It can be seen for each run that the velocities are highest at $t = 0.6$ s, where the maximum value is approximately $u_x = 1.2$ m s^{-1}. The maximum velocities, as well as the velocities below the height

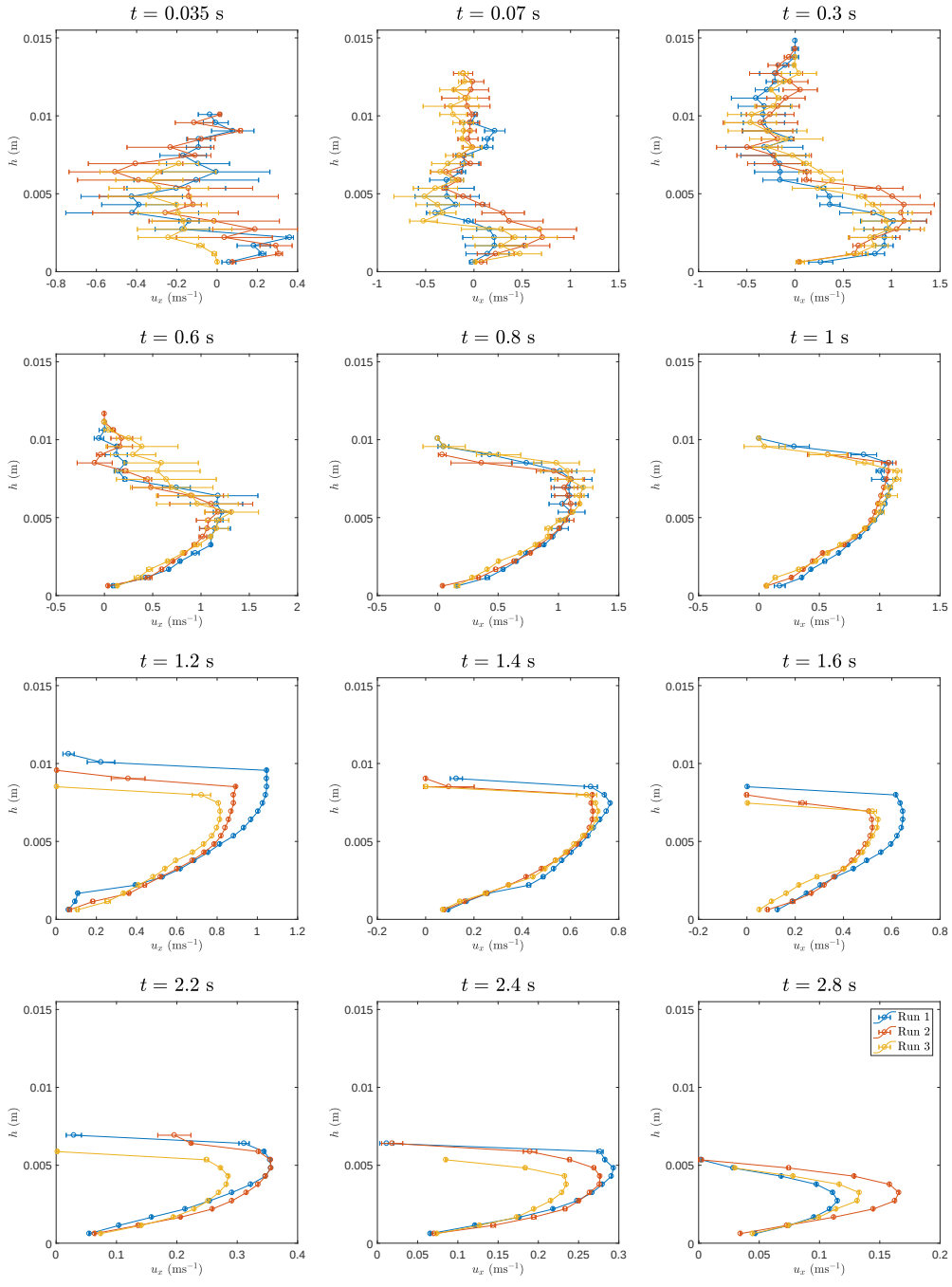

FIGURE 7.13: Velocity profiles obtained from the PIV data at various times for the three experimental runs. The horizontal position of the profiles is in the centre of the camera viewing frame (1.102 m downstream from the lock gate).

of the maximum, decrease with time. The height of the velocity maximum increases from $t = 0.6$ s to $t = 1.2$ s, where it then decreases until $t = 2.8$ s. The velocity profiles were normalised by dividing the velocity and the height by the maximum velocity u_{max} and the flow depth H respectively. Profiles of normalised velocity are plotted against normalised height in Figure 7.14b. For all runs, the majority of the normalised profiles approximately collapse onto one curve. A common exception is the profile at $t = 0.6$ s, which has a normalised height of the velocity maximum that is significantly lower than for the later times. Furthermore, there is some variation between the profiles at $t = 0.8$ s, $t = 1$ s and $t = 2.8$ s, although the overall shape corresponds the curve where the majority of the profiles lie. The three runs are consistent in that the velocity profiles between $t = 1.2$ and $t = 2.4$ are almost indistinguishable from one another. These profiles exhibit a velocity that is approximately zero at the flume bed, that steadily increases in the region close to the bed. The velocity gradient increases as the height approaches that of the velocity maximum, which has a non-dimensional height of approximately 0.8. Above this height, the velocity decreases towards the surface, although the velocity data in this area is subject to error, as discussed above. The collapse of the velocity profiles onto a single curve has been observed in previous experimental investigations of debris flows (Kaitna, Dietrich, and Hsu, 2014; Sanvitale and Bowman, 2017), and indicates the uniform behaviour within this region of the flow.

The PIV data can be utilised to obtain profiles of the internal shear stress rate. Neglecting the horizontal gradients of the vertical velocity u_y, the local shear rate $\dot{\gamma}$ is defined as

$$\dot{\gamma} = \frac{\partial u_x}{\partial y}. \tag{7.5}$$

The shear rate is approximated at each vertical height h_i:

$$\dot{\gamma}_i \approx \frac{u_{x,i+1} - u_{x,i}}{\Delta h}, \tag{7.6}$$

where $u_{x,i}$ is the velocity at the current vertical position h_i, and $u_{x,i+1}$ is the velocity at the subsequent vertical location h_{i+1}. The vertical sampling points are separated by the distance Δh. The profiles of local shear rate plotted against height are shown in Figure 7.15a for one of the experimental runs. In order to visualise the results more clearly, the profiles from $t = 0.6$ s to $t = 1.2$ s are plotted separately from the results between $t = 1.4$ s and $t = 2.8$ s. From $t = 0.6$ to $t = 1$ s, the shear is highest at the bed and sharply decreases in the region just above the bed. Above this, the overall shear decreases as the height increases, although the values fluctuate locally. At the boundary between the non-fluctuating and collisional regions of the flow at $t = 0.6$ s and $t = 0.8$ s (see Figures 7.9 and 7.10), the shear rate decreases to a large negative value. This is followed by an increase in shear above the interface between the two regions, highlighting the presence of a shearing layer in this region. The shear rate profiles at $t = 1$ s and $t = 1.2$ s display similar behaviour in that there is a steep increase in the region directly above the bed, followed by a uniform decrease

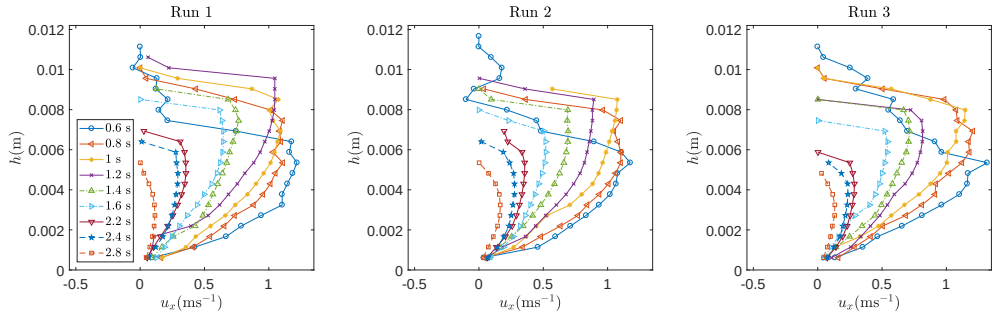

(A) Velocity profiles

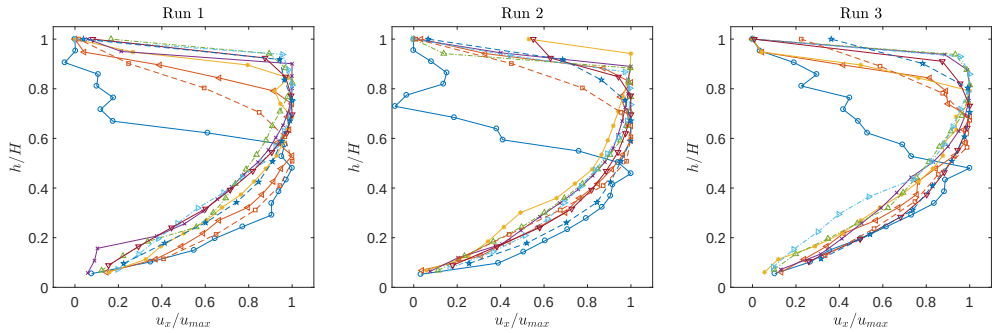

(B) Normalised velocity profiles

FIGURE 7.14: Plots of horizontal velocity against height at $x = 1.102$ m downstream from the lock gate. On each graph the plotted profiles are from eight different flow times, ranging between $t = 0.6$ s and $t = 2.8$ s, for the three different experimental runs.

until just below the free surface. At the free surface, there is a sudden decrease to a negative shear value. The profiles of internal shear rate between $t = 1.4$ s and 2.4 s exhibit a linear decrease with height from the flume bed, until the free surface. Again, in this region the shear profile sharply decreases to a large negative value. The spurious negative shear values at the free surface reflect the relatively large deviations from the velocity average in the area (see Figure 7.9). At the final considered time of $t = 2.8$ s, the shear rate profile decreases linearly until just below the free surface, before increasing towards the surface.

Following Sanvitale and Bowman (2017), the normalised shear rate $\hat{\dot{\gamma}}$ is obtained by dividing by the depth-averaged shear rate $\bar{\dot{\gamma}}$:

$$\hat{\dot{\gamma}} = \frac{\dot{\gamma}}{\bar{\dot{\gamma}}} = \frac{\partial u_x}{\partial y} \frac{H}{(u_H - u_{slip})}, \tag{7.7}$$

where u_H and u_{slip} are the values of horizontal velocity at the free surface and the bed respectively. Note that if both u_H and u_{slip} are zero, Equation (7.7) is inapplicable. In the current results, u_H and u_{slip} are small in comparison to the internal velocities, yet have non-zero values. Profiles of normalised local shear $\hat{\dot{\gamma}}$ are provided in Figure 7.15b. Bar a difference near the flume bed, the shear rate profiles from $t = 1.4$ s to $t = 2.4$ s almost collapse onto the same profile.

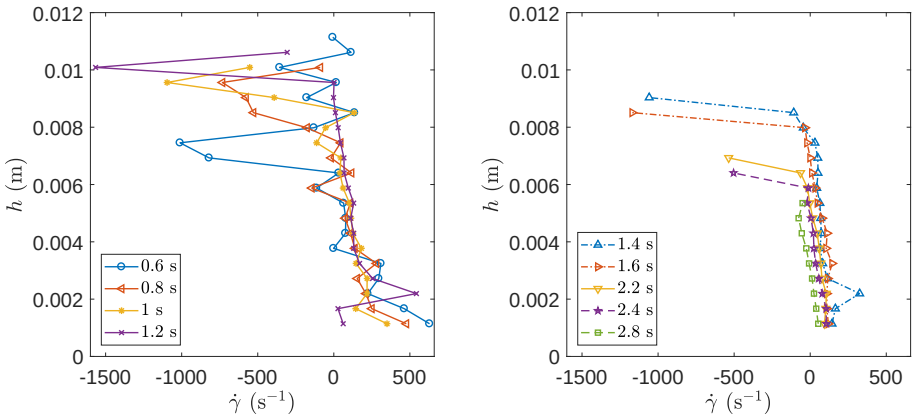

(A) Shear stress rate

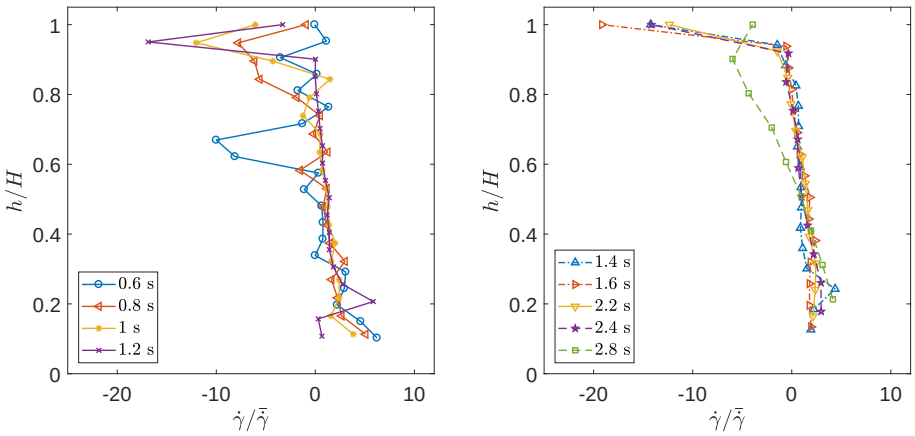

(B) Normalised shear stress rate

FIGURE 7.15: Plots of shear stress against height at $x = 1.102$ m downstream from the lock gate, for Run 1 of the experiment.

7.4 Discussion

The experimental debris flow described in the previous section exhibits complex behaviour throughout its evolution. This is immediately evident from the snapshots of the flow obtained with the high speed camera, shown in Figure 7.8. The front of the flow is dilute and turbulent, which develops into what appears to be a steady, water-granular mixture. In the transition between these two types of behaviour, the flow is composed of two distinct layers. The data obtained from the PIV analysis of the flow has allowed further insight into the mechanisms that are responsible for the observed experimental behaviour. By defining a threshold value of deviation from the locally averaged velocity, it is possible to distinguish two types of flow behaviour – non-fluctuating and collisional (Paleo Cageao, 2014). In the current analysis, the threshold between the two types of flow has been defined as a standard deviation that is 20% of the local average velocity. Furthermore, a constant threshold of $\bar{e} = 0.15$ m s^{-1} has also been implemented, following Paleo Cageao (2014). In both cases, contour plots of the velocity deviation (see Figures 7.9 and 7.10) have shown that the dilute front of the flow is dominated by collisional and turbulent behaviour. Behind the front, the flow transitions from collisional to non-fluctuating, and consists of both types of behaviour in between. Throughout the transition, the collisional region (with a high standard deviation) narrows in depth, decreases in magnitude and shifts towards the flow free surface. Simultaneously, the height of the non-fluctuating region increases with distance from the bed, until the flow is dominated by this type of behaviour. The non-fluctuating region corresponds to a shearing layer, where the mixture shears along the bed. This can be deduced from the velocity contours and vertical profiles (see Figures 7.11 and 7.12), where the initial presence of the non-fluctuating region coincides with the initiation of a layer of shear between the mixture and the bed. The height of the shearing layer increases due to the accumulation of granular material that is opposed by the frictional resistance of the bed, until the entire flow consists of a steady shear flow.

In the field, debris flows are typically composed of a dry head containing large particles, where the dynamics are dominated by granular collisions and exhibit frictional behaviour. Behind the head, the flow body contains smaller particles and interstitial fluid, exhibiting fluid-like behaviour (Iverson, 1997; McArdell, Bartelt, and Kowalski, 2007). The head-body architecture is attributed to complex couplings related to the grain size distribution, material fines content and pore water pressures (Iverson et al., 2010; Johnson et al., 2012). It has also been observed in small scale experiments (Kaitna, Dietrich, and Hsu, 2014; Sanvitale and Bowman, 2017; Parsons, Whipple, and Simoni, 2001), including those with monodispersed spherical mixtures (Paleo Cageao, 2014). In the current work, the high water content of the experimental mixture does not allow the formation of a dry, granular head, yet the front of the flow is also dominated by granular collisions, along with turbulent fluid behaviour. Furthermore, the experiment also exhibits a transition to a distinct flow

body, characterised by non-fluctuating behaviour (see Figures 7.9 and 7.10). The experimental flow therefore displays a unique head-body architecture, that has not been documented previously. Despite this, the head to body transition bears similarities to classic debris flows. Regarding small scale debris flow experiments within the literature, internal flow observations have contributed to a better understanding of the dynamics responsible for debris flow architecture (Kaitna et al., 2016). The majority of attention has previously been focused on the internal dynamics of steady granular flows, in order to approximate the rheology of granular material (Armanini et al., 2005; Kaitna, Rickenmann, and Schatzmann, 2007; Kaitna, Dietrich, and Hsu, 2014). Furthermore, in experiments of unsteady debris flows, the internal behaviour of the collisional flow head has not been taken into consideration. This has been a result of restrictions in software (Sanvitale and Bowman, 2017), or because the high velocity fluctuations in this region are the source of unreliable data (Paleo Cageao, 2014). In the experiments of Sanvitale and Bowman (2017), the flow head was dry – the laser-based PIV technique can only detect saturated particles. In the present analysis, the internal velocity profile has been examined within both the front of the flow and the body, which has highlighted how the flow progressively transitions between the collisional and non-fluctuating regimes. One of the most striking features of this transition is the presence of two distinct shearing layers, which can be seen at $t = 0.6$ s and $t = 0.8$ s (see Figures 7.9, 7.11 and 7.12). It should also be highlighted that previous investigations of internal granular flow dynamics have presented profiles of velocity, and the temporal evolution of the depth-averaged velocity (Armanini et al., 2005; Kaitna, Dietrich, and Hsu, 2014; Paleo Cageao, 2014; Sanvitale and Bowman, 2017). In addition to velocity profiles (Figure 7.13), the current work has produced velocity flow fields in an experimental debris flow for the first time (see Figure 7.12).

Considering the behaviour within the body of the experiment, the internal structure can be compared against that of existing experimental debris flows. The relevant details of a selection of experiments presented in the literature are provided in Table 7.2, along with the parameters in the current debris flow experiments. Armanini et al. (2005) observed the steady flow of a mixture of polyvinyl chloride (PVC) pellets in a recirculating flume, with a continuous influx of water. The inclination angle was varied and four different flow regimes were accordingly defined – immature, mature, plug and solid bed flow. A Voronoi imaging technique was used to obtain internal velocity and shear rate profiles for each regime. Disregarding the spurious values at the free surface, the profiles in the present investigation are similar to those of the solid bed flow, from $t = 1$ s onwards. Solid bed flows occurred for the highest bed inclinations and were characterised by the shearing flow of the granular phase over a fixed bed (as opposed to over a loose bed of deposited material for lower inclination angles). Profiles of horizontal velocity exhibited a convex shape, that increased with distance from the bed. The corresponding shear rate profiles decreased with distance from the bed, to a near zero value. The solid bed velocity profiles of Armanini et al.

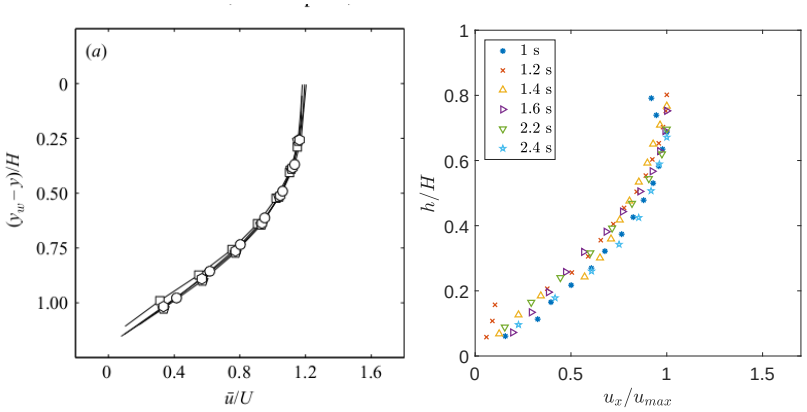

(A) Results of Armanini et al. (2005) (B) Results of the current work (Run 1)

FIGURE 7.16: A comparison of the internal velocity profiles in the steady, solid bed flow experiments of Armanini et al. (2005), and those in the body of the current experiment. For the former, plotted on the x-axis is horizontal velocity $\bar{u}$ normalised by the mean velocity U. The y-axis shows $(y_w - y)/H$, where y_w is the saturation line (obtained by visual inspection), and H is the flow free surface. The points correspond to the experimental velocity values, where the different symbols refer to results from different runs with the bed slope varying from $19° - 23°$. The solid line is the line of best fit.

(2005) are compared against those of the current work in Figure 7.16, where it is clear that the profiles exhibit the same behaviour. For the current results, the upper four data points (corresponding to 1.6 mm)have been omitted. Similar convex velocity profiles have also been recorded in the body of a steady debris flow consisting of gravel and water, in a rotating drum (Kaitna, Dietrich, and Hsu, 2014). The experiments were conducted for four different mixtures of gravel, mud and water, and it was found that each mixture exhibited a distinct, dimensionless velocity profile, for a number of different drum rotation velocities. Furthermore, solid bed profiles have been observed in the body of an unsteady, experimental debris flow, that was similar in set-up to that of the current work (Sanvitale and Bowman, 2017). The normalised velocity profiles at different flow times approximately collapsed onto a single curve. Similar to the findings of the Kaitna, Dietrich, and Hsu (2014), a distinct profile was exhibited for three different grain size distributions, mixed with water. In the current work, the normalised velocity profiles in the flow body also collapse onto a single curve for each experimental run, from $t = 1$ s onwards (see Figure 7.16b), showing the uniformity of the flow in this region.

TABLE 7.2: A summary of the relevant experimental parameters in the current work, and selected investigations in the literature. The notation x_f refers to the flume run-out length (from the lock gate position), c_w is the channel width, d_d is the diameter of the rotating drum, θ is the flume inclination, ϕ_s is solid volume fraction, d_{50} is the mean particle size and C_U is the coefficient of uniformity. The ✗symbol denotes information that was not provided in the literature.

Reference	Flume dimensions (m)	Inclination θ (°)	Volume fraction ϕ_s	Sediment	Fluid	d_{50} (mm)	C_U
Present work	x_f = 1.662 c_w = 0.1	31	0.44	Crushed glass grit	Water	0.917	5
Armanini et al. (2005)	$x_f = 6$, $c_w = 0.2$	$5 \leq \theta \leq 22$	0.346 - 0.529	PVC pellets	Water	3.7	1
Kaitna, Dietrich, and Hsu (2014)	$d_d = 4$, $c_w = 0.8$	n/a	0.6, 0.62, 0.7	Gravel	Water,mud	4, 8, 10, 13	✗
Paleo Cageao (2014)	x_f = 0.7, c_w = 0.156	27	0.4	Glass spheres	Water, glycerol	2	1
Sanvitale and Bowman (2017)	$x_f = 2$, $c_w = 0.15$	24.5	0.7	Crushed and sub-rounded glass	Hydrocarbon fluid	7.1	3,10,20

The rheological behaviour in the experimental flow body can be assessed by approximating the dimensionless velocity profile with a granular and viscous scaling. Figure 7.17 shows the normalised velocity profiles for Run 1 of the experiments between times of $t = 1$ s to $t = 2.4$ s, where the upper 1.6 mm of flow has been omitted. The profile of best fit has been included, assuming both a viscous and granular scaling according to Equations (7.1) and (7.2). The closest fit to the experimental results is found with the viscous scaling, which captures the overall velocity shape throughout the shear layer. In the experiments of Sanvitale and Bowman (2017), mixtures with a wide grain size distribution (with a coefficient of uniformity of $C_U = 20$) exhibited a viscous-type velocity profile. Conversely, for $C_U = 3$ a granular profile provided the best fit to the experimental data. A wider grain size distribution promotes particle segregation, which can lead to the finer particles being trapped within the solid matrix. The presence of these fine grains enhances the viscosity of the interstitial fluid, and viscous forces influence flow behaviour (Iverson, 1997). For a more uniform particle distribution, the dominating forces are generally inter-particle granular collisions. In the current experiments, the viscous profile provides the closest fit to the experimental results, despite a relatively small coefficient of uniformity of $C_U = 5$. This is possibly due to the proportion of very small particles with diameters less than 0.5 mm that are present within the mixture (see Figure 7.3), which add to the fluid viscosity. The results also suggest that the cut-off between granular and viscous-type flow may lie between $C_U = 3$ and $C_U = 5$.

The current experiments were performed with a significantly higher concentration of fluid than for the majority of similar, debris flow experiments (see Table 7.2). Despite this, the behaviour observed within the flow body is comparable to results presented in the literature, as discussed above. In terms of volume fraction, one set of a series of flume experiments performed by Paleo Cageao (2014) used a value of $\phi_s = 0.4$ (which is close to $\phi_s = 0.44$ in the current work). The mixture in Paleo Cageao (2014) consisted of water and monosized glass spheres with a diameter of 2 mm. The height evolution of the two phases was recorded at a distance 0.232 m downstream from the lock gate. Upon arrival at this location, the flow exhibited a dry, granular front. The height of the water phase increased with time, until the flow body was composed of a water-granular mixture, with an upper layer of water. The entire solid phase had propagated beyond the location of measurement by approximately 1.2 seconds, and the tail of the mixture consisted of water only. Conversely, for a higher solid volume fraction of $\phi_s = 0.6$, the tail of the flow contained a mixture of both spheres and water of approximately the same height (although a larger section of the flow front was dry) (Paleo Cageao, 2014). This behaviour suggests that for the higher water content ($\phi_s = 0.4$), the coupling between the two phases was less significant than in the current work. The current experimental flow did not exhibit any regions of dry granular material and had a tail composed of both water and granular material. The strong difference in behaviour of the current experiment and that of Paleo Cageao (2014) is attributed to the composition of the granular

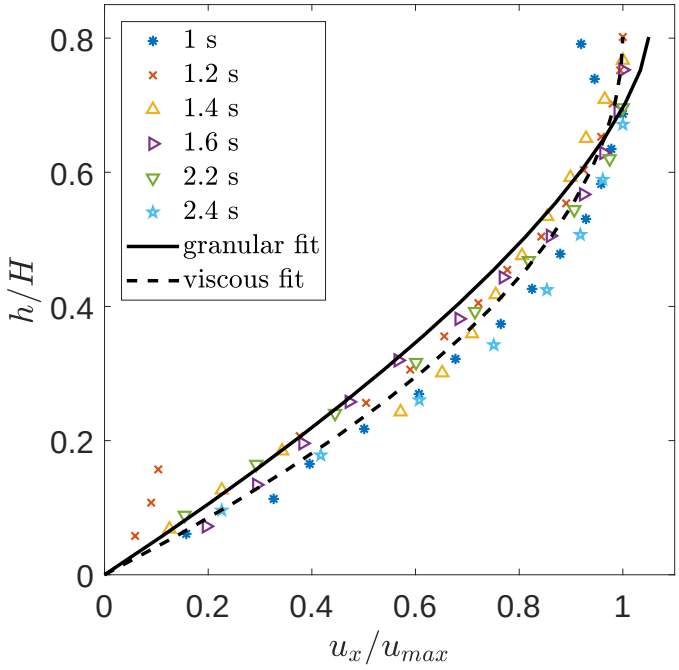

FIGURE 7.17: Normalised velocity profiles in the sheared region for Run 1 of the experimental debris flow, with a best fit granular and viscous scaling.

phase. As opposed to monosized spheres, the current experiment consists of crushed glass of varying diameter. The angular shape allows the interlocking of grains and adds extra frictional resistance that is not present for spherical grains. For angular, crushed material, inter-particle shearing is significant, in addition to the shearing between the material and the bed. Therefore a flow of angular granular material exhibits lower velocities than that of glass spheres. Furthermore, the dilation and contraction of the crushed glass particles regulates the motion of the water, enhancing the coupling between the two phases. Experiments involving spherical particles are beneficial in terms of simplicity, and allow the investigation of a wide range of factors affecting flow behaviour. However, the flow dynamics can be significantly different from that of a realistic granular material, as shown by the difference between the current experimental results and those of Paleo Cageao (2014).

In the transitional region between the head and body of the experimental debris flow, it is comprised of a concentrated lower layer and a more dilute upper layer (see $t = 0.3$ s and $t = 0.6$ s in Figure 7.8). The corresponding velocity profiles show that in the lower layer, the velocity increases with distance from the bed to a velocity maximum towards the top of the layer. Above the maximum, the velocity decreases rapidly and exhibits negative values due to shearing between the layers, and the inability of the PIV software to produce accurate velocity values. These profiles share similarities with those observed in the steady state profiles of some submarine gravity currents, where differences in density drive a dense fluid through a less dense,

ambient fluid (Simpson and Britter, 1979; Kneller, Bennett, and McCaffrey, 1999; Lowe, Linden, and Rottman, 2002). For some sediment-laden flows, notably high concentration turbidity currents, the settling of sediment can result in a layer of high concentration at the bed, while the upward mixing of turbulence produces a dilute upper layer that entrains sediment (Postma, Nemec, and Kleinspehn, 1988; Stevenson et al., 2018). In the internal profiles of these flows, the velocity maximum is located at the top of the lower layer due to the balance of the shear at the bed and at the interface between the dense fluid and the ambient fluid (Kneller, Bennett, and McCaffrey, 1999). These profiles are observed in steady state flows, and above the interface between the two layers of material the velocity steadily approaches a zero value. This overall shape is similar to the internal velocity profiles in the current experimental flow at $t = 0.3$ s and $t = 0.6$ s (see Figure 7.13). Although the flow is transient at these times, and shows large fluctuations in the upper layer, the analogy to high concentration turbidity currents provides a deeper understanding of the mechanism responsible for the observed velocity profiles. Furthermore, it has been postulated that the transport of sediment in high concentration turbidity currents is a result of the interaction between a high concentration lower layer, and a turbulent upper layer (Postma, Nemec, and Kleinspehn, 1988). This has potential relevance to the formation of the observed architecture in the current flow. However, it should be noted that two-layer turbidity currents have exclusively been observed in the laboratory, and in natural systems, many flows are likely to exhibit a more gradual stratification (Peakall and Sumner, 2015).

As discussed in Section 7.2.1, the PIV method requires the detection of individual particles over multiple frames in order to produce accurate velocity vectors. This wasn't possible at the head of the flow due to the low particle concentration and their turbulent behaviour. The velocity values recorded at the flow free surface were also subject to error, due to an overlying layer of water where particles were not present. The fact that particle tracking was not accurate at the front of the flow suggests that some particles were transported away from the flume walls in the cross stream direction, as a result of the high fluid turbulence. This implies that the two-dimensional flow approximation is subject to error, particularly at the front of the flow. Furthermore, the presence of the side wall may influence the flow dynamics. Despite these limitations, the experiments showed a high degree of repeatability, as shown in Figure 7.13. The small differences between the different runs at certain times may be a result of a delay in the opening of the lock gate, or variability in material composition.

7.5 Conclusion

The internal observations of the experimental debris flow presented in this chapter have provided insight into the complex interaction between propagating particulate and water phases. The experiments consisted of a relatively dilute water-granular

mixture ($\phi_s = 0.44$), which exhibited a spatial and temporal evolution from a transient, collisional, turbulent flow to a steady, non-fluctuating flow. A viscous-type profile is able to capture the velocity in the non-fluctuating region throughout the majority of its depth. The granular material in these experiments has a coefficient of uniformity C_U of 5. Integration with the work of Sanvitale and Bowman (2017) suggests that the transition from a granular profile to a viscous flow profile takes place between a coefficient of uniformity of 3 and 5. A suggested area for future work is to perform further experiments with different values of C_U, to test this hypothesis. Furthermore, the transition from the collisional flow front to the non-fluctuating body has been quantified in a small scale unsteady debris flow for the first time. A unique head-body architecture was observed during the flow evolution, where the initially turbulent head evolved into a uniform flow as a layer of shearing granular material increased in height. Unlike similar experiments with monosized spheres (Paleo Cageao, 2014), the body of the current flow exhibited a thin layer of water overlying the viscous mixture for the entirety of the flow duration. This indicates that the behaviour of the flow was influenced strongly by the coupling of the granular and liquid constituents. In order to model this experiment with SPH, the results suggest that the assumption of a single phase material is invalid. Therefore, in the subsequent chapter, water is introduced to Standard and Stress-Particle SPH in an attempt to capture the overall dynamics of the experimental debris flow, with a two-phase model.

Chapter 8

Two-phase Stress-Particle SPH

8.1 Introduction

In this chapter, the results of the experimental debris flow presented in Chapter 7 are modelled with SPH. The SPH model developed within the current research has so far been restricted to the analysis of a single phase material, with the implementation of both an elastoplastic and viscoplastic rheological model to describe soil behaviour. This has been successfully applied to model behaviour relevant to both landslide initiation and propagation (see Chapters 5 and 6). The experimental debris flow exhibited complex features, with a spatial and transient evolution between collisional and non-fluctuating behaviour. Furthermore, the flow consisted of distinct granular and water layers throughout its development. Consequently, it cannot be approximated as a single phase material. Moreover, in reality, problems involving soil typically consist of both a soil and a water phase. In order to provide a more accurate description of the experimental flow, as well as a more realistic model of granular material, the SPH model is here extended to include a water phase in addition to the soil. This extended model is denoted as *two-phase SPH*, and is implemented within both Standard and Stress-Particle SPH.

The interaction between both solid and fluid forces is considered to be the main feature that distinguishes debris flows from other natural events such as avalanches and turbidity currents (Iverson, 1997). In attempts to model the solid and fluid propagation in debris flows, extensive work has been devoted to the development of two-phase mathematical models (Iverson, 1997; Pitman and Le, 2005; Pudasaini, 2012; Pastor et al., 2015b). Within the literature, there are a number of alternative approaches in which two-phase debris flow models are derived. This includes the pioneering work of Iverson and co-workers (Iverson, 1997; Iverson and Denlinger, 2001; Iverson and George, 2014), who developed a two-phase solid-water model based upon the framework of mixture theory (Bedford and Drumheller, 1983). In this approach, the key factors that influence debris flow motion include pore water pressures and an evolving granular dilatancy. Alternative debris flow models have been derived from the so-called phase averaged 'two-fluid' theory (Anderson and Jackson, 1967), and include those of Pitman and Le (2005) and Pudasaini (2012). In these models, a liquid and a granular phase are treated as distinct fluids, with a term

describing their interaction. The same two-fluid debris flow equations were also derived independently from the multiphase mixture theory of linear elastic materials developed by Biot (1941). This theory was extended to account for large deformations by Zienkiewicz, Chang, and Bettess (1980) and Zienkiewicz and Shiomi (1984). The different two-phase mathematical models derived under the three alternative approaches mentioned above bear many similarities to one another. In the current research, the mathematical model used to describe the motion of the experimental debris flow is based upon the framework of the Zienkiewicz and Shiomi (1984) and Pitman and Le (2005).

In all existing numerical investigations of two-phase debris flow behaviour, the governing equations of motion are depth-integrated in order to reduce computational expense (Pitman and Le, 2005; Pastor, Blanc, and Pastor, 2009; Iverson and George, 2016). The equations are integrated between the upper and lower flow domains (the bed and the free surface), so that all flow variation in the direction normal to the bed is approximated with a single, averaged value. Depth-integration is appropriate for 'shallow flows', where the typical flow length is much larger than the height (Savage and Hutter, 1989). In such cases the normal flow variations are assumed to be negligible in comparison to the stream-wise and cross-stream variations. For the numerical solutions of these types of flow, meshless methods such as SPH are a valuable tool due to the large run-out lengths and displacements expected in depth-integrated debris flow models. Significant developments in this area have been achieved by Pastor and co-workers (Pastor et al., 2008; Pastor, Blanc, and Pastor, 2009; Pastor et al., 2014; Pastor et al., 2015b), where the governing equations of Zienkiewicz and Shiomi (1984) are depth-integrated and implemented within SPH. Various model assumptions are made, such as the assumption that the velocity differences between the two phases are negligible in comparison to the velocity of the solid skeleton. The two-phase mixture is consequently described with a single velocity vector, and a single set of nodes is used to describe the soil-water mixture in the depth-integrated SPH model. The coupling between the two phases is incorporated via an evolving pore water pressure and a phase interaction force. The model of Pastor and co-workers has been applied to a vast range of problems regarding landslides and debris flows (Cascini et al., 2009; Haddad et al., 2010; Calvo et al., 2015). In recent work, the depth-integrated SPH model was extended to explicitly account for two distinct soil and water phases with different velocities (Pastor et al., 2018). Two sets of SPH nodes were employed – one set to represent the soil, and the other to represent the water phase.

While depth-integration reduces computational expense, it results in the loss of essential flow features, such as the vertical pore water pressure and stress profiles. These features must be reintroduced via assumed relationships between the full vertical profile and the depth-averaged values (Iverson, 1997; Pastor et al., 2015b). Although all current SPH models of debris flows are depth-integrated, there are other SPH models of soil-water mixtures that are not depth-integrated. Most of these SPH

models are applied to small deformation problems (such as the strain localisation in a saturated soil), that exhibit low relative velocities between the soil and water phases (Bui, Sako, and Fukagawa, 2007; Blanc and Pastor, 2012; Bui and Fukagawa, 2013). A single set of SPH nodes are therefore employed to approximate the two-phase mixture, as described above. However, Bui and Nguyen (2017) recently incorporated the full two-phase model of Zienkiewicz and Shiomi (1984) into SPH, without any depth-integration. Two sets of SPH nodes were used to describe the soil and water phases, and applied to a range of problems including the development of stress in a submerged soil, and the flow of water through a soil embankment. The results compared well with both theoretical and experimental data.

In the current work, depth-integration cannot be justified. The internal velocity and stress profiles of the experimental debris flow vary with height in a complex manner which cannot be approximated with an averaged value. Furthermore, with regards to general landslide behaviour, depth-integration is only relevant when modelling landslides of the flow-type, where the run-out length is often large in comparison to the flow height. Concerning models of landslide initiation mechanisms, features such as the evolution of slip surfaces cannot be captured with a depth-integrated model. As the aim of the current research is to develop a numerical tool that is applicable to both landslide initiation and propagation, the two-phase SPH model presented in this chapter is not depth-integrated. One of the most interesting features of the experimental debris flow is the evolution of the two distinct layers – one consisting of a homogeneous water-granular mixture, and another consisting mainly of water, with turbulent features. For this reason, the granular material and the water are modelled as two distinct phases with different velocities, which is also more representative of reality (as opposed to a single set of SPH nodes for both phases). This involves the implementation of two sets of SPH nodes – one set for the granular material, and one set for the water. The general SPH implementation is therefore based upon that of Bui and Nguyen (2017), and is applied to an experimental debris flow for the first time. The two-phase model is incorporated within both Standard SPH and Stress-Particle SPH.

8.2 Mathematical framework

In the context of granular flows, Biot (1956) introduced a two-phase theory to model the propagation of elastic waves in a saturated, elastic solid. This theory was extended by Zienkiewicz, Chang, and Bettess (1980) to account for the large deformation of nonlinear materials. The subsequent model, often termed the Biot-Zienkiewicz model, has been frequently implemented in numerical models to simulated saturated granular materials (Li, Zienkiewicz, and Xie, 1990; Pastor, Li, and Fernández-Merodo, 1997; Pastor et al., 2009a; Bui and Nguyen, 2017; Pastor et al., 2018). The fundamental framework of the coupled solid-fluid model assumes that the mixture consists of a soil skeleton with fluid filling the pores. In the present

application the two phases are considered to be soil and water. The volume fraction of the soil is denoted by ϕ_s, and the volume fraction of the water phase (the porosity) is defined as $\phi_w = 1 - \phi_s$, such that the sum of the volume fractions of the two phases is equal to 1. The partial densities of soil and water in the mixture, $\rho^{(s)}$ and $\rho^{(w)}$, are defined as

$$\rho^{(s)} = \phi_s \rho_s, \qquad \rho^{(w)} = \phi_w \rho_w, \tag{8.1}$$

where the subscripts s and w refer to the soil and water phases respectively. The total mixture density is

$$\rho = \rho^{(s)} + \rho^{(w)} = \phi_s \rho_s + \phi_w \rho_w. \tag{8.2}$$

Similarly, the partial stresses of the two phases are

$$\boldsymbol{\sigma}^{(s)} = \phi_s \boldsymbol{\sigma}_s, \quad \boldsymbol{\sigma}^{(w)} = \phi_w \boldsymbol{\sigma}_w, \tag{8.3}$$

where $\boldsymbol{\sigma}_s$ and $\boldsymbol{\sigma}_w$ are the intrinsic stresses of soil and water. The total stress of the mixture is

$$\boldsymbol{\sigma} = \boldsymbol{\sigma}^{(s)} + \boldsymbol{\sigma}^{(w)}. \tag{8.4}$$

Equations (8.1) to (8.4) comprise the underlying framework of a two-phase mixture. Under this general framework, the governing equations of motion of the soil-water mixture can be defined.

8.3 Equations of motion

The equations describing the conservation of mass (in a Lagrangian framework) for soil and water are

$$\frac{\partial \rho^{(s)}}{\partial t} + \nabla \cdot \left(\rho^{(s)} \mathbf{u}_s \right) = 0, \tag{8.5}$$

$$\frac{\partial \rho^{(w)}}{\partial t} + \nabla \cdot \left(\rho^{(w)} \mathbf{u}_w \right) = 0. \tag{8.6}$$

Following Bui and Nguyen (2017), it is assumed that the spatial gradients of the void fractions are negligible. With this assumption, and the substitution of the partial densities (Equation (8.1)), the mass conservation equations are

$$\frac{\partial \left(\phi_s \rho_s \right)}{\partial t} + \phi_s \rho_s \nabla \cdot \mathbf{u}_s = 0, \tag{8.7}$$

$$\frac{\partial \left(\phi_w \rho_w \right)}{\partial t} + \phi_w \rho_w \nabla \cdot \mathbf{u}_w = 0. \tag{8.8}$$

The first term of Equation (8.7) is expanded, and the density gradient is neglected as the deformation of the intrinsic solid phase is small in comparison to the deformation of the soil skeleton as a whole (Bui and Nguyen, 2017). This results in an equation

governing the evolution of the solid volume fraction:

$$\frac{\partial \phi_s}{\partial t} = -\phi_s \nabla \cdot \boldsymbol{u}_s. \tag{8.9}$$

Equation (8.8) is also expanded:

$$\phi_w \frac{\partial \rho_w}{\partial t} + \rho_w \frac{\partial \phi_w}{\partial t} = -\phi_w \rho_w \nabla \cdot \mathbf{u}_w, \tag{8.10}$$

where the second term on the left hand side can be rearranged in terms of the solid volume fraction:

$$\phi_w \frac{\partial \rho_w}{\partial t} - \rho_w \frac{\partial \phi_s}{\partial t} = -\phi_w \rho_w \nabla \cdot \mathbf{u}_w. \tag{8.11}$$

Utilising Equation (8.9), the fluid continuity equation can be written as

$$\phi_w \frac{\partial \rho_w}{\partial t} = -\phi_w \rho_w \nabla \cdot \mathbf{u}_w - \rho_w \frac{1-\phi_w}{\phi_w} \nabla \cdot \mathbf{u}_s. \tag{8.12}$$

If the final term is neglected, Equation (8.12) reduces to the usual mass conservation equation of a fluid. In the current work, it is assumed that local density variations are independent of the soil matrix deformations, and the final term of Equation (8.12) is ignored:

$$\phi_w \frac{\partial \rho_w}{\partial t} = -\phi_w \rho_w \nabla \cdot \mathbf{u}_w. \tag{8.13}$$

The equations governing the conservation of momentum of soil and water are

$$\rho^{(s)} \frac{\partial \mathbf{u}_s}{\partial t} = \nabla \cdot \boldsymbol{\sigma}^{(s)} + \rho^{(s)} \mathbf{g} + \mathbf{R} \tag{8.14}$$

$$\rho^{(w)} \frac{\partial \mathbf{u}_w}{\partial t} = \nabla \cdot \boldsymbol{\sigma}^{(w)} + \rho^{(w)} \mathbf{g} - \mathbf{R}, \tag{8.15}$$

where $\mathbf{R}$ is the interaction force between the solid and fluid phase, defining the momentum exchange between them. In Equations (8.14) and (8.15), the body force $\boldsymbol{b}$ is assumed to consist of gravity $\mathbf{g}$ only. Upon substitution of the partial densities, the momentum equations are written as

$$\phi_s \rho_s \frac{\partial \mathbf{u}_s}{\partial t} = \nabla \cdot \boldsymbol{\sigma}^{(s)} + \phi_s \rho_s \mathbf{g} + \mathbf{R}, \tag{8.16}$$

$$\phi_w \rho_w \frac{\partial \mathbf{u}_w}{\partial t} = \nabla \cdot \boldsymbol{\sigma}^{(w)} + \phi_w \rho_w \mathbf{g} - \mathbf{R}. \tag{8.17}$$

Note that Equation (8.16) reduces to the momentum conservation equation for a single phase soil, when $\phi_s = 1$ and $\mathbf{R} = 0$. The completion of the two-phase soil-water mixture equations requires the definition of the partial stresses $\boldsymbol{\sigma}^{(s)}$, $\boldsymbol{\sigma}^{(w)}$ and the interaction force $\mathbf{R}$. With regards to the soil phase, the concept of Terzaghi's effective stress is assumed, and the soil partial stress is written as:

$$\boldsymbol{\sigma}^{(s)} = \boldsymbol{\sigma}' - \phi_s p_w \mathbf{I}, \tag{8.18}$$

where $\boldsymbol{\sigma}'$ is the effective stress tensor of the soil skeleton and p_w is the pore water pressure (note that the viscosity of water has been neglected). The rheological behaviour of the soil skeleton is determined by the evolution of $\boldsymbol{\sigma}'$, which is defined in the same way as for a single phase material. Here, the soil is described with a rate dependent elastoplastic law is, as described in Chapter 3. Recall that for a single phase material, the stress tensor $\boldsymbol{\sigma}$ is written as a vector for convenience (as opposed to a tensor). This convention is also applied in the present two-phase analysis, so that upon substitution of the partial stress, the equation of momentum for the soil phase in two dimensions is

$$\phi_s \rho_s \frac{\partial \mathbf{u}_s}{\partial t} = \nabla \cdot \mathbf{f}^{\sigma\prime} - \phi_s \nabla p_w + \phi_s \rho_s \mathbf{g} - \mathbf{R}, \tag{8.19}$$

where in the plane strain condition

$$\boldsymbol{\sigma}' = \begin{pmatrix} \boldsymbol{\sigma}'_{xx} \\ \boldsymbol{\sigma}'_{yy} \\ \boldsymbol{\sigma}'_{xy} \\ \boldsymbol{\sigma}'_{zz} \end{pmatrix}, \quad \mathbf{f}^{\sigma\prime} = \begin{pmatrix} \boldsymbol{\sigma}'_{xx} & \boldsymbol{\sigma}'_{xy} \\ \boldsymbol{\sigma}'_{xy} & \boldsymbol{\sigma}'_{yy} \end{pmatrix}. \tag{8.20}$$

The spatial gradients of the solid volume fraction have been ignored in the derivation of Equation (8.19). The intrinsic stress of water consists of a deviatoric viscous term $\boldsymbol{\tau}$, and a volumetric pressure term $p_w \mathbf{I}$:

$$\boldsymbol{\sigma}_w = \boldsymbol{\tau} - p_w \mathbf{I}. \tag{8.21}$$

The effects of viscosity are often neglected in soil dynamics and debris flow models as they are assumed to be significantly less influential than the role of pore water pressures (Pitman and Le, 2005; Pelanti, Bouchut, and Mangeney, 2008; Pastor et al., 2015b; Bui and Nguyen, 2017). Although viscous stresses are an important aspect of debris flow dynamics (Iverson and George, 2014; Pudasaini, 2012), the viscosity is neglected in the current work, and pore water pressure is considered to be the only contribution to the fluid stress. Upon substitution of the fluid stress, the momentum equation for the water phase is

$$\phi_w \rho_w \frac{\partial \mathbf{u}_w}{\partial t} = -\phi_w \nabla p_w - \phi_w \rho_w \mathbf{g} - \mathbf{R}, \tag{8.22}$$

where spatial gradients of the fluid volume fraction have been neglected.

Finally, a definition is required for the interaction force $\mathbf{R}$. This includes a description of the drag between the water and the soil, which is a function of the velocity differences between the two phases. In the simplest approach, the drag is assumed to be linearly proportional to the velocity differences (Pitman and Le, 2005; Pastor et al., 2018). However, a quadratic drag dependence is better suited for high

velocity flows (Pudasaini, 2012; Bui and Nguyen, 2017), where

$$\mathbf{R}_D = C_D(\boldsymbol{u}_w - \boldsymbol{u}_s)|\boldsymbol{u}_w - \boldsymbol{u}_s|. \tag{8.23}$$

The drag coefficient C_D is problem dependent. For the relatively slow seepage of water through a low permeability material a Darcy drag coefficient is appropriate, whereas for the rapid flow of water through a high permeability material, an Anderson or Darcy-Forcheimer law is better suited (Bui and Nguyen, 2017; Pastor et al., 2018). Pudasaini (2012) combined two types of drag via a parameter to switch from one to the other:

$$C_D = \frac{\phi_s\phi_w(\rho_s - \rho_f)g}{(U_t(PF(Re_p) + (1-P)\phi_w^{M-2}))^l}, \tag{8.24}$$

where g is the magnitude of gravity (9.8), U_t is the terminal velocity of a single particle falling through a fluid, $P \in (0,1)$, l and M are model parameters and F is a particle Reynolds number (Re_p) dependent parameter: $F = \frac{\rho_f}{\rho_s}\left(\frac{\phi_w}{\phi_s}\right)^3 \frac{Re_p}{180}$. The parameter P can be adjusted according to the problem for model calibration. At the limiting cases, $P = 0$ corresponds to the movement of solid particles through a fluid, while $P = 1$ corresponds to fluid flow through densely packed grains (Pudasaini, 2012). The experimental flow exhibits a complex combination of this type of behaviour. The parameter l in Equation (8.24) was introduced by Pudasaini (2012), where $l = 1$ corresponds to laminar drag at low velocities and $l = 2$ represents turbulent drag, at high velocities. In the current work, values of $P = 1$ and $j = 1$ are implemented, for which Equation (8.24) reduces to

$$C_D = \frac{\phi_s\phi_w(\rho_s - \rho_f)g}{U_t F(Re_p)}. \tag{8.25}$$

Equation (8.25) is the same expression for drag as that employed by Pailha and Pouliquen (2009), in the investigation of underwater granular avalanches.

In summary, the governing two-phase equations of a soil-water mixture are:

$$\text{(Evolution of solid volume fraction)} \quad \frac{\partial \phi_s}{\partial t} = -\phi_s \nabla \cdot \boldsymbol{u}_s, \tag{8.26}$$

$$\text{(Conservation of mass for water phase)} \quad \frac{\partial \rho_w}{\partial t} = -\rho_w \nabla \cdot \mathbf{u}_w, \tag{8.27}$$

$$\text{(Conservation of momentum for soil phase)} \quad \frac{\partial \mathbf{u}_s}{\partial t} = \frac{1}{\rho^{(s)}}\left(\nabla \cdot \mathbf{f}^{\sigma\prime} - \phi_s \nabla p_w\right) + \mathbf{g} + \frac{1}{\rho^{(s)}}\mathbf{R}, \tag{8.28}$$

$$\text{(Conservation of momentum for water phase)} \quad \frac{\partial \mathbf{u}_w}{\partial t} = -\frac{1}{\rho_w}\nabla p_w + \mathbf{g} - \frac{1}{\rho^{(w)}}\mathbf{R}, \tag{8.29}$$

$$\text{(Interaction force)} \quad \mathbf{R} = C_D(\boldsymbol{u}_w - \boldsymbol{u}_s)|\boldsymbol{u}_w - \boldsymbol{u}_s|, \tag{8.30}$$

$$\text{(Constitutive equation for soil phase)} \quad \frac{\partial \boldsymbol{\sigma}'}{\partial t} = \tilde{\boldsymbol{\sigma}}' + \nabla \cdot \mathbf{f}^u - \mathbf{g}^{\epsilon^p}. \tag{8.31}$$

Note that the constitutive equation (Equation (8.31)) is the same as for a single phase material. It describes the constitutive behaviour of the soil phase only, and

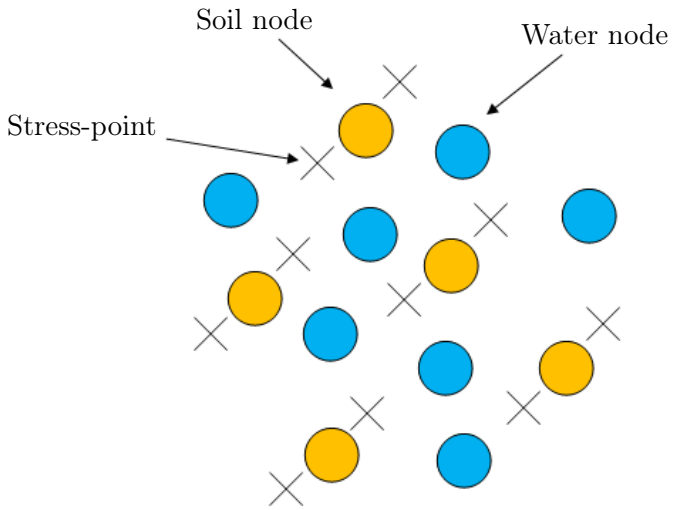

FIGURE 8.1: A depiction of the two-phase Stress-Particle SPH method.

not the total mixture. In addition to the system defined by Equations (8.26) - (8.31), a description of the pore water pressure evolution is required. This can be related to the density via an equation of state (Batchelor and Batchelor, 1967), which is defined in Section 8.4.6.

8.4 Two-phase Stress-Particle SPH

In this section the two-phase model described by Equations (8.26) - (8.31) is defined within the SPH framework. The two distinct phases – soil and water – are described by two different sets of nodes in SPH. One set of nodes represents the water and the governing equations of motion for the water are solved on these nodes. The other set of nodes describe the soil skeleton, and carry information about the soil. In Stress-Particle SPH, stress-points are attached to the soil nodes, and function in the same way as detailed in Chapter 4. A depiction of the two-phase model in Stress-Particle SPH is provided in Figure 8.1. Recall that in the Stress-Particle SPH methodology, the subscripts i and j denote the nodes and stress-points respectively. Here, the water nodes must also be distinguished from the soil nodes and stress-points. In the following definitions, the water nodes are referred to by the subscripts α and β (two subscripts are required to distinguish water nodes from other water nodes). Furthermore, there are some calculations that involve node-node interactions – for this purpose, SPH nodes are denoted by the subscripts i and k. In the remainder of this section, SPH approximations are directly applied to the governing equations. For further details on the derivation of the SPH approximations see Chapter 4.

8.4.1 SPH approximation of the volume fraction

The evolution of the solid volume fraction is described by the following equation:

$$\frac{\partial \phi_s}{\partial t} = -\phi_s \nabla \cdot \boldsymbol{u}_s, \tag{8.32}$$

which is solved on the SPH soil nodes, using information from the neighbouring soil nodes. The SPH divergence approximation (Equation (4.19)) is applied to the right hand side term of Equation (8.32):

$$-\left(\phi_s \nabla \cdot \boldsymbol{u}_s\right)_i = -\phi_{s,i} \sum_{k=1}^{N_k} \frac{m_k}{\rho_k^{(s)}} \left(\boldsymbol{u}_{s,i} - \boldsymbol{u}_{s,k}\right) \cdot \nabla W_{ik}, \tag{8.33}$$

where the density of the soil skeleton $\rho^{(s)}$ is used within the SPH summation, as opposed to the intrinsic soil density ρ_s. The SPH approximation of the rate of change of solid volume fraction is therefore

$$\frac{\partial \phi_{s,i}}{\partial t} = -\phi_{s,i} \sum_{k=1}^{N_k} \frac{m_k}{\rho_k^{(s)}} \left(\boldsymbol{u}_{s,i} - \boldsymbol{u}_{s,k}\right) \cdot \nabla W_{ik}. \tag{8.34}$$

The calculation of the fluid volume fraction first requires the approximation of the solid volume fraction at each water node, which is interpolated from the surrounding soil nodes via the SPH-CSPM method:

$$\phi_{s,\alpha} = \frac{\sum_{i=1}^{N_i} \frac{m_i}{\rho_i^{(s)}} \phi_{s,i} W_{i\alpha}}{\sum_{i=1}^{N_i} \frac{m_i}{\rho_i^{(s)}} W_{i\alpha}}. \tag{8.35}$$

The fluid volume fraction is then obtained at each water node:

$$\phi_{w,\alpha} = 1 - \phi_{s,\alpha}. \tag{8.36}$$

In this way, a fluid volume fraction of $\phi_w = 1$ is calculated at the water nodes that do not contain any soil nodes in their neighbourhood.

8.4.2 SPH approximation of mass conservation for water

The equation describing the conservation of mass for the water phase is

$$\frac{\partial \rho_w}{\partial t} = -\rho_w \nabla \cdot \mathbf{u}_w. \tag{8.37}$$

As described in Section 4.3, there are a number of different ways in which to approximate the density in SPH. Here, the SPH continuity density approach (Equation

(4.27)) is employed to discretise Equation (8.37):

$$\frac{\partial \rho_{w,\alpha}}{\partial t} = -\rho_{w,\alpha} \sum_{\beta=1}^{N_\beta} \frac{m_\beta}{\rho_\beta^{(w)}} \left(\boldsymbol{u}_{w,\alpha} - \boldsymbol{u}_{w,\beta}\right) \cdot \nabla W_{\alpha\beta}. \tag{8.38}$$

Note that the density of the water phase $\rho^{(w)}$ is used within the summation in Equation (8.38), rather than the intrinsic water density ρ_w. Equation (8.38) is solved on each water node α, using information from the surrounding water nodes β.

8.4.3 SPH approximation of momentum conservation for soil

The equation describing the conservation of momentum of soil in a two-phase soil-water mixture is:

$$\frac{\partial \mathbf{u}_s}{\partial t} = \frac{1}{\rho^{(s)}} \left(\nabla \cdot \mathbf{f}^{\sigma\prime} - \phi_s \nabla p_w\right) + \mathbf{g} + \frac{1}{\rho^{(s)}} \mathbf{R}. \tag{8.39}$$

The soil stress term on the right hand side of Equation (8.39) is discretised in the same way as for a single phase soil, except that the single phase soil density ρ_s is replaced by the soil phase density in a two-phase mixture $\rho^{(s)} = \phi_s \rho_s$:

$$\frac{1}{\rho_i^{(s)}} \left(\nabla \cdot \mathbf{f}^{\sigma\prime}\right) i = \sum_{j=1}^{N_j} m_j \left(\frac{\mathbf{f}_i^{\sigma\prime}}{\rho_i^{(s)2}} + \frac{\mathbf{f}_j^{\sigma\prime}}{\rho_j^{(s)2}}\right) \cdot \nabla W_{ij}. \tag{8.40}$$

The second term on the right hand side of Equation (8.39) is the gradient of the pore water pressure within the soil. As the pore water pressure is a variable of the water phase, it is calculated and stored on the water nodes. Therefore the pore water pressure must first be approximated on each soil particle, via an SPH-CSPM interpolation over the surrounding water nodes:

$$p_{w,i} = \frac{\sum_{\alpha=1}^{N_\alpha} \frac{m_\alpha}{\rho_\alpha^{(w)}} p_{w,\alpha} W_{i\alpha}}{\sum_{\alpha=1}^{N_\alpha} \frac{m_\alpha}{\rho_\alpha^{(w)}} W_{i\alpha}}. \tag{8.41}$$

The pore water pressure gradient can then be approximated on the soil phase by applying the SPH gradient approximation, in the same way as for the stress terms in Equation (8.40). However it was shown by Bui and Fukagawa (2013) that numerical instabilities can arise at the soil-water interface when the pore water pressure gradient is approximated in this way, unless a dynamic boundary condition is applied at the interface. To avoid the additional computational cost that this brings, they proposed an alternative gradient approximation for the pore water pressure:

$$\left(\frac{1}{\rho^{(s)}} \phi_s \nabla p_w\right)_i = \phi_s \sum_{k=1}^{N_k} m_k \left(\frac{p_{w,i} - p_{w,k}}{\rho_i^{(s)} \rho_k^{(s)}}\right) \nabla W_{ik}. \tag{8.42}$$

Equation (8.42) automatically accounts for the dynamic boundary condition at the soil-water interface, and is solved at every soil node i by summing over the neighbouring soil nodes k.

With Equations (8.40) and (8.42), the discrete momentum equation for the soil phase is

$$\frac{\partial \mathbf{u}_{s,i}}{\partial t} = \sum_{j=1}^{N_j} m_j \left(\frac{\mathbf{f}_i^{\sigma\prime}}{\rho_i^{(s)2}} + \frac{\mathbf{f}_j^{\sigma\prime}}{\rho_j^{(s)2}} \right) \nabla W_{ij} - \phi_s \sum_{k=1}^{N_k} m_k \left(\frac{p_{w,i} - p_{w,k}}{\rho_i^{(s)} \rho_k^{(s)}} \right) \nabla W_{ik} + \mathbf{g}_i + \frac{1}{\rho_i^{(s)}} \mathbf{R}_i. \tag{8.43}$$

Equation (8.43) is written in the Stress-Particle SPH framework. Note that in the outside approach, the volume fraction of each stress-point (required for the calculation of $\rho^{(s)}$) is assumed to be equal to the volume fraction of its corresponding node. For the Standard SPH method, the subscript j is replaced with the subscript k in the first term on the right hand side of Equation (8.43). Artificial viscosity may also be included on the right hand side of Equation (8.43), in the same way as outlined in Section 4.5.1.

8.4.4 SPH approximation of the soil constitutive equation

The constitutive equation of the soil phase (Equation (8.31)) is solved in the same way as described in Chapter 4, except the soil phase density $\phi_s \rho_s$ is included in the SPH summation approximation (rather than the intrinsic soil density ρ_s). In discrete form, the soil constitutive equation is

$$\frac{\partial \boldsymbol{\sigma}_j}{\partial t} = \tilde{\boldsymbol{\sigma}}_j + \sum_{i=1}^{N} \frac{m_i}{\rho_i^{(s)}} \left(\mathbf{f}_i^u - \mathbf{f}_j^u \right) \cdot \nabla W_{ji} - \mathbf{g}_j^{\epsilon^p}, \tag{8.44}$$

where $\mathbf{f}^u$ is a function of velocity and $\mathbf{g}^{\epsilon^p}$ is a function of the plastic strain.

8.4.5 SPH approximation of momentum conservation for water

The momentum conservation equation for the water phase is:

$$\frac{\partial \mathbf{u}_w}{\partial t} = -\frac{1}{\rho_w} \nabla p_w + \mathbf{g} - \frac{1}{\rho^{(w)}} \mathbf{R}. \tag{8.45}$$

In the same way as for the stress terms in the single phase soil model, the first term on the right hand side of Equation (8.45) can be written as

$$\frac{1}{\rho_w} \nabla p_w = \nabla \left(\frac{p_w}{\rho_w} \right) + \frac{p_w}{\rho_w^2} \nabla \rho_w. \tag{8.46}$$

The SPH gradient approximation (Equation (4.18)) is then applied to Equation (8.46):

$$\frac{1}{\rho_{w,\alpha}} \left(\nabla p_w \right)_\alpha = \sum_{\beta=1}^{N_\beta} \frac{m_\alpha}{\rho_\alpha^{(w)}} \left(\frac{p_{w,\alpha}}{\rho_{w,\alpha}} + \frac{p_{w,\beta}}{\rho_{w,\beta}} \right) \nabla W_{\alpha\beta}. \tag{8.47}$$

The discrete equation of the conservation of momentum for water is therefore written as

$$\frac{\partial \mathbf{u}_{w,\alpha}}{\partial t} = -\sum_{\beta=1}^{N_\beta} \frac{m_\alpha}{\rho_\alpha^{(w)}} \left(\frac{p_{w,\alpha}}{\rho_{w,\alpha}} + \frac{p_{w,\beta}}{\rho_{w,\beta}} \right) \nabla W_{\alpha\beta} + \mathbf{g}_\alpha - \frac{1}{\rho_\alpha^{(w)}} \mathbf{R}_\alpha. \tag{8.48}$$

In addition to the interaction force, Equation (8.48) requires a definition of the pore water pressure evolution. Furthermore, an artificial viscosity term may be included on the right hand side of Equation (8.48). This is calculated in the same way as for a soil (see Section 4.5.1), replacing the soil node interactions with the water node. Moreover, the numerical speed of sound for water is included, as opposed to the speed of sound for soil. Equation (8.48) is solved on each water node by summing over the surrounding water nodes.

8.4.6 Pore water pressure

Within the vast application of SPH to fluids, there are two existing techniques in which to calculate the pressure – according to an equation of state (Monaghan, 1994; Violeau and Issa, 2007; Gómez-Gesteira et al., 2010), or by solving an additional partial differential equation (the Poisson equation) (Shao and Lo, 2003; Lee et al., 2008; Bui and Nguyen, 2017). In the latter method, the pressure is evolved as a function of velocity according to the Poisson equation, which is derived under the condition of incompressibility. This method is utilised within the so-called truly incompressible SPH, as the density can be kept constant at each particle (Lee et al., 2008). Solving the Poisson equation involves the solution of a Laplacian equation, as well as the enforcement of a zero pressure condition on the free surface nodes.

Conversely, the pressure can be related to the density according to an equation of state:

$$p_w = B \left(\left(\frac{\rho_w}{\rho_{w0}} \right)^\gamma - 1 \right), \tag{8.49}$$

where B is a constant determined by the numerical speed of sound, $\gamma = 7$ is a model constant and ρ_{w0} is a reference density – usually taken to be the density of water. Equation (8.49) requires local density variations to calculate a non-zero pressure, so that the model cannot be truly incompressible. However the speed of sound $\tilde{c}$ can be chosen to be sufficiently large to reduce the density fluctuations to less than 1%. This method is referred to as weakly compressible SPH, and $\tilde{c}$ is typically taken to be 10 times the value of the predicted velocity maximum (Monaghan and Kos, 1999; Lee et al., 2008). Solving Equation (8.49) in weakly compressible SPH is more straightforward and less computationally expensive than obtaining the solution to the Poisson equation in truly incompressible SPH. Therefore, in the current application Equation (8.49) is used to obtain the pore water pressure.

Speed of sound

The speed of sound for the fluid $\tilde{c}$ is a function of the derivative of the pressure with respective to the density (Batchelor and Batchelor, 1967):

$$\tilde{c}^2 = \frac{\partial p_w}{\partial \rho_w} = \frac{B\gamma}{\rho_0}\left(\frac{\rho_w}{\rho_{w0}}\right)^{\gamma-1}. \tag{8.50}$$

The constant $B = \frac{c_0^2 \rho_{w0}}{\gamma}$, where $\tilde{c}_0$ is the speed of sound at the reference density. It is not possible to use a realistic value of $\tilde{c}_0$ in the computation of fluids, as the time step imposed by the CFL condition would be excessively small. It has been shown that a reference speed of sound that is approximately ten times the maximum velocity is usually sufficient for reasonable pressure calculations (Monaghan and Kos, 1999; Gómez-Gesteira et al., 2010). With the specification of the reference density, the pore water pressure is defined according to Equation (8.49).

8.4.7 SPH approximation of the interaction force

The interaction force that is implemented in the current two-phase SPH model is defined as

$$\mathbf{R} = C_D(\boldsymbol{u}_w - \boldsymbol{u}_s)|\boldsymbol{u}_w - \boldsymbol{u}_s|, \tag{8.51}$$

$$C_D = \frac{\phi_s \phi_w (\rho_s - \rho_f) g}{U_t F(Re_p)}. \tag{8.52}$$

The discrete forms of Equation (8.51) for the water and soil phases respectively are:

$$\mathbf{R}_\alpha = C_{D,\alpha}(\boldsymbol{u}_{w,\alpha} - \boldsymbol{u}_{s,\alpha})|\boldsymbol{u}_{w,\alpha} - \boldsymbol{u}_{s,\alpha}|, \tag{8.53}$$

$$\mathbf{R}_i = C_{D,i}(\boldsymbol{u}_{w,i} - \boldsymbol{u}_{s,i})|\boldsymbol{u}_{w,i} - \boldsymbol{u}_{s,i}|. \tag{8.54}$$

The evaluation of Equation (8.53) on the water phase requires the approximation of the soil phase velocity at each water particle. Similarly, to solve Equation (8.54) on the soil phase, the water velocity is required at each soil particle. The soil and water velocities are approximated on the water and soil phases respectively via an SPH-CSPM interpolation:

$$\boldsymbol{u}_{s,\alpha} = \frac{\sum_{i=1}^{N_i} \frac{m_i}{\rho_i^{(s)}} \boldsymbol{u}_{s,i} W_{i\alpha}}{\sum_{i=1}^{N_i} \frac{m_i}{\rho_i^{(s)}} W_{i\alpha}}, \quad \boldsymbol{u}_{w,i} = \frac{\sum_{\alpha=1}^{N_\alpha} \frac{m_\alpha}{\rho_\alpha^{(w)}} \boldsymbol{u}_{w,\alpha} W_{i\alpha}}{\sum_{\alpha=1}^{N_\alpha} \frac{m_\alpha}{\rho_\alpha^{(w)}} W_{i\alpha}}. \tag{8.55}$$

Furthermore, the solid volume fraction is interpolated on the water nodes in the same way, while the fluid volume fraction is obtained on the soil nodes as $\phi_w = 1 - \phi_s$. The remaining terms in the interaction force are model constants.

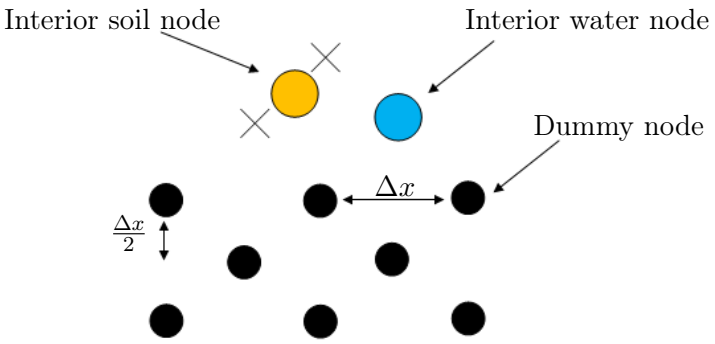

FIGURE 8.2: A depiction of the boundary treatment in the two-phase Stress-Particle SPH method.

8.4.8 Boundary treatment

The boundaries of interest in the current applications are wall boundaries. Recall that for a single phase soil, dummy nodes are employed to simulate a wall. Dummy nodes can also be utilised to prevent the water nodes from penetrating the boundaries and to improve the kernel approximation in the boundary region. The simplest method is to calculate and evolve the fluid density and pressure on the dummy nodes, while keeping their positions unchanged. The dummy node variables are included in the calculation of the density of the water nodes, to implicitly account for the presence of wall boundaries. This method was introduced by Dalrymple and Knio (2001) in the application of SPH to water waves. In the present two-phase SPH model, dummy nodes are employed to simulate the no-slip condition for the soil phase, in the same way as detailed in Section 4.4. In addition, the fluid continuity and pressure equations are solved on the dummy nodes. The only difference regarding the dummy node implementation in the single phase and two-phase SPH models is the arrangement of the dummy nodes. For the single phase model, the dummy nodes are positioned in a regular arrangement to simulate the wall boundaries, with the rows spaced apart by the initial particle spacing Δx (see Figure 4.6 in Chapter 4). To ensure that the water particles do not penetrate the boundary, it is recommended to place the dummy nodes in a staggered arrangement, with the row spacing equal to $\frac{\Delta x}{2}$ (Crespo, Gómez-Gesteira, and Dalrymple, 2007). A depiction of the dummy node placement in two-phase Stress-Particle SPH is provided in Figure 8.2.

8.4.9 Computational implementation

In the same way as for the single phase Stress-Particle SPH method, the RK4 scheme is used to update each variable in time, which is described in detail in Chapter 4. The additional routines required for the implementation of the two-phase SPH method were written in Fortran 90 by the author of the current research. The extra routines consist of: the initialisation of the separate soil and water nodes, the soil-water node interaction, the drag force calculations, the solid volume fraction evaluation,

the solution of the water momentum equation, the water density update and the calculation of the pore water pressures. A summary of the computational procedure that is performed at each time step for two-phase Stress-Particle SPH is provided in Figure 8.3. The two-phase SPH model has also been implemented within a Standard SPH framework. For Standard SPH, the stress-points are disabled for the soil phase and node-stress-point interactions are redefined as node-node interactions.

In the remainder of this chapter, the results of the two-phase Stress-Particle and Standard SPH methods are presented and assessed. First, the two-phase model is validated with the simulation of two benchmark problems from the literature. Next, the model is applied to the experimental flow, described in Chapter 7. Note that in all subsequent results, the XSPH method was not used to update the particle positions. The positions of both the soil and water nodes are updated according to

$$\frac{\mathrm{d}\mathbf{x}_i}{\mathrm{d}t} = \boldsymbol{u}_{s,i}, \quad \frac{\mathrm{d}\mathbf{x}_\alpha}{\mathrm{d}t} = \boldsymbol{u}_{w,\alpha}, \tag{8.56}$$

which is solved as described in Section 4.6.

8.4.10 Model validation

Collapse of a water column

To ensure that the water phase has been correctly implemented within the current SPH model, the benchmark problem of a two-dimensional water column collapse has been simulated. The two-phase SPH model has been reduced to a single phase water model to simulate this problem – the soil nodes are not included and the fluid volume fraction is defined as one. The problem is based on experiments performed by Koshizuka and Oka (1996), and has been frequently used to validate SPH models in the literature (Violeau and Issa, 2007; Crespo, Gómez-Gesteira, and Dalrymple, 2007; Gómez-Gesteira et al., 2010). A volume of water with an initial height of 2 m and a length of 1 m is allowed to collapse in a tank that is 2 m in height and 4 m in length. Here, the current SPH model is validated by comparing with the numerical results of Crespo, Gómez-Gesteira, and Dalrymple (2007), who employed 40000 nodes to describe the water column. Crespo, Gómez-Gesteira, and Dalrymple (2007) did not include the effects of turbulence or viscous stresses, yet included artificial viscosity with the parameter $\alpha_\Pi = 0.5$. Here, a total of 20302 SPH nodes have been used, with a time step of $\Delta t = 2 \times 10^{-5}$ s. Artificial viscosity has also been included with $\alpha_\Pi = 0.5$, $\beta_\Pi = 0$, and the reference speed of sound was defined as $\tilde{c}_0 = 60$ m s^{-1}. The results of the column collapse simulated with the current SPH model are shown in Figure 8.4, along with the results of Crespo, Gómez-Gesteira, and Dalrymple (2007). It is evident that the water displays the same behaviour, confirming that the water phase has been implemented correctly in the current research.

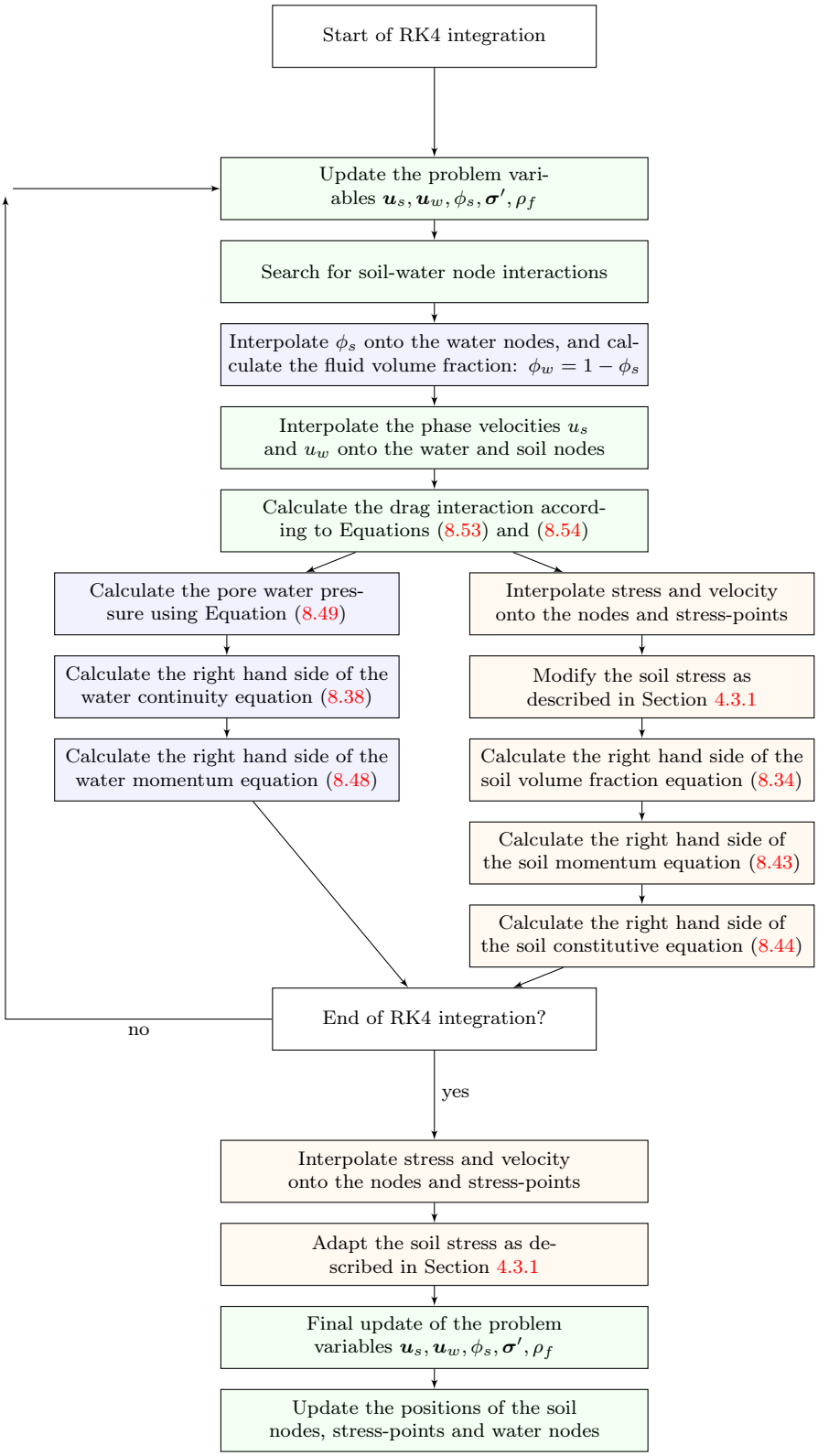

FIGURE 8.3: A flow chart depicting the calculation steps of two-phase Stress-Particle SPH. The blue and orange entries represent the water and soil phase calculations respectively, while the green entries correspond to actions that are relevant to both the water and soil phase.

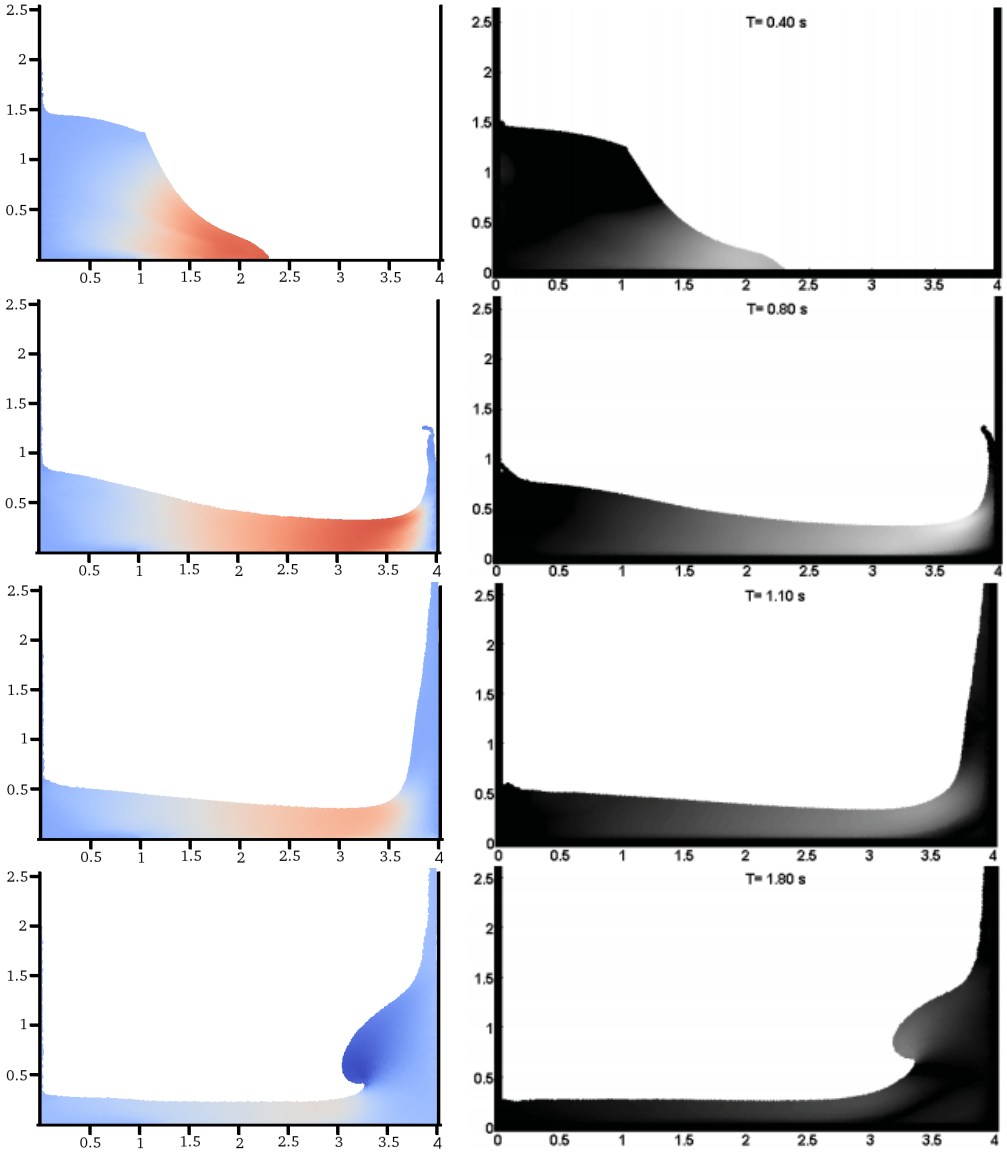

(A) Current SPH model

(B) Crespo, Gómez-Gesteira, and Dalrymple (2007)

FIGURE 8.4: The collapse of a water column, comparing the results of the current SPH model with those of Crespo, Gómez-Gesteira, and Dalrymple (2007) at $t = 0.4$ s, $t = 0.8$ s, $t = 1.1$ s and $t = 1.8$ s. The nodes are coloured by contours of horizontal velocity.

TABLE 8.1: Material parameters for the submerged, elastic soil.

E (Pa)	ν	ρ_s (kg m^{-3})	ρ_w (kg m^{-3})	γ_{sat} (kN m^{-3})	γ_w (kN m^{-3})	ϕ_s
1×10^8	0.3	2600	1000	20.797	9.81	0.7

Submerged soil sample

To verify that the soil and water mixture model has been implemented correctly, both the Standard SPH and Stress-Particle SPH models have been applied to simulate the in-situ stresses in a saturated, elastic soil. This problem has been considered by previous authors for two-phase model validation (Bui and Fukagawa, 2013; Bui and Nguyen, 2017). The problem consists of a 10 m $\times$ 10 m elastic soil sample that is fully submerged in water of 12 m in height. The purpose is to examine the soil stress profiles in an approximately stationary water sample. The vertical distribution of stress and pore water pressure within the soil can be compared to an analytical solution. The vertical effective stress profile is expected to vary with height as:

$$\sigma'_{yy}(y) = (\gamma_{\text{sat}} - \gamma_w)(H_s - y), \tag{8.57}$$

where γ_{sat} is the unit weight of the saturated soil (kN m^{-3}), γ_w is the unit weight of water and H_s is the total height of the soil (m). The pore water pressure is expected to have a hydrostatic profile:

$$p_w(y) = g\rho_w(H_w - y), \tag{8.58}$$

where H_w is the total height of the water.

A total of 5500 nodes were used to model the submerged soil ($n_s = 2500$ soil nodes and $n_w = 3000$ water nodes), with an initial spacing of $\Delta x = 0.2$ m. Following Bui et al., 2008, the soil volume fraction was defined as $\phi_s = 0.7$, and was not updated throughout the simulation. The material parameters are provided in Table 8.1. Gravity was applied progressively over one second, and artificial viscosity was included with $\alpha_\Pi = 0.5, \beta_\Pi = 0$. The simulation was ran for a total of 3 seconds, with a time step of $\Delta t = 1 \times 10^{-5}$ s and a smoothing length of $1.2\Delta x$. Dummy nodes were employed at the lower, left and right boundaries. The problem was simulated with Standard SPH, in addition to SP1, SP2 and SP3. The inside Stress-Particle approach was used because the material displacements are small.

Contours of effective vertical stress are shown in Figure 8.5, for Stress-Particle SPH with configuration SP3. As expected, the effective stress is zero at the soil surface, and increases in magnitude towards the base of the sample. Plots of vertical stress and pore pressure are provided in Figure 8.6 for Standard SPH, SP1, SP2 and SP3, compared against the analytical solution. In all cases, the expected pore water pressure profile is predicted well throughout the majority of the sample height. Regarding the vertical effective stress, the results of Standard SPH match the overall

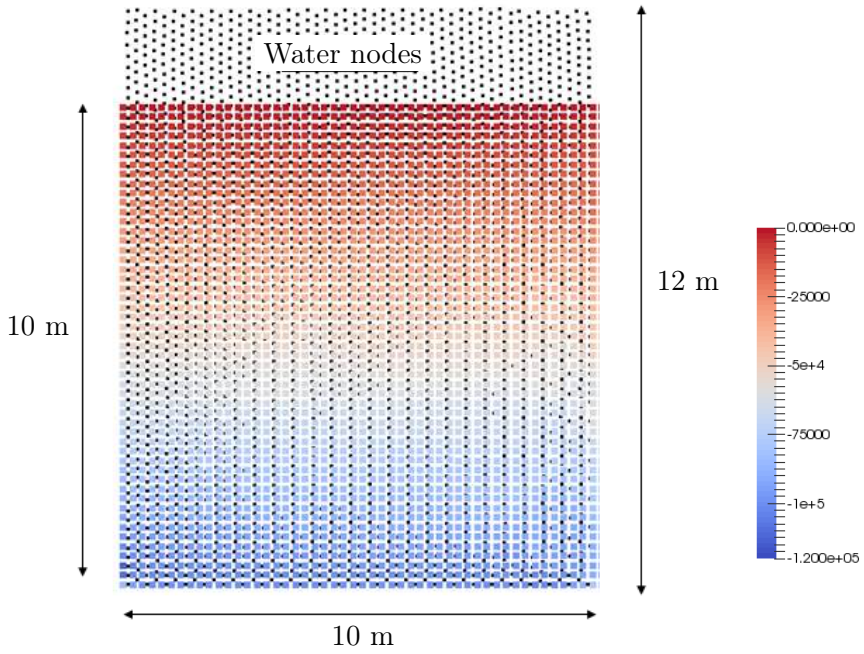

FIGURE 8.5: Contours of vertical effective stress σ'_{yy} (Pa) in a submerged elastic soil sample, calculated with Stress-Particle SPH (for the SP3 configuration).

profile. The individual SPH particles show signs of an unstable, non-smooth configuration, and the results diverge from the analytical profile around the centre of the sample. Conversely, the Stress-Particle SPH particles show a smooth and stable profile throughout depth. The results in Figure 8.6 confirm that the soil-water mixture model has been correctly applied, and also highlight the benefits of using stress-points within two-phase soil-water problems.

8.5 Experimental debris flow

The experimental set-up has been implemented within the two-dimensional SPH model, where two layers of granular material and water are released from behind a lock gate in a dam break scenario. The granular material used in the experiment has been approximated as a purely frictional, elastoplastic soil with a Drucker-Prager yield criterion. The model parameters for the soil in the numerical model are the same as those determined for the experimental material, provided in Section 7.2. Furthermore, the Poisson ratio is assumed to be $\nu = 0.3$. The experimental flow exhibited regions of viscous behaviour (see Section 7.4), which suggests that the soil could also be approximated with a viscoplastic Perzyna model. However this model requires the tuning of additional parameters, which are not possible to measure. Furthermore, the viscous behaviour is representative of the soil-water mixture as a single phase. In the current application, the two distinct phases are considered and a frictional Drucker-Prager model is a more physical representation of the granular phase. The relevant material parameters are provided in Table 8.2.

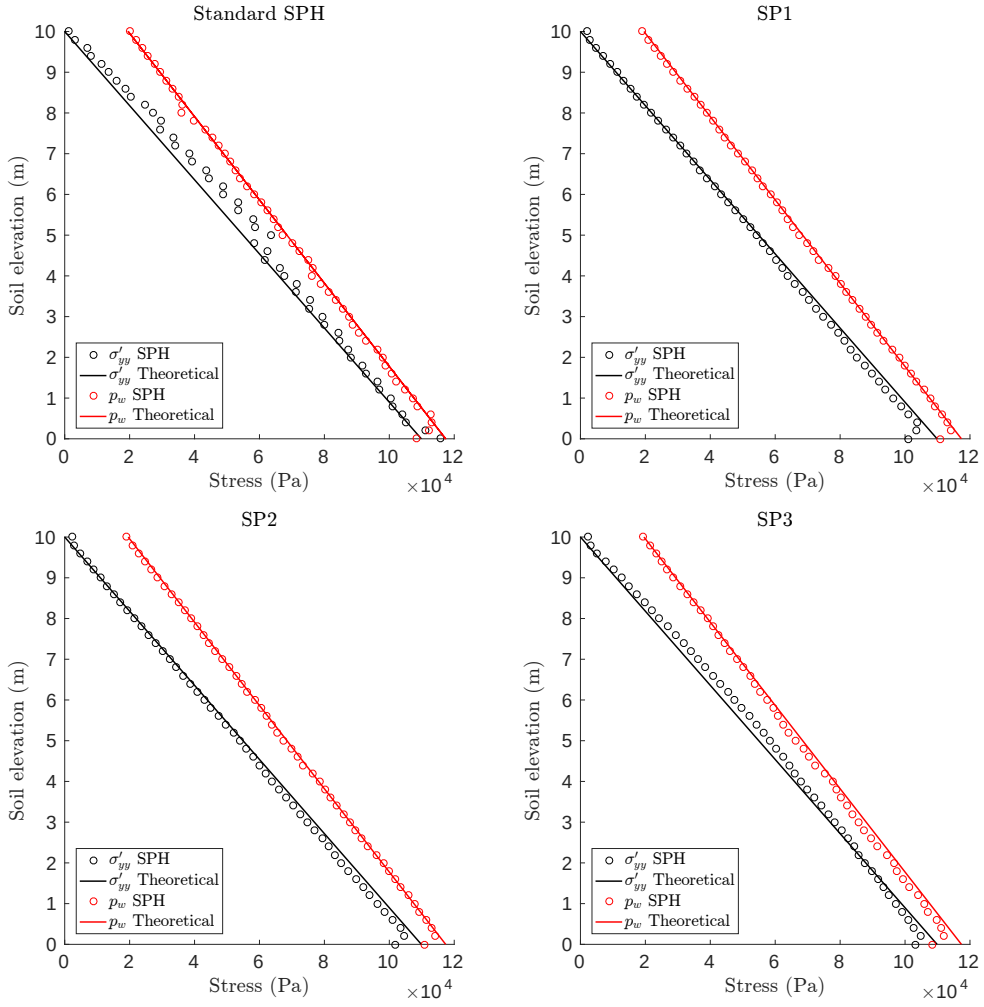

FIGURE 8.6: Plots of vertical effective stress σ'_{yy} (Pa) and pore water pressure p_w (Pa) against soil elevation (m), for Standard SPH, SP1, SP2 and SP3. The data correspond to a horizontal location of $x = 5$ m. The SPH solution is depicted by the markers, while the continuous line represents the analytical solution. Note the change in sign convention for the stress – the compressive stress is positive, for plotting purposes only.

TABLE 8.2: Elastoplastic material parameters for the soil and water phases in the experimental debris flow.

E (Pa)	ν	ϕ (°)	c_{oh} (Pa)	ρ_w (kg m^{-3})	ρ_s (kg m^{-3})	ϕ_s
6.916×10^5	0.3	39	0	997	1851	0.44

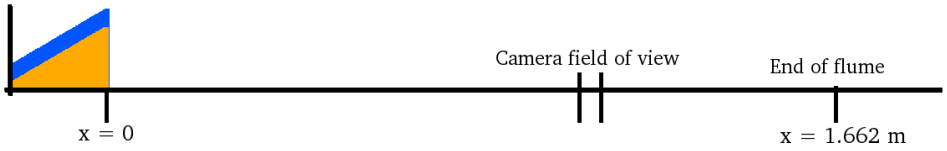

(A) The implementation of the experimental set-up in SPH. The orange layer depicts the soil nodes while the upper blue layer represents the water nodes.

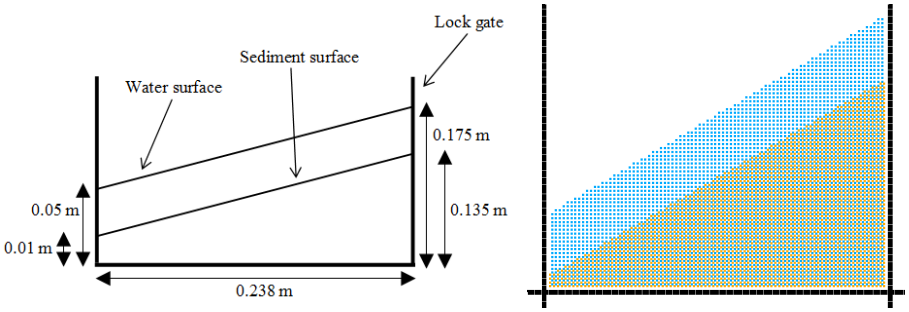

(B) The initial soil-water placement in the experiments

(C) The initial node placement in SPH

FIGURE 8.7: The initial material placement in the simulation of the experimental debris flow.

Two layers of soil and water nodes are positioned behind the lock gate, in the same configuration as for the experiment (see Figure 8.7). The soil and water nodes are initially placed in a staggered arrangement, as shown in Figure 8.7c. Three layers of dummy nodes (also staggered) are used to represent the flume bed, the left vertical wall and the lock gate. The release of the material from the lock gate is simulated by disabling the relevant dummy nodes. The length of the flume in the numerical simulation is 0.25 m longer than the experimental flume, to ensure that the material that exceeds the extent of the horizontal boundary does not influence the succeeding flow. The slope of the experimental flume (31°) is incorporated by adapting the gravity terms in the body force component of the soil and water momentum equations. To allow the full development of the pore water pressure and soil stress profiles, the lock gate dummy nodes are kept in place for 2 seconds. Furthermore, the gravity force is applied progressively over 1 second to prevent the occurrence of numerical instabilities. The interaction force is not included during this time as the material movement is minimal and the interaction can be considered to be negligible. After the material initialisation, the lock gate dummy nodes are disabled. Note that this initialisation process only needs to be performed once, and simulations can be restarted from the initialised state.

A total of $n_s = 9949$ soil nodes and $n_w = 15344$ water nodes were employed to simulate the experimental debris flow, with an initial particle spacing of $\Delta x = 0.00125$ m. The smoothing length was chosen to be $h_s = 1.2\Delta x$. The speed of sound for the soil phase was defined as $c = 100$ m s^{-1}, and the reference sound speed for the water phase was defined as $\tilde{c}_0 = 70$ m s^{-1}. A time step of $\Delta t = 5 \times 10^{-6}$ s was employed, providing an acceptable Courant number of $C_o = 0.\dot{3}$. Artificial viscosity

was included in all simulations with model parameters $\alpha_\pi = \beta_\pi = 0.1$.

A particle resolution test was performed with Standard SPH to assess the influence of the number of particles on the results. Figure 8.8 shows the positions of the soil and water phases after 0.5 and 0.75 seconds of flow, for three different particle resolutions. The tests were performed with 6873, 9949 and 15555 soil nodes, and 10402, 15344 and 23843 water nodes respectively. For these simulations, the solid and fluid volume fractions were not updated, and no interaction force was included. The overall profiles align closely for the three resolutions, although the front position of the material increases slightly with an increase in the number of particles. The evolution of the soil and water particles are shown in close detail in Figure 8.9. The vertical boundaries signify the field of view of the camera in the experiments, which is the area of interest in the current work. The red horizontal line depicts the height of the experimental flow at each time. The time labels correspond to the time since the material entered the camera field of view (coinciding with the experimental results). Comparing the results in Figures 8.9a to 8.9e, it can be seen that the simulation with $n_s = 9949$ replicates the features from the simulation with the highest particle resolution ($n_s = 15555$) to a reasonable extent. This is in terms of the height of the material, and the respective behaviour of the soil and water phases. Meanwhile, the results for the coarsest particle resolution overpredict the material height quite significantly, and do not show sufficient detail. Note that as the SPH model is currently only implemented as a serial process, the simulation with the highest particle number takes an excessive amount of time to run, which increases with the addition of stress-points. Furthermore, the overall qualitative soil-water behaviour is the factor that is of interest in the current work, rather than the precise detail. Therefore, a particle resolution of $n_s = 9949$ and $n_w = 15344$ is assumed to provide a suitable compromise between accuracy and computational time, and has been employed to obtain all subsequent results.

Both Standard SPH and Stress-Particle SPH were used to simulate the experimental debris flow. In Chapter 6, it was shown that the Stress-Particle SPH method has an optimal performance when the stress-points are aligned with the direction of the flow. In the simulations of the experimental debris flow, the overall flow direction is approximately parallel to the bed due to the high slope inclination. This can be seen in the velocity vectors calculated with Standard SPH shown in Figure 8.10. Note that in this case, the time corresponds to the time since the flow initiation (as opposed to the arrival of the front at the camera field of view). Therefore, for the simulation of the experimental flow with Stress-Particle SPH, each stress-point has been positioned at a horizontal distance of $\frac{\Delta x}{3}$ on either side of each node, as shown in Figure 8.10b.

Figure 8.11 shows the evolution of the soil and water nodes for both Standard SPH and Stress-Particle SPH. As a first approximation, the volume fractions were not updated and no interaction force was included. This does not represent the behaviour of the experimental debris flow, but it provides an initial simplified case

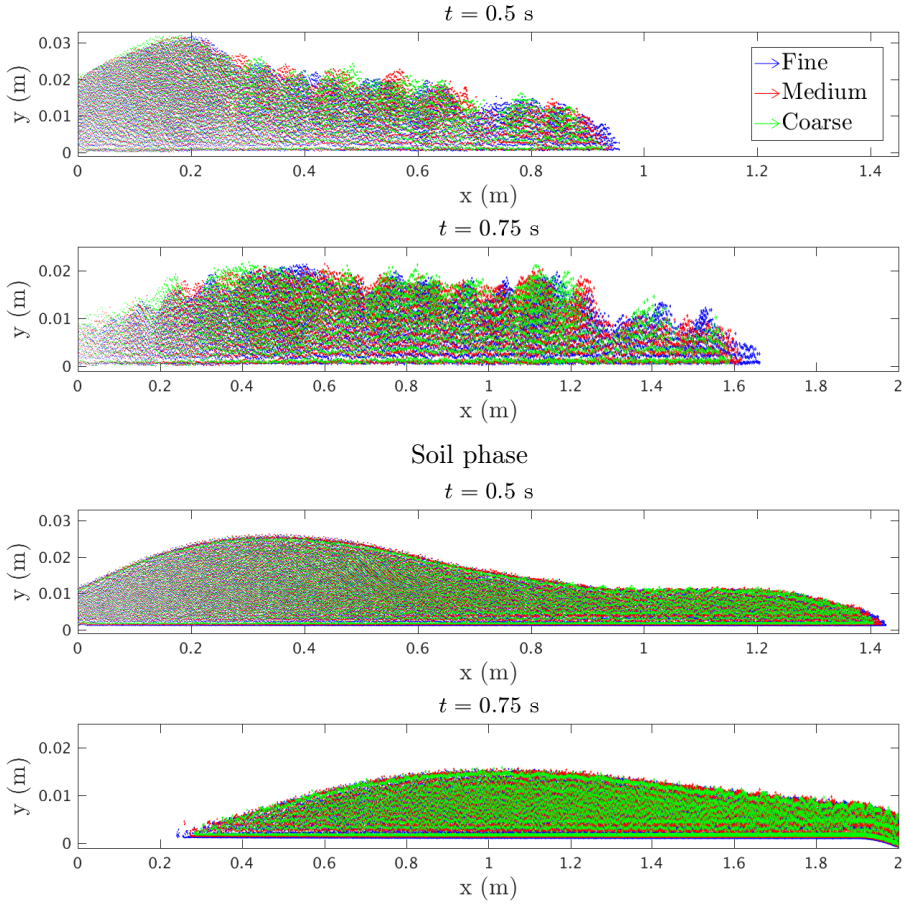

FIGURE 8.8: A comparison of the soil and water phases for the Standard SPH simulation of the experimental debris flow, for three different particle resolutions. The labels 'Fine', ' Medium' and 'Coarse' correspond to 15555, 9949 and 6873 soil particles respectively, with 23843, 15344 and 10402 water particles. The fine, medium and coarse results are represented by the blue, red and green vectors respectively. The volume fraction was not updated, and no interaction force was included.

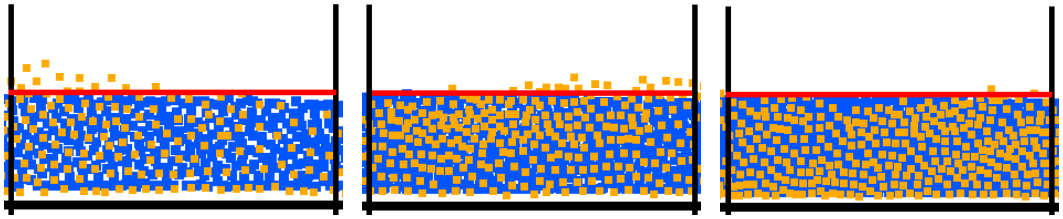

(A) $t = 0.3$ s

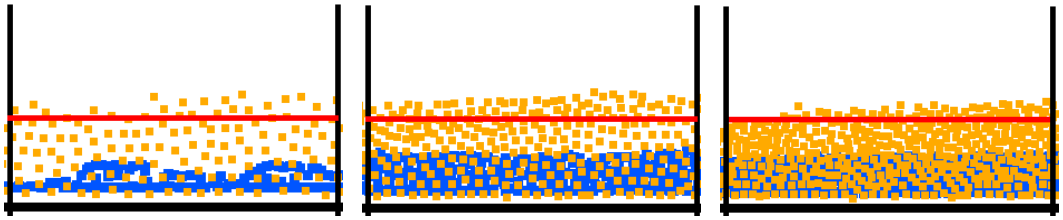

(B) $t = 0.6$ s

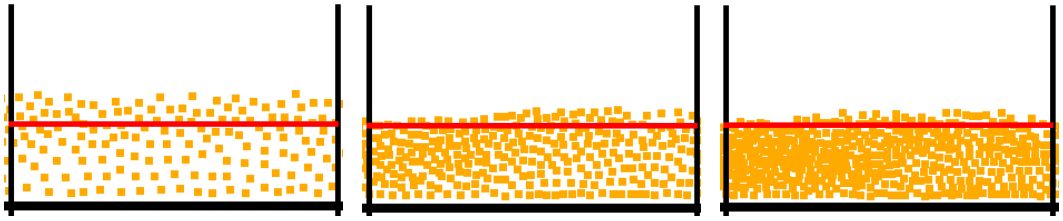

(C) $t = 0.8$ s

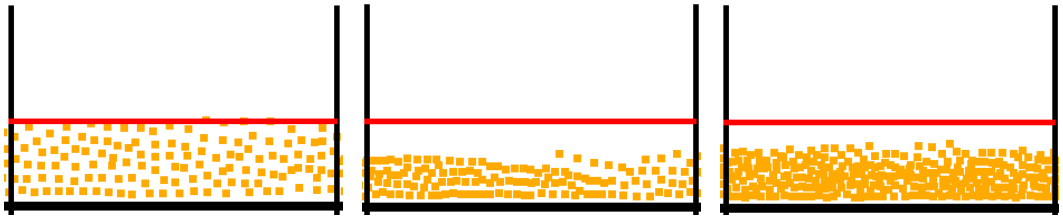

(D) $t = 1.2$ s

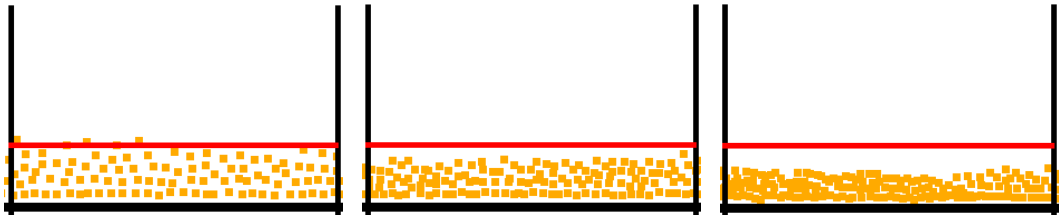

(E) $t = 1.6$ s

FIGURE 8.9: Soil (orange) and water (blue) node evolution for three different particle resolutions, within the area corresponding to the camera field of view in the experiments (0.05×0.03 m^2). In each subfigure, the particle resolution increases from left to right, where $n_s = 6873, 9949, 15555$ and $n_w = 10402, 15344, 23843$. For visualisation purposes, the water nodes are approximately 1.2 times larger than the soil nodes.

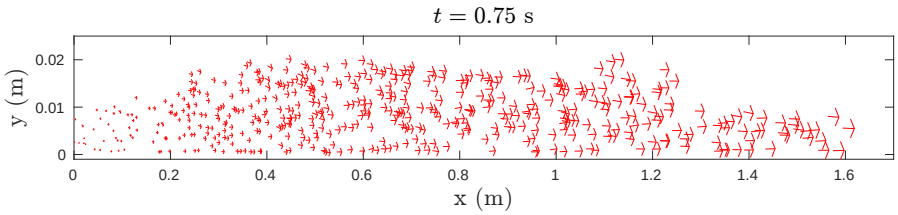

(A) Velocity vectors computed with Standard SPH (with no interaction force)

(B) A depiction of the node-stress-point configuration

FIGURE 8.10: SPH velocity vectors for the simulation of the experimental debris flow, with the chosen node-stress-point configuration for the Stress-Particle method.

for the comparison of the Stress-Particle method with Standard SPH. In Figure 8.11, the red, horizontal lines provide a point of reference for the height of the material free surface, and correspond to the height of the experimental flow. It can be seen that for both Standard SPH and Stress-Particle SPH, the water separates from the soil phase completely, due to there being no interaction force between the two phases. By $t = 0.8$ s the material consists of soil nodes only. Overall, the height of the experimental flow is reasonably predicted up to $t = 0.8$ s. The soil nodes from the Stress-Particle method show an uneven distribution at $t = 0.6$ s, with a bumpy free surface profile. In contrast, the corresponding free surface profile of Standard SPH is approximately straight along the extent of the displayed section. At $t = 1.2$ s, the Standard SPH results show a thinner flow than that of the experiment. Meanwhile, the Stress-Particle SPH results display the same, uneven, distribution as for $t = 0.6$ s, resulting in a slightly thicker flow than for the Standard SPH. The difference in behaviour between the Standard SPH and Stress-Particle SPH results potentially highlights a shortcoming of the latter approach. However, it should also be noted that the differences described above are relatively minimal – aside from the thicker flow in certain areas, the Standard SPH and Stress-Particle SPH results display the same overall behaviour. Moreover, there is no analytical solution to this problem and the 'correct' behaviour is not intuitive.

To provide a more realistic representation of the experimental debris flow, the volume fraction evolution and drag interaction have been included within the SPH models, as described in Sections 8.4.1 and 8.4.7 respectively. In the experimental mixture, the initial bulk value of the solid volume fraction is $\phi_s = 0.44$ (which was used to produce the results in Figure 8.11). When solving the volume fraction evolution equation, an initial value of ϕ_s is required. It is more realistic to provide an initial value that is representative of the volume fraction in the two distinct layers (see Figure 8.7), as opposed to a bulk value. The upper layer initially consists of water only and the solid volume fraction is therefore equal to zero. The initial volume fraction of water in the lower layer is $\phi_w == 0.32$, with a solid volume fraction of

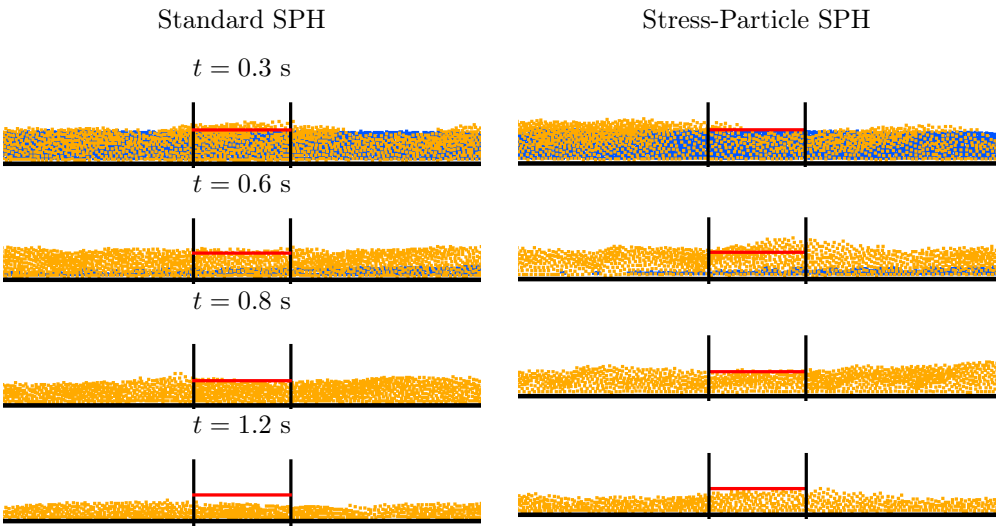

FIGURE 8.11: The evolution of the soil and water phases in the numerical simulation of the experimental debris flow, with no interaction force. The soil and water phases are represented by the orange and blue nodes respectively. The red, horizontal line represents the height of the experimental flow at the corresponding times.

$\phi_s = 1 - \phi_w = 0.68$ (see Section 7.2). When evolving the solid volume fraction (according to Equation (8.35)), an initial value of $\phi_s = 0.68$ is defined, and the fluid volume fraction is calculated as $\phi_w = 1 - \phi_s$.

Recall that the definition of the drag in the current work is

$$C_D = \frac{\phi_s \phi_w (\rho_s - \rho_f) g}{U_t F(Re_p)}, \tag{8.59}$$

where U_t is the terminal velocity of a representative particle falling in a fluid, and F is a particle Reynolds number dependent parameter. The terminal velocity is approximated according to an empirical relationship with the representative particle diameter d_p:

$$U_t = \sqrt{\frac{(\rho_s - \rho_f) g d_p}{\rho_f 0.91}}. \tag{8.60}$$

Equation (8.60) was determined according to 115 different measurements of the settling velocity of sand grains with a range of diameters (Hallermeier, 1981). For the representative particle diameter of $d_{50} = 0.917$ mm in the experiments, Equation (8.60) gives a terminal velocity of $U_t = 0.091$ m s^{-1}. Regarding the particle Reynolds number dependent parameter: $F(Re_p) = \frac{\rho_f}{\rho_s} \left(\frac{\phi_w}{\phi_s}\right)^3 \frac{Re_p}{180}$. The dimensionless particle Reynolds number characterises the flow of a particle as it falls through a fluid (Lloyd, 2003). Considering the fluid to be water, Re_p is defined as $Re_p = \frac{d_p U_t \rho_f}{\mu}$, where μ is the dynamic viscosity of water (kg m^{-1}s^{-1}). For values of $d_{50} = 0.917$ mm, $U_t = 0.091$ m s^{-1}, and $\mu = 0.001$ kg m^{-1}s^{-1}, the particle Reynolds number for the experimental flow is approximated as $Re_p = 83.2$ (to one decimal place). The terms U_t, Re_p and ρ_s are constants in Equation (8.59). The remaining terms are problem

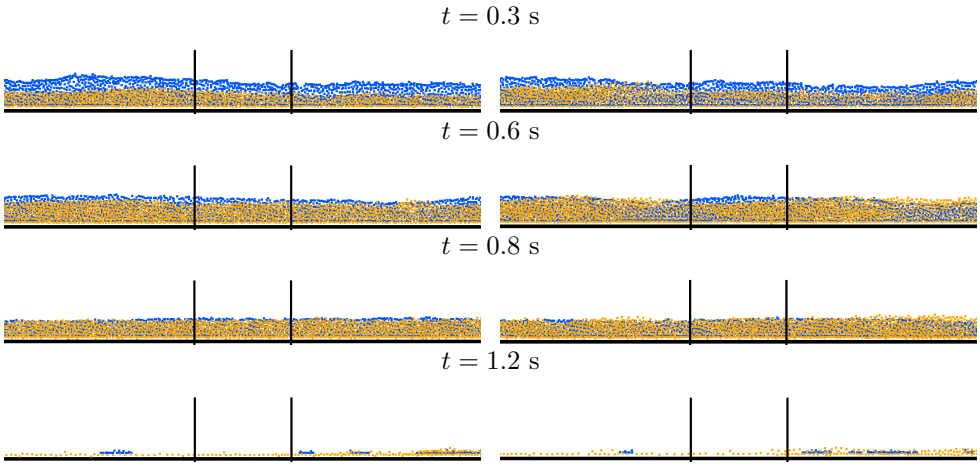

FIGURE 8.12: The evolution of the soil and water phases in the numerical simulation of the experimental debris flow, with the volume fraction update. The soil and water phases are represented by the orange and blue nodes respectively. The vertical lines encompass the area captured by the camera field of view.

variables, which are used to update the drag coefficient at each calculation step.

The development of the soil and water nodes with the evolving volume fraction and drag interaction is provided in Figure 8.12, for Standard SPH and Stress-Particle SPH. At $t = 0.3$ s, the results of both SPH models show two distinct layers of soil and water, which develop into an approximately uniform soil-water mixture. This behaviour is qualitatively similar to what was observed in the experiments. However, unlike the experiments, the majority of the material has propagated beyond the extent of the flume by $t = 1.2$ s. Overall, the results of Stress-Particle SPH are qualitatively similar to the Standard SPH results. The soil nodes in the Stress-Particle SPH results exhibit a slightly bumpy free surface profile at $t = 0.6$ s. As a result, the height of the soil phase is greater than that of the water phase in certain areas (e.g. at the far right of Figure 8.12 at $t = 0.6$ s).

The soil and water nodes within the region of the camera field of view are compared against the experimental snapshots in Figure 8.12. At $t = 0.3$ s, the experimental flow exhibits turbulent, collisional behaviour throughout its depth (see Section 7.3). The effects of turbulence have not been included in the current two-phase SPH model, and as such turbulent behaviour cannot be captured. However, the snapshots of the experimental flow show that there are two distinct layers visible at $t = 0.3$ s – a lower, high concentration layer and an upper, dilute layer. These layers are distinguished by the dashed line on the snapshots in Figure 8.12. The SPH results also exhibit the 'two layer' feature of the experiment, although the height of the free surface has been underestimated slightly. At $t = 0.6$ s, the experiment shows a thin, watery layer at the flow free surface. This feature is also present in the SPH results (for Standard and Stress-Particle SPH), and the height of the free surface approximately coincides with that of the experiment. The experimental flow has transitioned into a single layer at $t = 0.8$ s, consisting of a granular-water mixture.

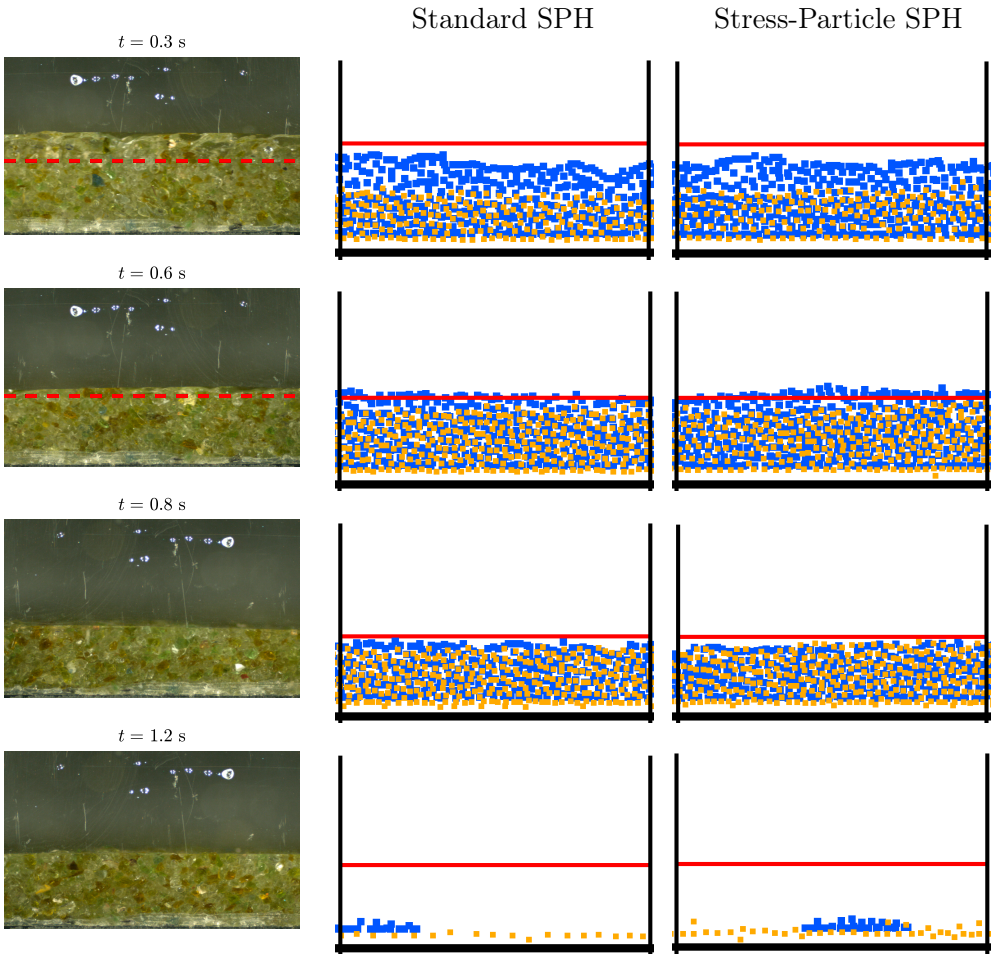

FIGURE 8.13: Snapshots of the experimental debris flow, with the SPH results. The orange nodes depict the soil phase while the blue nodes depict the water. The solid red line corresponds to the free surface of the experiment. The area of the camera field of view is 0.05×0.03 m^2. From top to bottom, the results are shown at $t = 0.3$ s, $t = 0.6$ s, $t = 0.8$ s and $t = 1.2$ s. For visualisation purposes, the water nodes are approximately 1.2 times larger than the soil nodes.

This behaviour is represented in the SPH model, where the soil and water nodes have approximately the same thickness, and the height of the experimental free surface is only slightly underpredicted. By $t = 1.2$ s, only a single layer of nodes is present in the SPH results, which does not coincide with the experimental behaviour. Figure 8.14 shows the SPH soil nodes along the length of the lower boundary, coloured by contours of horizontal velocity. The Standard SPH and Stress-Particle SPH results both exhibit horizontal velocities up to 3 m s^{-1}. This is significantly higher than the maximum observed velocity in the experiment (≈ 1.2 m s^{-1}). While the qualitative behaviour of the experimental flow has been captured with SPH, the velocities in the simulation are much higher than the experiment, and the simulated flow consequently evolves over a shorter time frame.

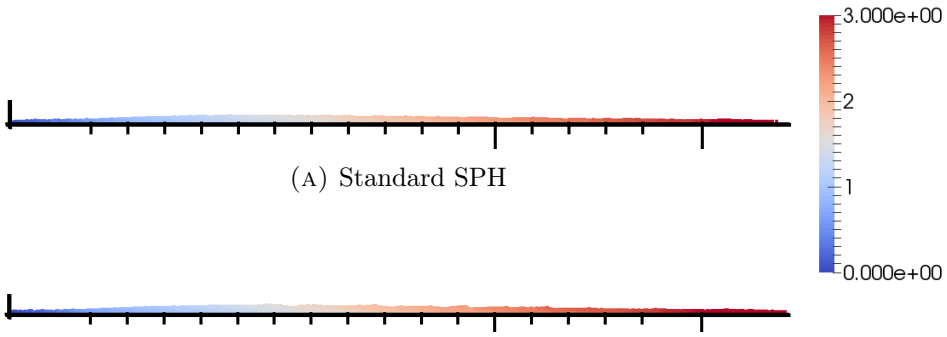

(A) Standard SPH

(B) Stress-Particle SPH

FIGURE 8.14: The positions of the soil nodes at the point of the material reaching the end of the flume ($t = 0.35$ s). The nodes are coloured by horizontal velocity u_x (m s^{-1}).

8.6 Conclusion

The purpose of implementing a two-phase soil-water model within SPH was to simulate the experimental debris flow described in the previous chapter. The behaviour of the flow up to $t = 0.8$ s has been qualitatively captured with the two-phase SPH model, for both Standard SPH and Stress-Particle SPH. The experimental flow initially exhibits two distinct layers consisting of a lower, soil-water mixture and an upper dilute layer (discussed in detail in Chapter 7). This progressively develops into a single layer consisting of a soil-water mixture. The qualitative transition has been simulated with the two-phase SPH model, as shown in Figure 8.13. These results were obtained when a drag interaction law was included in the model, and the solid volume fraction was updated according to Equation (8.34). The relative behaviour of the two phases, as well as the height of the free surface, compares well to the experimental results up to $t = 0.8$ s. However, the material velocity is significantly higher in the numerical results than in the experimental flow, and by $t = 1.2$ s the majority of the simulated material has propagated beyond the camera field of view. This is at a contrast with the experimental results, where the material is still in motion at $t = 1.2$ s (and closely resembles the flow at $t = 0.8$ s). The experimental flow does not stop moving until an approximate time of $t = 2.6$ s.

The inability of the SPH model to represent the full experimental flow, and the over-estimation of the flow velocities, could be attributed to a number of possible factors. The two-phase model lacks many physical features that are likely to affect the debris flow motion. For example, the SPH model does not include the effects of turbulence, which was exhibited in the initial stages of the debris flow (see Chapter 7). It is plausible that in the experiments, the turbulent energy resulted in a decrease of kinetic energy and a subsequent reduction of flow velocity. An additional constitutive term accounting for extra frictional resistance, such as that of Voellmy (1964), may improve the results of SPH. In fact, a constitutive model with a higher complexity than the elastoplastic Drucker-Prager model may be more appropriate for the description of the material in the experimental flow. Another feature that has

been neglected from the two-phase SPH model is the effect of viscosity. Viscosity is often neglected in debris flow models (Pitman and Le, 2005; Pelanti, Bouchut, and Mangeney, 2008; Pastor et al., 2015b; Bui and Nguyen, 2017), yet it was shown by Pudasaini (2012) that viscous forces can significantly impact model results. The experimental flow has a high content of fine particles that may contribute to the viscosity of the interstitial fluid, and the velocity profiles in the flow body are of a viscous-type (see Figure 7.17 in Chapter 7). Therefore, the neglect of viscous effects in the SPH model could be partly responsible for the excessive simulated velocities. Furthermore, pore water pressures are considered to be one of the key factors governing debris flow behaviour (Iverson, Reid, and LaHusen, 1997; Pastor et al., 2015b). Often, there is a feedback mechanism between excess pore water pressures, soil dilation and grain size segregation (Johnson et al., 2012; Kaitna, Dietrich, and Hsu, 2014). Such effects have been neglected in the current two-phase SPH model, and the pore water pressure is governed by an equation of state. However, the short duration of the experimental flow and the high material permeability indicates that excess pore water pressures do not have a significant effect on the flow behaviour. It is highly likely that the flow was influenced by three-dimensional effects. The two-dimensional approximation is a significant simplification, that neglects channel effects and all cross-stream flow mechanisms. All of the aforementioned factors highlight areas that require further attention in the current two-phase SPH model.

It is relevant to highlight that when no drag interaction force is included in the model (and the volume fractions are not updated), the Standard SPH results provide a reasonable approximation of the experimental flow in terms of the height of the free surface (see Figure 8.11). However, with no interaction force the water phase separates completely from the soil, and by $t = 0.8$ s, the SPH results consist of the soil phase only. The phase separation does not resemble the experimental behaviour. Nonetheless, these results show that while the presence of the interaction force is essential for the coupled behaviour of the soil and water phases, the tail of the experimental flow is better predicted as a dry, granular flow. The drag interaction force is included in the equation of momentum of both phases, where it is added to the right hand side of the soil momentum equation (see Equation (8.14)), and subtracted from the right hand side of the water momentum equation (see Equation (8.15)). The term therefore acts to increase the velocity of the soil, while decreasing the velocity of the water. In the application to the experimental debris flow, the soil velocity increase is much larger than expected. Recall that in the application to the experimental debris flow, assumptions were made regarding certain parameters in the full drag description of Pudasaini (2012), defined by Equation (8.24). Recall that the full drag definition:

$$C_D = \frac{\phi_s \phi_w (\rho_s - \rho_f) g}{(U_t (PF(Re_p) + (1-P)\phi_w^{M-2}))^l}. \tag{8.61}$$

For simplicity, in the current work, the parameter P was defined to be 1, corresponding to the flow of fluid through a dense grain packing (Pudasaini, 2012). For $P \neq 1$, calibration is also required for the parameter M in Equation (8.61), which can vary from $2.4 - 4.65$ (Pitman and Le, 2005). Furthermore, the parameter l can be defined as 1 or 2, corresponding to laminar and quadratic drag coefficients respectively. The value $l = 1$ was chosen in the present investigation. A thorough investigation of these parameters is required to assess the implication of these values. It is possible that an alternative, more sophisticated drag interaction law is required to describe the different stages of the experimental flow.

There is no evidence of numerical instability in the simulation of the experimental debris flow, suggesting that the Standard SPH method is a suitable model. The results of Standard SPH provide a point of comparison to the assess of the performance of the Stress-Particle SPH method. Overall, the results of Standard SPH and Stress-Particle SPH display the same behaviour. This shows that the Stress-Particle method (with the outside approach) is capable of modelling small-scale, rapid flows, to a certain extent. However, the results of Stress-Particle SPH display some areas where the soil nodes appear to have a slightly uneven distribution. This creates a bumpy free surface profile, which is evident at $t = 0.6$ s in Figures 8.11 and 8.12. Further investigation is required to assess this apparent instability in the Stress-Particle method. It is possible that the method is unsuitable for flows that exceed a certain velocity. For such problems, it may be inappropriate to use an interpolation technique to obtain the stress and velocity on the nodes and stress-points respectively. This could be tested by performing alternative methods to transfer the information between the nodes and stress-points. For example, assigning the velocity of the stress-points to be equal to that of their associated node, and the stress of the node to be the average of the corresponding stress-points. Moreover, an alternative possibility is that the Stress-Particle method is unsuitable for thin flows, where the surrounding neighbourhood of particles is relatively sparse. However, the expected behaviour of the soil phase in the experimental flow simulation is not intuitive. There is no analytical solution to compare the results to. Therefore, it is unclear at this stage whether or not the Stress-Particle SPH results are in fact incorrect, and to what degree.

It was shown in Chapter 6 that the performance of Stress-Particle SPH is optimum when the stress-point positions are assigned to align with the direction of the flow. In extreme cases, the simulations exhibited severe instabilities when the stress-points did not align with the flow direction (see Section 6.5). The experimental debris flow rapidly propagates downstream and the velocity vectors within the flow body are mostly parallel to the lower boundary in the SPH simulation (see Figure 8.10a). Therefore, to simplify the implementation of the Stress-Particle method, two stress-points were positioned horizontally on either side of each node, as shown in Figure 8.10b. To test this assumption, the simulation of the experimental flow (with no interaction force or volume fraction evolution) was conducted with the

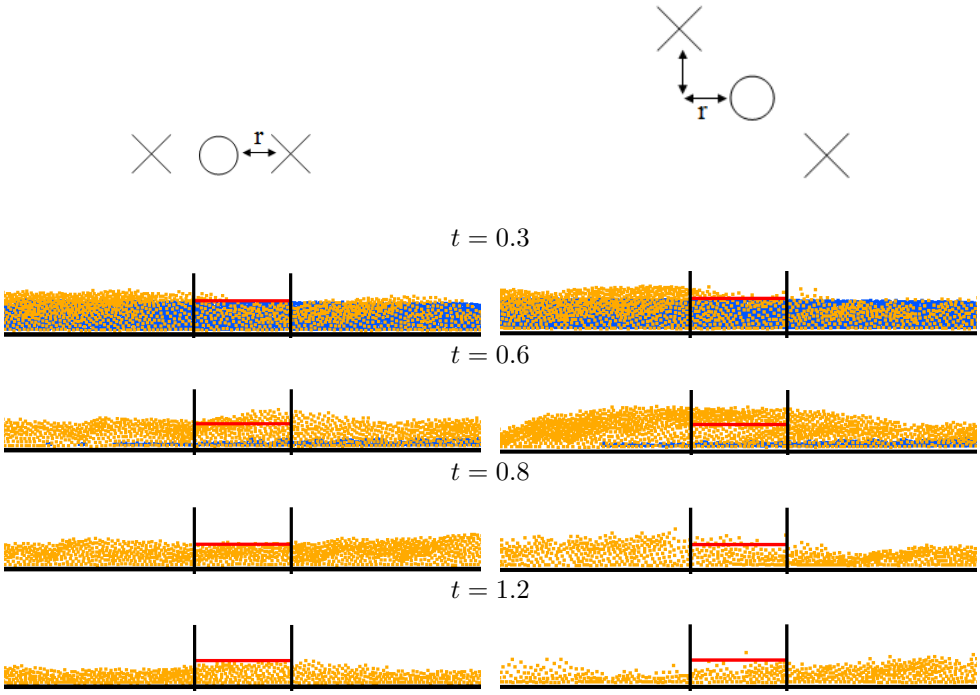

FIGURE 8.15: The effect of stress-point placement on the Stress-Particle SPH simulation of the two-phase experimental debris flow. The results on the left correspond to the horizontal stress-point placement as shown, where $r = \frac{\Delta x}{3}$. The results on the right were simulated with a diagonal stress-point placement, also for $r = \frac{\Delta x}{3}$.

stress-point positions not aligned with the flow direction. The results are shown in Figure 8.15, where they are compared with the results obtained with the horizontal node-stress-point arrangement. The corresponding node-stress-point configurations are depicted. It can be seen that the soil node behaviour is significantly less stable for the simulation with the stress-points unaligned with the flow direction. This provides further verification that the stress-point positions are an important factor, and that the best results are obtained when they align with the flow. For the application to the experimental flow, the results of Stress-Particle SPH may be improved if the stress-point orientation is updated according to the velocity vector at each node, as described in Section 6.4.2.

Chapter 9

Conclusions

The primary aim of this research was to develop a numerical model that can simulate landslide behaviour with accuracy – including both initiation (failure), and propagation (post-failure). In fulfilment of the aim of this research, a novel numerical model has been developed within the framework of SPH. The numerical model – Stress-Particle SPH – is capable of simulating the failure and post-failure of soil while eliminating numerical instabilities that are often detrimental to the performance of SPH. What's more, this model removes instabilities in a way that does not require artificial parameter tuning.

Two variations of Stress-Particle SPH have been developed and implemented in this research – the *inside approach* and the *outside approach*. The former variation consists of a specified number of stress-points positioned inside virtual quadrilaterals, which are formed by four neighbouring nodes. In this approach, the positions of the stress-points are updated according to an interpolated velocity, which is transferred from the neighbouring nodes via the SPH approximation. In Chapter 5, the inside approach was applied to a range of soil dynamics problems that are relevant to the formation of slope failure surfaces. These problems consisted of a simplified elastic and viscoplastic slope, strain localisation in a soil sample, and the formation of a slip surface in a cohesive soil. In all cases, the Stress-Particle SPH method provided smooth profiles of stress, and generally produced more accurate results than for Standard SPH. In the case of the strain localisation problem, well-defined shear bands were simulated with Stress-Particle SPH, while Standard SPH was unable to simulate the problem on account of numerical instabilities (see Section 5.4). Different node-stress-point configurations were explored and applied to all problems in Chapter 5. This is the first time that stress-point quantity and arrangement has been examined in the numerical simulation of a nonlinear system. It was shown that, in general, there is a correlation between stress-point quantity and result accuracy. It was also deduced that the simulation results are dependent on the stress-point orientation. This was particularly evident in the strain localisation problem, where the shear band inclination approximately aligned with the orientation of the stress-points. In the simulation of the cohesive soil, Stress-Particle SPH was able to completely eliminate the non-physical fracturing that occurred for Standard SPH (as a result of the tensile instability), for a sufficient quantity of stress-points (see Section 5.5.1). In Chapter

5, the inside approach was also applied to model the collapse of a purely frictional, non-cohesive soil. This problem exhibited high displacements and rapid velocities – representative of the post-failure behaviour of landslides. The inside approach was unable to capture the dynamics of this problem, due to the way in which the stress-point positions were updated (see Section 5.5.2).

As opposed to arranging the nodes and stress-points within virtual quadrilaterals, the outside approach consists of a specified number of stress-points positioned around individual nodes. Therefore, every node is associated with one or more stress-point, and every stress-point is associated with a single node. By arranging the nodes and stress-points in this way, the stress-points can be assigned to follow their associated node for the duration of the simulation, thereby solving the problems regarding the stress-point position update. In Chapter 6, the outside approach was applied to problems involving the post-failure behaviour of soil, including the collapse of the non-cohesive soil. Unlike the inside approach, the new method was able to model the large material displacements well, with two or more stress-points per node (see Section 6.2). The outside approach was also used to simulate the cohesive soil, to ensure that the new approach was still able to prevent the formation of non-physical fractures (see Section 6.3). Here, it was found that the performance of the outside approach is strongly dependent of the positions of the stress-points with respect to their associated node. For certain node-stress-point configurations, the method was not capable of completely eliminating the non-physical fractures. What's more, the overall material behaviour and deformation was also affected by the node-stress-point configuration. It was deduced that although stress-points are interpolation points (as opposed to material points), they should not be positioned in areas where there would not usually be a material point to influence the nodes. A new technique was developed to account for this feature: the stress-points are assigned to follow each node (allowing the simulation of large displacements), yet their orientations are regularly adapted so that they align with the general flow field (to ensure accurate numerical calculations). With this updated technique, the fractures in the cohesive soil problem were completely eliminated, and the large displacements of the non-cohesive soil were also captured. The technique was also applied to the collapse of a viscoplastic material, that exhibited both large displacements and severe effects of the tensile instability for Standard SPH. The outside approach was able to eliminate the instabilities and capture the rapid flow dynamics.

Following the development and validation of Stress-Particle SPH, in Chapter 7 the results of a small scale debris flow were presented. One of the reasons for conducting these experiments was to provide a physical problem for further validation of the Stress-Particle SPH method. However, the experiments also provided insight into the internal dynamics of a small scale debris flow – a particularly destructive type of landslide (Iverson, Reid, and LaHusen, 1997). The experiment consisted of the sudden release of a granular-water mixture along an inclined flume. The flow dynamics were captured with a high speed camera, and a PIV technique was used to

obtain internal profiles of velocity and shear stress. The head-body architecture of the flow was examined and quantified in more detail than in previous investigations. Velocity flow fields were produced for the first time, for both the head and the body. The internal observations showed a spatial and temporal evolution from a transient, collisional, turbulent flow (at the head) to a steady, non-fluctuating flow (in the body). In the transition between these two flow regimes, the experiment consisted of a two layer region – a lower non-fluctuating layer and an upper turbulent layer (see Section 7.3). Furthermore, the velocity profiles in the steady flow body exhibited a viscous-type profile (see Section 7.4). Similar experiments were presented in the literature, for different values of the material coefficient of uniformity C_U (Sanvitale and Bowman, 2017). There, viscous-type profiles were obtained for a wide grain size distribution ($C_U = 20$), and granular-type profiles were obtained for a narrow distribution ($C_U = 3$). In the current work, $C_U = 5$. Therefore, comparing the experimental results of Chapter 7 with those from the literature, it is suggested that granular and viscous-type flow is distinguished by a limiting value of C_U, between 3 and 5.

In an attempt to simulate the results of the experimental debris flow, a two-phase soil-water model, derived under the framework of Biot (1956) and Zienkiewicz, Chang, and Bettess (1980), was implemented within Standard SPH and Stress-Particle SPH in Chapter 8. This is the first time that a two-phase, non-depth-integrated SPH model has been applied to a debris flow problem. Due to its complexity, the comparison of the experiment with the SPH model was restricted to the first 1.2 seconds of flow, and the relative positions of the soil and water phases in the camera field of view were compared with snapshots from the experiment. The SPH models were able to capture the qualitative features of the experimental flow up to $t = 0.8$ s, in terms of the relative soil and water behaviour (see Section 8.5). However, the velocities were significantly overpredicted with the SPH model, and further work is required to develop the two-phase model and investigate its capabilities. No numerical instabilities were observed in the SPH simulations, and Standard SPH provided a suitable point of comparison for the Stress-Particle SPH method. There was a large degree of similarity between the results of the two SPH models. Overall, the behaviour of the soil and water phases coincided for the two methods. However, the Stress-Particle SPH results exhibited some areas with an apparent uneven soil node distribution. It is not clear at this stage whether or not these features are unrealistic.

In summary, the most significant findings of this investigation are:

- Stress-Particle SPH is capable of eliminating or significantly reducing the effects of the two most serious instabilities in SPH – zero energy modes and the tensile instability – in problems regarding the failure and post-failure behaviour of soil.
- Stress-Particle SPH can also be applied to problems with high velocities and large displacements when the stress-points are defined to follow specified nodes,

where optimum results are obtained when the stress-point positions are aligned in the direction of the material velocity.

- A dilute two-phase experimental debris flow exhibits a spatial and temporal evolution from collisional to non-fluctuating behaviour, with a two-layer transition between the two regimes.

9.0.1 Suggestions for future work

The results presented in this investigation have shown that the Stress-Particle SPH method has stabilising effects, which are vital for the accurate simulation of problems related to landslide behaviour. It would be beneficial to quantify the stabilising effects through a linear stability analysis of the system. Although such analyses have been conducted previously for SPH with stress-points (Belytschko et al., 2000; Xiao and Belytschko, 2005), they were restricted to rate-independent, elastic materials, with simple node-stress-point configurations. The results of these analyses suggested that stress-points within SPH were capable of increasing the threshold at which the tensile instability occurred, but not eliminating it completely. In the current research, the Stress-Particle SPH method was able to completely eliminate the effects of the tensile instability in a cohesive soil (see Chapters 5.5.1 and 6.4.2) and a viscoplastic material (see Chapter 6.5). Therefore, future work may involve conducting a stability analysis of Stress-Particle SPH when applied to soil, with the configurations that were considered in this research. This would provide further insight into the underlying stabilising mechanism of the method.

Regarding the current application of interest, Stress-Particle SPH is capable of simulating problems that are representative of both landslide initiation and propagation. These stages have been considered separately for the purpose of implementing and validating the Stress-Particle method. A natural extension of this work is to combine both initiation and propagation as a single problem, and model a landslide event as a continuous process with Stress-Particle SPH. This task is a major challenge, which would also require the implementation of a rheological model that is more advanced than what is currently available. Furthermore, it was shown by An et al. (2016) that three-dimensional effects play a vital role in landslide simulations, exhibiting features that cannot be captured with a two-dimensional model. For applicability to real events, the Stress-Particle method should be extended to three dimensions.

With regards to the numerical method, there are several areas that could be developed and improved in future work. Potentially the most significant drawback of the Stress-Particle method is the associated computational expense. As discussed in Chapter 5.6, simulations with the inside approach – with one stress-point per virtual quadrilateral – take approximately twice as long as for Standard SPH with the artificial stress method. The computational expense increases with a higher node-stress-point ratio. Improvements to the efficiency of Stress-Particle SPH may

include implementing the method in parallel computing, or utilising graphics processing units. Furthermore, an issue that was encountered in many problems within the current research was the implementation of the boundary conditions within Stress-Particle SPH (see Chapters 5 and 6). This has been a long-standing issue in conventional SPH, and the subject of numerous investigations within the literature (Takeda, Miyama, and Sekiya, 1994; Morris, Fox, and Zhu, 1997; Wang, Ge, and Li, 2006; Crespo, Gómez-Gesteira, and Dalrymple, 2007). Further attention is required regarding the adaptation of existing boundary techniques for use in the Stress-Particle method. It is likely that the approach undertaken in this research – using dummy nodes to simulate wall boundaries – would be better suited for the Stress-Particle method if dummy stress-points were also considered.

Regarding the experimental debris flow, there are numerous factors that are of interest for future investigations. Factors such as grain size distribution, solid volume fraction, bed roughness and particle fine content are known to have a high influence on debris flow dynamics (Iverson, Reid, and LaHusen, 1997). There are limited studies in the literature that investigate these features, with regards to the internal dynamics of small scale flows. Several of these variables have been explored in detail in the work of Paleo Cageao (2014), yet for idealised spherical particles. There is a significant difference in the dynamics of granular flows of idealised spheres, against flows of realistic, angular particles. The experimental results in Chapter 7 suggest the existence of a cut-off between viscous and granular-type flow, defined in terms of the coefficient of uniformity C_U. This hypothesis could be tested in future work, by repeating the experiments detailed in Chapter 7 for granular material with different values of C_U. Furthermore, the internal observations of the experimental flow in the current work were recorded through the clear, perspex wall. It is likely that the flow is affected by the presence of the wall, and more accurate observations would be obtained in the flow centreline. This could be achieved with an advanced planar laser-induced fluorescence technique, which was used in the experiments of Sanvitale and Bowman (2017).

The inability of two-phase SPH to recreate the experimental flow for its entire duration highlights the need for the future development of the two-phase model. Several assumptions were made regarding the derivation of the two-phase system. Of these assumptions, those that are of most significance include the role of viscous effects, the phase interaction force and the assumption of a two-dimensional flow. It is suggested that future work includes viscous forces in the two-phase SPH model, and investigates alternative descriptions of the soil-water interaction force. Furthermore, three-dimensional effects are likely to be significant. The latter factor could also be investigated experimentally, by recording the velocities of the flow surface from above. In the experimental simulations, some differences were observed in the results of Standard SPH and Stress-Particle SPH. As the expected behaviour of the SPH soil nodes is not exactly clear for this problem (i.e. there is no known solution), further simulations of two-phase, high velocity problems should be performed to fully assess

the capabilities of Stress-Particle SPH with the outside approach.

9.1 Concluding remarks

This research has been devoted to the development and implementation of a numerical model that is capable of simulating landslide behaviour at both initiation and propagation. This has been achieved, in the form of Stress-Particle SPH. The model has been validated with numerous problems relating to the failure and post-failure stages of landslides, and consistently performed better than Standard SPH in terms of accuracy and stability. Not only is the model applicable for general landslide behaviour, it also offers the possibilities of simulating a broader range of problems with SPH than is currently possible.

References

Abe, K., Soga, K., and Bandara, S. (2013). "Material point method for coupled hydromechanical problems". In: *Journal of Geotechnical and Geoenvironmental Engineering* 140.3, p. 04013033.

Adamo, F., Andria, G., Attivissimo, F., and Giaquinto, N. (2004). "An acoustic method for soil moisture measurement". In: *IEEE Transactions on Instrumentation and Measurement* 53.4, pp. 891–898.

Adrian, R. J. and Westerweel, J. (2011). *Particle image velocimetry*. 30. Cambridge University Press.

An, Y., Wu, Q., Shi, C., and Liu, Q. (2016). "Three-dimensional smoothed-particle hydrodynamics simulation of deformation characteristics in slope failure". In: *Geotechnique* 66.8, pp. 670–680.

Anand, L., Aslan, O., and Chester, S. A. (2012). "A large-deformation gradient theory for elastic–plastic materials: strain softening and regularization of shear bands". In: *International Journal of Plasticity* 30, pp. 116–143.

Ancey, C. (2007). "Plasticity and geophysical flows: a review". In: *Journal of Non-Newtonian Fluid Mechanics* 142.1-3, pp. 4–35.

Anderson, J. D. (1982). *Modern Compressible Flow With Historical Perspective*. McGraw-Hill New York.

Anderson, T. and Jackson, R. (1967). "A fluid mechanical description of fluidized beds: equations of motion". In: *Industrial and Engineering Chemistry Fundamentals* 6, pp. 527–539.

Antuono, M., Bouscasse, B., Colagrossi, A., and Marrone, S. (2014). "A measure of spatial disorder in particle methods". In: *Computer Physics Communications* 185.10, pp. 2609–2621.

Armanini, A., Capart, H., Fraccarollo, L., and Larcher, M. (2005). "Rheological stratification in experimental free-surface flows of granular–liquid mixtures". In: *Journal of Fluid Mechanics* 532, pp. 269–319.

Bagnold, R. (1954). "Experiments on the Gravity-Free Dispersion of Large Solid Spheres in a Newtonian Fluid under Shear (1954)". In: *The Physics of Sediment Transport by Wind and Water*. ASCE, pp. 114–129.

Bandara, S. and Soga, K. (2015). "Coupling of soil deformation and pore fluid flow using material point method". In: *Computers and Geotechnics* 63, pp. 199–214.

Bardet, J.-P. and Proubet, J (1991). "A numerical investigation of the structure of persistent shear bands in granular media". In: *Geotechnique* 41.4, pp. 599–613.

Barla, G. and Paronuzzi, P. (2013). "The 1963 Vajont Landslide: 50th Anniversary". In: *Rock Mechanics and Rock Engineering* 46.6, pp. 1267–1270.

Batchelor, C. K. and Batchelor, G. (1967). *An introduction to fluid dynamics*. Cambridge university press.

Bedford, A. and Drumheller, D. S. (1983). "Theories of immiscible and structured mixtures". In: *International Journal of Engineering Science* 21.8, pp. 863–960.

Belytschko, T. and Bachrach, W. E. (1986). "Efficient implementation of quadrilaterals with high coarse-mesh accuracy". In: *Computer Methods in Applied Mechanics and Engineering* 54.3, pp. 279–301.

Belytschko, T., Lu, Y. Y., and Gu, L. (1994). "Element-free Galerkin methods". In: *International Journal for Numerical Methods in Engineering* 37.2, pp. 229–256.

Belytschko, T., Ong, J. S.-J., Liu, W. K., and Kennedy, J. M. (1984). "Hourglass control in linear and nonlinear problems". In: *Computer Methods in Applied Mechanics and Engineering* 43.3, pp. 251–276.

Belytschko, T., Guo, Y., Liu, W. K., and Xiao, S. P. (2000). "A unified stability analysis of meshless particle methods". In: *International Journal for Numerical Methods in Engineering* 48.9, pp. 1359–1400.

Belytschko, T., Liu, W. K., Moran, B., and Elkhodary, K. (2013). *Nonlinear finite elements for continua and structures*. John Wiley & Sons.

Bingham, E. C. (1922). *Fluidity and plasticity*. Vol. 2. McGraw-Hill.

Biot, M. A. (1941). "General theory of three-dimensional consolidation". In: *Journal of Applied Physics* 12.2, pp. 155–164.

— (1956). "Theory of propagation of elastic waves in a fluid-saturated porous solid. II. Higher frequency range". In: *The Journal of the Acoustical Society of America* 28.2, pp. 179–191.

Bird, R. B., Dai, G. C., and Yarusso, B. J. (1983). "The rheology and flow of viscoplastic materials". In: *Reviews in Chemical Engineering* 1.1, pp. 1–70.

Bishop, A. W. (1955). "The use of the slip circle in the stability analysis of slopes". In: *Geotechnique* 5.1, pp. 7–17.

Bitelli, G., Dubbini, M., and Zanutta, A. (2004). "Terrestrial laser scanning and digital photogrammetry techniques to monitor landslide bodies". In: *International Archives of Photogrammetry, Remote Sensing and Spatial Information Sciences* 35.Part B5, pp. 246–251.

Blanc, T. and Pastor, M. (2013). "A stabilized smoothed particle hydrodynamics, Taylor–Galerkin algorithm for soil dynamics problems". In: *International Journal for Numerical and Analytical Methods in Geomechanics* 37.1, pp. 1–30.

Blanc, T. (2011). "The Runge-Kutta Taylor-SPH model, a new improved model for soil dynamics problems". PhD thesis. Universidad Politécnica de Madrid.

Blanc, T. and Pastor, M. (2012). "A stabilized Runge–Kutta, Taylor smoothed particle hydrodynamics algorithm for large deformation problems in dynamics". In: *International Journal for Numerical Methods in Engineering* 91.13, pp. 1427–1458.

Box, G. E., Jenkins, G. M., Reinsel, G. C., and Ljung, G. M. (2015). *Time series analysis: forecasting and control*. John Wiley & Sons.

Brockwell, P. J., Davis, R. A., and Calder, M. V. (2002). *Introduction to time series and forecasting*. Vol. 2. Springer.

Bui, H. H. and Fukagawa, R. (2013). "An improved SPH method for saturated soils and its application to investigate the mechanisms of embankment failure: Case of hydrostatic pore-water pressure". In: *International Journal for Numerical and Analytical methods in Geomechanics* 37.1, pp. 31–50.

Bui, H. H. and Nguyen, G. D. (2017). "A coupled fluid-solid SPH approach to modelling flow through deformable porous media". In: *International Journal of Solids and Structures*.

Bui, H. H., Sako, K., and Fukagawa, R. (2007). "Numerical simulation of soil–water interaction using smoothed particle hydrodynamics (SPH) method". In: *Journal of Terramechanics* 44.5, pp. 339–346.

Bui, H. H., Fukagawa, R., Sako, K., and Ohno, S. (2008). "Lagrangian meshfree particles method (SPH) for large deformation and failure flows of geomaterial using elastic–plastic soil constitutive model". In: *International Journal for Numerical and Analytical Methods in Geomechanics* 32.12, pp. 1537–1570.

Bui, H. H., Fukagawa, R., Sako, K., and Wells, J. C. (2011). "Slope stability analysis and discontinuous slope failure simulation by elasto-plastic smoothed particle hydrodynamics (SPH)". In: *Geotechnique* 61.7, pp. 565–574.

Bui, H. H., Kodikara, J. K., Bouazza, A., Haque, A., and Ranjith, P. G. (2014). "A novel computational approach for large deformation and post-failure analyses of segmental retaining wall systems". In: *International Journal for Numerical and Analytical Methods in Geomechanics* 38.13, pp. 1321–1340.

Calvo, L., Haddad, B., Pastor, M., and Palacios, D. (2015). "Runout and deposit morphology of Bingham fluid as a function of initial volume: implication for debris flow modelling". In: *Natural Hazards* 75.1, pp. 489–513.

Caretto, L., Curr, R., and Spalding, D. (1972). "Two numerical methods for three-dimensional boundary layers". In: *Computer Methods in Applied Mechanics and Engineering* 1.1, pp. 39–57.

Carrara, A. and Merenda, L. (1976). "Landslide inventory in northern Calabria, southern Italy". In: *Geological Society of America Bulletin* 87.8, pp. 1153–1162.

Cascini, L. (2004). "The flowslides of May 1998 in the Campania region, Italy: the scientific emergency management". In: *Italian Geotechnical Journal* 2, pp. 11–44.

Cascini, L., Cuomo, S., Pastor, M., and Sorbino, G. (2009). "Modeling of rainfall-induced shallow landslides of the flow-type". In: *Journal of Geotechnical and Geoenvironmental Engineering* 136.1, pp. 85–98.

Cascini, L., Cuomo, S., Pastor, M., Sorbino, G., and Piciullo, L. (2014). "SPH run-out modelling of channelised landslides of the flow type". In: *Geomorphology* 214, pp. 502–513.

Chau, K. and Chan, J. (2005). "Regional bias of landslide data in generating susceptibility maps using logistic regression: case of Hong Kong Island". In: *Landslides* 2.4, pp. 280–290.

Chen, J. and Beraun, J. (2000). "A generalized smoothed particle hydrodynamics method for nonlinear dynamic problems". In: *Computer Methods in Applied Mechanics and Engineering* 190.1-2, pp. 225–239.

Chen, J., Beraun, J., and Carney, T. (1999). "A corrective smoothed particle method for boundary value problems in heat conduction". In: *International Journal for Numerical Methods in Engineering* 46.2, pp. 231–252.

Chen, W.-F. (2013). *Limit analysis and soil plasticity*. Elsevier.

Chen, W. F., Mizuno, E, et al. (1990). *Nonlinear analysis in soil mechanics. Theory and implementation*. Elsevier.

Chung, C.-J. and Fabbri, A. G. (2008). "Predicting landslides for risk analysis—spatial models tested by a cross-validation technique". In: *Geomorphology* 94.3-4, pp. 438–452.

Conte, E., Donato, A., and Troncone, A. (2014). "A finite element approach for the analysis of active slow-moving landslides". In: *Landslides* 11.4, pp. 723–731.

Cook, R., Malkus, D., Plesha, M., and Witt, R. (2001). *Concepts and applications of finite element analysis*. John Wiley and Sons.

Costa, J. E. (1984). "Physical geomorphology of debris flows". In: *Developments and Applications of Geomorphology*. Springer, pp. 268–317.

Coulomb, C.-A. (1773). "Sur une application des règles de maxima & minima à quelques problèmes de statique relatifs à l'architecture". In: *Mémoires de Mathématique et de Physique*. Académie Royale de Sciences, Imprimerie Royale, Paris, pp. 343–382.

Courant, R., Friedrichs, K., and Lewy, H. (1967). "On the partial difference equations of mathematical physics". In: *IBM Journal of Research and Development* 11.2, pp. 215–234.

Coussot, P. (2017). *Mudflow rheology and dynamics*. Routledge.

Crespo, A. J., Gómez-Gesteira, M., and Dalrymple, R. A. (2008). "Modeling dam break behavior over a wet bed by a SPH technique". In: *Journal of Waterway, Port, Coastal, and Ocean Engineering* 134.6, pp. 313–320.

Crespo, A. J., Gómez-Gesteira, M., Dalrymple, R. A., et al. (2007). "Boundary conditions generated by dynamic particles in SPH methods". In: *CMC Tech Science Press* 5.3, p. 173.

Crosta, G. B., Imposimato, S., and Roddeman, D. (2015). "Granular flows on erodible and non erodible inclines". In: *Granular Matter* 17.5, pp. 667–685.

Crosta, G. B., Imposimato, S., Roddeman, D., Chiesa, S., and Moia, F. (2005). "Small fast-moving flow-like landslides in volcanic deposits: the 2001 Las Colinas Landslide (El Salvador)". In: *Engineering Geology* 79.3-4, pp. 185–214.

Cruden, D. and Varnes, D. (1996). "Landslides: Investigation and Mitigation, Chapter 3: Landslides Types and Processes". In: *Transportation Research Board Special Report* 247, pp. 36–75.

Dai, F. C., Lee, C. F., Li, J. X.Z. W., and Xu, Z. W. (2001). "Assessment of landslide susceptibility on the natural terrain of Lantau Island, Hong Kong". In: *Environmental Geology* 40.3, pp. 381–391.

Dai, Z., Huang, Y., Cheng, H., and Xu, Q. (2014). "3D numerical modeling using smoothed particle hydrodynamics of flow-like landslide propagation triggered by the 2008 Wenchuan earthquake". In: *Engineering Geology* 180, pp. 21–33.

— (2017). "SPH model for fluid–structure interaction and its application to debris flow impact estimation". In: *Landslides* 14.3, pp. 917–928.

Dalrymple, R. A. and Rogers, B. D. (2006). "Numerical modeling of water waves with the SPH method". In: *Coastal Engineering* 53.2-3, pp. 141–147.

Dalrymple, R. A. and Knio, O. (2001). "SPH modelling of water waves". In: *4th Conference on Coastal Dynamics*. American Society of Civil Engineers (ASCE), pp. 779–787.

Dilts, G. A. (1999). "Moving-least-squares-particle hydrodynamics—I. Consistency and stability". In: *International Journal for Numerical Methods in Engineering* 44.8, pp. 1115–1155.

Dolag, K. and Stasyszyn, F. (2009). "An MHD GADGET for cosmological simulations". In: *Monthly Notices of the Royal Astronomical Society* 398.4, pp. 1678–1697.

Domínguez, J. M., Crespo, A. J., and Gómez-Gesteira, M. (2011). "Optimization strategies for parallel CPU and GPU implementations of a meshfree particle method". In: *arXiv preprint arXiv:1110.3711*.

Drake, T. G. (1990). "Structural features in granular flows". In: *Journal of Geophysical Research: Solid Earth* 95.B6, pp. 8681–8696.

Drucker, D. C. and Prager, W. (1952). "Soil mechanics and plastic analysis or limit design". In: *Quarterly of Applied Mathematics* 10.2, pp. 157–165.

Duncan, J. M., Wright, S. G., and Brandon, T. L. (2014). *Soil strength and slope stability*. John Wiley & Sons.

Dutto, P., Stickle, M. M., Pastor, M., Manzanal, D., Yague, A., Moussavi Tayyebi, S., Lin, C., and Elizalde, M. (2017). "Modelling of fluidised geomaterials: the case of the Aberfan and the gypsum tailings impoundment flowslides". In: *Materials* 10.5, p. 562.

Dyka, C., Randles, P., and Ingel, R. (1995). "An approach for tension instability in smoothed particle hydrodynamics (SPH)". In: *Computers & Structures* 57.4, pp. 573–580.

— (1997). "Stress points for tension instability in SPH". In: *International Journal for Numerical Methods in Engineering* 40.13, pp. 2325–2341.

Dynamics, D. (2018). *DynamicStudio user manual*. Dantec Dynamics.

Fang, J., Owens, R. G., Tacher, L., and Parriaux, A. (2006). "A numerical study of the SPH method for simulating transient viscoelastic free surface flows". In: *Journal of Non-Newtonian Fluid Mechanics* 139.1-2, pp. 68–84.

Fannin, R. and Wise, M. (2001). "An empirical-statistical model for debris flow travel distance". In: *Canadian Geotechnical Journal* 38.5, pp. 982–994.

Fernández-Merodo, J. A., Pastor, M., Mira, P., Tonni, L., Herreros, M. I., Gonzalez, E., and Tamagnini, R. (2004). "Modelling of diffuse failure mechanisms of catastrophic landslides". In: *Computer Methods in Applied Mechanics and Engineering* 193.27, pp. 2911–2939.

Fernández-Merodo, J. A., García-Davalillo, J. C., Herrera, G., Mira, P., and Pastor, M. (2014). "2D viscoplastic finite element modelling of slow landslides: the Portalet case study (Spain)". In: *Landslides* 11.1, pp. 29–42.

Flammer, I., Blum, A., Leiser, A., and Germann, P. (2001). "Acoustic assessment of flow patterns in unsaturated soil". In: *Journal of Applied Geophysics* 46.2, pp. 115–128.

Flanagan, D. P. and Belytschko, T. (1981). "A uniform strain hexahedron and quadrilateral with orthogonal hourglass control". In: *International Journal for Numerical Methods in Engineering* 17.5, pp. 679–706.

Fraccarollo, L. and Papa, M. (2000). "Numerical simulation of real debris-flow events". In: *Physics and Chemistry of the Earth, Part B: Hydrology, Oceans and Atmosphere* 25.9, pp. 757–763.

Genevois, R., Ghirotti, M., et al. (2005). "The 1963 vaiont landslide". In: *Giornale di Geologia Applicata* 1.1, pp. 41–52.

George, D. L. and Iverson, R. M. (2014). "A depth-averaged debris-flow model that includes the effects of evolving dilatancy. II. Numerical predictions and experimental tests". In: *Proceedings of the Royal Society A: Mathematical, Physical and Engineering Sciences* 470.2170, p. 20130820.

Gingold, R. A. and Monaghan, J. J. (1977). "Smoothed particle hydrodynamics: theory and application to non-spherical stars". In: *Monthly Notices of the Royal Astronomical Society* 181.3, pp. 375–389.

Gómez-Gesteira, M and Dalrymple, R. A. (2004). "Using a three-dimensional smoothed particle hydrodynamics method for wave impact on a tall structure". In: *Journal of Waterway, Port, Coastal, and Ocean Engineering* 130.2, pp. 63–69.

Gómez-Gesteira, M., Rogers, B. D., Dalrymple, R. A., and Crespo, A. J. (2010). "State-of-the-art of classical SPH for free-surface flows". In: *Journal of Hydraulic Research* 48.S1, pp. 6–27.

Gray, J. P., Monaghan, J. J., and Swift, R. P. (2001). "SPH elastic dynamics". In: *Computer Methods in Applied Mechanics and Engineering* 190.49-50, pp. 6641–6662.

Griffiths, D. and Marquez, R. (2007). "Three-dimensional slope stability analysis by elasto-plastic finite elements". In: *Geotechnique* 57.6, pp. 537–546.

Gutfraind, R. and Savage, S. B. (1997). "Smoothed particle hydrodynamics for the simulation of broken-ice fields: Mohr–Coulomb-type rheology and frictional boundary conditions". In: *Journal of Computational Physics* 134.2, pp. 203–215.

Haddad, B., Pastor, M., Palacios, D., and Munoz-Salinas, E. (2010). "A SPH depth integrated model for Popocatépetl 2001 lahar (Mexico): Sensitivity analysis and runout simulation". In: *Engineering Geology* 114.3, pp. 312–329.

Hallermeier, R. J. (1981). "Terminal settling velocity of commonly occurring sand grains". In: *Sedimentology* 28.6, pp. 859–865.

Harlow, F. H. and Welch, J. E. (1965). "Numerical calculation of time-dependent viscous incompressible flow of fluid with free surface". In: *The Physics of Fluids* 8.12, pp. 2182–2189.

Heeres, O. M., Suiker, A. S., and Borst, R. de (2002). "A comparison between the Perzyna viscoplastic model and the consistency viscoplastic model". In: *European Journal of Mechanics-A/Solids* 21.1, pp. 1–12.

Henn, B., Cao, Q., Lettenmaier, D. P., Magirl, C. S., Mass, C., Brent Bower, J., St. Laurent, M., Mao, Y., and Perica, S. (2015). "Hydroclimatic conditions preceding the March 2014 Oso landslide". In: *Journal of Hydrometeorology* 16.3, pp. 1243–1249.

Herschel, W. H. and Bulkley, R. (1926). "Konsistenzmessungen von gummi-benzollösungen". In: *Colloid & Polymer Science* 39.4, pp. 291–300.

Hockney, R., Goel, S., and Eastwood, J. (1973). "A 10000 particle molecular dynamics model with long range forces". In: *Chemical Physics Letters* 21.3, pp. 589–591.

Holtz, R. D. and Schuster, R. L. (1996). "Landslides: investigation and mitigation. Chapter 17-Stabilization of soil slopes". In: *Transportation Research Board Special Report* 247, pp. 439–473.

Hu, M., Liu, M., Xie, M., and Liu, G. (2015). "Three-dimensional run-out analysis and prediction of flow-like landslides using smoothed particle hydrodynamics". In: *Environmental Earth Sciences* 73.4, pp. 1629–1640.

Huang, Y., Cheng, H., Dai, Z., Xu, Q., Liu, F., Sawada, K., Moriguchi, S., and Yashima, A. (2015). "SPH-based numerical simulation of catastrophic debris flows after the 2008 Wenchuan earthquake". In: *Bulletin of Engineering Geology and the Environment* 74.4, pp. 1137–1151.

Hughes, T. J. (2012). *The finite element method: linear static and dynamic finite element analysis*. Courier Corporation.

Hungr, O. (2008). "Numerical modelling of the dynamics of debris flows and rock avalanches". In: *Geomechanics and Tunnelling* 1.2, pp. 112–119.

— (2018). "Some methods of landslide hazard intensity mapping". In: *Landslide Risk Assessment*. Routledge, pp. 215–226.

Hunt, B. (1994). "Newtonian fluid mechanics treatment of debris flows and avalanches". In: *Journal of Hydraulic Engineering* 120.12, pp. 1350–1363.

Hutchinson, J. W. and Tvergaard, V. (1981). "Shear band formation in plane strain". In: *International Journal of Solids and Structures* 17.5, pp. 451–470.

Idelsohn, S. R., Onate, E., Calvo, N., and Del Pin, F. (2003). "The meshless Finite Element Method". In: *International Journal for Numerical Methods in Engineering* 58.6, pp. 893–912.

Imran, J., Parker, G., Locat, J., and Lee, H. (2001). "1D numerical model of muddy subaqueous and subaerial debris flows". In: *Journal of Hydraulic Engineering* 127.11, pp. 959–968.

Iverson, R. M. and George, D. L. (2016). "Modelling landslide liquefaction, mobility bifurcation and the dynamics of the 2014 Oso disaster". In: *Geotechnique* 66, pp. 175–187.

Iverson, R. M. (1997). "The physics of debris flows". In: *Reviews of Geophysics* 35.3, pp. 245–296.

— (2003). "The debris-flow rheology myth". In: *Debris-Flow Hazards Mitigation: Mechanics, Prediction, and Assessment* 1, pp. 303–314.

— (2015). "Scaling and design of landslide and debris-flow experiments". In: *Geomorphology*.

Iverson, R. M. and Denlinger, R. P. (2001). "Flow of variably fluidized granular masses across three-dimensional terrain: 1. Coulomb mixture theory". In: *Journal of Geophysical Research: Solid Earth* 106.B1, pp. 537–552.

Iverson, R. M. and George, D. L. (2014). "A depth-averaged debris-flow model that includes the effects of evolving dilatancy. I. Physical basis". In: *Proceedings of the Royal Society of London A: Mathematical, Physical and Engineering Sciences*. Vol. 470. 2170. The Royal Society, p. 20130819.

Iverson, R. M. and Ouyang, C. (2015). "Entrainment of bed material by Earth-surface mass flows: Review and reformulation of depth-integrated theory". In: *Reviews of Geophysics* 53.1, pp. 27–58.

Iverson, R. M., Reid, M. E., and LaHusen, R. G. (1997). "Debris-flow mobilization from landslides". In: *Annual Review of Earth and Planetary Sciences* 25.1, pp. 85–138.

Iverson, R. M., Logan, M., LaHusen, R. G., and Berti, M. (2010). "The perfect debris flow? Aggregated results from 28 large-scale experiments". In: *Journal of Geophysical Research: Earth Surface* 115.F3.

Iverson, R. M., Reid, M. E., Logan, M., LaHusen, R. G., Godt, J. W., and Griswold, J. P. (2011). "Positive feedback and momentum growth during debris-flow entrainment of wet bed sediment". In: *Nature Geoscience* 4.2, pp. 116–121.

Johnson, A. M. (1970). *Physical processes in geology: a method for interpretation of natural phenomena; intrusions in igneous rocks, fractures, and folds, flow of debris and ice*. Freeman, Cooper.

Johnson, C. G., Kokelaar, B. P., Iverson, R. M., Logan, M., LaHusen, R. G., and Gray, J. M.N. T (2012). "Grain-size segregation and levee formation in geophysical mass flows". In: *Journal of Geophysical Research: Earth Surface* 117.F1.

Johnson, G. R. and Beissel, S. R. (1996). "Normalized smoothing functions for SPH impact computations". In: *International Journal for Numerical Methods in Engineering* 39.16, pp. 2725–2741.

Johnson, P. C. and Jackson, R. (1987). "Frictional–collisional constitutive relations for granular materials, with application to plane shearing". In: *Journal of Fluid Mechanics* 176, pp. 67–93.

Kaitna, R., Dietrich, W. E., and Hsu, L. (2014). "Surface slopes, velocity profiles and fluid pressure in coarse-grained debris flows saturated with water and mud". In: *Journal of Fluid Mechanics* 741, pp. 377–403.

Kaitna, R., Rickenmann, D., and Schatzmann, M. (2007). "Experimental study on rheologic behaviour of debris flow material". In: *Acta Geotechnica* 2.2, pp. 71–85.

Kaitna, R., Palucis, M. M., Hill, K. M., and Dietrich, W. E. (2016). "Effects of coarse grain size distribution and fine particle content on pore fluid pressure and shear behavior in experimental debris flows". In: *Journal of Geophysical Research: Earth Surface*.

King, J. P. (2001). *The 2000 Tsing Shan debris flow and debris flood. Landslide study report LSR 2/2001*. Geotechnical Engineering Office, Civil Engineering and Development Department, The Government of the Hong Kong Special Administrative Region, Hong Kong.

Kneller, B. C., Bennett, S. J., and McCaffrey, W. D. (1999). "Velocity structure, turbulence and fluid stresses in experimental gravity currents". In: *Journal of Geophysical Research: Oceans* 104.C3, pp. 5381–5391.

Koshizuka, S. and Oka, Y. (1996). "Moving-particle semi-implicit method for fragmentation of incompressible fluid". In: *Nuclear Science and Engineering* 123.3, pp. 421–434.

Laigle, D. and Coussot, P. (1997). "Numerical modeling of mudflows". In: *Journal of Hydraulic Engineering* 123.7, pp. 617–623.

Laouafa, F. and Darve, F. (2002). "Modelling of slope failure by a material instability mechanism". In: *Computers and Geotechnics* 29.4, pp. 301–325.

Lee, E.-S., Moulinec, C., Xu, R., Violeau, D., Laurence, D., and Stansby, P. (2008). "Comparisons of weakly compressible and truly incompressible algorithms for the SPH mesh free particle method". In: *Journal of Computational Physics* 227.18, pp. 8417–8436.

Legros, F. (2002). "The mobility of long-runout landslides". In: *Engineering Geology* 63.3-4, pp. 301–331.

Li, S. and Liu, W. K. (1999). "Reproducing kernel hierarchical partition of unity, part I—formulation and theory". In: *International Journal for Numerical Methods in Engineering* 45.3, pp. 251–288.

— (2002). "Meshfree and particle methods and their applications". In: *Applied Mechanics Reviews* 55.1, pp. 1–34.

Li, X., Zienkiewicz, O. C., and Xie, Y. M. (1990). "A numerical model for immiscible two-phase fluid flow in a porous medium and its time domain solution". In: *International Journal for Numerical Methods in Engineering* 30.6, pp. 1195–1212.

Lind, S. J., Xu, R., Stansby, P. K., and Rogers, B. D. (2012). "Incompressible smoothed particle hydrodynamics for free-surface flows: A generalised diffusion-based algorithm for stability and validations for impulsive flows and propagating waves". In: *Journal of Computational Physics* 231.4, pp. 1499–1523.

Liu, M. and Liu, G. (2006). "Restoring particle consistency in smoothed particle hydrodynamics". In: *Applied Numerical Mathematics* 56.1, pp. 19–36.

— (2010). "Smoothed particle hydrodynamics (SPH): an overview and recent developments". In: *Archives of Computational Methods in Engineering* 17.1, pp. 25–76.

Liu, M., Liu, G., and Lam, K. (2003). "Constructing smoothing functions in smoothed particle hydrodynamics with applications". In: *Journal of Computational and Applied Mathematics* 155.2, pp. 263–284.

Liu, M., Shao, J., and Chang, J. (2012). "On the treatment of solid boundary in smoothed particle hydrodynamics". In: *Science China Technological Sciences* 55.1, pp. 244–254.

Liu, W. K., Jun, S., and Zhang, Y. F. (1995). "Reproducing kernel particle methods". In: *International Journal for Numerical Methods in Fluids* 20.8-9, pp. 1081–1106.

Lloyd, P. (2003). "Particle Size Analysis". In: *Encyclopedia of Physical Science and Technology (Third Edition)*. Academic Press, pp. 649 –654.

Lowe, R. J., Linden, P., and Rottman, J. W. (2002). "A laboratory study of the velocity structure in an intrusive gravity current". In: *Journal of Fluid Mechanics* 456, pp. 33–48.

Lu, Y. Y., Belytschko, T., and Gu, L. (1994). "A new implementation of the element free Galerkin method". In: *Computer Methods in Applied Mechanics and Engineering* 113.3-4, pp. 397–414.

Lucy, L. B. (1977). "A numerical approach to the testing of the fission hypothesis". In: *The Astronomical Journal* 82, pp. 1013–1024.

Mabssout, M. and Herreros, M. I. (2013). "Runge–Kutta vs Taylor-SPH: Two time integration schemes for SPH with application to soil dynamics". In: *Applied Mathematical Modelling* 37.5, pp. 3541–3563.

Maeda, K. and Sakai, M. (2004). "Development of seepage failure analysis procedure of granular ground with Smoothed Particle Hydrodynamics (SPH) method". In: *Journal of Applied Mechanics* 7, pp. 775–786.

Maenchen, G. and Sack, S. (1963). *The TENSOR code*. Tech. rep. California. Univ., Livermore. Lawrence Radiation Lab.

Mansour, M. F., Morgenstern, N. R., and Martin, C. D. (2011). "Expected damage from displacement of slow-moving slides". In: *Landslides* 8.1, pp. 117–131.

Mao, Z. and Liu, G. (2018). "A Lagrangian gradient smoothing method for solid-flow problems using simplicial mesh". In: *International Journal for Numerical Methods in Engineering* 113.5, pp. 858–890.

Marrone, S., Colagrossi, A., Le Touzé, D., and Graziani, G. (2010). "Fast free-surface detection and level-set function definition in SPH solvers". In: *Journal of Computational Physics* 229.10, pp. 3652–3663.

Martel, S. (2004). "Mechanics of landslide initiation as a shear fracture phenomenon". In: *Marine Geology* 203.3-4, pp. 319–339.

McArdell, B. W., Bartelt, P., and Kowalski, J. (2007). "Field observations of basal forces and fluid pore pressure in a debris flow". In: *Geophysical Research Letters* 34.7.

McDougall, S. and Hungr, O. (2004). "A model for the analysis of rapid landslide motion across three-dimensional terrain". In: *Canadian Geotechnical Journal* 41.6, pp. 1084–1097.

Merritt, A., Chambers, J., Murphy, W, Wilkinson, P., West, L., Uhlemann, S, Meldrum, P., and Gunn, D (2018). "Landslide activation behaviour illuminated by electrical resistance monitoring". In: *Earth Surface Processes and Landforms* 43.6, pp. 1321–1334.

Minatti, L. and Paris, E. (2015). "A SPH model for the simulation of free surface granular flows in a dense regime". In: *Applied Mathematical Modelling* 39.1, pp. 363–382.

Mohr, O. (1900). "Welche Umstände bedingen die Elastizitäsgrenze und den Bruch eines Materials". In: *Zeit. Vereines Deutsch. Ing* 44, pp. 1–12.

Monaghan, J. J. (1989). "On the problem of penetration in particle methods". In: *Journal of Computational Physics* 82.1, pp. 1–15.

Monaghan, J. J. and Gingold, R. A. (1983). "Shock simulation by the particle method SPH". In: *Journal of Computational Physics* 52.2, pp. 374–389.

Monaghan, J. J. and Kocharyan, A. (1995). "SPH simulation of multi-phase flow". In: *Computer Physics Communications* 87.1-2, pp. 225–235.

Monaghan, J. J. and Kos, A. (1999). "Solitary waves on a Cretan beach". In: *Journal of Waterway, Port, Coastal, and Ocean Engineering* 125.3, pp. 145–155.

Monaghan, J. J. (1982). "Why particle methods work". In: *SIAM Journal on Scientific and Statistical Computing* 3.4, pp. 422–433.

— (1992). "Smoothed particle hydrodynamics". In: *Annual review of Astronomy and Astrophysics* 30.1, pp. 543–574.

Monaghan, J. J. (1988). "An introduction to SPH". In: *Computer Physics Communications* 48.1, pp. 89–96.

— (1994). "Simulating Free Surface Flows with SPH". In: *Journal of Computational Physics* 110.2, pp. 399–406.

— (2000). "SPH without a tensile instability". In: *Journal of Computational Physics* 159.2, pp. 290–311.

Monaghan, J. J. (2012). "Smoothed particle hydrodynamics and its diverse applications". In: *Annual Review of Fluid Mechanics* 44, pp. 323–346.

Moresi, L., Dufour, F., and Mühlhaus, H.-B. (2003). "A Lagrangian integration point finite element method for large deformation modeling of viscoelastic geomaterials". In: *Journal of Computational Physics* 184.2, pp. 476–497.

Morris, J. P., Fox, P. J., and Zhu, Y. (1997). "Modeling low Reynolds number incompressible flows using SPH". In: *Journal of Computational Physics* 136.1, pp. 214–226.

Nguyen, C. T., Nguyen, C. T., Bui, H. H., Nguyen, G. D., and Fukagawa, R. (2017). "A new SPH-based approach to simulation of granular flows using viscous damping and stress regularisation". In: *Landslides* 14.1, pp. 69–81.

Oger, G., Marrone, S., Le Touzé, D., and De Leffe, M. (2016). "SPH accuracy improvement through the combination of a quasi-Lagrangian shifting transport velocity and consistent ALE formalisms". In: *Journal of Computational Physics* 313, pp. 76–98.

Oldroyd, J. G. (1947). "A rational formulation of the equations of plastic flow for a Bingham solid". In: *Mathematical Proceedings of the Cambridge Philosophical Society*. Vol. 43. 1. Cambridge University Press, pp. 100–105.

Pailha, M. and Pouliquen, O. (2009). "A two-phase flow description of the initiation of underwater granular avalanches". In: *Journal of Fluid Mechanics* 633, pp. 115–135.

Paiva, A., Petronetto, F., Lewiner, T., and Tavares, G. (2009). "Particle-based viscoplastic fluid/solid simulation". In: *Computer-Aided Design* 41.4, pp. 306–314.

Paleo Cageao, P. (2014). "Fluid-particle interaction in geophysical flows: debris flow". PhD thesis. University of Nottingham.

Palmer, A. C. and Rice, J. R. (1973). "The growth of slip surfaces in the progressive failure of over-consolidated clay". In: *Proceedings of the Royal Society of London. A. Mathematical and Physical Sciences* 332.1591, pp. 527–548.

Parsons, J. D., Whipple, K. X., and Simoni, A. (2001). "Experimental study of the grain-flow, fluid-mud transition in debris flows". In: *The Journal of Geology* 109.4, pp. 427–447.

Pastor, M, Blanc, T, and Pastor, M. (2009). "A depth-integrated viscoplastic model for dilatant saturated cohesive-frictional fluidized mixtures: application to fast catastrophic landslides". In: *Journal of Non-Newtonian Fluid Mechanics* 158.1, pp. 142–153.

Pastor, M., Li, T., and Fernández-Merodo, J. A. (1997). "Stabilized finite elements for harmonic soil dynamics problems near the undrained-incompressible limit". In: *Soil dynamics and Earthquake engineering* 16.3, pp. 161–171.

Pastor, M., Haddad, B., Sorbino, G., Cuomo, S., and Drempetic, V. (2009a). "A depth-integrated, coupled SPH model for flow-like landslides and related phenomena". In: *International Journal for Numerical and Analytical Methods in Geomechanics* 33.2, pp. 143–172.

Pastor, M., Herreros, M. I., Fernández-Merodo, J., Mira, P., Haddad, B., Quecedo, M., González, E., Alvarez-Cedrón, C., and Drempetic, V. (2009b). "Modelling of fast catastrophic landslides and impulse waves induced by them in fjords, lakes and reservoirs". In: *Engineering Geology* 109.1, pp. 124–134.

Pastor, M., Blanc, T., Haddad, B., Petrone, S., Morles, M. S., Drempetic, V., Issler, D., Crosta, G. B., Cascini, L., Sorbino, G., et al. (2014). "Application of a SPH depth-integrated model to landslide run-out analysis". In: *Landslides* 11.5, pp. 793–812.

Pastor, M., Stickle, M. M., Dutto, P., Mira, P., Fernández-Merodo, J. A., Blanc, T., Sancho, S., and Benítez, A. S. (2015a). "A viscoplastic approach to the behaviour of fluidized geomaterials with application to fast landslides". In: *Continuum Mechanics and Thermodynamics* 27.1-2, pp. 21–47.

Pastor, M., Blanc, T., Haddad, B., Drempetic, V., Morles, M. S., Dutto, P., Stickle, M. M., Mira, P., and Fernández-Merodo, J. A. (2015b). "Depth averaged models for fast landslide propagation: mathematical, rheological and numerical aspects". In: *Archives of Computational Methods in Engineering* 22.1, pp. 67–104.

Pastor, M., Yague, A., Stickle, M. M., Manzanal, D., and Mira, P. (2018). "A two-phase SPH model for debris flow propagation". In: *International Journal for Numerical and Analytical Methods in Geomechanics* 42.3, pp. 418–448.

Pastor, M., Fernández-Merodo, J. A., Haddad, B., Manzanal, D., Mira, P., Herreros, M. I., and Drempetic, V. (2008). "Modelling of fluidized geomaterials: application to fast landslides". In: *Journal of Theoretical and Applied Mechanics* 38.1-2, pp. 101–134.

Patankar, S. (1980). *Numerical heat transfer and fluid flow*. CRC press.

Patankar, S. V. and Spalding, D. B. (1983). "A calculation procedure for heat, mass and momentum transfer in three-dimensional parabolic flows". In: *Numerical Prediction of Flow, Heat Transfer, Turbulence and Combustion*. Elsevier, pp. 54–73.

Peakall, J. and Sumner, E. J. (2015). "Submarine channel flow processes and deposits: A process-product perspective". In: *Geomorphology* 244, pp. 95–120.

Pelanti, M., Bouchut, F., and Mangeney, A. (2008). "A Roe-type scheme for two-phase shallow granular flows over variable topography". In: *ESAIM: Mathematical Modelling and Numerical Analysis* 42.5, pp. 851–885.

Peng, C., Wu, W., Yu, H.-s., and Wang, C. (2015). "A SPH approach for large deformation analysis with hypoplastic constitutive model". In: *Acta Geotechnica* 10.6, pp. 703–717.

Perzyna, P. (1966). "Fundamental Problems in Viscoplasticity". In: *Advances in Applied Mechanics* 9, p. 243.

Petley, D. (2012). "Global patterns of loss of life from landslides". In: *Geology* 40.10, pp. 927–930.

Pirulli, M. and Pastor, M (2012). "Numerical study on the entrainment of bed material into rapid landslides". In: *Geotechnique* 62.11, pp. 959–972.

Pirulli, M. and Sorbino, G. (2008). "Assessing potential debris flow runout: a comparison of two simulation models". In: *Natural Hazards and Earth System Science* 8, pp. 961–971.

Pitman, E. B. and Le, L. (2005). "A two-fluid model for avalanche and debris flows". In: *Philosophical Transactions of the Royal Society of London A: Mathematical, Physical and Engineering Sciences* 363.1832, pp. 1573–1601.

Plafker, G. and Ericksen, G. (1978). "Nevados Huascaran avalanches, Peru". In: *Developments in Geotechnical Engineering*. Vol. 14. Elsevier, pp. 277–314.

Postma, G., Nemec, W., and Kleinspehn, K. L. (1988). "Large floating clasts in turbidites: a mechanism for their emplacement". In: *Sedimentary Geology* 58.1, pp. 47–61.

Powrie, W. (2004). *Soil mechanics: concepts and applications*. Abingdon, Oxon: Spon Press.

Prager, W. (2004). *Introduction to mechanics of continua*. Courier Corporation.

Pudasaini, S. P. (2012). "A general two-phase debris flow model". In: *Journal of Geophysical Research: Earth Surface* 117.F3.

Pudasaini, S. P., Hsiau, S.-S., Wang, Y., and Hutter, K. (2005). "Velocity measurements in dry granular avalanches using particle image velocimetry technique and comparison with theoretical predictions". In: *Physics of Fluids (1994-present)* 17.9, p. 093301.

Quinlan, N. J., Basa, M., and Lastiwka, M. (2006). "Truncation error in mesh-free particle methods". In: *International Journal for Numerical Methods in Engineering* 66.13, pp. 2064–2085.

Rabczuk, T. and Belytschko, T. (2007). "A three-dimensional large deformation meshfree method for arbitrary evolving cracks". In: *Computer Methods in Applied Mechanics and Engineering* 196.29-30, pp. 2777–2799.

Rabczuk, T., Belytschko, T., and Xiao, S. P. (2004). "Stable particle methods based on Lagrangian kernels". In: *Computer Methods in Applied Mechanics and Engineering* 193.12-14, pp. 1035–1063.

Rabczuk, T., Areias, P. M. A., and Belytschko, T. (2007). "A simplified mesh-free method for shear bands with cohesive surfaces". In: *International Journal for Numerical Methods in Engineering* 69.5, pp. 993–1021.

Rabczuk, T. and Belytschko, T. (2004). "Cracking particles: a simplified meshfree method for arbitrary evolving cracks". In: *International Journal for Numerical Methods in Engineering* 61.13, pp. 2316–2343.

Rabczuk, T., Gracie, R., Song, J.-H., and Belytschko, T. (2010). "Immersed particle method for fluid–structure interaction". In: *International Journal for Numerical Methods in Engineering* 81.1, pp. 48–71.

Randles, P. and Libersky, L. (1996). "Smoothed particle hydrodynamics: some recent improvements and applications". In: *Computer Methods in Applied Mechanics and Engineering* 139.1-4, pp. 375–408.

— (2000). "Normalized SPH with stress points". In: *International Journal for Numerical Methods in Engineering* 48.10, pp. 1445–1462.

Roache, P. J. (1972). *Computational fluid dynamics*. Hermosa publishers.

Rowe, P. W. (1962). "The stress-dilatancy relation for static equilibrium of an assembly of particles in contact". In: *Proceedings of the Royal Society of London. Series A. Mathematical and Physical Sciences* 269.1339, pp. 500–527.

Sanchez, J. and Randles, P. (2012). "Dynamic failure simulation of quasi-brittle material in dual particle dynamics". In: *International Journal for Numerical Methods in Engineering* 91.11, pp. 1227–1250.

— (2013). "A quasi-static dual particle method for solids based on dual particle dynamics". In: *International Journal for Numerical Methods in Engineering* 94.2, pp. 183–203.

Sanvitale, N. and Bowman, E. T. (2012). "Internal imaging of saturated granular free-surface flows". In: *International Journal of Physical Modelling in Geotechnics* 4.12, pp. 129–142.

— (2017). "Visualization of dominant stress-transfer mechanisms in experimental debris flows of different particle-size distribution". In: *Canadian Geotechnical Journal* 54.2, pp. 258–269.

Savage, S. B. and Hutter, K. (1989). "The motion of a finite mass of granular material down a rough incline". In: *Journal of Fluid Mechanics* 199, pp. 177–215.

Schuessler, I. and Schmitt, D. (1981). "Comments on smoothed particle hydrodynamics". In: *Astronomy and Astrophysics* 97, pp. 373–379.

Schuster, R. L. (1996). "Landslides: Investigation and Mitigation. Chapter 2-Socioeconomic Significance of Landslides". In: *Transportation Research Board Special Report* 247, pp. 12–35.

Schuster, R. L. and Fleming, R. W. (1986). "Economic losses and fatalities due to landslides". In: *Bulletin of the Association of Engineering Geologists* 23.1, pp. 11–28.

Shao, S. and Gotoh, H. (2005). "Turbulence particle models for tracking free surfaces". In: *Journal of Hydraulic Research* 43.3, pp. 276–289.

Shao, S. and Lo, E. Y. (2003). "Incompressible SPH method for simulating Newtonian and non-Newtonian flows with a free surface". In: *Advances in Water Resources* 26.7, pp. 787–800.

Shield, R. (1955). "On Coulomb's law of failure in soils". In: *Journal of the Mechanics and Physics of Solids* 4.1, pp. 10–16.

Simpson, J. C. (1995). "Numerical techniques for three-dimensional smoothed particle hydrodynamics simulations: applications to accretion disks". In: *The Astrophysical Journal* 448, p. 822.

Simpson, J. and Britter, R. (1979). "The dynamics of the head of a gravity current advancing over a horizontal surface". In: *Journal of Fluid Mechanics* 94.3, pp. 477–495.

Sluys, L. J. (1992). "Wave propagation, localisation and dispersion in softening solids". In:

Soga, K., Alonso, E., Yerro, A., Kumar, K., and Bandara, S. (2015). "Trends in large-deformation analysis of landslide mass movements with particular emphasis on the material point method". In: *Géotechnique*, pp. 1–26.

Steinmetz, M. and Mueller, E. (1993). "On the capabilities and limits of smoothed particle hydrodynamics". In: *Astronomy and Astrophysics* 268, pp. 391–410.

Stevenson, C. J., Feldens, P., Georgiopoulou, A., Schönke, M., Krastel, S., Piper, D. J. W., Lindhorst, K., and Mosher, D. (2018). "Reconstructing the sediment concentration of a giant submarine gravity flow". In: *Nature Communications* 9.1, p. 2616.

Swegle, J. W., Attaway, S. W., Heinstein, M. W., Mello, F. J., and Hicks, D. L. (1994). *An analysis of smoothed particle hydrodynamics*. Tech. rep. Sandia National Labs., Albuquerque, New Mexico (United States).

Swegle, J. W. (2000). *Conservation of momentum and tensile instability in particle methods*. Tech. rep. Sandia National Labs., Albuquerque, NM, and Livermore, CA (US).

Takahashi, T. (1981). "Debris flow". In: *Annual Review of Fluid Mechanics* 13.1, pp. 57–77.

Take, W. A., Bolton, M. D., Wong, P. C. P., and Yeung, F. J. (2004). "Evaluation of landslide triggering mechanisms in model fill slopes". In: *Landslides* 1.3, pp. 173–184.

Takeda, H., Miyama, S. M., and Sekiya, M. (1994). "Numerical simulation of viscous flow by smoothed particle hydrodynamics". In: *Progress of Theoretical Physics* 92.5, pp. 939–960.

Tarchi, D., Casagli, N., Fanti, R., Leva, D. D., Luzi, G., Pasuto, A., Pieraccini, M., and Silvano, S. (2003). "Landslide monitoring by using ground-based SAR interferometry: an example of application to the Tessina landslide in Italy". In: *Engineering Geology* 68.1-2, pp. 15–30.

Taylor, D. W. (1937). "Stability of earth slopes". In: *Journal of the Boston Society of Civil Engineers* 24.3, pp. 197–247.

Taylor, G. I. (1948). "The use of flat-ended projectiles for determining dynamic yield stress I. Theoretical considerations". In: *Proceedings of the Royal Society of London* 194.1038, pp. 289–299.

Terzaghi, K. v. (1936). "The shearing resistance of saturated soils". In: *Proceedings of the First International Conference on Soil Mechanics*. Vol. 1, pp. 54–56.

Tresca, H. (1864). "Memoir on the flow of solid bodies under strong pressure". In: *Comptes-Rendus de l'Académie des Sciences* 59, pp. 754–758.

Troncone, A. (2005). "Numerical analysis of a landslide in soils with strain-softening behaviour". In: *Geotechnique* 55.8, pp. 585–596.

Troncone, A., Conte, E., and Donato, A. (2014). "Two and three-dimensional numerical analysis of the progressive failure that occurred in an excavation-induced landslide". In: *Engineering Geology* 183, pp. 265–275.

Turnbull, B., Bowman, E. T., and McElwaine, J. N. (2015). "Debris flows: Experiments and modelling". In: *Comptes Rendus Physique* 16.1, pp. 86–96.

Varnes, D. J. (1958). "Landslide types and processes". In: *Landslides and Engineering Practice* 24, pp. 20–47.

— (1978). "Slope movement types and processes". In: *Transportation Research Board Special Report* 176, pp. 11–33.

Vidal, Y., Bonet, J., and Huerta, A. (2007). "Stabilized updated Lagrangian corrected SPH for explicit dynamic problems". In: *International Journal for Numerical Methods in Engineering* 69.13, pp. 2687–2710.

Vignjevic, R., Campbell, J., and Libersky, L. (2000). "A treatment of zero-energy modes in the smoothed particle hydrodynamics method". In: *Computer Methods in Applied Mechanics and Engineering* 184.1, pp. 67–85.

Violeau, D. and Issa, R. (2007). "Numerical modelling of complex turbulent free-surface flows with the SPH method: an overview". In: *International Journal for Numerical Methods in Fluids* 53.2, pp. 277–304.

Voellmy, A. (1964). "Uber die zerstorungskraft von lawinen". In: *Schweizerische Bauzeitung* 73.12, pp. 159–165,212–217,246–249,280–285.

Von Mises, R. (1913). "Mechanik der festen Körper im plastisch-deformablen Zustand". In: *Nachrichten von der Gesellschaft der Wissenschaften zu Göttingen, Mathematisch-Physikalische Klasse* 1913, pp. 582–592.

Von Neumann, J. and Richtmyer, R. D. (1950). "A method for the numerical calculation of hydrodynamic shocks". In: *Journal of Applied Physics* 21.3, pp. 232–237.

Wang, C., Wang, Y., Peng, C., and Meng, X. (2016a). "Smoothed particle hydrodynamics simulation of water-soil mixture flows". In: *Journal of Hydraulic Engineering* 142.10, p. 04016032.

Wang, L., Ge, W., and Li, J. (2006). "A new wall boundary condition in particle methods". In: *Computer Physics Communications* 174.5, pp. 386–390.

Wang, W., Chen, G., Han, Z., Zhou, S., Zhang, H., and Jing, P. (2016b). "3D numerical simulation of debris-flow motion using SPH method incorporating non-Newtonian fluid behavior". In: *Natural Hazards* 81.3, pp. 1981–1998.

Wieczorek, G. F. (1996). "Landslides: investigation and mitigation. Chapter 4-Landslide triggering mechanisms". In: *Transportation Research Board Special Report* 247, pp. 76–90.

Willemsen, S., Hoefsloot, H., and Iedema, P. (2000). "No-slip boundary condition in dissipative particle dynamics". In: *International Journal of Modern Physics C* 11.05, pp. 881–890.

Wyllie, D. C. and Norrish, N. I. (1996). "Landslides: investigation and mitigation. Chapter 18-Stabilization of rock slopes". In: *Transportation Research Board Special Report* 247, pp. 474–504.

Xiao, S. P. and Belytschko, T. (2005). "Material stability analysis of particle methods". In: *Advances in Computational Mathematics* 23.1-2, pp. 171–190.

Xu, R., Stansby, P., and Laurence, D. (2009). "Accuracy and stability in incompressible SPH (ISPH) based on the projection method and a new approach". In: *Journal of Computational Physics* 228.18, pp. 6703–6725.

Xu, X. and Yu, P. (2018). "A technique to remove the tensile instability in weakly compressible SPH". In: *Computational Mechanics* 62.5, pp. 963–990.

Zabala, F. and Alonso, E. (2011). "Progressive failure of Aznalcóllar dam using the material point method". In: *Géotechnique* 61.9, pp. 795–808.

Zheng, H., Liu, D., and Li, C. (2005). "Slope stability analysis based on elastoplastic finite element method". In: *International Journal for Numerical Methods in Engineering* 64.14, pp. 1871–1888.

Žic, E., Arbanas, Ž., Bicanic, N., and Ožanic, N. (2015). "A model of mudflow propagation downstream from the Grohovo landslide near the city of Rijeka (Croatia)". In: *Natural Hazards and Earth System Sciences* 15, pp. 293–313.

Zienkiewicz, O. C., Chang, C. T., and Bettess, P. (1980). "Drained, undrained, consolidating and dynamic behaviour assumptions in soils". In: *Geotechnique* 30.4, pp. 385–395.

Zienkiewicz, O. C. and Shiomi, T. (1984). "Dynamic behaviour of saturated porous media; the generalized Biot formulation and its numerical solution". In: *International Journal for Numerical and Analytical Methods in Geomechanics* 8.1, pp. 71–96.